RXTE Monitoring of 5 Anomalous X-ray Pulsars

Rim Dib
Department of Physics
McGill University

October 06, 2009

A thesis submitted to McGill University in partial fulfillment
of the requirements of the degree of Doctor of Philosophy

Abstract

Anomalous X-ray Pulsars (AXPs) are a group of neutron stars that share several common properties. They are dubbed "anomalous" because their observed luminosity exceeds the rate of loss of their rotational kinetic energy. According to the magnetar model, they are young, isolated neutron stars, powered by a large magnetic energy reservoir. Five of these AXPs (1E 2259+586, 4U 0142+61, RXS J170849.0−400910, 1E 1841−045, 1E 1048.1−5937) have been monitored with the Rossi X-ray Timing Explorer (RXTE) since 1997 (1998 for two of the sources). The goal of the monitoring program is to study the timing behaviour of these sources including glitches, and the radiative variability in the soft X-ray band including pulsed flux changes, pulse profile changes, and bursts. The program provides a detailed description of the evolving properties of these objects, which can then be used to test AXP models, such as the magnetar model. In this thesis, I present some of my co-authored contributions to the AXP monitoring program.

I first present a long-term (1998−2006) study of AXP 4U 0142+61 in which we show that from 2000 to 2006 the pulse profile of the pulsar slowly evolved, and the pulsed flux increased by 29±8%.

AXP 4U 0142+61 then entered an active phase in 2006 March that lasted several months and included several X-ray bursts. I present a study of the behaviour of AXP 4U 0142+61 during this active phase.

I then present a long-term (1998−2007) study of AXPs RXS J170849.0−400910 and 1E 1841−045 in which we report on four new glitches. We show that AXPs are very active glitchers and that some AXP glitch properties are challenging to interpret in standard glitch models. Furthermore, we note that AXP glitches appear to fall in two classes: radiatively loud and radiatively quiet.

Finally, I present a long-term (1997−2008) study of AXP 1E 1048.1−5937 in which we show that three timing events occurred contemporaneously with the onset of three pulsed flux flares. We note that every observed AXP flare or outburst thus far has been accompanied by a timing event, but that the converse is not true. We also comment on various unusual timing and radiative properties of this source.

In each of the above contributions, we discuss the relationships between the observed properties in the framework of the magnetar model.

Résumé

Les pulsars X anormaux (AXPs) sont des étoiles à neutrons qui partagent certaines propriétés spécifiques. Ils sont dits "anormaux" car leur luminosité est supérieure au taux de perte de leur énergie de rotation. Selon le modèle des "magnétars", ces pulsars sont des étoiles à neutrons jeunes, isolées, et dont la luminosité provient d'un grand réservoir d'énergie magnétique. Cinq de ces AXPs (1E 2259+586, 4U 0142+61, RXS J170849.0−400910, 1E 1841−045, 1E 1048.1−5937) sont sous observation depuis 1997 dans le cadre d'un programme de surveillance utilisant le Rossi X-ray Timing Explorer (RXTE). Le but de ce programme est d'étudier les propriétés temporelles de ces pulsars tels les changements soudains de fréquence, et d'étudier leurs propriétés radiatives tels les changements de flux pulsé, les changements de profil de pulse, et les sursauts d'énergie. Ce programme de surveillance aide à obtenir une description détaillée des propriétés de ces objets, qui servira à tester les modèles théoriques des AXPs, dont le modèle des "magnétars". Dans cette thèse, je présente quelques-unes de mes contributions au programme de surveillance.

D'abord, je présente une étude à long terme (1998−2006) du AXP 4U 0142+61 où nous montrons qu'entre 2000 et 2006, le profil de pulse du pulsar a lentement évolué, et que le flux pulsé a augmenté de 29±8%.

Le AXP 4U 0142+61 est ensuite entré dans une phase active en mars 2006, dans laquelle il a émis plusieurs sursauts d'énergie. Je présente une étude du comportement du AXP 4U 0142+61 pendant cette phase active.

Ensuite, je présente une étude à long terme (1998−2007) des AXPs RXS J170849.0−400910 et 1E 1841−045. Dans cette étude, nous avons détecté quatre nouveaux changements soudains de fréquence. Nous montrons que dans le contexte de changements soudains de fréquence, les AXPs sont très actifs. Nous montrons aussi que les modèles théoriques de changements soudains de fréquence ont de la difficulté à expliquer certains comportements des AXPs. De plus, nous montrons que les changements soudains de fréquence des AXPs sont divisés en deux catégories: ceux qui sont "radiativement bruyants", et ceux qui sont "radiativement calmes".

Finalement, je présente une étude à long terme (1997−2008) du AXP 1E 1048.1 −5937 où nous montrons que trois événements temporels se sont produits en même temps que trois augmentations significatives de flux pulsé. Nous montrons aussi que les événements radiatifs détectés dans les AXPs sont toujours accompagnés d'événements temporels, mais que le contraire n'est pas nécessairement vrai. Nous étudions aussi certaines propriétés temporelles et radiatives peu communes de ce pulsar.

Dans chacune des contributions ci-dessus, nous discutons des relations entre les différentes propriétés observées et ce, dans le contexte du modèle des "magnétars".

Acknowledgments

First, I would like to thank my supervisor, Professor Vicky Kaspi: despite being incredibly busy, she always made time for one-on-one meetings with me, to check on my progress and to help me stay on the right track. I would also like to thank her for having proposed that I work on this exciting project in the first place. This project was a grad student's dream: you could always count on one of the Anomalous X-ray Pulsars to do something interesting and worth reporting!

Fotis Gavriil was the person who was responsible for monitoring the Anomalous X-ray Pulsars before I took over. I would like to thank him for answering the million questions that I had at the time he handed the project to me, and for being a helpful collaborator since then.

I would like to thank A. Archibald for spending many hours with me in coffee shops and restaurants discussing pulsars and helping increase my knowledge of them.

I would also like to thank our system administrator, Paul, for having fixed the computers that we run all our analysis on every time they crashed, broke, froze, disappeared from the network, or had a fit.

⋆ ⋆ ⋆

My greatest thanks go to my dad without whose long-term vision I would not have been able to do a PhD in astrophysics in North America. He left his old life and moved to a new country so that his kids can study whatever they wish. He worked really hard to be able to afford a house near a metro station for us to live in. And he was always there for me if I needed anything, including when I needed chocolate snacks necessary to keep awake at night when the thesis deadline was approaching.

Thanks also go to Nour Dib for occasionally proofreading short excerpts of this thesis. Le Wookie lui dit qu'il n'est pas fake, Finn lui dit qu'il n'est pas Irish, et Zonko lui dit "pas chat".

⋆ ⋆ ⋆

I would like to thank the few friends who checked on me every now and then while I was writing the thesis, especially my oldest friend Cristina who, to cheer me up, invited me to play with her cute pets Bill, Sasha (RIP), Oscar, and Lola.

Finally, thanks go to past and present members of the McGill Pulsar Group, especially Maggie, Cindy, and Marjorie, for making the work environment a fun environment during my PhD years.

⋆ ⋆ ⋆

The research presented in the manuscripts on which this thesis is based has been generously funded by various Canadian and international agencies. Below, I reproduce the acknowledgment sections of the individual manuscripts.

- Acknowledgments for the manuscript "*10 Years of RXTE Monitoring of the Anomalous X-Ray Pulsar 4U 0142+61: Long-Term Variability*" on which Chapter 2 is based:

  We thank Andrew Cumming for helpful conversations. This work was supported by the Natural Sciences and Engineering Research Council (NSERC) PGSD scholarship to RD. FPG is supported by the NASA Postdoctoral Program administered by Oak Ridge Associated Universities at NASA Goddard Space Flight Center. Additional support was provided by NSERC Discovery Grant Rgpin 228738-03, NSERC Steacie Supplement Smfsu 268264-03, FQRNT, CIAR, and CFI. VMK is a Lorne Trottier and Canada Research Chair.

- Acknowledgments for the manuscript "*The 2006−2007 Active Phase of Anomalous X-ray Pulsar 4U 0142+61: Radiative and Timing Changes, Bursts, and Burst Spectral Features*" on which Chapter 3 is based:

  We thank P. M. Woods and A. M. Beloborodov for useful discussion. This research has made use of data obtained through the High Energy Astrophysics Science Archive Research Center Online Service, provided by the NASA/Goddard Space Flight Center. Support was provided to VMK by NSERC Discovery Grant Rgpin 228738-08, an FQRNT Centre Grant, CIFAR, the Canada Research Chairs Program and the Lorne Trottier Chair in Astrophysics and Cosmology.

- Acknowledgments for the manuscript "*Glitches in Anomalous X-ray Pulsars*" on which Chapter 4 is based:

  We are grateful to Andrew Lyne for providing his unpublished glitch catalog. We thank Andrew Cumming, Chris Thompson and Pete Woods for useful comments. This work was supported by the Natural Sciences and Engineering Research Council (NSERC) PGSD scholarship to RD. FPG is supported by the NASA Postdoctoral Program administered by Oak Ridge Associated Universities at NASA Goddard Space Flight Center. Additional support was provided by NSERC Discovery Grant Rgpin 228738-03, NSERC Steacie Supplement Smfsu 268264-03, FQRNT, cifar, and CFI. VMK holds the Lorne Trottier in Astrophysics and Cosmology and a Canada Research Chair in Observational Astrophysics.

- Acknowledgments for the manuscript "*RXTE Monitoring of the Anomalous X-ray Pulsar 1E 1048.1-5937: Long-Term Variability and the 2007 March Event*" on which Chapter 5 is based:

  We thank A. Cumming and D. Eichler for useful discussions. Support was provided to VMK by NSERC Discovery Grant Rgpin 228738-08, an FQRNT Centre Grant, CIFAR, the Canada Research Chairs Program and the Lorne Trottier Chair in Astrophysics and Cosmology.

Contribution of Authors

The university guidelines for a manuscript-based thesis state that *"PhD candidates have the option of including, as part of the thesis, the text of one or more papers submitted, or to be submitted, for publication, or the clearly duplicated text of one or more published papers"*.

In accordance with the above, the results presented in this thesis are original work that was, or will be, published in the following refereed articles:

- Chapter 2 contains the lightly edited text of: Dib R., Kaspi V. M., & Gavriil F. P., *10 Years of RXTE Monitoring of the Anomalous X-Ray Pulsar 4U 0142+61: Long-Term Variability*, the Astrophysical Journal, Volume 666, Issue 2, pp. 1152-1164, 2007.

- Chapter 3 is based on excerpts from: Gavriil F. P., Dib R., & Kaspi V. M., *The 2006−2007 Active Phase of Anomalous X-ray Pulsar 4U 0142+61: Radiative and Timing Changes, Bursts, and Burst Spectral Features*, submitted to the Astrophysical Journal in 2009 April. Eprint arXiv:0905.1256.

- Chapter 4 contains the lightly edited text of: Dib R., Kaspi V. M., & Gavriil F. P., *Glitches in Anomalous X-ray Pulsars*, the Astrophysical Journal, Volume 673, Issue 2, pp. 1044-1061, 2008.

- Chapter 5 contains the lightly edited text of: Dib R., Kaspi V. M., & Gavriil F. P., *RXTE Monitoring of the Anomalous X-ray Pulsar 1E 1048.1-5937: Long-Term Variability and the 2007 March Event*, the Astrophysical Journal, Volume 702, Issue 1, pp. 614-630, 2009.

- Chapter 6: some of the material presented in Chapter 6 will most likely be used towards the future manuscript "More Glitches in Anomalous X-ray Pulsars".

Here I would like to specify my contributions and acknowledge those of my co-authors to the above manuscripts:

- Chapter 2: The data analysis was entirely performed and the manuscript was entirely written by me. My supervisor, Victoria M. Kaspi, offered continuous guidance about the scientific content and interpretation of the results. Both Victoria M. Kaspi and Fotis P. Gavriil provided valuable comments during the writing process of the manuscript.

- Chapter 3: The manuscript that this Chapter is based on was originally intended to be two separate manuscripts which were, at the end, merged. In the final manuscript, the burst temporal and spectral analyses were performed by Fotis P. Gavriil. All Sections related to the burst temporal and spectral properties were

written by Fotis P. Gavriil. These Sections are only summarized in this thesis, with the details left out. *The timing analysis, pulse profile analysis, pulsed flux analysis, and burst phase analysis were performed by me. All Sections related to the timing properties, pulsed flux changes, and pulse profile evolution were written by me*. The discussion Section was a joint effort but was mostly written by Victoria M. Kaspi. Victoria M. Kaspi provided very valuable comments during the writing process of the manuscript.

- Chapter 4: The data analysis was entirely performed by me. The analysis and results Sections of the manuscript were mostly written by me, with some input from Victoria M. Kaspi. The discussion Section was jointly written by Victoria M. Kaspi and me, with the greater part contributed by Victoria M. Kaspi. Fotis P. Gavriil provided comments during the writing process of the manuscript.

- Chapter 5: The data analysis was performed by me except for *a)* the temporal and spectral analyses of the burst and *b)* analysis of any *Chandra* data, which were performed by Fotis P. Gavriil. The manuscript was entirely written by me. My supervisor, Victoria M. Kaspi, offered continuous guidance about the scientific content and interpretation of the results. Both Victoria M. Kaspi and Fotis P. Gavriil provided valuable comments during the writing process of the manuscript.

Note: The bulk of the data presented in the above manuscripts were reduced and analyzed by me using `FTOOLS`[1], `XSPEC`[2], `TEMPO`[3], `DS tools`[4], `fluxtools`[5], software written by Fotis Gavriil before he passed the lead of the AXP monitoring project to me, and software written by me.

[1] http://heasarc.gsfc.nasa.gov/ftools
[2] http://xspec.gsfc.nasa.gov
[3] http://www.atnf.csiro.au/research/pulsar/tempo
[4] `DS` tools are provided by MIT.
[5] `fluxtools` are written by A. Archibald.

Contents

List of Figures

List of Tables

Chapter 1

Introduction and Background Information

1.1 Pulsars

1.1.1 Introducing Pulsars

A pulsar is a neutron star from which we have detected electromagnetic pulses.

The great majority of pulsars are rotation-powered: the energy measured in the observed emission comes from the loss of rotational kinetic energy. Unless otherwise specified, the descriptions in the following Sections apply only to rotation-powered pulsars.

More than 1800 rotation-powered pulsars[1] have been detected across the sky since 1967, the year of the discovery of the first pulsar. If a pulsar is observed to emit pulsations at radio wavelengths, then it is called a radio pulsar. Over 95% of pulsars are of this type.

1.1.2 Neutron Stars

It is generally accepted that when an isolated star runs out of fuel at its center, one of the following scenarios happens. If the star is not very massive ($M \lesssim 8$ $M_\odot$, where $M_\odot$ is the mass of the Sun), it will expel most of its outer material, and the core will collapse to form a compact object called a white dwarf. A white dwarf is supported against gravitational collapse by electron degeneracy pressure. If the star is

[1] see the ATNF pulsar catalog (http://www.atnf.csiro.au/research/pulsar/psrcat/), whose contents are described by Manchester et al. 2005.

of intermediate-to-high mass ($8\ M_\odot \lesssim M \lesssim 25\ M_\odot$), the mass of its core will exceed the largest possible mass supportable by electron degeneracy pressure. At this point, the core will collapse into either a neutron star or a black hole, and the outer parts will explode in a core-collapse supernova[2] (*e.g.* Chapter 6 of Carroll & Ostlie 2006).

A neutron star is then a compact object resulting, most of the time[3], from the gravitational collapse of the core of a massive star. It is mostly made of neutrons: in pressures as high as the ones involved in the core collapse, it is energetically favourable to combine protons and electrons to form neutrons plus neutrinos. In addition to the ones from the original star, this is where the neutrons in a neutron star come from. A neutron star is supported against gravitational collapse by the neutron degeneracy pressure.

The first pulsating neutron star (now pulsar) was observed in 1967 by J. Bell and A. Hewish, while working on a large receiving antenna for long radio wavelengths. Large fluctuations in the signal were seen, and occurred four minutes earlier each day. This proved that the signal was of celestial origin. Further investigation showed that the signal consisted of amazingly regular pulses, with a period of about 1.34 seconds. In 1968 February, the results were published in Hewish et al. (1968), describing the signal and discussing a possible origin. The paper mentions neutron stars among other possibilities.

The existence of neutron stars was proposed for the first time as an end point of stellar evolution in 1934, decades before the discovery of the first pulsar, by Baade & Zwicky (1934). Later, in 1967, shortly before the discovery of the first pulsar, Pacini (1967) postulated that a rapidly rotating highly magnetized neutron star could provide a source of energy for radiation from a surrounding nebula. Then, in 1968 June, Gold (1968) suggested that pulsars were rotating neutron stars. But it was not until the discovery of the short-period (33 ms) pulsations from the pulsar in the Crab nebula (Staelin & Reifenstein, 1968) that it became accepted that pulsars are rotating neutron stars. This is because only an object as small and massive as neutron stars could rotate this fast. Later, the slowdown of the Crab pulsar (Richards & Comella, 1969) was found to be consistent with the age of the Crab supernova remnant, strengthening that association.

[2]Core-collapse supernovae are classified into type Ib, type Ic, and type II.

[3]Scenarios in which a neutron star is formed when a white dwarf subject to accretion collapses have been modelled (*e.g.* Canal & Gutiérrez 1997; Dessart et al. 2007). However, it is generally believed that a runaway fusion reaction occurs before the mass of the white dwarf reaches the maximum value that can be supported by electron degeneracy pressure, making the white dwarf explode violently.

Today, in 2008, after many improvements in observation techniques, over 1800 pulsars are known. It is now generally accepted that pulsars are rotating neutron stars that emit a beam of electromagnetic radiation. As the star rotates, we see a pulse every time the beam crosses our line of sight. The mechanism which generates this directional emission is still far from clear, but it is believed to be related to the large magnetic field of the pulsars.

1.1.3 Pulsar Locations

A few pulsars have been detected in the Magellanic Clouds, and about a hundred more in globular clusters. The remaining pulsars are, like massive stars, concentrated strongly along the Galactic plane (*e.g.* Section 1.3.1 of Lorimer & Kramer 2004). This is consistent with massive stars being the progenitors of neutron stars. Between 20 and 50 pulsars are associated with supernova remnants (*e.g.* Kaspi & Helfand 2002). In general, pulsars have high velocities (*e.g.* Gunn & Ostriker 1970, Lyne & Lorimer 1994), probably a consequence of their violent birth.

Distances to pulsars are estimated using various methods (see Frail & Weisberg 1990 for an evaluation of different pulsar distance measurements). Parallax is used to measure the distance to nearby pulsars. For pulsars at low Galactic latitudes, Doppler shifts in the neutral hydrogen absorption line (at 21 cm) can be used to estimate the location of the pulsar. The absorption effects of neutral hydrogen also affect the spectra of X-ray pulsars, and this can be used to estimate the distance to these pulsars as well. Pulsar locations can also be determined when the pulsar is associated with a companion or a supernova remnant to which the distance is known. Other less-common methods to estimate pulsar distances exist (*e.g.* Durant & van Kerkwijk 2006a), but for the great majority of pulsars, the distance is estimated by observing the propagation delay of the radio pulses in the ionized interstellar medium: the delay is obtained from the differences in arrival time of the signal at different radio frequencies. A model of the electron distribution in the interstellar space can then be used to find pulsar distances (*e.g.* Cordes & Lazio 2002).

1.1.4 Pulsar Masses and Radii

Neutron stars have a density and a composition that we cannot recreate here on Earth. This is why theoretical calculations of the equation of state of neutron stars, using models of the interior of neutron stars, are uncertain. These models return on average

a mass estimate of $M \sim 2$ $M_\odot$(where $M_\odot = 2\times10^{30}$ kg is the mass of the sun), a radius R near 10 km, and a moment of inertia near $0.4MR^2$[4] (see Lattimer & Prakash 2001 for a comparison of different equations of state). For $M \sim 1.4$ $M_\odot$, and $R \sim 10$ km, the moment of inertia I is $\sim 1\times10^{45}$ g cm^2.

The only accurate mass measurement of neutron stars comes from observations of pulsars in binary systems. These measurements typically return values near 1.4 $M_\odot$ (*e.g.* Stairs 2004). Constraining the radii of neutron stars is more difficult. In the few pulsars where thermal emission in the optical, UV, or X-ray bands can be detected, the size of the emitting region is estimated from the spectra. Otherwise, an upper limit on the radius can be set by requiring that the star is stable against being ripped apart by the centrifugal force. For the fastest pulsar known (1.42 ms, see Hessels et al. 2006), and for an assumed mass of 1.4 $M_\odot$, this upper limit is 21.0 km. Note that this radius is only six times larger than the Schwarzchild radius[5] of a pulsar of mass 1.4 $M_\odot$ (Section 3.1.1 of Lorimer & Kramer 2004). This indicates that pulsars are extremely dense objects subject to extreme gravitational effects near the surface.

For rough calculations presented in the rest of this thesis, I will use a mass of 1.4 $M_\odot$, a radius of 10 km, and a moment of inertia of 1×10^{45} g cm^2.

1.1.5 Pulsar Temperatures

A neutron star is formed in a supernova explosion. After the explosion, the neutron star cools. The cooling rate of the star is dependent on the equation of state, available cooling mechanisms, and internal heat sources (*e.g.* Page et al. 2004).

The surface temperature of pulsars is difficult to measure. The peak of the thermal radiation of pulsars, at least the young ones, is expected to be in the UV band. Hence, a large amount of the thermal radiation emitted by these pulsars is visible in the X-ray band. But even when pulsars are observed to emit X-rays, which is the case of several young ones, the X-ray spectra are hard to interpret because of the reprocessing of the thermal surface emission in the magnetosphere, or because of surface hot spots that are sometimes caused by magnetospheric processes. In fact, the spectra of young pulsars are usually completely dominated by the magnetospheric emission, and the thermal component of the spectrum is very difficult to see.

[4]Most models predict values between $0.30MR^2$ and $0.45MR^2$. For most practical applications $0.4MR^2$ even though this is the moment of inertia of a uniform sphere.

[5]If a neutron star mass were to be compressed into the Schwarzchild radius associated with that mass, it would collapse into a black hole.

The above explains why there are only about a dozen measurements available of surface temperature of rotation-powered pulsars. These measurements are extracted from soft X-ray spectra, and they yield temperatures $\lesssim$ 1 MK (0.09 keV), generally decreasing with neutron star age (*e.g.*, Zavlin & Pavlov 2004).

In addition, X-ray observations have unveiled the existence of the X-ray Dim Isolated Neutron Stars (XDINs), a family of radio-quiet isolated neutron stars with purely thermal spectra and low pulsed fractions. Their periods are $P \sim 3{-}12$ s, and their X-ray spectra yield surface temperatures between 0.08 keV and 0.1 keV (Haberl, 2007). Theoretical cooling curves yield an age estimate near 10^6 yr for neutron stars with these temperatures.

1.1.6 Pulsar Magnetic Fields

Many observations indicate the presence of magnetic fields in astrophysical sources. These include, but are not limited to, splitting of spectral lines, detections of cyclotron emission or absorption lines in the spectra of astrophysical sources, observations of synchrotron spectra, and detections of polarized light.

Because of the above evidence, we know that stars have magnetic fields. This magnetic field is most likely being maintained by the dynamo process: in a conductive liquid core which is continuously being stirred (by convection, differential rotation, the coriolis force, or any other means), when conductive fluid flows across an existing magnetic field, currents are induced, which in turn create another magnetic field that reinforces the original magnetic field.

We also know that pulsars have a magnetic field because of the phase dependence of their polarized emission, and because the spin-down predicted from a rotating dipole model (see below) fits the data well. The origins of this field are not entirely clear. It may come from the field of the progenitor star amplified by $(R/r)^2$, where R is the radius of the progenitor star and r is the radius. It can also have been created in a dynamo process that was set up immediately after the supernova explosion (Thompson & Duncan, 1993). This field could either be continuously sustained by a dynamo process, or it could not be maintained at all, but slowly dissipating.

The configuration of that magnetic field is also uncertain. Away from the pulsar, only the dipolar component of that magnetic field is observed. This is because the higher order multipoles fall quickly as a function of the radius. Close to the surface of the pulsar, and inside it, the relative strengths of the different magnetic multipoles

are uncertain.

A spinning pulsar is surrounded by plasma (ionized gas). The presence of plasma is discussed further in Section 1.1.12. If plasma is a perfect conductor, it moves with the rotating magnetic field lines. However, far from the pulsar, the plasma cannot co-rotate with the pulsar, otherwise its speed will exceed the speed of light. Because of this, torque is exerted on the pulsar, slowing it down. Note that even without the presence of the plasma, a rotating pulsar in vacuum will slow down. This is because a rotating magnetic field creates electromagnetic waves. The energy of these waves comes from the loss of rotational kinetic energy of the pulsar. This phenomenon is called magnetic braking.

Assuming *a)* that the magnetic field near the surface is *dipolar*, *b)* that the pulsar is in *vacuum*, *c)* that it is slowing down *exclusively* due to magnetic braking, and *d)* that its mass, radius, and moment of inertia have the values discussed in Section 1.1.4, then, equating the rate of loss of rotational kinetic energy of the pulsar with the power of a rotating dipole (see, for example, Section 5.10 of Lyne & Graham-Smith 2005) yields a useful expression relating the magnetic field of the pulsar to its spin parameters:

$$B \sim 3.2 \times 10^{19} (P\dot{P})^{1/2} \mathrm{G}, \tag{1.1}$$

where B is the magnetic field at the surface of the pulsar, P is the period of the pulsar, measured in seconds, and $\dot{P}$ is the period derivative.

Note that because of all the assumptions that went into it, the above expression only yields an order of magnitude estimate of pulsar magnetic fields. More direct measurements of the magnetic fields of pulsars come from cyclotron radiation features in the spectra of some X-ray pulsars (*e.g.* Bignami et al. 2003). These yield magnetic fields on the order of 10^{11-12} G.

1.1.7 Pulsar Spin-down Luminosities

Due to external torques and to magnetic braking, pulsars slow down. The rate of loss of their rotational kinetic energy, $\dot{E}$, can be expressed as follows:

$$\dot{E} = (I/4\pi^2)\nu\dot{\nu} = (4\pi^2 I)\dot{P}P^{-3}, \tag{1.2}$$

where ν is the frequency, $\dot{\nu}$ is the frequency derivative, and I is the moment of inertia of the pulsar. For $I = 10^{45}$ g cm^2 (see Section 1.1.4), the expression for $\dot{E}$ becomes:

$$\dot{E} \sim (3.95 \times 10^{46} \mathrm{erg/s}) \dot{P} P^{-3}, \tag{1.3}$$

where P is measured in seconds. This quantity is called the spin-down luminosity. For most pulsars, the radio luminosity (and X-ray, when detected) is only a small fraction of the spin-down luminosity.

1.1.8 Pulsar Characteristic Ages

Using the assumptions that went into Equation 1.1, an expression for the age of the pulsar in terms of its spin parameters can be derived (see, for example, Section 3.2.2 of Lorimer & Kramer 2004). If we further assume that the spin period at birth is much shorter than the currently observed value of the period (an assumption that is probably wrong, especially for young pulsars), we obtain an expression for the "characteristic age" (τ_c) of the pulsar:

$$\tau_c = P/(2\dot{P}). \tag{1.4}$$

1.1.9 Pulsar Timing

Pulsars are extremely stable rotators. They are stable enough that we are able to track the exact number of a pulsar's rotations for years (see Figure 1.1). Pulsar timing usually refers to the analysis done in order to extract pulse Times of Arrival (TOAs), and then using these TOAs to obtain an ephemeris (or timing solution), which is an expression of the pulsar's rotational phase as a function of time.

In this thesis, a TOA corresponding to a given observation is defined as the arrival time of a particular feature in the pulse nearest to the mid-point of the observation. To obtain a TOA, the lightcurve of an observation is usually folded at the best-fit frequency (determined from a periodogram or from an ephemeris whenever one is available), after having removed the time delays due to the Earth orbit and due to the orbit of the observatory, when the observatory is not on Earth. The folded lightcurve is called a pulse profile. The pulse profile is then cross-correlated with a long-term average pulse profile for that pulsar, and the phase difference between the two is determined. Using this phase difference and the frequency used in the fold, a TOA can be extracted.

At any time t, the pulse phase ϕ can be expressed as a Taylor series polynomial

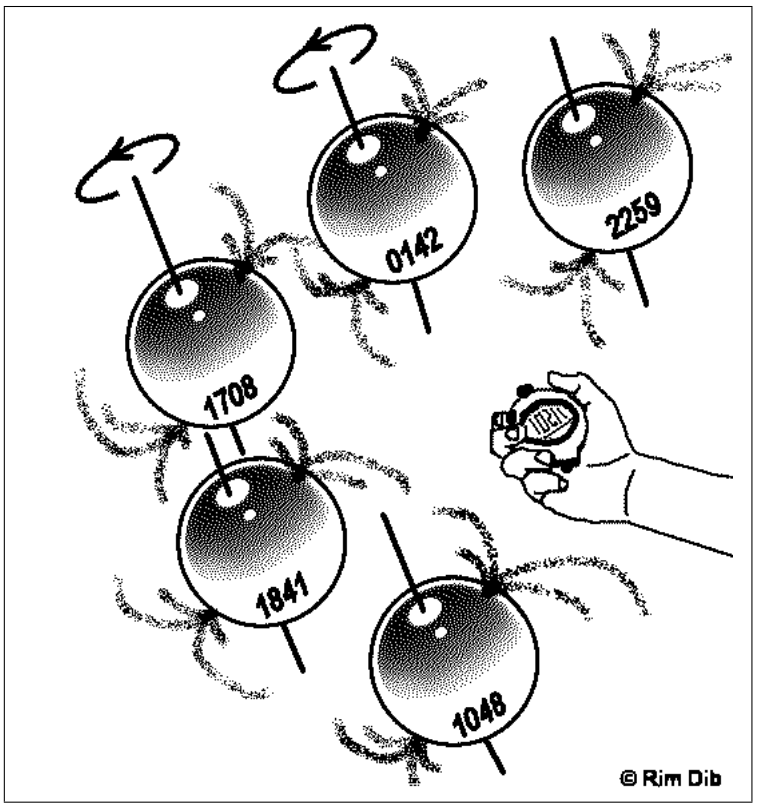

Figure 1.1 Pulsar timing essentially amounts to counting the number of times the pulsar rotates about itself over time.

$$\phi(t) = \phi_0(t_0) + \nu_0(t - t_0) + \frac{1}{2}\dot{\nu}_0(t - t_0)^2 + \frac{1}{6}\ddot{\nu}_0(t - t_0)^3 + \ldots, \qquad (1.5)$$

where subscript "0" denotes a parameter evaluated at the reference epoch $t = t_0$.

Setting ϕ_0 to be the phase of the first TOA, setting ν and its derivatives to be the exact spin parameters of the pulsar, and substituting a set of TOAs extracted from the data into Equation 1.5 returns integer values for ϕ. But the exact spin parameters of the pulsar are never known (see below). Timing residuals are then obtained by subtracting the nearest integers from the values of ϕ obtained after substituting the TOAs into Equation 1.5. Specially designed pulsar timing software such as `TEMPO`[6] adjusts the guessed pulsar spin parameters to minimize the timing residuals for a given set of TOAs. The software returns *a)* a best-fit set of spin parameters, *b)* a number associated with each TOA showing the number of times the pulsar spun since the first TOA, and *c)* the minimized timing residuals.

Assuming *a)* that the magnetic field near the surface of the pulsar is *dipolar*, *b)*

[6]See http://www.atnf.csiro.au/research/pulsar/tempo.

that the pulsar is in *vacuum*, and *c)* that it is slowing down *exclusively* due to magnetic braking, the frequency of the pulsar ν obeys the following differential equation (see, for example, Section 5.10 of Lyne & Graham-Smith 2005):

$$\dot{\nu} = -K\nu^3, \tag{1.6}$$

where K is a constant which depends on the magnetic moment and on the geometry.

The Taylor expansion of the pulsar frequency is given by

$$\nu - \nu_o = \frac{\dot{\nu}_o \Delta t}{1!} + \frac{\ddot{\nu}_o (\Delta t)^2}{2!} + \frac{\dddot{\nu}_o (\Delta t)^3}{3!} + \ldots. \tag{1.7}$$

Using Equation 1.6 to write the frequency derivatives of the second order and higher in terms of $\dot{\nu}$, Equation 1.7 takes on the following form:

$$\nu - \nu_o = (\dot{\nu}_o \Delta t) + (\frac{3}{2!})(\dot{\nu}_o \Delta t)(\frac{\dot{\nu}_o \Delta t}{\nu_o}) + (\frac{3 \times 5}{3!})(\dot{\nu}_o \Delta t)(\frac{\dot{\nu}_o \Delta t}{\nu_o})^2 + \ldots \tag{1.8}$$

The range of observed pulsar frequencies[7] extends from 0.084 s^{-1} to 716 s^{-1}. The range of observed pulsar frequency derivatives[8] extends from -4$\times 10^{-18}$ s^{-2} to -4$\times 10^{-10}$ s^{-2}. For these parameters, the change in ν over a period of time Δt (Equation 1.8), is greatly dominated by the linear term. In fact, for an ordinary radio pulsar with ν=2 s^{-1} and $\dot{\nu}$= -1$\times 10^{-15}$ s^{-2}, the change in ν due to the quadratic term in 10 years is the same as the change in ν due to the linear term in 75 seconds.

The above shows that the observed spin-down of pulsars is greatly dominated by the linear term. This is what is observed after one takes into account all known effects that leave a signature in the observed timing residuals of the pulsar such as the position of the pulsar, the proper motion of the pulsar, and the effects of any binary parameters in the case of binary systems. But even after taking all the known effects into account, there are many apparently random variations in the rotational parameters of pulsars on time scales from minutes to years, which manifest themselves as features in the timing residuals. These variations are suggestive of unmodelled physics. They are called "timing noise", and they are not well understood (Hobbs et al., 2006). The spectrum of timing noise (the amplitude of the deviations from a linear spin-down as a function of time scale of the deviations) is different from pulsar to pulsar.

[7]From the ATNF Pulsar Catalog.
[8]From the ATNF Pulsar Catalog.

1.1.10 Pulsar Populations

Pulsar timing can lead to accurate measurements of the spin parameters of pulsars. Figure 1.2 shows pulsar distribution in a period derivative ($\dot{P}$) versus period (P) diagram. Most ordinary pulsars cluster near 0.5 s in period, and near 1×10^{-15} in period derivative. Young pulsars have smaller periods and they are to the upper-left of ordinary radio pulsars. Many of them are associated with supernova remnants. Many of them are observed to pulsate in the X-ray band as well as in the radio band.

The millisecond pulsars, which are believed to have been spun-up by accreting from a binary companion, are in the lower-left part of the diagram. Most of them are in binary systems.

Of great interest to this thesis are the pulsars in the top-right part of the diagram: the pulsars with large P and $\dot{P}$. Assuming pulsars are dipoles spinning in a vacuum, Equation 1.1 yields estimates of magnetic fields near 10^{14} G and above for these pulsars. No other astrophysical source in the current observable universe is believed to have a magnetic field of this magnitude. This corner of the diagram is shared by the magnetars, (divided into Anomalous X-ray Pulsars and Soft Gamma Repeaters, see Section 1.2), the three XDINs for which $\dot{P}$ has been measured (not shown in the Figure, see Sections 1.1.5 and 1.2.6, Haberl 2007), and some high-magnetic-field radio pulsars ($B>10^{13}$ G).

1.1.11 Pulsar Power Sources

Pulsars can be classified according to the source of power of the emission that we detect from them.

The previous Sections primarily dealt with rotation-powered pulsars. As mentioned in Section 1.1.1, the great majority of pulsars are rotation-powered: the energy measured in the observed emission comes from the loss of rotational kinetic energy. The radio/X-ray luminosity of these pulsars is usually at least an order of magnitude smaller than their spin-down luminosity. The great majority of these pulsars are observed exclusively in the radio band. About 7 rotation-powered pulsars are not seen in the radio. Isolated millisecond pulsars, and millisecond pulsars in non-accreting binary systems are also rotation-powered.

Another class of pulsars are the accretion-powered pulsars (not shown on the diagram in Figure 1.2). In these pulsars, the X-ray pulses are generated by the accretion flow striking the neutron star: the flow of matter from the companion star is channeled

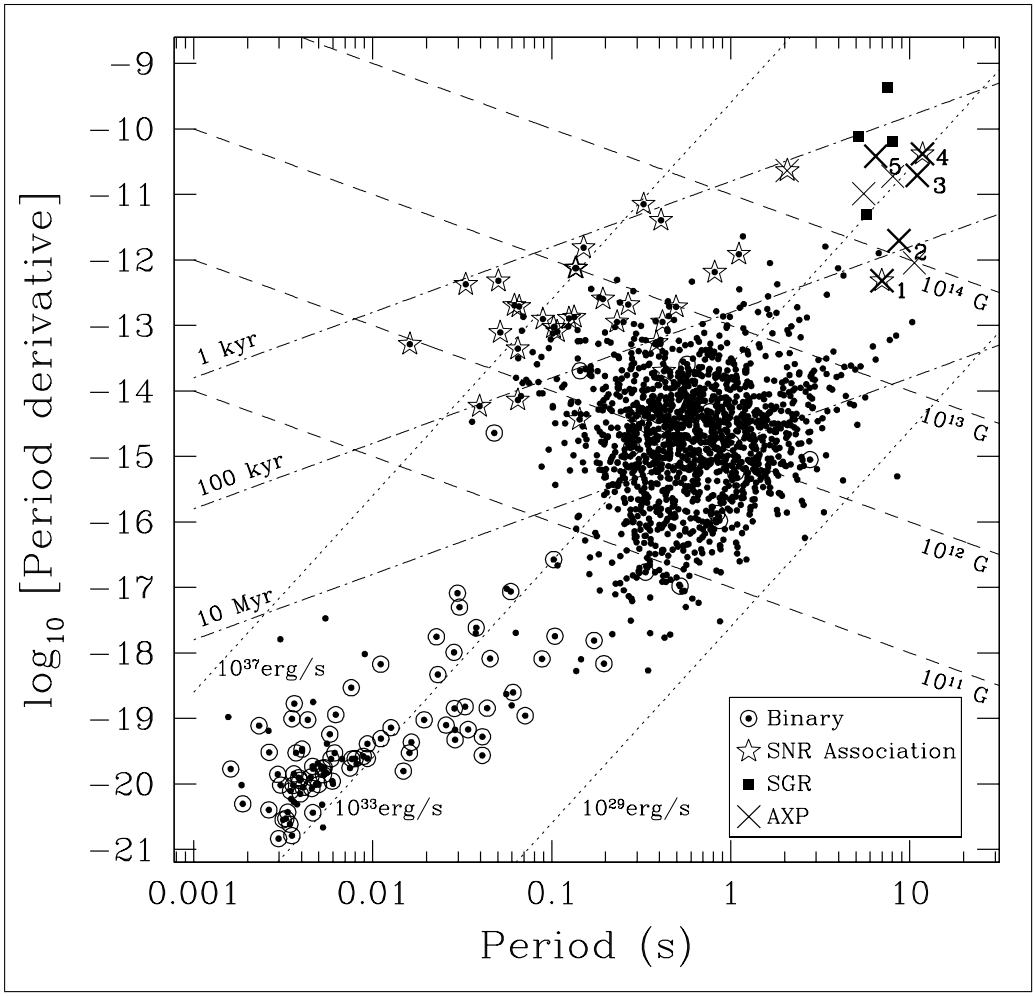

Figure 1.2 The P-$\dot{P}$ Diagram for 1629 Pulsars in the ATNF Catalog. Anomalous X-ray Pulsars (AXPs) are indicated with a $\times$. The five AXPs regularly monitored with *RXTE* are labelled from 1 to 5. They are 1: 1E 2259+586 (Chapter 6), 2: 4U 0142+61 (Chapters 2, 3, and 6), 3: RXS J170849.0−400910 (Chapters 4 and 6), 4: 1E 1841−045 (Chapters 4 and 6), and 5: 1E 1048.1−5937 (Chapters 5 and 6). Soft Gamma Repeaters (SGRs) are indicated with solid squares. All remaining pulsars are indicated with a small solid circle. Pulsars in binaries are surrounded by a hollow circle. Pulsars in supernova remnants are surrounded by a star. Lines of constant magnetic field (dashed, see Equation 1.1), spin-down luminosity (dotted, see Equation 1.3), and characteristic age (dot-dashed, see Equation 1.4) are shown.

by the pulsar's magnetic field onto the magnetic poles of the neutron star, resulting in a pair of "hot spots" on the pulsar surface, and giving rise to the X-ray pulses as the pulsar spins.

For the magnetars, a special class of the pulsars located in the top-right corner of the $P-\dot{P}$ diagram and having a magnetic field $B \gtrsim 10^{14}$ G, the observed X-ray

luminosity is much larger than the spin-down luminosity. It is believed that these objects are powered by the decay of their large magnetic field (see Section 1.2).

Pulsars for which the observed emission is not well understood and therefore cannot quite fit in the above categories include the XDINs, which have observational characteristics different from their neighbours on the $P-\dot{P}$ diagram (see Section 1.2.6). They also include a handful of radio-quiet, thermally emitting, pulsating compact objects located at the centers of supernova remnants (de Luca 2008, also see Section 1.2.6).

1.1.12 Simplified Model of a Pulsar: The Exterior

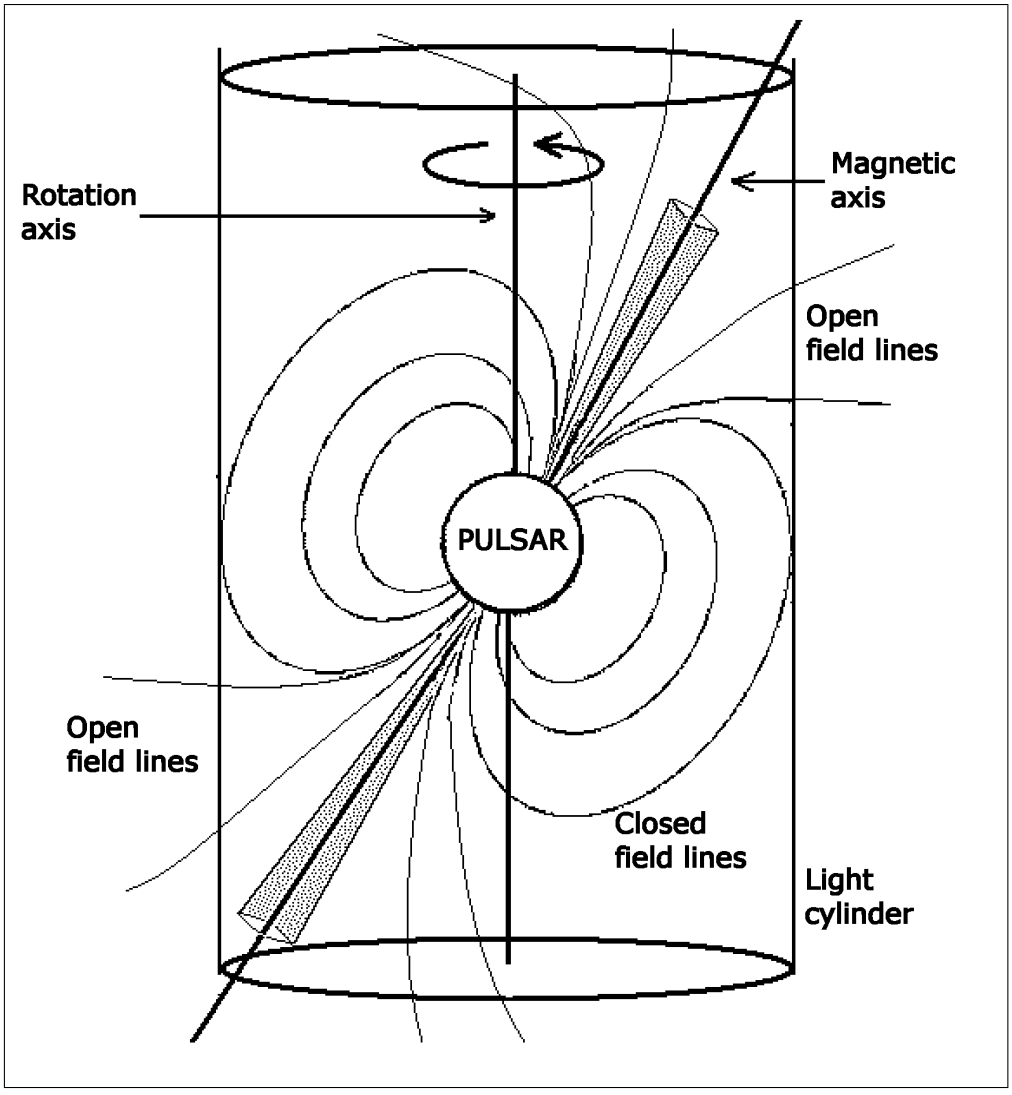

Figure 1.3 Model of a rotating pulsar and its magnetosphere. Not to scale.

Assuming a pulsar is a conductive sphere rotating in vacuum with an external dipole

magnetic field, and writing down Maxwell's equations for this system with the correct boundary conditions, gives a solution in which a very large electric potential and an external electric field will be created, ultimately leading to the extraction of plasma from the pulsar surface (Goldreich & Julian, 1969). Hence, pulsars are surrounded by plasma. In fact, for many proposed pulsar emission mechanisms, large plasma densities, exceeding those proposed in Goldreich & Julian (1969) are required (*e.g.* Melrose 2004).

If the plasma is a perfect conductor, we expect it to obey ideal magnetohydrodynamics equations. In particular, we expect any magnetic field B to be stuck to the plasma, that is, if B moves, the plasma moves in such a way that the B lines cannot slide across the plasma (*e.g.* Goossens 2003). Compressing the plasma results in higher density of field lines, and hence a higher magnetic field. Stretching the field lines increases the tension and the energy stored in them. If the magnetic field is deformed anywhere, currents are created to try and maintain the field in its original configuration.

Near the surface then, the magnetic field and the plasma that it is dragging are rotating with the star. At a certain distance from the star, the field lines, and the plasma they are dragging, would have to move at the speed of light in order to keep corotating with the star. This distance is the radius of the "light cylinder" (see Figure 1.3). For a 1-s pulsar, this distance is approximately 50000 km, large compared to the radius of the pulsar. Magnetic field lines inside the light cylinder form closed loops. Magnetic field lines which meet the cylinder do not, possibly causing magnetic reconnection events to happen at the boundary of the light cylinder. The regions near the poles where the open field lines originate are the "polar caps". Some emission mechanisms place the source of the radio emission somewhere along the first open field lines (*e.g.* Cheng et al. 1986). The plasma-filled region roughly inside the light cylinder is called the "magnetosphere".

1.1.13 Simplified Model of a Pulsar: The Interior

The interior composition of pulsars is not known with any certainty. Pulsars are believed to have a $\sim$1 cm thick atmosphere (see, for example, Miller 1992). This atmosphere affects the spectra of emitted surface photons. Below the atmosphere, the star is divided into layers: the crust, the superfluid (intermingled with the inner crust), the outer core, and the inner core (see Figure 1.4). The densities range from from 10^6 g/cm^3

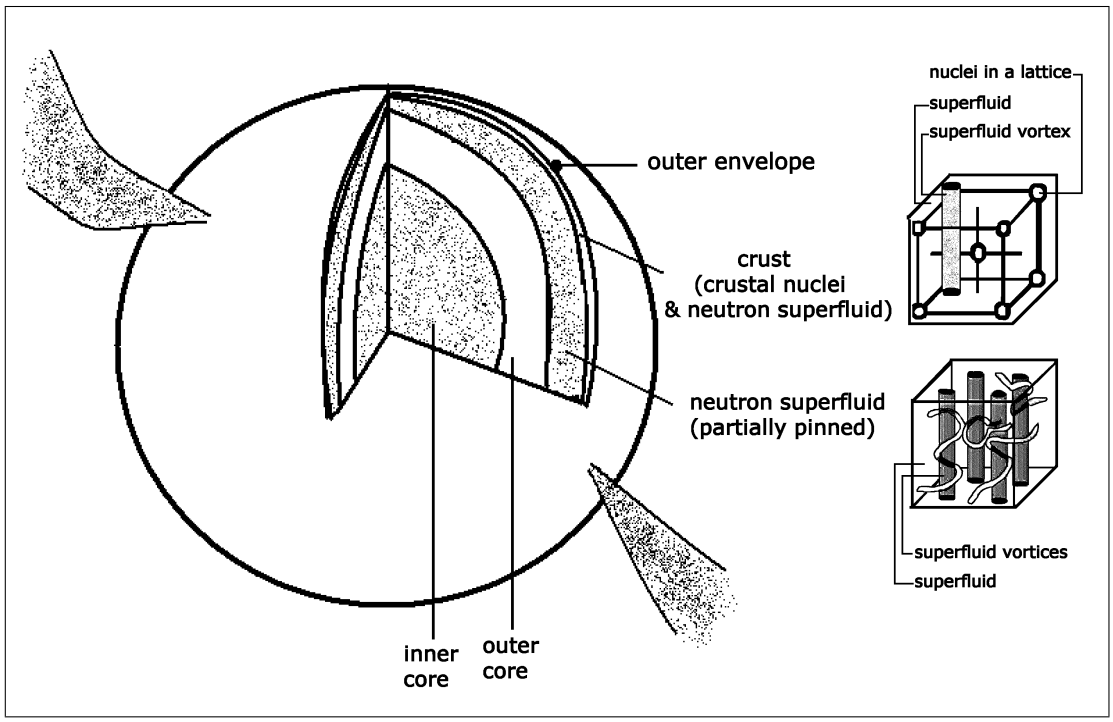

Figure 1.4 Model of the interior of a pulsar. Not to scale. Adapted from Figure 5.10 in Rosswog & Bruggen (2003).

in the outer crust to 10^{15} g/cm^3 in the inner core (*e.g.* Shapiro & Teukolsky 1983).

The outer part of the crust consists of ions (charged atomic nuclei) and of degenerate electrons (Shapiro & Teukolsky, 1983). The ions form a conductive hard crystalline solid that is hard to break and easier to shear. As we move deeper into the crust, the density grows, and it becomes energetically favourable to convert electrons and protons into neutrons. This region consists of electrons, some free neutrons, and neutron-rich atomic nuclei (Yakovlev & Pethick, 2004). With increasing depth the nuclei become less spherical and more elongated (Pethick & Ravenhall, 1999). Hundreds of meters below the surface, at the base of the crust, more neutrons start to drip out of nuclei forming a neutron-liquid between nuclei.

The neutron (and some proton) matter inside a neutron star is thought to form a superfluid underneath the crust. A superfluid is a Bose-Einstein condensate, a quantum state of minimum energy containing most of the particles of the fluid. When this condensate is able to be stable enough not to jump to an excited state easily, then it flows without friction and it is called a superfluid. Observations of pulsar glitches (see Section 1.1.14) suggest the existence of an angular momentum reservoir below the surface of neutron stars, which occasionally transfers some of this momentum to the

crust. The neutron superfluid is believed to be that reservoir, with a small percentage of superconducting protons. This superfluid penetrates into the crust, in the space between the nuclei (Shapiro & Teukolsky, 1983; Yakovlev et al., 1999).

In the outer core the neutrons and protons are interacting via nuclear forces and are believed to form a "non-ideal fluid" (Yakovlev & Pethick, 2004). The composition of the inner core is uncertain.

1.1.14 Pulsar Glitches

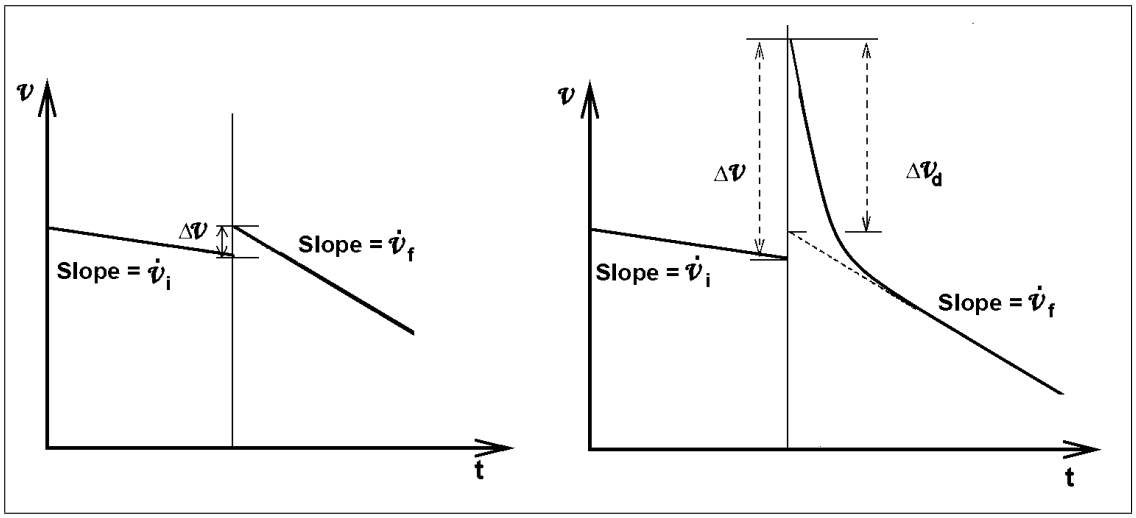

Figure 1.5 Two frequency versus time sketches showing glitch events. *Left:* $\Delta\nu$ is the sudden change in frequency at the glitch epoch. It is often accompanied by a sudden change in frequency derivative $\dot{\nu}$. *Right:* $\Delta\nu$ is the frequency jump at the glitch epoch. A portion of this jump ($\Delta\nu_d$) recovers on time scales of minutes to years. After the relaxation, there is sometimes a permanent change in the spin-down rate $\dot{\nu}$.

Pulsar timing has revealed that as the pulsar spins down, the phase of the pulses sometimes drifts by a small fraction of a pulse period in a given amount of time. The drift is due to timing noise (*e.g.* Hobbs et al. 2006, see Section 1.1.9), and the amount of drift is different from pulsar to pulsar. Pulsar timing has also revealed the existence of sudden spin-up events in pulsars called glitches (see references below).

The first glitch event was discovered in the Vela pulsar (Radhakrishnan & Manchester, 1969). Since then, and as of September 2006, 287 events have been detected in 101 of the 1730 known pulsars (Lyne et al., 1992; Lyne et al., 1995; Flanagan, 1996; Shemar & Lyne, 1996; Lyne et al., 2000; Wang et al., 2000; Wong et al., 2001; Hobbs et al., 2002; Krawczyk et al., 2003; Hobbs et al., 2004). The rotational parameters for

all 287 glitches are compiled in Table 1.2 of C. Peralta's PhD thesis (Peralta, 2006). For a short discussion on glitch statistics extracted from this table, see Appendix A.

A glitch is an apparently sudden jump in the frequency, possibly accompanied by a sudden change in the frequency derivative. It may or may not be followed by a recovery (see Figure 1.5). A recovery lasts anywhere from minutes to years, and it is usually fit by a combination of decaying exponentials. For the very closely monitored Vela pulsar, an upper limit of < 40 s has been placed on the rise time of the glitches (McCulloch et al., 1990; Dodson et al., 2002). Two of the glitches of the Crab pulsar had partially resolved rises: each glitch consisted of an unresolved portion followed by an exponential rise with a time constant ~ 1 day (Lyne et al., 1992; Wong et al., 2001). Note that "slow-rise glitches" which do not fit the above picture have been reported for PSR B1822-09 by Shabanova (1998, 2005, 2007). They show that the rise in the frequency of PSR B1822-09 happens on time scales of months. But their data can as well be fit by a series of "usual" glitches, separated by a few months, each accompanied by a change in the frequency derivative, or by timing noise.

Glitches are generally attributed to variable coupling between the crust of the star and the superfluid beneath the crust (*e.g.* Chapter 7 of Lyne & Graham-Smith 2005). They are believed to be instances of angular momentum transfer from the superfluid to the crust.

In most glitch models, the superfluid is spinning faster than the crust, but on average, over long times, they have the same $\dot{\nu}$. Some of the quantized vortex lines that carry angular momentum in the superfluid are "pinned" to crustal nuclei, inhibiting any outward motion of these lines. This creates an excess rotation of the superfluid relative to the outer crust (*e.g.* Anderson & Itoh 1975; Alpar et al. 1981; Anderson et al. 1982; Alpar et al. 1984a; Alpar & Pines 1993; Alpar et al. 1989). Because of the pinning, a portion of the superfluid is "coupled" to the crust, and the outside torque acting on the pulsar equal $I \times (2\pi\dot{\nu})$, where I is sum of the moments of inertia of the crust, of the portion of the superfluid coupled to it, and of the moment of inertia of the layers below the superfluid. For various reasons, for example, torques on the crust, heat-releasing internal starquakes, and thermal agitations, an unpinning of the vortex lines may happen in some locations (*e.g.* Link & Epstein 1996; Larson & Link 2002). The vortices could then move outward, and the superfluid angular frequency can decrease and approach that of the crust. At that moment, angular momentum is transferred from the superfluid to the crust, and a glitch occurs. Also at that moment, the effective moment of inertia resisting the outside torques is smaller, and

the observed $\dot{\nu}$ immediately after the glitch, most of the time, has a larger magnitude than the pre-glitch value. The different post-glitch recovery time scales are believed to be due to adjustments in the variable coupling between the crust and the superfluid.

1.2 Magnetars

1.2.1 Introducing Magnetars

Magnetars are apparently isolated pulsars in the top-right corner of the P-$\dot{P}$ diagram (Figure 1.2). Their periods are clustered near 5 s, and their period derivatives are clustered near 10^{-11} (frequency derivatives near 10^{-13} s^{-2}). Using Equation 1.1, the periods and period derivatives imply an external dipolar magnetic field $\gtrsim 10^{14}$ G for magnetars.

What physically distinguishes these objects from ordinary high-magnetic-field pulsars is the likely source of energy for their radiative emission: magnetism. Indeed, we know that these sources are not rotation-powered, because for non-transient magnetars, the observed luminosity in quiescence ($\sim 10^{35}$ erg s^{-1}), *i.e.* when not in outburst, is larger than their spin-down luminosity. These pulsars are believed to be powered by the decay of their very large magnetic field (see Section 1.2.4 for a brief description of the magnetar model). For recent reviews, see Woods & Thompson (2006); Kaspi (2007); Mereghetti (2008).

Magnetars are historically divided into two classes of neutron stars that were independently discovered through different manifestations of their high-energy emission: the Soft Gamma Repeaters (SGRs) and the Anomalous X-ray Pulsars (AXPs)[9]. SGRs were discovered through the detection of *short bursts* in the hard X-ray/soft gamma ray range (*e.g.* Mazets et al. 1979a; Laros et al. 1986). AXPs were first detected as pulsating sources in the soft X-ray range ($<$ 10keV) (*e.g.* Fahlman & Gregory 1981; Seward et al. 1986), and were thought to be accreting binaries. Deeper X-ray, infrared (IR), and optical searches excluded the presence of a companion star (*e.g.* Mereghetti & Stella 1995).

As of 2008 December, there are 5 known and 2 candidate SGRs (observational characteristics described in Section 1.2.2 and in Appendix B), and 9 known and 1 candidate AXPs (observational characteristics described in Sections 1.2.3 and in Appendix C). With the exception of 1 SGR located in the Large Magellanic Cloud (LMC) and 1 AXP located in the Small Magellanic Cloud (SMC), magnetars are located in the Galactic plane (see, for example, Table 14.4 in Woods & Thompson 2006), in all directions.

Magnetars are predominantly studied in the soft X-rays, although for many of

[9]An online summary of magnetar properties and references is maintained at McGill University (http://www.physics.mcgill.ca/~pulsar/magnetar/main.html.).

them, emission at other wavelengths is detected. This emission is briefly described in Section 1.2.5.

1.2.2 Soft Gamma Repeaters: an Overview

Soft Gamma Repeaters were discovered through the detection of short bursts in the hard X-ray/soft gamma ray range. Some were later found to be persistent X-ray pulsars, with periods of several seconds, that are spinning down rapidly. In this Section we provide a brief description of SGR activity and observational characteristics, based on reviews by Hurley (2000); Kouveliotou (2004); Woods & Thompson (2006); Mereghetti (2008). In Appendix B, we discuss the properties of the individual SGRs.

Soft Gamma Repeaters randomly go through periods of activity (outbursts) lasting between days and years and separated by months or years, during which they emit hundreds of predominantly soft ($kT \sim 30$ keV), and short (0.1−100 ms) bursts, with characteristic peak luminosities on the order of 10^{39}−10^{41} erg s^{-1}. In these periods of activity, SGRs are also known to emit "intermediate flares". These are periods of unusually high flux outputs lasting a few seconds, and accompanied by bursts. "Giant flares" have been observed from three SGRs. A giant flare is a sudden release of an enormous amount of energy. It consists of a short spike with typical durations of 0.5 s during which luminosities up to 10^{47} erg s^{-1} can be achieved. The spike is followed by a decaying flux tail lasting hundreds of seconds on which pulsations are clearly superposed. The total energy released during the tail is on the order of 10^{44} erg. Several models were put forth to try to explain the giant flare emission from SGRs. But only the magnetar model (Section 1.2.4) offered an adequate explanation for *both* the giant flares and the more common recurrent bursts which have much lower peak luminosities.

During quiescence (outside active periods), SGRs have the following characteristics: they are persistent X-ray sources in the range (0.1−10 keV), with luminosities ranging between 10^{34}−10^{36} erg s^{-1}. The X-ray emission is pulsed at the spin period. The spin periods are narrowly clustered between 5−8 s (Figure 1.2). Measurements of SGR spin-down rates, when interpreted in terms of the magnetic braking of isolated neutron stars, indicate that SGR magnetic fields are on the order of 10^{14}−10^{15} G. The soft X-ray spectra of the emission outside the active periods are interpreted as predominantly thermal with magnetospheric effects, and are usually fitted by a combination of a power-law (photon index ~ -2) and a blackbody with temperature $kT \sim 0.5$ keV.

SGRs tend to have harder spectra below 10 keV than their cousins the Anomalous X-ray Pulsars (Section 1.2.3). They also suffer larger interstellar absorption because they are further away on average, making the thermal component difficult to measure. The spectra, the pulse morphology, and the timing properties of SGRs are known to change during the pulsating tail of the giant flares.

The list of the currently known Soft Gamma Repeaters (not including candidate extra-galactic bursting SGRs) is below. See Appendix B for the characteristics of the individual SGRs.

- SGR 0526-66.
- SGR 1627-41.
- SGR 1806-20.
- SGR 1900+14.
- Recently discovered SGR 0501+4516.
- Candidate Soft Gamma Repeater SGR 1801-23.
- Candidate Soft Gamma Repeater SWIFT J195509+261406.

1.2.3 Anomalous X-ray Pulsars: an Overview

Anomalous X-ray Pulsars were discovered through the detection of coherent pulsations in the soft X-ray band. The first AXP for which a period was measured was 1E 2259+586 at the center of supernova remnant CTB 109 (Gregory & Fahlman 1980; Fahlman & Gregory 1981). Eventually several other sources with similar properties (similar luminosities, periods, period derivatives and spectra) were found. They were recognized as a distinct class of objects in Mereghetti & Stella (1995) and Stella et al. (1996). These objects spun down regularly within the limited timing observations available. They were found in the plane of the Galaxy, and two of them appeared to be located at the geometric centers of supernova remnants.

At first, because their observed X-ray luminosity was much greater than the rate of loss of rotational kinetic energy inferred from the observed spin-down, AXPs were interpreted as peculiar X-ray binaries; peculiar because their energy spectrum was much softer than is typical of accreting pulsars (*e.g.* Mereghetti & Stella 1995). However, the binary accretion model slowly became difficult to reconcile with observations. The absence of Doppler shifts, even on short time scales (*e.g.* Mereghetti et al. 1998),

the absence of a detectable optical/IR companion or accretion disk (*e.g.* Mereghetti & Stella 1995), and the apparent associations with supernova remnants, all argued against an accretion origin for the X-rays. Eventually, from a timing point of view, the presence of binary companions was practically ruled out (*e.g.* Wilson et al. 1999), and subsequently the great rotational stability of AXPs was demonstrated (Kaspi et al., 1999).

On the theoretical front, van Paradijs et al. (1995) mentioned the possibility that the power source of the AXPs may be magnetic. This was based on earlier work presented in Thompson & Duncan (1993); Thompson & Duncan (1993); Thompson & Duncan (1995a). But they also suggested that 1E 2259+586 and sources with similar properties are the recent remnants of the common-envelope evolution of a high-mass X-ray binary, and proposed that these sources were isolated neutron stars accreting from a disk. Along the same lines, Ghosh et al. (1997) suggested that AXPs are objects forming after a complete spiral-in of a neutron star in the envelope of its giant companion (Thorne-Zytkov objects). Then, in 1996, Thompson & Duncan (1996) proposed that AXPs *and* SGRs are young and highly magnetized neutron stars ("magnetars") where the magnetic field rather than rotation or accretion provides the main source for the emitted energy. The fact that they are young is supported by two apparent supernova remnant associations and from the fact that the AXPs are located close to the Galactic plane, consistent with their being isolated neutron stars near their birth place. Heyl & Hernquist (1997a) and Heyl & Hernquist (1997b) also suggested that the pulsed X-ray emission from AXPs 1E 2259+586 and 1E 1841-045 and several SGRs can be explained by photon cooling of highly magnetized neutron stars.

Not everyone agreed with the magnetar hypothesis, and some favoured the hypothesis of a fossil disk accretion (Chatterjee & Hernquist, 2000; Chatterjee et al., 2000; Marsden et al., 2001), arguing that AXPs and SGRs originated in dense environments and that this can be consistent with these sources accreting from fossil disks. However Gaensler et al. (2001) found no evidence that the density of the ambient medium around AXPs is higher than that in the vicinity of rotation-powered pulsars. More details of the magnetar model were worked out in Thompson et al. (2002) following the second giant flare from an SGR. The authors suggested that some of the radiative variability exhibited by AXPs and SGRs is caused by magnetic stresses acting deep inside the star, which generate both sudden disruptions (SGR outbursts) and more gradual plastic deformations of the rigid crust. In an episode of variability, the internal

twists of the magnetic field propagate outward causing a twist in the magnetosphere. They suggested that the hard power-law tail of the spectra in these sources is due to thermal surface photons undergoing inverse Compton scattering in the highly twisted magnetosphere. In their model, the hardness of the spectra and the luminosity are expected to be correlated during outbursts (for further details about the magnetar model see Section 1.2.4).

On the observational front, AXPs have relatively recently been revealed to be much more variable than first thought: from the timing point of view, glitches (*e.g.* Kaspi et al. 2000; Kaspi & Gavriil 2003; Dall'Osso et al. 2003, Chapter 4, Chapter 5) were discovered in several sources, and large (factor of $\sim$10) torque variations (Gavriil & Kaspi 2004, Chapter 5) were discovered in AXP 1E 1048.1−5937. From the radiative point of view, AXPs are now known to show a variety of different variability phenomena on many different time scales: a few short SGR-like bursts (*e.g.* 1E 1048.1−5937: Gavriil et al. 2002, 1E 2259+586: Gavriil et al. 2004, XTE J1810−197: Woods et al. 2005), minutes-long pulsed-flux enhancements (*e.g.* 4U 0142+61: Chapter 3, 1E 1048.1−5937: Chapter 5), slow-rise flares (*e.g.* 1E 1048.1−5937: Gavriil & Kaspi 2004), large outbursts (*e.g.* 1E 2259+586: Kaspi et al. 2003, XTE J1810−197: Ibrahim et al. 2004, CXOU J164710.2−455216: Israel et al. 2007), and years-long slow pulsed flux evolution (*e.g.* AXP 4U 0142+61: Chapter 2). The pulse profiles of AXPs are also known to vary (*e.g.* Sections 2.3.2, 3.3.2, 4.4, 5.4, and 6.6)

The variability phenomena described in the above paragraph can partially be explained by theoretical models. For example, the bursts can be explained in the magnetar model as sudden crustal yields. Also, the slower flux evolution (*e.g.* Gavriil & Kaspi 2004; Dib et al. 2007a) has been suggested to be due to slow magnetospheric twists (Thompson et al., 2002). Some support for this picture has been argued to come from observed correlations between flux and spectral hardness (Woods et al., 2004; Rea et al., 2005; Campana et al., 2007), although Özel & Guver (2007) argue that such a correlation need not originate uniquely from the magnetosphere and could be purely thermal.

The question of why some of the timing variability is accompanied by radiative changes and some not is not clearly answered by theory. At least some radiative variability has been seen to be correlated with timing behaviour. The best example of this occurred in the 2002 outburst of AXP 1E 2259+586 in which the pulsar suffered a large spin-up glitch apparently simultaneously with a major X-ray outburst (Kaspi et al., 2003; Woods et al., 2004). Israel et al. (2007) described a similar

radiative outburst in AXP CXOU J164710.2−455216, and reported a large contemporaneous glitch, as did Dib et al. (2007b) for AXP 1E 1048.1−5937. By contrast, AXP 1RXS J170849.0−400910 exhibited several glitches with no evidence for a corresponding radiative event (Kaspi et al. 2000; Kaspi & Gavriil 2003, Chapter 4) although Rea et al. (2005); Campana et al. (2007); Israel et al. (2007) suggested that observed flux and spectral changes may be associated with the glitches in this source.

Perhaps the least understood form of variability are the changes in the pulse profiles. The first observed pulse profile change in an AXP was reported by Iwasawa et al. (1992) using *GINGA* data obtained in 1989. They witnessed a large change in the ratio of the amplitudes of the two peaks in the pulse profile of 1E 2259+586. They also reported a contemporaneous timing anomaly. A very similar pulse profile change was witnessed during and immediately following the 2002 outburst of 1E 2259+586 (Kaspi et al., 2003; Woods et al., 2004). Given the nature of this event, a likely explanation for the pulse profile change is a magnetospheric reconfiguration following a crustal fracture that simultaneously affected the inside and outside of the star.

When not in outburst, the following description applies to AXPs: They are persistent X-ray sources in the range (0.1−10 keV), with luminosities ranging between 10^{34}−10^{36} erg s^{-1} (except for XTE J1810−197, 1E 1547.0−5408, and CXOU J164710.2−4552161647 which are transient, *i.e.,* variable by 2−3 orders of magnitude in luminosity). The X-ray emission is pulsed at the spin period, and the pulsed fraction varies from source to source. The spin periods are narrowly clustered between 2−12 s. Measurements of the AXP spin-down rates, when interpreted in terms of the magnetic braking of isolated neutron stars, indicate that AXP magnetic fields are on the order of 10^{14} G. The soft X-ray spectra of the emission outside the active periods are interpreted as predominantly thermal with magnetospheric effects, and are usually fitted by a combination of a power-law (photon index ~ -3) and a blackbody with temperature $kT\sim$ 0.5 keV. AXPs tend to have softer spectra below 10 keV than their cousins the Soft Gamma Repeaters (Section 1.2.2). The spectra, the pulse morphology, and the timing properties of AXPs are known to change during outbursts. Spectrally, though previously studied only in the soft X-ray band, AXPs are now seen in many different bands. AXP emission at other wavelengths is discussed in Section 1.2.5.

The currently known Anomalous X-ray Pulsars are listed in Table 1.1 below. A literature review of the observational properties of these 10 sources reported as of 2008 December is presented in Appendix C.

AXP	Notes
1E 2259+586	monitored with *RXTE*
4U 0142+61	monitored with *RXTE*
1RXS J170849.0−400910	monitored with *RXTE*
1E 1841−045	monitored with *RXTE*
1E 1048.1−5937	monitored with *RXTE*
CXOU J010043.1−721134	
CXO J164710.2−455216	"Transient" AXP
XTE J1810−197	"Transient" AXP
1E 1547.0−5408	"Transient" AXP
1E 1845−0258	Candidate AXP

Table 1.1 List of the known Anomalous X-ray Pulsars as of 2008 December.

1.2.4 The Magnetar Model

In this Section, I provide a brief description of the magnetar model. When additional information is needed, it is provided in the subsequent Chapters.

Magnetar Fields and Magnetic Energy

In the magnetar model, AXPs and SGRs are young highly magnetized ($10^{14}-10^{15}$ G) neutron stars. The fact that magnetars are young is supported by the association of several of the sources with supernova remnants (see Appendix C) (and Appendix B). It is also supported by their small scale height on the Galactic plane, and by their tendency to be found in regions of active star formation and close to clusters of massive stars (*e.g.* Eikenberry et al. 2004).

The magnetar model was initially put forth to try to explain the properties of giant flares. As discussed in Section 1.2.2, giant flares are characterized by an initial hard spike of emission lasting a fraction of a second, followed by a long tail (several minutes) with a softer spectrum, and clearly showing the periodic modulation due to the neutron star rotation. One motivation for a high magnetic field includes the necessity to provide energy to power the giant flares. The time scale of the original spike in a giant flare is consistent with the propagation speed of a magnetic instability over the whole neutron star surface, making this explanation plausible (Duncan & Thompson, 1992; Thompson & Duncan, 1995b). In addition, the magnetic confinement of the hot plasma responsible for the pulsating tail is considered to be strong evidence for the presence of a high magnetic field (Duncan & Thompson, 1992; Thompson & Duncan, 1995b).

As far as direct measurements of the magnetic field are concerned, in periods of quiescence, no spectral features at X-ray energies where proton-cyclotron resonances occur in magnetar-strength field have been reported. The only exception is the detection of a possible 8 keV absorption line in the BeppoSax spectrum of AXP 1RXS J170849.0−400910 (Rea et al., 2003), later not confirmed (Rea et al., 2005). During outbursts however, there were some reported broad features (Mazets et al., 1979b; Strohmayer & Ibrahim, 2000; Ibrahim et al., 2003b). The authors have argued that these lines represent proton cyclotron absorption features in a strong magnetic field. In addition emission features near 14 keV have been discovered in the spectra of bursts from AXPs 1E 1048.1−5937, XTE J1810−197, and 4U 0142+61 (*e.g.* Gavriil et al. 2002, also see Chapter 3). It should be emphasized that the same spectral feature has not yet been detected in the same burst by independent instruments.

In Section 1.1.6, I mentioned that the origins of the magnetic field of pulsars is not entirely clear. This is even more true for the even higher magnetic field of magnetars. One theory is that it is due to an efficient dynamo operating in the new neutron star (if it is born with sufficiently small periods) or in the layers of the progenitor star (Duncan & Thompson, 1992; Thompson & Duncan, 1993). Another theory is the "fossil field" scenario in which the magnetars would be the descendent of the massive stars with the highest fields (see Section 1.2.7). In a third recently proposed scenario, magnetars have a strongly magnetized core, initially shielded by crustal currents, that slowly emerges outward (Bhattacharya & Soni, 2007). In the first two scenarios, magnetars are born with high magnetic fields which subsequently decay. In the third recently proposed scenario, the very large magnetic fields of magnetars slowly emerge as the shielding currents decay.

Recall from Section 1.1.6 that even in the simplified model where there is no plasma surrounding pulsars, a rotating pulsar in vacuum will slow down. This is because a rotating magnetic field creates electromagnetic waves. The energy of these waves comes from the loss of rotational kinetic energy of the pulsar. Young magnetars, having higher fields, would undero a rapid spin-down, reaching periods of several seconds in a few thousand years. If the formation scenario in which magnetars are born spinning very rapidly is true, this explanation provides a natural way to slow down a neutron star to the long periods typical for magnetars in relatively short time. In this picture, it does not take very long for a magnetar to slow down to a point when its magnetic energy is larger its their rotational kinetic energy. For a magnetar of magnetic field $\sim 10^{15}$ G and a radius of 10 km, the stored magnetic energy is 10^{47} erg, which is

sufficient to power a magnetar with a luminosity of 10^{35} erg s^{-1} for 10^4 years.

Magnetar Emission and the Twisted Magnetosphere Model

The X-ray emission from non-transient magnetars (luminosity $\sim 10^{35}$ erg s^{-1}) is larger than the rate of loss of their rotational energy. The magnetic field decay provides a significant source of heating which partly explains the X-ray emission (Thompson & Duncan 1996; Heyl & Hernquist 1997a,b). This internal heating source yields a surface temperature higher than that of a cooling neutron star of the same age and smaller magnetic field. In addition to the heating caused by the decay, persistent emission can be induced by the twisting of the magnetosphere caused by internal magnetic field twists propagating outward. Thompson et al. (2002) studied the properties of twisted magnetospheres, with induced currents going through them (see below).

It is believed that the magnetar internal field is tightly wound up and that it might be up to a factor of ~ 10 stronger than the external field (Thompson & Duncan, 2001). The unwinding of the internal field shears the neutron star crust. In the case for which the crust is not easily deformable, this can generate multiple small fractures in the crust, providing a possible explanation for short bursts (Thompson & Duncan, 1995b). Alternatively, the bursts could be caused by the sudden loss of magnetic equilibrium through the development of a tearing instability (Lyutikov, 2002, 2003). By twisting the footpoints of the external magnetic field, we get local and global twists in the magnetosphere. The magnetospheric twisting induces electric currents in the magnetosphere. Repeated inverse Compton scattering of the thermal photons emitted at the stellar surface with the accelerating electrons gives rise to the significant high-energy tail observed in the spectrum of the source. Some particles are scattered back towards the surface providing an additional source of heat.

The outbursts/flares of magnetars are hypothesized to arise from the direct injection of energy into the magnetosphere, through a rearrangement of the magnetic field in the magnetosphere (either locally or globally) and through the dissipation of strong localized currents.

Torques

Another consequence of the twisted magnetosphere is that the torque on the star is different for different field configurations. A more highly twisted magnetosphere leads to larger torques because of the presence of large-scale currents. Given that both the

spectral hardening and the spin-down rate of the star increase with twist angle (for a global twist), one would expect a correlation between these quantities and one has been reported (Marsden & White, 2001). A progressional increase in the twist angle is also expected to be accompanied by bursts if the crust breaks. The luminosity is expected to be correlated with the amount of twist as well, since an increase in the twist angle means an increase in the currents, leading to an increase in the up-scattering and in the back-scattering. The energetic outbursts/flares seen in magnetars are believed to be the result of global reconfigurations of the neutron star magnetosphere.

For the interior compositon of magnetars, the magnetar model assumes the standard neutron-star composition, distinguished only from rotation-powered pulsars by a strongly wound-up internal magnetic field (Thompson & Duncan, 2001). The general description of the interior in Section 1.1.13 still applies here, and in particular, there is expected to be a neutron superfluid beneath the crust. Glitches can then in principle occur due to a sudden unpinning of the vortex lines in the superfluid (Thompson & Duncan 1993, also Section 1.1.14). Alternatively, a glitch can occur if the crust is twisted adiabatically about an axis that is tilted with respect to the rotation axis: more superfluid vortices move out from the rotation axis than move towards it, even though they are still pinned to the crust (Thompson et al., 2002; Woods & Thompson, 2006)

Other Models

The magnetar model is not the only model that people use to try to explain the properties of AXPs and SGRs. There are several other models based on surrounding residual disks. In this class of models, generally a strong magnetic field is not required, but the presence of a disk is invoked to account for the large spin-down. The formation of the disk is different from model to model (*e.g.* van Paradijs et al. 1995; Alpar 2001; Marsden et al. 2001). The most severe criticism of these scenarios is that they cannot easily account for bursts or flares. Other criticisms are based on the fact that the disks should be visible in the optical and IR bands. There have been claims that the optical and IR emission of AXP 4U 0142+61 is due to a disk: Wang et al. (2006) suggested that this emission is due to a passive disk, while Ertan et al. (2007) suggested that it is due to an active accretion disk.

Hybrid models also exist in which there is a disk and a magnetar-strength non-dipolar magnetic field. In this scenario the dipole component is similar to that of ordinary rotation-powered pulsars (*e.g.* Ekşı & Alpar 2003; Ertan & Alpar 2003).

1.2.5 Magnetar Observations at Other Wavelengths

Spectrally, though previously studied only in the soft X-ray band, AXPs and SGRs are now seen in the radio band (Camilo et al., 2006), through the mid- (Wang et al., 2006) and near-IR (*e.g.* Israel et al. 2002; Wang & Chakrabarty 2002; Hulleman et al. 2004; Tam et al. 2004; Rea et al. 2004a; Durant & van Kerkwijk 2005, in the optical range (*e.g.* Kern & Martin 2002; Dhillon et al. 2005), up to hard X-ray energies (Kuiper et al., 2006). For a summary of the detections at other wavelengths, see Table 1.2 below, based on Table 1 in Mereghetti (2008). This thesis primarily deals with the soft X-ray emission of AXPs, but I briefly comment on the detections at other wavelengths below.

In the infrared, all known counterparts are very faint. This excludes the presence of normal stars as companions. The origin of the infrared emission is debated. For example, after the 2002 June outburst of 1E 2259+586, the IR counterpart was a factor ~ 3 brighter than the pre-outburst level (Kaspi et al., 2003). The IR and X-ray subsequenty decayed in a similar way. This was interpreted as a decaying magnetospheric disturbance (Tam et al., 2004), however Ertan et al. (2006) showed that the data can be explained as emission from a disk pushed away by the outburst. Other correlations between X-ray and IR fluxes have sometimes been confirmed, but a single coherent picture has not yet emerged.

In accreting pulsars, radio pulsations are not expected because accretion is thought to stop the creation of the cascades of charged particles responsible for the radio emission. However for magnetars, the reason for the lack of radio pulsations is unclear (*e.g.* Camilo et al. 2000; McLaughlin et al. 2004). As of 2008 December, there were radio pulsations detected from two magnetars. The pulsations came from two "transient" AXPs (see Table 1.2). For XTE J1810−197, the radio emission started about a year after the dramatic sudden brightening (Camilo et al., 2007a). The spectrum of the radio emission was different from that of ordinary rotation-powered pulsars. For 1E 1547.0−5408 the radio emission was first detected before the pulsations became visible in the soft X-rays.

The softness of magnetar spectra below 10 keV (power-law indices between -2 and -4) predicts non-detections for energies above 10 keV, and thus explains the initial lack of studies of the spectral properties of AXPs at energies above 10 keV (see a typical AXP spectrum in the soft X-rays in Figure 1.6). It was then a great surprise that the high-resolution imaging instrument IBIS/ISGRI aboard the *INTEGRAL* satellite

Table 1.2. Multiwavelength emission from AXPs and SGRs[a]

Source[b,c]	Emission[d]
AXP 1E 2259+586[e]	Soft X-rays:P, IR:D.
AXP 4U 0142+61	Hard X-rays:P, Soft X-rays:P, Optical:P, IR:D.
AXP 1RXS J170849.0−400910	Hard X-rays:P, Soft X-rays:P, IR:D?.
AXP 1E 1841−045[e]	Hard X-rays:P, Soft X-rays:P, IR:D?.
AXP 1E 1048.1−5937	Hard X-rays:D, Soft X-rays:P, Optical:P, IR:D.
AXP CXOU J010043.1−721134 (in the SMC)	Soft X-rays:P.
AXP CXO J164710.2−455216[f]	Soft X-rays:P.
AXP XTE J1810−197[f]	Soft X-rays:P, IR:D, Radio:P.
AXP 1E 1547.0−5408[e,f,g]	Soft X-rays:P, Radio:P.
AXP Candidate 1E 1845−0258[e]	Soft X-rays:P.
SGR 0526−66[e](in the LMC)	Soft X-rays:P.
SGR 1627−41[f]	Soft X-rays:P.
SGR 1806−20	Hard X-rays:D, Soft X-rays:P, IR:D.
SGR 1900+14	Hard X-rays:D, Soft X-rays:P, IR:D?.

[a]For references, see Table 1 in Mereghetti (2008) and the magnetar catalog. Also see Dhillon et al. (2009) for the optical pulsations of AXP 1E 1048.1−5937 and Esposito et al. (2008b) for the soft X-ray pulsations of SGR 1627−41.

[b]Candidate SGRs and the most-recently discovered SGR 0501+4516 are not included.

[c]The first five sources are the monitored AXPs.

[d]P indicates pulsed emission. D indicates unpulsed detection.

[e]Associated with a supernova remnant.

[f]Indicates a transient AXP/SGR, *i.e.,* variable by 2−3 orders of magnitude in luminosity.

[g]The emission in this table predates the entry of 1E 1547.0−5408 into an active phase in 2008 October.

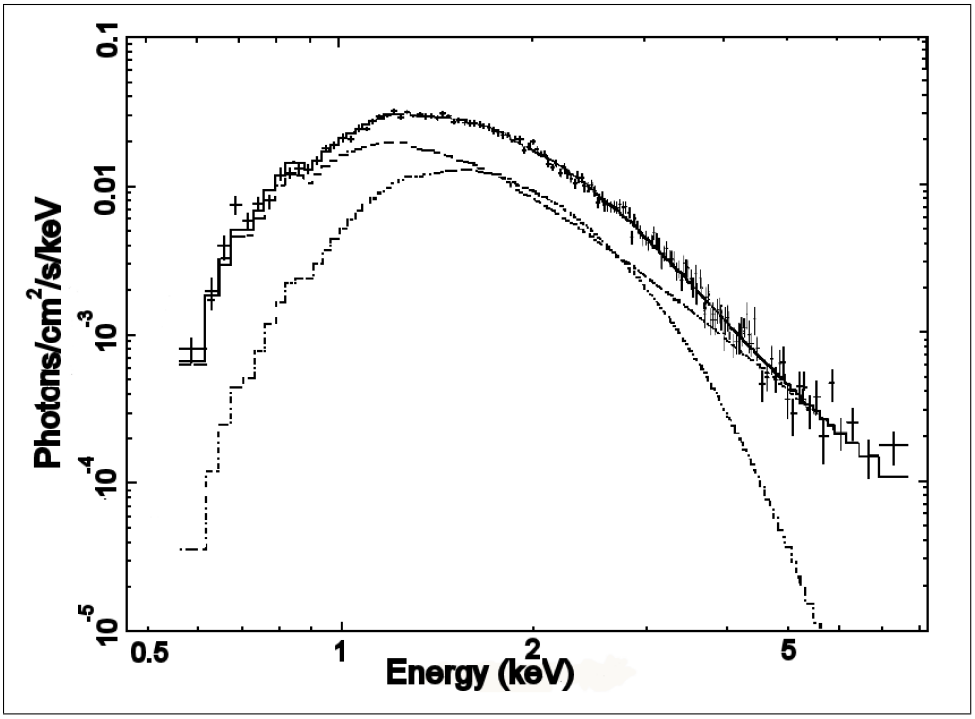

Figure 1.6 *ASCA* spectrum of 4U 0142+61 (crosses). The histograms show the individual contributions of the blackbody (dot-dash), power-law (dashed), and combined spectral components (solid). The power law dominates at low and high energies. The turn-over at low energies and edges at 0.6 and 0.85 keV are caused by absorbing material in the line of sight. (Figure from White et al. 1996).

measured hard X-rays from the direction of several AXPs (Molkov et al., 2004; Kuiper et al., 2004; Kuiper et al., 2006). Figure 1.7 shows the spetrum of AXP 4U 0142+61 at high energies. Beloborodov & Thompson (2007) proposed the existence of a plasma corona contained within the closed magnetosphere to explain the broad band spectrum of magnetars that extends from the infrared to hard X-rays beyond 100 keV.

1.2.6 Magnetars in a Larger Context

Magnetars are isolated neutron stars. Observations over the whole range of the electromagnetic spectrum allowed the discovery of many classes of isolated pulsars: magnetars (AXPs and SGRs), XDINs (introduced in Section 1.1.5), Central Compact Objects (CCOs), and "ordinary" rotation-powered pulsars. It is possible that the existence of all these classes reflects a large variety in the birth properties of neutron stars, but it is also possible that some of these classes are linked by evolutionary paths. Comparing the observational properties of the different classes of isolated neutron stars,

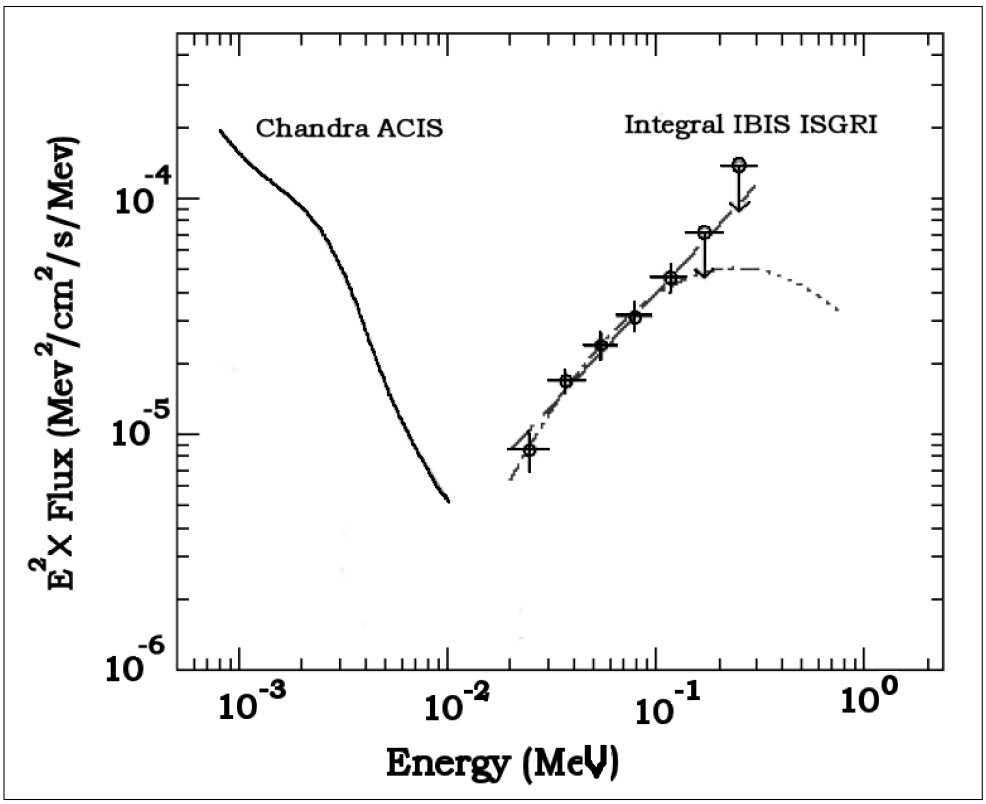

Figure 1.7 A spectral representation of the total high-energy emission of 4U 0142+61. *Left:* the 0.4−10 keV *Chandra ACIS* spectrum. *Right:* the 20−300 keV *INTEGRAL IBIS ISGRI* spectrum. (Figure adapted from Kuiper et al. 2006).

is useful because it can provide clues about what physically differentiates magnetars from other pulsars. Such a discussion is beyond the scope of this introduction, but is presented in Appendix D.

1.2.7 Magnetar Progenitors

As explained in Section 1.2.6, a fundamentally unresolved issue in the study of compact objects is why some neutron stars are ordinary radio pulsars, while others are magnetars (AXPs and SGRs). The answer is possibly related to mass of their respective progenitors.

Since the probability of creation of massive stars declines sharply with the mass, most neutron star progenitors are expected to have masses near the minimum mass for core collapse, *i.e.*, 8−9 $M_{\odot}$.

However, two SGRs are associated with clusters of massive stars (Eikenberry et al., 2004; Corbel & Eikenberry, 2004; Mereghetti et al., 2005). Also, Gaensler et al. (2005)

presented evidence that the progenitor of AXP 1E 1048.1−5937 was considerably more massive than $8M_{\odot}$. In addition, Muno et al. (2007) observed the cluster of massive stars Westerlund 1, which is just old enough for $> 40M_{\odot}$ stars to have undergone supernovae (Muno, 2007), and found the 10.6 s AXP CXO J164710.2−455216. Muno et al. (2007) proposed that the difference between normal pulsars and magnetars is the progenitor mass. They noted that massive (> 25 $M_{\odot}$) stars do not always form black holes and sometimes form neutron stars, either because of their metallicity, or because of mass loss due to a companion.

Recall from Section 1.2.4 that magnetars are believed to result from rapidly rotating ($P \sim 1$ ms) proto-neutron stars, in which an efficient large-scale dynamo operates in the first few seconds after birth, generating a super-strong magnetic field (Duncan & Thompson, 1992; Thompson & Duncan, 1993). Gaensler et al. (2005) argue that for more massive progenitors, the reduced time interval between hydrogen depletion and the supernova results in limited braking of the core, producing the very rapidly spinning predicted young neutron stars (also see Heger et al. 2005). This view is supported by the fact that AXP CXO J164710.2−455216, SGR 1806−20 and SGR 1900+14 are associated with massive star clusters.

If indeed very massive stars are responsible for AXPs, this would mean low birthrates for AXPs as very massive stars are rare. There are ~ 10 magnetar candidates in our Galaxy and a conservative estimate of their average age is $\sim 10^4$ years as derived from their spin down. Thus, a lower limit to the Galactic birth rate is 1 per 1000 years, or $\sim 10\%$ of the radio pulsar birth rate (Lyne et al., 1998; Woods & Thompson, 2006). However, the birth rate that we infer for AXPs and SGRs depends critically upon our overall efficiency at identifying magnetar candidates.

1.3 The AXP Monitoring Program

When people began to realize that Anomalous X-ray Pulsars formed a distinct class of objects, there were questions about what the driving force of these objects is: accretion or magnetism. One way to test both the magnetar and accretion models was through timing observations. The spin-down of some AXPs had been "monitored" by considering the measured frequency at individual epochs using a variety of instruments (*e.g.* Baykal et al. 1998; Gotthelf et al. 1999). However, those measurements were sparse and were only marginally sensitive to spin irregularities on time scales of weeks to months, relevant to glitches or accretion torque fluctuations. Further, it was hard

to determine whether AXPs exhibited timing noise and glitches similar to those seen in rotation-powered pulsars, because high-precision determination of the spin evolution over a long baseline was lacking. This is why the AXP monitoring program was initiated in 1997.

When the program was initiated, it became for the first time clear that high precision is possible to achieve with AXP timing. Ever since its start, the project has provided a wealth of information about the behaviour of AXPs both in quiescence and in outburst. It first provided accurate spin parameters using long-term phase-coherent timing of several AXPs. It showed that, like rotation-powered pulsars, AXPs glitch (*e.g.* Kaspi et al. 2000). It showed that AXPs exhibit strong timing noise and sometimes, unusually large torque variations (*e.g.* Kaspi et al. 2003; Woods et al. 2004). It also showed that when in outburst, AXPs exhibit pulsed flux changes and bursts that are similar to those of SGRs (*e.g.* Gavriil & Kaspi 2004), a result which helped unify the two classes as magnetars.

The Proportional Counter Array (PCA) on board of *RXTE* is an ideal instrument for the task of phase-coherently timing the AXPs because of its high time resolution and because of the high manoeuvrability of *RXTE* (See Section 1.4 for a description of *RXTE*). With the help of *RXTE* data, the monitoring project has provided information about the following four aspects of AXPs:

1. The timing parameters.
2. The pulsed flux (measurements of the total flux were not provided because of the large field of view of *RXTE*).
3. The pulse profile evolution.
4. Bursts.

Unfortunately, it was not possible to monitor all magnetars with *RXTE* because some are far too faint, or have spectra that are too soft. But five AXPs are monitored regularly: 1E 2259+586, 4U 0142+61, RXS J170849.0−400910, 1E 1841−045, 1E 1048.1−5937, and several others are monitored when in outburst. The estimated average distance to the monitored AXPs is $\sim$ 5 kpc[10], implying that on average, it took 16000 years for the X-ray photons studied as a part of this project to travel from the AXPs to Earth.

[10]Data from the online magnetar catalog.

RXTE is scheduled to be operational and to continue the AXP monitoring until 2010 September.

For the duration of the monitoring program, *RXTE* observations complemented the imaging observations of many other contemporary X-ray satellites. The X-ray missions whose functioning overlapped with *RXTE* included: *ROSAT* (1990−1999), *ASCA* (1993−2000), *BeppoSax* (1996−2002), *the Chandra X-ray Observatory (CXO, or Chandra)* (1999−present), *the X-ray Multi-Mirror Mission (XMM, or XMM-Newton)* (1999−present), *Swift* (2004−present), and *Suzaku* (2005-present).

1.4 The Rossi X-ray Timing Explorer

1.4.1 Overall Description

The Rossi X-Ray Timing Explorer (*RXTE*) satellite was launched in December of 1995. Since then, it has been orbiting the Earth every ∼100 minutes in a circular low Earth orbit with an altitude of ∼600km and an inclination of ∼23°. The main objective of *RXTE* is to study the timing properties and spectra of X-ray sources in the energy range from 2 to 200 keV (Jahoda et al., 1996; Swank et al., 1995; Bradt et al., 1993).

RXTE carries three instruments on board. The Proportional Counter Array (PCA), the High Energy X-ray Timing Experiment (HEXTE), and the All Sky Monitor (ASM). The two large area instruments (PCA and HEXTE) are X-ray telescopes that can view a single source in their common one degree field of view. The PCA and HEXTE measure short-term variability of the observed sources to microsecond levels. The ASM scans most of the sky every 1.5 hours in order to monitor the intensity and spectra of the brightest sources in the sky. In this thesis we used *RXTE* data from the PCA instrument only. The PCA data became publicly available a year after being collected, except in 2009 when it becamse public immediately.

1.4.2 The Spacecraft

The *RXTE* instruments and the service hardware are all integrated onto a common spacecraft structure (Figure 1.8). The spacecraft permits rapid pointing to almost any position on the sky. It is highly maneuverable ($> 6°$/min). The PCA/HEXTE field can be pointed to any position on the sky on any day of the year, provided the angle to the Sun is $> 30°$ (the Earth constraint angle is smaller, however, users are advised to

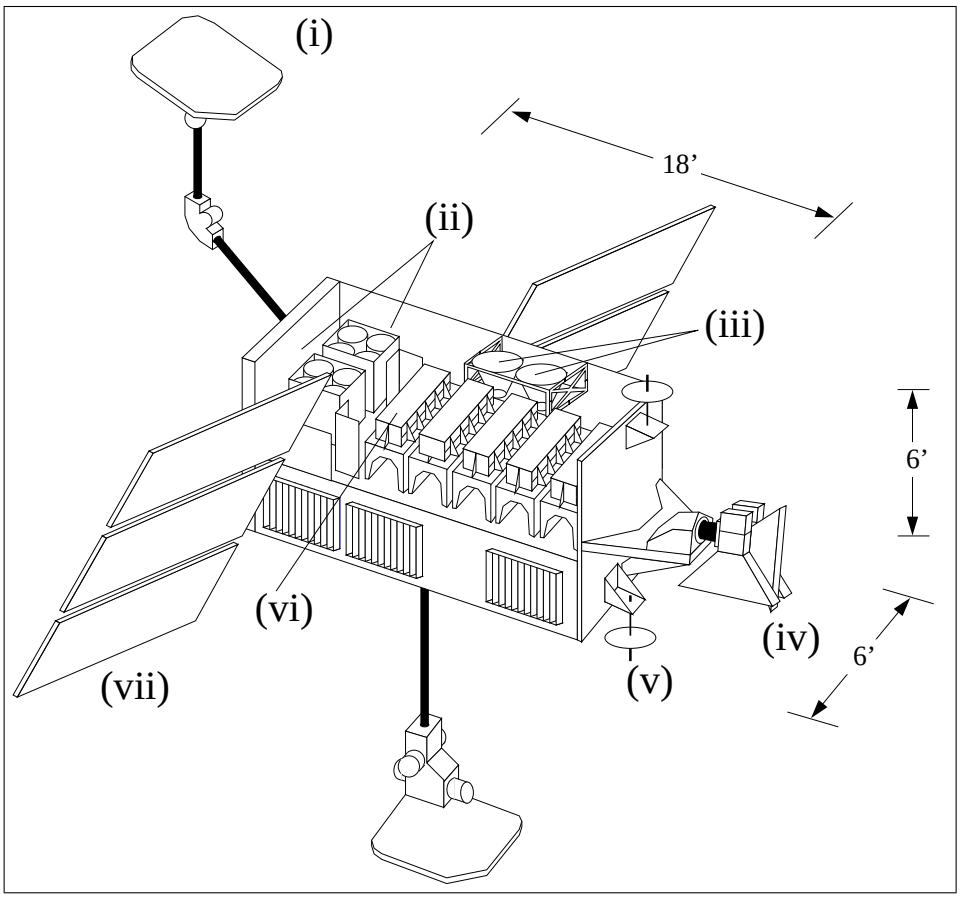

Figure 1.8 The *RXTE* spacecraft: (i) High-gain antenna; (ii) High-Energy X-ray Timing Experiment (HEXTE); (iii) Star trackers; (iv) All-Sky Monitor (ASM); (v) Low-gain antenna; (vi) Proportional Counter Array (PCA, 1 of 5); (vii) Solar-power array. (Figure from Gavriil 2001, adapted from a Figure in Bradt et al. 1993).

filter out data where the angle to the Earth is $< 10^{\circ}$). The pointing accuracy is $< 0.1^{\circ}$ (Bradt et al., 1993).

1.4.3 The Proportional Counter Array (PCA)

The Proportional Counter Array (PCA) consists of 5 large multi-anode Proportional Counter Units (PCUs) (Figure 1.9) with a total net area of $\sim$ 6500 cm^2 (Jahoda et al., 1996). Proportional counters operate on the following principle: when a photon coming from the source interacts with the gas inside the detector it creates a cloud of electron-ion pairs. Applying voltage to the gas causes the electrons and ions to drift to their respective readout electrodes: The electrons drift towards the anode (or anodes, since there are many in multi-anode detectors), and the ions drift towards the cathode. During the migration, collisions occur with the neutral gas molecules. But because of

their high mass, the ions achieve very little average energy between collisions. Free electrons, on the other hand, are easily accelerated by the applied field and may have a significant kinetic energy when colliding with atoms on the way. If this energy is greater than the ionization energy of the gas, it is possible for additional electron-ion pairs to be created in these collisions. These secondary electrons are then accelerated, undergo collisions, and create further ionizations. Hence there is a cascade of charged particles. Within a specific range of voltages (which is a property of the gas used inside the detector) the size of this avalanche, and therefore the amount of charge collected at the electrodes, is nearly linearly proportional to the incident photon energy. This is the region that the PCA operates in, hence the name proportional counter. Every photon collected by the PCA is tagged with an arrival time and with an incident energy.

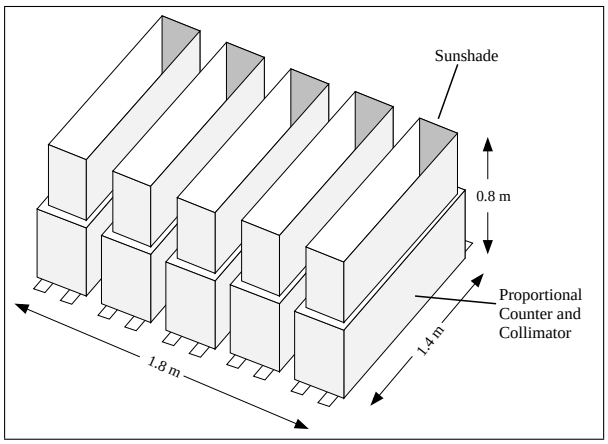

Figure 1.9 The PCA assembly (5 units). (Figure from Gavriil 2001, adapted from a Figure in Bradt et al. 1993).

The PCA is effective over the range of 2−60 keV. Each PCU is collimated to a 1° field of view by a tubular collimator (Figure 1.10). Behind the collimator there are two mylar windows, each 1 mm thick and coated on both sides by a thin layer of aluminum. These windows are separated by 1.3 cm and contain a layer of propane used to screen out low energy electrons ($E_e < 2$ keV). The propane layer may also be used as a signal layer in the energy range 1−3 keV. Behind the second mylar window is the main detector volume filled with a 90% Xenon and 10% Methane mixture. This section is 3.6 cm thick and is maintained at 1 atmosphere. Inside the xenon/methane chamber are three layers of signal anodes which collect the charge deposited by incident X-rays. To obtain the highest possible signal-to-noise ratio, it is preferable to use data from the first layer only. The gas chamber is followed by an anti-coincidence node layer at the bottom of the chamber. Side anodes provide further anti-coincidence. The counters

are shielded to provide further background reduction. The gain of each counter is monitored continuously with an americium radioactive source. Photons that are due to the radioactive source are registered simultaneously by the counter and by an alpha particle detector placed at the bottom of the PCU. These are the calibration X-rays (Bradt et al., 1993). It is important to note that PCUs are regularly turned off (and later back on) in order to extend their useful lifetime. One must keep track of the number of PCUs on during an observation and take it into account while doing the data analysis.

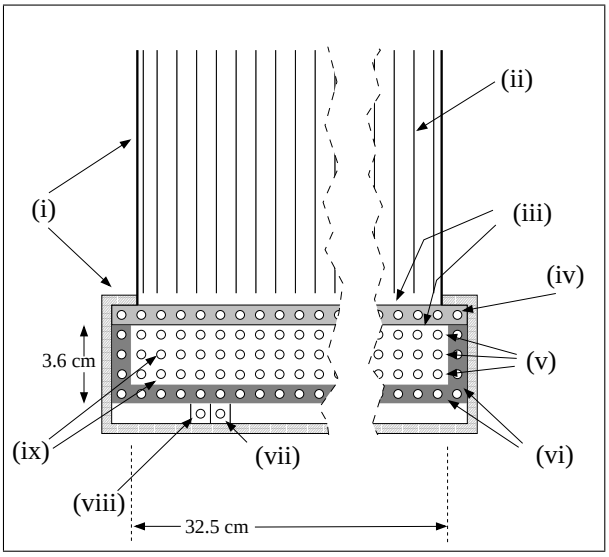

Figure 1.10 One of the five proportional counters: (i) X-ray shielding; (ii) Collimator (hexagonal) 1° FWHM; (iii) Mylar windows; (iv) Anticoincidence layer (Propane); (v) Three signal layers (xenon/methane); (vi) Anticoincidence chambers (xenon/methane); (vii) Americium source; (viii) Alpha detector; (ix) Anodes. (Figure from Gavriil 2001, adapted from a Figure in Bradt et al. 1993).

1.4.4 The Experiment Data System

The Experiment Data System (EDS) was built in order to compress the data and to select only the information requested by the observer before sending it to the ground. The EDS consists of eight Event Analyzers (EA), of which six are dedicated to the PCA and two to the ASM. Each EA contains an Intel processor and some associated memory. Each EA sees all the PCA data, just as if the original incoming data stream were duplicated 6 times. Each EA can process the incoming events in one of many available ways according to criteria requested by the observer. All EAs

work simultaneously. The EDS is capable of processing count rates from the PCA up to $\gtrsim$ 500000 counts per second and is able to time photon arrival times to $\sim 1\mu s$.

Each EA can run in any of seven basic modes. Some mode are available in many different configurations. A configuration is a prescription for compressing the data based on time and energy information. The first available mode is *(i)* event data mode which can be further divided into three submodes: transparent mode, good xenon mode, and generic data mode. In event data mode, each photon is registered as an event and tagged with an arrival time and energy information. We used good xenon mode in this thesis. For brighter sources the count rate increases. In this case *(ii)* binned mode is available where histograms rather than events are telemetered to the ground. Event mode and binned mode are very frequently used. Each EA can also function in *(iii)* burst catcher mode, *(iv)* pulsar fold mode, *(v)* Fast Fourier Transform mode, *(vi)* delta-binned mode, *(vii)* and single bit mode. The data from each mode follows one of two basic formats: science event data and science array data. Both of these formats follow the guidelines of the FITS format. FITS stands for 'Flexible Image Transport System' and is the standard astronomical data format endorsed by both NASA and the International Astronomical Union (IAU).

Two of the PCA EAs always run in binned mode, in the 'Standard1' and 'Standard2' configurations, with timing and spectral parameters that remain unchanged throughout the *RXTE* mission. The other four EAs run in modes/configurations specified by the observer.

The EDS, rather than the PCA, stamps events with their arrival times and performs background rejection. Background rejection is the sifting out of non-cosmic-X-ray events by on-board electronics. Background subtraction is the derivation of the true net signal from a cosmic source, and is done, if needed, when the data are filtered by the observer on the ground.

Once the EAs are done processing, they create data packets for transfer to the spacecraft memory from which they are transmitted via the telemetry stream to the ground at a rate of 256 kb/s for ∼30 minutes a day (Bradt et al., 1993).

1.4.5 Preliminary Data Preparation

As explained in the data analysis Sections of the individual manuscripts included in this thesis, for the purposes of the AXP monitoring program, we needed to extract a binned time series (photon counts versus time) from each *RXTE* observation. This

time series was then used to extract *a)* burst statistics, *b)* a pulse profile, *c)* a pulsed flux measurement, and *d)* a pulse Time of Arrival (TOA, see Section 1.1.9).

To obtain a time series, we first downloaded the data for each observation, complete with information about the status of the operating instruments and an exact ephemeris of the satellite. The data for the individual observations were available in 'ds' format from MIT 2 days after the observation was taken. The data in FITS format were available on the NASA archives[11] $\sim$ 10 days after the observation was taken. The *RXTE* monitoring program is of a time-sensitive nature: in the case of an AXP outburst, we need to obtain additional *RXTE* observations, and we need to alert the astronomical community so they can use telescopes with other wavelength capabilities to look at the source in outburst as quickly as possible. Because of this, we used the data in 'ds' format for the preliminary data analysis. Later, when came the time to prepare manuscripts based on the monitoring program, we downloaded the data in FITS format, and updated the burst statistics, pulse profile, and pulsed flux results. We preferred the FITS to the 'ds' data for final reports because the FTOOLS, software used to analyse the fits data, is more complete.

After downloading the data for a given observation, we did the following. We gave as input to our time-series preparation script the downloaded data files and a filter file containing information about the location of *RXTE* and the status of the instruments on board during the observation. The script removed any data segments in which *RXTE* was not pointed at the right source, in which all PCUs were off, and in which the Earth elevation angle was less than 15.5 degrees. The script then translated the arrival time of the photons from the location of the satellite to the barycenter of the solar system. To do this, the script used the information provided in the filter file to remove time delays due to the motion of Earth and that of *RXTE*. The script then selected all photons in a user-specified energy band that were detected by user-specified PCUs. Finally the script created the final time series by placing the remaining photons into bins of size 31.25 ms = (1/32 s).

Once we obtained the time series, we then *a)* searched it for bursts, *b)* folded it using an up-to-date ephemeris (or a periodogram) to obtain a pulse profile, *c)* fed it into a secondary script that calculated either an RMS or area pulsed flux (see Sections 2.3.3, 3.3.4, 4.5, and 5.5), and *d)* folded it and cross-correlated the resulting profile with a long-term pulse profile template to extract a TOA (see Section 1.1.9),

[11]For real-time data, use http://heasarc.gsfc.nasa.gov/docs/xte/SOF/SOF_data_hp.html, and for public archival data, use ftp://legacy.gsfc.nasa.gov/xte/data/archive/

which was later used for phase-coherent timing.

1.5 Outline of This Thesis

In Chapters 2−5 of this thesis, I present the latest results of the AXP monitoring program; results which appeared in 4 co-authored published/submitted manuscripts. The relative contributions of the different authors are stated in the "Contribution of Authors" Section of the thesis directly before the Table of Contents. Brief connecting texts as well as the original abstracts of the manuscripts are presented at the beginning of each Chapter to provide continuity.

In Chapter 2 we study the slowly evolving timing, pulsed flux, and pulse profile properties of AXP 4U 0142+61 from 1997 to 2006 February.

Chapter 3 is about the changes in the properties of AXP 4U 0142+61 that occured when this source entered an active phase in 2006 March and subsequently recovered.

Chapter 4 summarizes the timing, pulsed flux, and pulse profile history of AXPs 1RXS J170849.0−400910 and 1E 1841−045 since the beginning of the monitoring program. The fact that each of these AXPs exhibited several glitches allows us to start comparing the properties of AXP glitches to those of rotation-powered pulsar glitches.

Chapter 5 summarizes the timing, pulsed flux, and pulse profile history of AXP 1E 1048.1−5937. In addition, in this chapter we revisit the 2001−2002 pulsed flux flares, and the subsequent large spin-down variations. We also report on the changes in the properties of 1E 1048.1−5937 that occured during the 2007 outburst.

Finally, in Chapter 6, I present summary plots of the evolution of the timing, pulsed flux, and pulse profile properties for all five monitored AXPs. The implications of the findings are reported in the discussion Sections of the individual Chapters. A final discussion is included in Chapter 6.

Chapter 2

Long-Term Variability in the Anomalous X-Ray Pulsar 4U 0142+61

This chapter is based on the manuscript "10 Years of RXTE Monitoring of the Anomalous X-Ray Pulsar 4U 0142+61: Long-Term Variability", published in *the Astrophysical Journal* in 2007 September (reference: Dib, Kaspi, & Gavriil, 2007a). In the manuscript, we discuss the timing properties, the pulsed flux evolution, and the pulse profile evolution of AXP 4U 0142+61 from 1996 to 1998 and from 2000 to 2006 February. The original abstract is below.

We report on 10 years of monitoring of the 8.7-s Anomalous X-ray Pulsar 4U 0142+61 using the *Rossi X-Ray Timing Explorer (RXTE)*. This pulsar exhibited stable rotation from 2000 March until 2006 February: the RMS phase residual for a spin-down model which includes ν, $\dot{\nu}$, and $\ddot{\nu}$ is 2.3%. We report a possible phase-coherent timing solution valid over a 10-yr span extending back to March 1996. A glitch may have occurred between 1998 and 2000, but is not required by the existing timing data. The pulse profile has been evolving since 2000. In particular, the dip of emission between its two peaks got shallower between 2002 and 2006, as if the profile were evolving back to its pre-2000 morphology, following an earlier event, which possibly also included the glitch suggested by the timing data. These profile variations are seen in the 2−4 keV band but not in 6−8 keV. We also detect a slow increase in the pulsed flux between 2002 May and 2004 December, such that it has risen

by $36\pm3\%$[1] over 2.6 years in the $2-10$ keV band. The pulsed flux variability and the narrow-band pulse profile changes present interesting challenges to aspects of the magnetar model.

[1]The increase in the pulsed flux was $36\pm3\%$ when the flux was measured in Count/s/PCU and $29\pm8\%$ when the flux was measured in erg/s/cm^2.

2.1 Introduction

The existence of magnetars – young, isolated neutron stars powered by the decay of an ultrahigh magnetic field – is now well supported by many independent lines of evidence (Woods & Thompson, 2006). This comes from the study of soft-gamma repeaters (SGRs, Section 1.2.2, Appendix B) and anomalous X-ray pulsars (AXPs, Section 1.2.3, Appendix C). AXPs and SGRs, in the magnetar model, are ultimately powered by the internally decaying magnetic field. In the magnetar model, the pulsed X-rays are suggested to be the result of a combination of surface thermal emission and a non-thermal high-energy component from resonant scattering of thermal photons off magnetospheric currents (Thompson, Lyutikov, & Kulkarni, 2002). Magnetar bursting, the hallmark of SGRs and also seen in AXPs, is believed to be a result of crustal yield and subsequent magnetospheric disturbances ultimately caused by stresses on the crust by the decaying internal field (see for example Kaspi et al. 2003).

Recently, thanks in large part to long-term monitoring campaigns, it has become clear that AXPs exhibit a variety of types of aperiodic X-ray variability that can in principle be useful for testing aspects of the magnetar model. This variability can be categorized into four types, some of which are seen contemporaneously with each other: very short-duration SGR-like bursts, sudden outbursts and transient brightenings with decays lasting months or longer, slow-rise long-term flux variations also with slow decays, and pulse profile changes.

Classic examples of SGR-like bursts and an outburst were seen in 2002 for AXP 1E 2259+586, which exhibited a sudden order-of-magnitude increase in the pulsed and total flux, followed by a one-year-long flux decay (Kaspi et al. 2003; Woods et al. 2004). The outburst was accompanied by over 80 short SGR-like bursts, a rotational glitch with interesting recovery on a time-scale of 2 weeks, short-lived spectral changes, and dramatic broad-band pulse morphology changes which included the two profile peaks swapping heights and which lasted 2–3 weeks. The event was consistent with the picture of sudden crustal yield influencing both the interior and the exterior of the AXP, in analogy with large SGR bursts.

Several observations of this same source and others suggest similar outbursts in AXPs that went undetected. *GINGA* observations of 1E 2259+586 reported by Iwasawa, Koyama, & Halpern (1992) also showed a factor-of-two pulsed flux change and pulse profile variations, both of which, in hindsight, could be explained by a contemporaneous but short-lived outburst that went unseen. In AXP 1RXS J170849−4000910,

two rotational glitches were discovered (Kaspi, Lackey, & Chakrabarty, 2000; Kaspi & Gavriil 2003; Dall'Osso et al. 2003). Dall'Osso et al. (2003) reported possible small pulse morphology changes associated with these glitches. Whether these glitches were accompanied by bursting that went unobserved is unknown but plausible. The transient AXP XTE J1810−197 underwent a dramatic sudden brightening by nearly two orders of magnitude (Ibrahim et al., 2004) followed by a total flux decay that lasted years (Halpern & Gotthelf, 2005); this may well have been an outburst similar to, though larger than that in 1E 2259+586, but for which the brief main event went observed. Similarly, the transient candidate AXP AX J1845−0258 underwent a factor > 100 decay in flux after an initial brightening that lead to its discovery (Vasisht et al., 2000; Tam et al., 2006). This too could have been the result of an unseen outburst.

AXP outbursts appear to be fundamentally different from the slow-rise, long-term flux variations seen in AXP 1E 1048.1−5937. Gavriil & Kaspi (2004) discovered two long-lived, slow-rise X-ray pulsed flux flares from this source. The first flare had peak pulsed flux a factor of ∼2 greater than the quiescent level, and lasted ∼100 days. The second, larger flare had peak a factor of > 4 higher than in quiescence, and lasted over one year. The flares were accompanied by an increase in the phase-averaged flux of the source and a decrease in pulsed fraction, although the time scale and full dynamic range of the these changes have not been clearly established (Mereghetti et al., 2004; Tiengo et al., 2005). No simultaneous pulse morphology changes were detected, and though the source did exhibit some SGR-like bursts (Gavriil, Kaspi, & Woods, 2004), they were not obviously correlated with pulsed flux. Large (factor of 10) torque changes were seen especially during the large flare, but the correlation between torque and pulsed flux, at least on time scales smaller than the flare itself, was marginal. Overall, the slow-rise flares seen in 1E 1048.1−5937 are not thought to result from crustal cracking as in outbursts. They can, however, be explained by a spontaneous increase in the magnetic field twist in the magnetosphere. However what might trigger such events is unclear. Nevertheless, Rea et al. (2005) and Campana et al. (2007) found, using observations of 1RXS J170849.0−400910 which has also shown phase-averaged flux variability, that one important prediction of the twisted magnetosphere model appears to hold, namely a correlation between spectral hardness and flux.

4U 0142+61 is an 8.7-s AXP. It has $\dot{P} = 0.2 \times 10^{-11}$, implying a surface dipole magnetic field of 1.3×10^{14} G. From continuous *RXTE* monitoring, Gavriil & Kaspi (2002) showed that 4U 0142+61 rotates with high stability. However, Morii, Kawai,

& Shibazaki (2005) reported a possible timing glitch in 1999 on the basis of an *ASCA* observation in which the value of the frequency was marginally discrepant with the frequency as reported by Gavriil & Kaspi (2002). Morii et al. also reported simultaneous pulse morphology changes. As of 2006 April, in the published flux history of this source, there had been no reports of any X-ray activity like the flares of 1E 1048−5937 and the outburst of 1E 2259+586. However, very recently, in 2006 April and June and again in 2007 February (Kaspi et al., 2006; Dib et al., 2006; Gavriil et al., 2007a) SGR-like bursts were seen from 4U 0142+61, along with a sudden pulse profile change and a timing anomaly. In this paper we refer to the history prior to April 2006.

Here we report on continued *RXTE* monitoring observations in which we find a possibly new type of AXP variability, namely a slow, long-term increase in the pulsed flux accompanied by slow pulse profile evolution. We also report on 10 years of timing and investigate the possibility of a glitch having occured in 1998 or 1999, during an observing gap, which may have precipitated the evolution we are witnessing today. Our observations are described in Section 2.2. Our timing, pulsed morphology, and pulse flux analysis are presented, respectively, in Sections 2.3.1, 2.3.2, and 2.3.3. We present a combined pulse shape and pulsed flux analysis in Section 2.3.4. In Section 2.4, we discuss the possible origins of this behaviour and the implications for the magnetar model.

2.2 Observations

The results presented here were obtained using the Proportional Counter Array (PCA) on board *RXTE* (see Section 1.4). Our 136 observations are of various lengths (see Table 2.1). Most were obtained over a period of several years as part of a long-term monitoring program, but some are isolated observations (see Fig. 2.1).

Note that there is a 2-year gap in the observations on which we are reporting: no *RXTE* observations were made from 03/21/1998 (MJD 50893.083) to 03/07/2000 (MJD 51610.617). The gap exists because 4U 0142+61 was only added to our regular AXP monitoring program at the start of *RXTE* Cycle 5. Prior to the gap, our observations consist of a) 4 very closely spaced *RXTE* Cycle 1 observations, b) 14 short Cycle 2 observations spanning a period of a year, and c) a single Cycle 3 observation. No observations were made in Cycle 4 (see Table 2.1, Fig. 2.1).

For the monitoring, we used the `GoodXenonwithPropane` data mode except during Cycle 10 when we used the `GoodXenon` mode. Both data modes record photon arrival

Table 2.1. Summary of *RXTE* Observations

Observing Cycle	Typical Exposure[a] (ks)	Typical Separation[a] (weeks)	Number of Obs.[b]	Total Exposure[c] (ks)	First MJD − Last MJD[d]	First Date − Last Date
1	11	0.1	4	45	50170.469−50171.904	29/03/1996−29/03/1996
2	1	4	14	16	50411.684−50795.523	24/11/1996−13/12/1997
3	20	...	1	20	50893.083−50893.083	21/03/1998−21/03/1998
4	...	...	0	0	...	...
5	3	4	15	46	51610.617−51950.256	07/03/2000−10/02/2001
6	7	6	10	54	51986.347−52282.163	18/03/2001−08/01/2002
7	15	6	9	100	52339.621−52634.456	06/03/2002−26/12/2002
8	5	2	21	124	52726.197−53046.235	28/03/2003−11/02/2004
9	5	2	27	86	53066.586−53420.507	02/03/2004−19/02/2005
10	5	2	36	120	53438.151−53787.328	09/03/2005−21/02/2006

[a] The exposure and separation are only approximate.

[b] When the last digit of the observation ID of two successive data sets is different, the two data sets are considered separate observations.

[c] The total exposure does not include Earth occultation periods.

[d] First MJD and Last MJD are the epochs, in Modified Julian Days, of the first and the last observations in a Cycle.

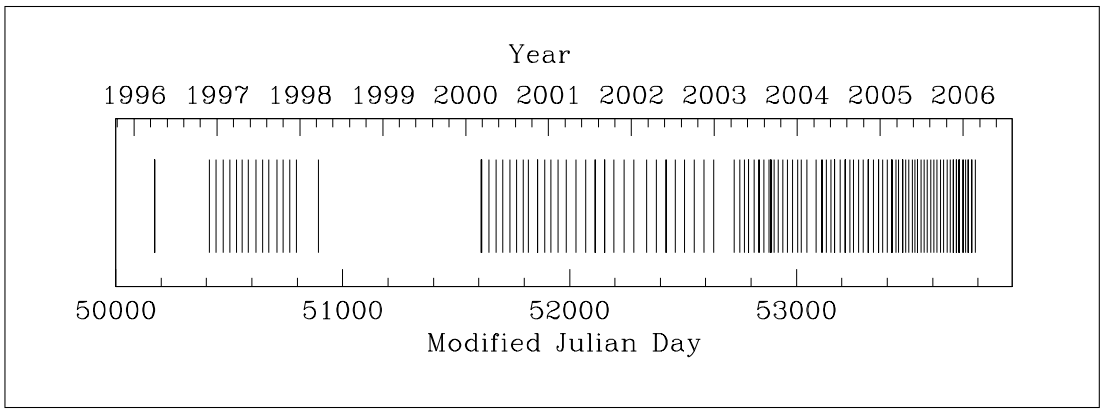

Figure 2.1 Epochs of observations of 4U 0142+61 with *RXTE*.

times with 1-μs resolution and bin energies into one of 256 channels. To maximize the signal-to-noise ratio, we analysed only those events from the top xenon layer of each PCU.

2.3 Analysis and Results

2.3.1 Phase-coherent Timing

Photon arrival times at each epoch were adjusted to the solar system barycenter using the position obtained by Patel et al. (2003) from *Chandra* data. They were then binned with 31.25-ms time resolution. In the timing analysis presented below, we included only the events in the energy range 2−10 keV (unless otherwise specified) to maximize the signal-to-noise ratio of the pulse.

Each barycentric binned time series was epoch-folded using an ephemeris determined iteratively by maintaining phase coherence; see below. Resulting pulse profiles, with 64 phase bins, were cross-correlated in the Fourier domain with a high signal-to-noise template created by adding phase-aligned profiles from all observations. The cross-correlation returned an average pulse time of arrival (TOA) for each observation corresponding to a fixed pulse phase. The pulse phase ϕ at any time t can be expressed as a Taylor expansion,

$$\begin{aligned} \phi(t) &= \phi_0(t_0) + \nu_0(t-t_0) + \frac{1}{2}\dot{\nu_0}(t-t_0)^2 \\ &\quad + \frac{1}{6}\ddot{\nu_0}(t-t_0)^3 + \ldots, \end{aligned} \tag{2.1}$$

where $\nu \equiv 1/P$ is the pulse frequency, $\dot{\nu} \equiv d\nu/dt$, etc., and subscript "0" denotes a parameter evaluated at the reference epoch $t = t_0$. The TOAs were fitted to the above polynomial using the pulsar timing software package TEMPO[2] (also see Section 1.1.9).

We report an unambiguous phase-coherent timing solution that spans the post-gap (i.e. after March 2000, MJD 51610) 6-yr period up until February 2006 (MJD 53787) including all data in *RXTE* Cycles 5−10. The parameters of our best-fit spin-down model which includes ν, $\dot{\nu}$, and $\ddot{\nu}$ are presented in Table 2.2. The corresponding phase residuals are shown in Figure 2.2. Note the unmodelled features in the residuals; these may be caused by a noise process similar to that commonly seen in radio pulsar timing (e.g. Livingstone et al. 2005).

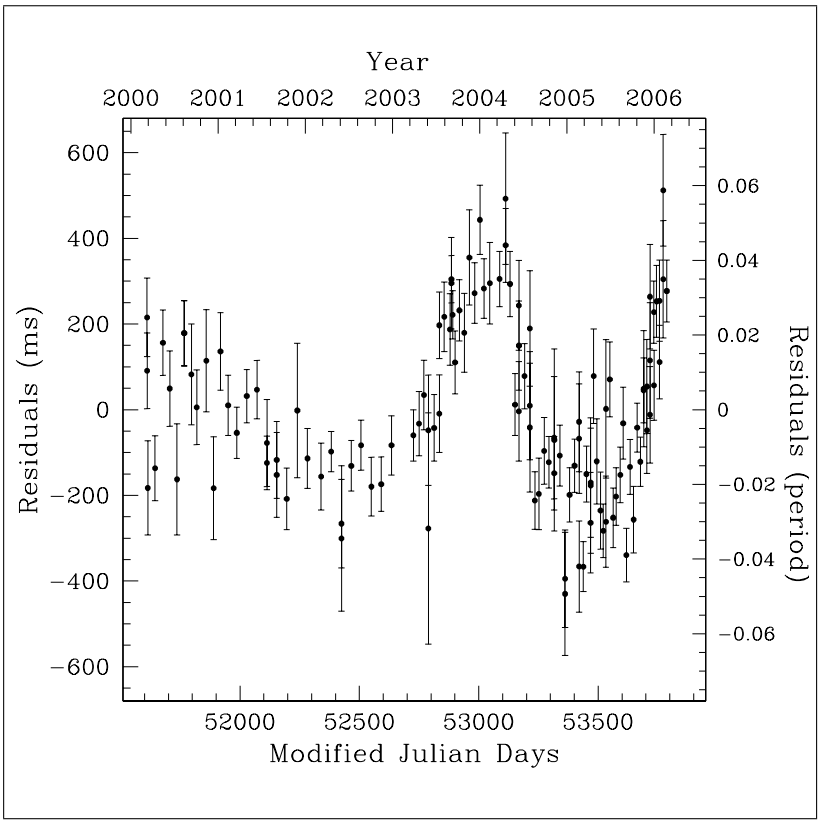

Figure 2.2 Arrival time residuals for 4U 0142+61 for the post-gap period, using the post-gap ephemeris given in Table 2.2. The residuals have RMS 2.3% of the pulse period.

The best-fit post-gap ephemeris does not, however, fit the pre-gap TOAs well. Figure 2.3 shows a clear systematic deviation in the pre-gap residuals obtained after subtracting the post-gap ephemeris. The best-fit frequency obtained from the post-

[2]See http://www.atnf.csiro.au/research/pulsar/tempo.

Table 2.2. Spin Parameters for 4U 0142+61[a]

Parameter	Pre-Gap Ephemeris[b] Spanning Cycles 1 to 3	Post-Gap Ephemeris Spanning Cycles 5 to 10	Possible Ephemeris[c] Spanning All Cycles
MJD range	50170.693−50893.288	51610.636−53787.372	50170.693−53787.372
TOAs	19	118	137
ν (Hz)	0.115099566(3)	0.1150969337(3)	0.1150969304(2)
$\dot{\nu}$ (10^{-14} Hz s^{-1})	−2.659(3)	−2.6935(9)	−2.6514(7)
$\ddot{\nu}$ (10^{-23} Hz s^{-2})	—	0.417(10)	−1.7(2)
$d^3\nu/dt^3$ (10^{-31} Hz s^{-3})	—	—	3.62(12)
$d^4\nu/dt^4$ (10^{-39} Hz s^{-4})	—	—	8.7(3)
$d^5\nu/dt^5$ (10^{-46} Hz s^{-5})	—	—	−5.01(13)
$d^6\nu/dt^6$ (10^{-54} Hz s^{-6})	—	—	6.6(4)
Epoch (MJD)	50530.000000	51704.000025	51704.000000
RMS residual	0.019	0.023	0.019

[a] Numbers in parentheses are TEMPO-reported 1σ uncertainties.

[b] The pre-gap ephemeris reported here is slightly different from that reported in Gavriil & Kaspi (2002) because here we take into account Cycle 1 and 3 observations. Note that both ephemerides return the same number of pulsar rotation cycles between the first and last pre-gap observations used by Gavriil & Kaspi (2002).

[c] It is possible to find a different overall ephemeris after adding an arbitrary but constant time jump to all post-gap TOAs.

gap model at the reference epoch is larger than the frequency obtained from the best-fit model of the pre-gap TOAs at the same epoch (see Table 2.2). This, in principle, could indicate that a glitch occured at some time during the gap. At MJD 51250, midway between the pre-gap and the post-gap ephemerides, the fractional change in frequency due to the possible glitch is $\Delta\nu/\nu = (7.11\pm0.15)\times10^{-7}$. However, by using six frequency derivatives, we found a possible ephemeris that fits the entire Cycle 1 to 10 range (MJDs 50170 to 53787, see Table 2.2). The RMS phase residual for that ephemeris is 0.019 (see Fig. 2.4). Note that when finding an ephemeris that spans several years, it is not uncommon to require a large number of frequency derivatives in order to reduce the RMS phase residuals to a number on the order of 5%. This is typical especially in young pulsars and is generally attributed to timing noise (e.g. Livingstone et al. 2005).

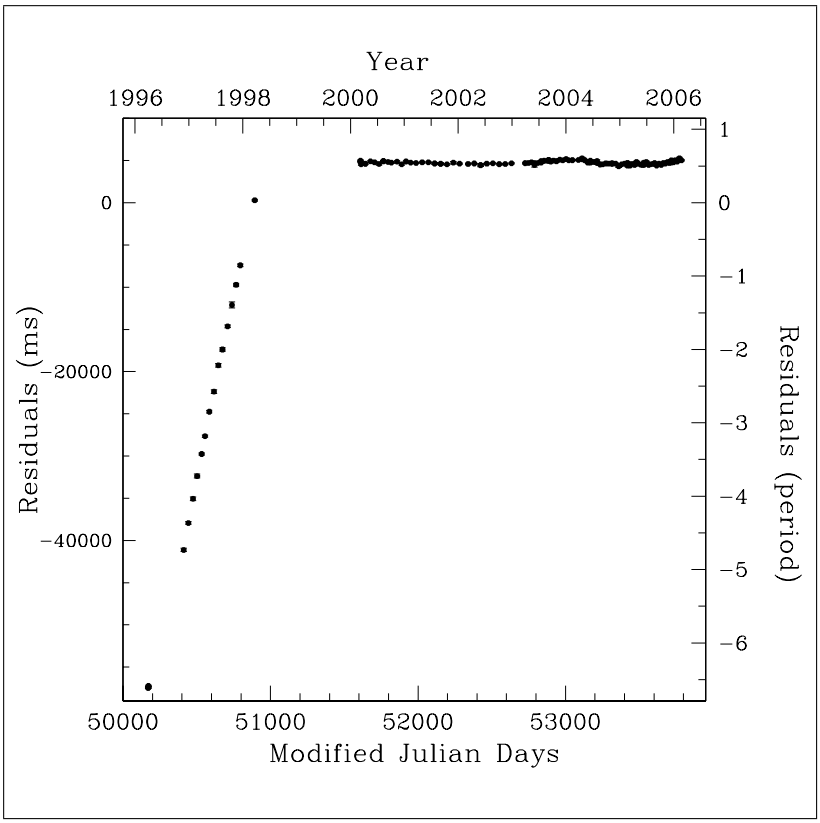

Figure 2.3 Arrival time residuals for 4U 0142+61 for all *RXTE* Cycles using the post-gap ephemeris.

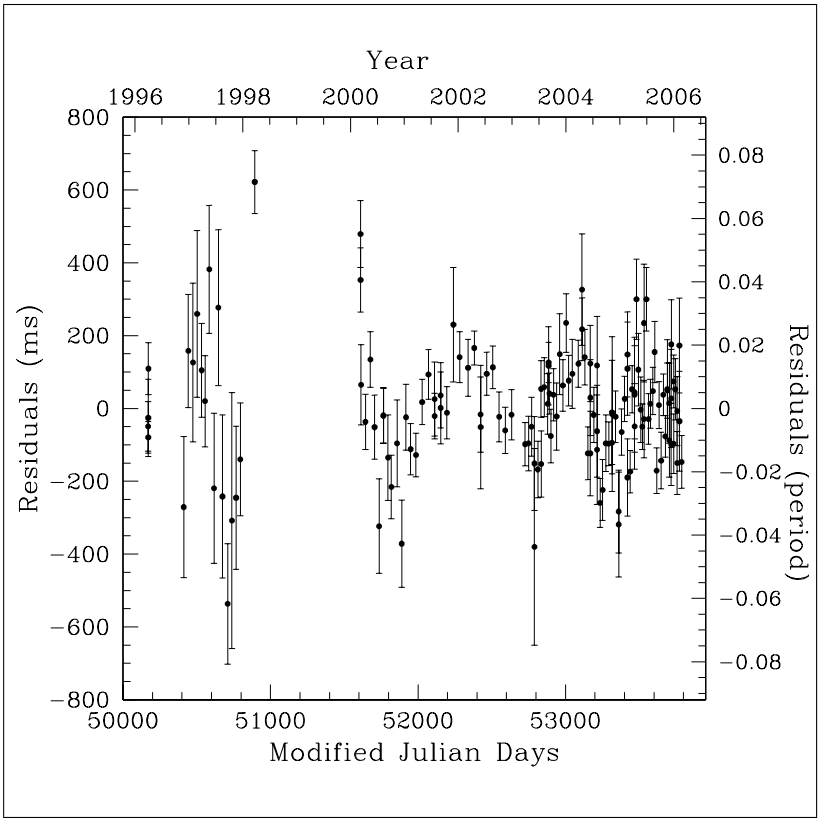

Figure 2.4 Arrival time residuals for 4U 0142+61 for all *RXTE* Cycles using the overall ephemeris (see Table 2.2). The residuals have RMS 1.9% of the pulse period.

The possibility of a glitch in 4U 0142+61 during our gap was in fact examined by Morii et al. (2005). The authors showed that the frequency obtained from a 1998 August *ASCA* observation of 4U 0142+61 (MJD 51046.699; 154 days after the start of our gap), differs from the frequency predicted at the epoch of the observation by the ephemerides previously reported for 4U 0142+61 in Gavriil & Kaspi (2002). Morii et al., reported a frequency $f = 0.1150972(6)$ Hz at MJD 51046.69875 for the *ASCA* observation. Our overall ephemeris (see Table 2.2) predicts $f = 0.115098404(3)$ Hz at the same epoch. Their measurement is within 2σ of our prediction, indicating a $\sim$5% possibility that the two values are the same. Therefore, their measured f can be explained by a gradual change of the spin-down rate without invoking a glitch.

However, the existence of our overall ephemeris cannot rule out the possibility of the glitch: in some rotational glitches, the frequency evolution, given some relaxation time after the glitch epoch, returns to what it was prior to the glitch (see for example the glitch reported in Kaspi & Gavriil 2003). If a glitch of this kind had happened inside the two-year gap, and if the length of the gap was much greater than the relaxation

time, the only long-term effect of the glitch that could still be observable with a timing analysis would be a random phase jump in the post-relaxation TOAs relative to the pre-glitch TOAs. To investigate this possibility, we added an arbitrary but constant time jump to all the post-gap TOAs. We were still able to find a new ephemeris that connected the TOAs through the two-year gap. This indicates that our overall ephemeris is not unique. Hence, we cannot rule out the possibility of a random phase jump between Cycles 3 and 5, and therefore, a glitch cannot be ruled out.

It is important to note that our method for obtaining TOAs, (cross-correlating the folded profiles of given observations with a high signal-to-noise template obtained from all the observations combined), assumes a constant pulse profile. In the next Section, we show that the pulse profile is actually varying during our monitoring program. However, we performed simulations which showed that these changes do not result in timing offsets significantly larger than the reported TOA uncertainties. Hence the profile variations do not affect the above analysis.

2.3.2 Pulse Profile Changes

Qualitative Observations

We performed a pulse profile analysis using FTOOLS version 5.3.1[3]. We used the following steps: for each observation, we ran the FTOOL `make_se` to combine the `GoodXenon` files. We then used the FTOOL `fasebin` to make a phase-resolved spectrum of the entire observation with 64 phase bins across the profile. When we ran `fasebin`, we selected layer 1 of the detector, disregarded the propane photons, and included the photons from PCUS 1, 2, 3, and 4. We disregarded photons from PCU 0 because of the loss of its propane layer in 2000 (Jahoda et al., 2006) and because it gave different results from the other PCUs. `fasebin` also took care of barycentering the data. For each observation, we then used `seextrct` to make a phase-averaged spectrum for the same set of detector layers and PCUs. The phase-averaged spectrum was then used by the perl script `pcarsp` to make a response matrix.

We loaded the phase-resolved spectra and the response matrices into the X-ray Spectral Fitting Package (XSPEC[4]) and selected photons belonging to three energy bands: 2−10, 2−4, and 6−8 keV. Using XSPEC, we extracted an ASCII count rate pulse profile for each of the energy bands. The profiles included XSPEC-obtained 1σ

[3]http://heasarc.gsfc.nasa.gov/ftools
[4]http://xspec.gsfc.nasa.gov Version: 11.3.1

error bars on each of the phase bins in the profiles. To obtain a pulse profile in units of count rate per PCU, we divided the overall profile by a PCU coverage factor that took into account the amount of time each PCU was on.

We then aligned the 64-bin profiles with a high signal-to-noise template using a similar cross-correlation procedure to the one described in the timing analysis. Then, for each *RXTE* Cycle, we summed the aligned profiles, extracted the DC component from the summed profile, and scaled the resulting profile so that the value of the highest bin is unity and the lowest point is zero.

The average profiles in all three bands are presented in Figure 2.5 for comparison. In a given band, the different profile qualities are due to different net exposure times.

It is important to note that the two narrow energy bands that we are using contain photons belonging to different spectral components: from the spectrum of 4U 0142+61 (see, for example, White et al. 1996), under the assumption that the spectrum is well described by a blackbody plus power-law tail, we know that the higher energy band (6−8 keV) contains negligible blackbody emission, while the lower energy band (2−4 keV) contains comparable amounts of blackbody and power-law emission.

Qualitatively, the evolution of the pulse profiles in the first two bands of Figure 2.5 is clear to the eye. In Cycles 1 and 2, the smaller peak, obvious in later Cycles, is not very well defined. After the two-year gap, in Cycle 5, the 'dip' between the peaks is much more pronounced. The emission in the dip starts to most noticeably rise in Cycles subsequent to Cycle 7. In the 6−8 keV band, the smaller peak appears to have lower amplitude in the normalized profiles than in 2−4 keV, indicating that it has a softer spectrum relative to the larger peak.

Another qualitative observation is that the ratio of the heights of the two peaks in the 2−10 keV and 2−4 keV bands appears to be closest to unity in the first Cycle after the gap. The ratio starts to decrease in the Cycles subsequent to Cycle 5. Note that from this Figure alone we can compare the sizes of the two peaks, but we cannot track the evolution of the heights of each peak separately. In order to do that, we need to scale the pulse profile of each Cycle by the average pulsed flux. This analysis is presented in Section 2.3.4.

Fourier Analysis

To quantify the changes in the pulse profile, we computed the first six Fourier amplitudes of the average profiles of each Cycle in each energy band. Harmonic numbers larger than 6 were always consistent with zero. The results are shown in Figures 2.6,

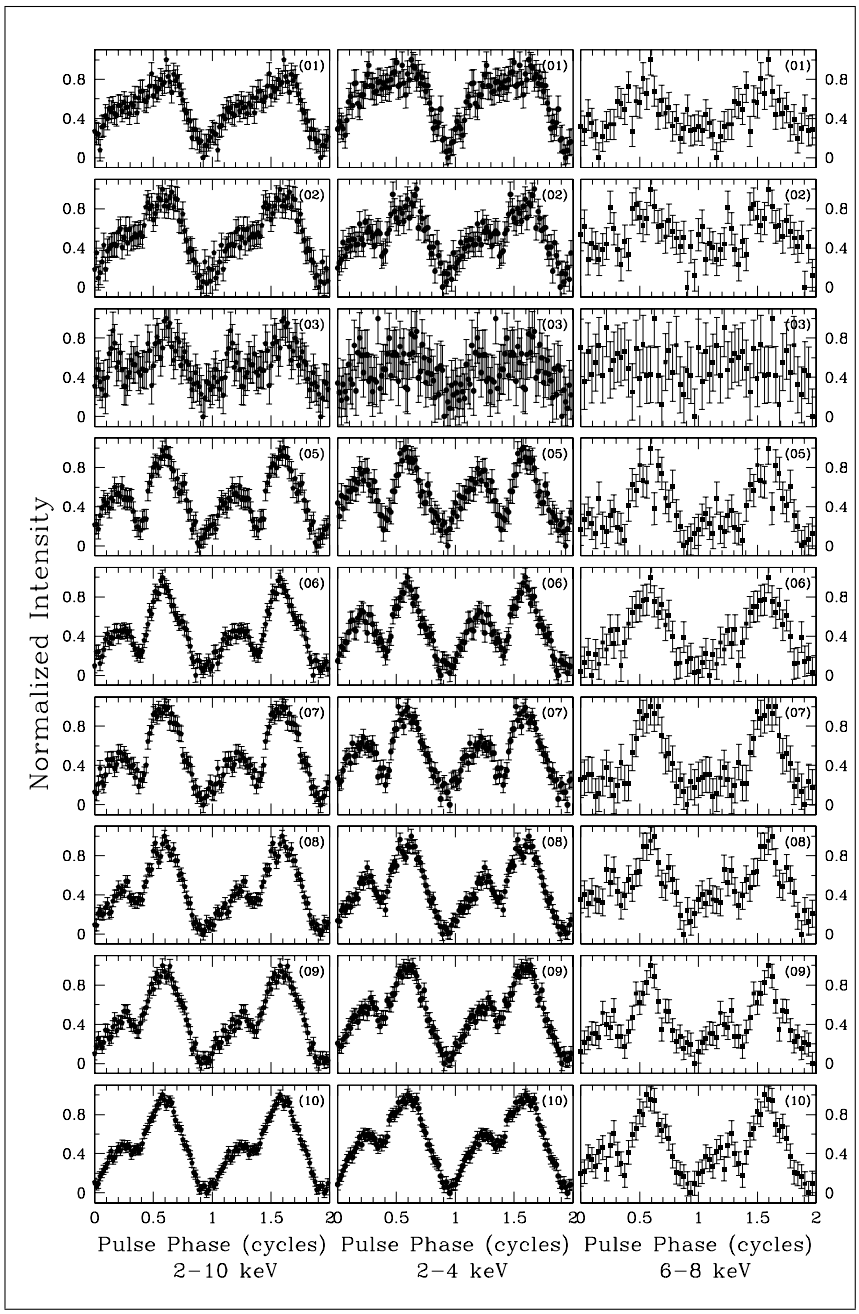

Figure 2.5 Pulse profiles in all *RXTE* Cycles in three different PCA energy bands (2−10 keV with 64 bins across the profile, 2−4 keV with 64 bins across the profile, and 6−8 keV with 32 bins across the profile for clarity). Note that no observations were made in Cycle 4. Two full periods are shown. The normalization is such that the values of the lowest and highest bins in each profile are 0 and 1, respectively. The Cycle number is shown in the top right corner of each pulse profile plot.

2.7, and 2.8. In each of the three Figures, the plots on the right show the power in each harmonic divided by the total power in all harmonics (not including the DC

term). In the plots on the left, the observed pulse profiles are in the background (hollow squares without error bars). The superimposed smooth curve in the foreground is made from the first six calculated Fourier components. The ratios of the first three Fourier harmonics relative to the fundamental are presented in Figure 2.9. Note that the ratios of the Fourier harmonics are not presented for Cycle 3 in Figures 2.6, 2.7, and 2.8 due to the very low signal-to-noise ratio.

Significant variations were seen in the pulse profile of 4U 0142+61 in the 2−10 keV band and in 2−4 keV; on the left side of both Figures 2.6 and 2.7, the most striking variable feature is the difference in the relative heights between the top of either peak and the bottom of the dip. On the right side, considering the first two Fourier components, the ratio of the second to first amplitudes (A_2/A_1) is significantly bigger than unity only in Cycle 5. It then falls steadily until, in Cycle 10, it reaches the same ratio as in Cycle 1. The evolution of the A_2/A_1 ratio in 2−4 keV is shown in Figure 2.9. In the pre-gap Cycles, harmonics of order higher than 2 are only marginally significant. In the post-gap Cycles, harmonics 3 and 4 are most significant in Cycles 5 and 6, coinciding with the Cycles where the dip in the time-domain curve is sharpest. The evolution of the A_3/A_1 and the A_4/A_1 ratios is also shown in Figure 2.9. Note the obvious rise in the harmonic ratios just post-gap in the soft-band, with apparent subsequent evolution to pre-gap values.

In the 6−8 keV band (see Fig. 2.8), statements about the behaviour of the Fourier components are harder to make because of the poor signal-to-noise ratio; nevertheless some trends are clear. Unlike in the lower energy band, the A_2/A_1 ratio does not appear to systematically increase or decrease. Also unlike in the lower band, harmonics 3 and 4 do not appear to vary systematically (see Fig. 2.9). Thus, in the band where all the emission is from the power-law component of the spectrum, the variations in the shape of the pulse profile, if any, are much less significant than the variation in the 2−4 keV band which contains photons belonging to both components of the spectrum.

2.3.3 Pulsed Flux Time Series

To obtain a pulsed flux time series for 4U 0142+61, we did the following. First, for each PCU in each observation, we used a procedure similar to that described in Section 2.3.2 to make a phase resolved spectrum (with 16 phase bins across the profile) and a response matrix. We then used the FTOOL `fmodtab` to correct the exposure value in the phase resolved spectrum of each PCU in order to take into account the

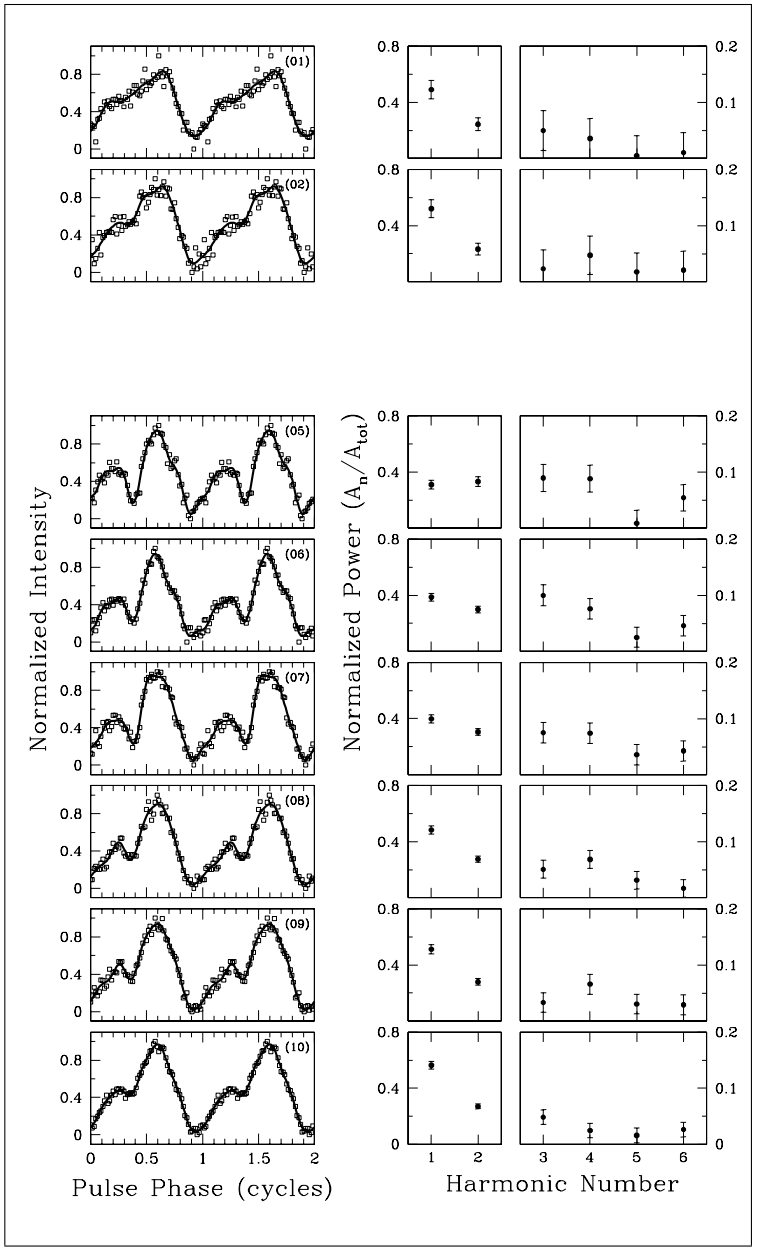

Figure 2.6 Fourier analysis of the pulse profiles in the 2−10 keV energy band. *Left:* Pulse profile curves made of the first six calculated Fourier components in each *RXTE* Cycle, superposed on the measured pulse profile points for that Cycle. *Right:* Harmonic content of the average pulse profiles for each Cycle. Note that Cycle 3 was not included because of the poor signal-to-noise ratio.

amount of time that each PCU was on. Then, for each observation, we added the spectra obtained from PCUs 1 to 4 using the FTOOL `fbadd` and added the responses using the FTOOL `addrmf`. We used `fbadd` and `addrmf` again to add the spectra and responses of all observations in a given *RXTE* Cycle. For each *RXTE* Cycle, we

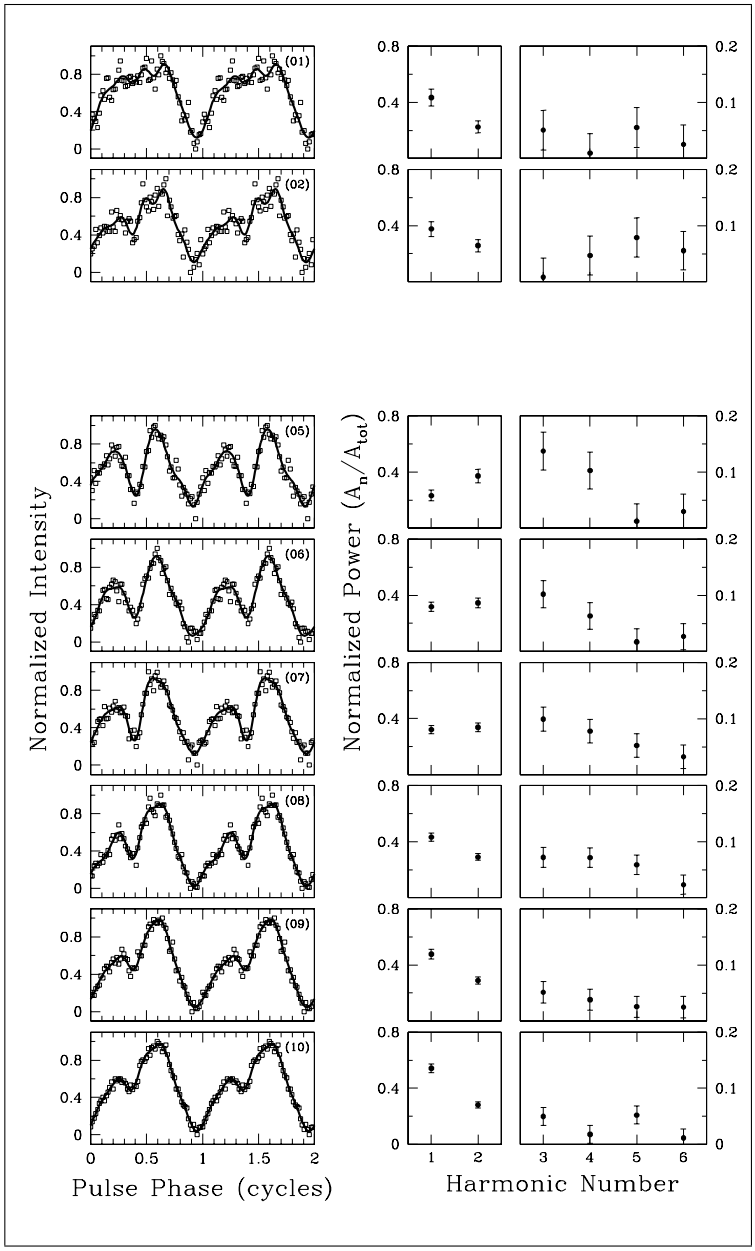

Figure 2.7 Same as Figure 2.6 but for 2−4 keV.

loaded the phase resolved spectra into XSPEC, and selected photons in the 2−10 keV range. Using XSPEC, we extracted an ASCII count rate pulse profile for each *RXTE* Cycle. The profiles included XSPEC-determined 1σ error bars on each of the phase bins. We then smoothed each of the profiles by eliminating the Fourier components corresponding to harmonic numbers larger than five. The pulsed flux for each of the

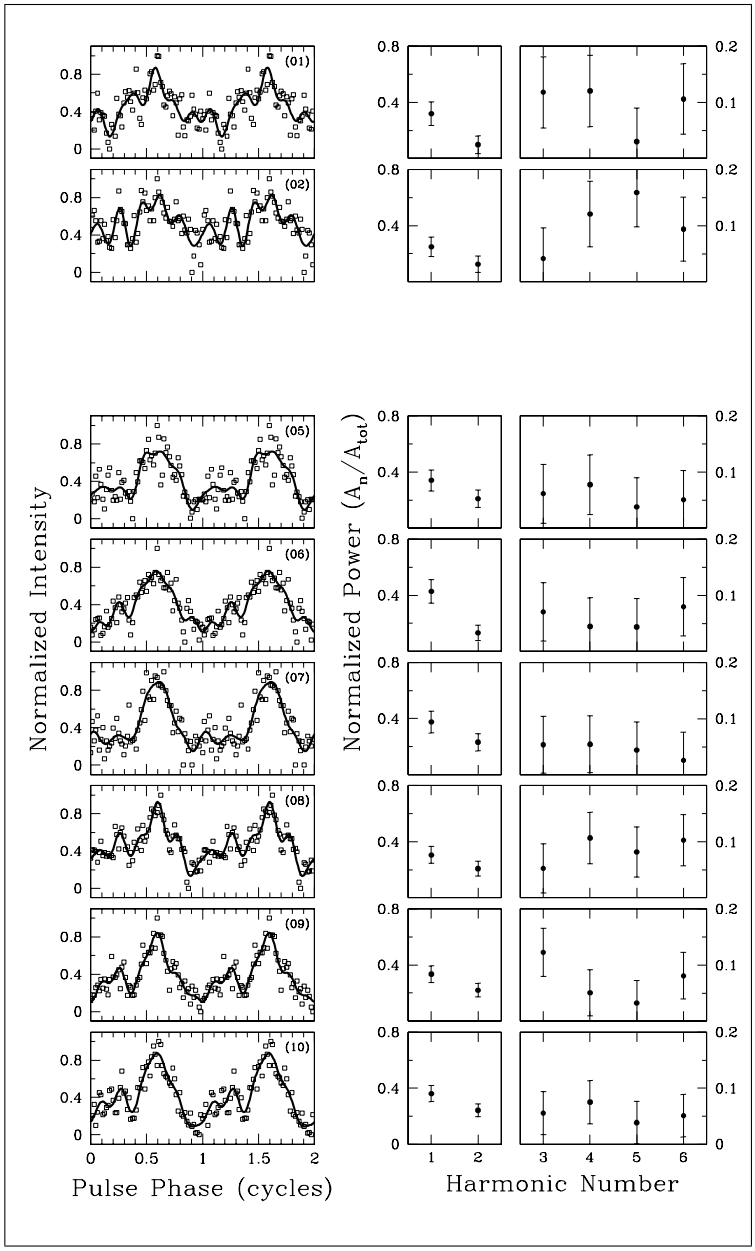

Figure 2.8 Same as Figure 2.6 but for 6−8 keV.

smoothed profiles was calculated using the following discrete area formula:

$$F = \frac{1}{N}\sum_{i=1}^{N}(p_i - p_{min}). \tag{2.2}$$

where i refers to the phase bin, N=16 is the total number of phase bins, p_i is the count rate in the $i^{\rm th}$ phase bin of the smoothed pulse profile, and p_{min} is the value of the minimum of the continuous smooth function that is made from the first five

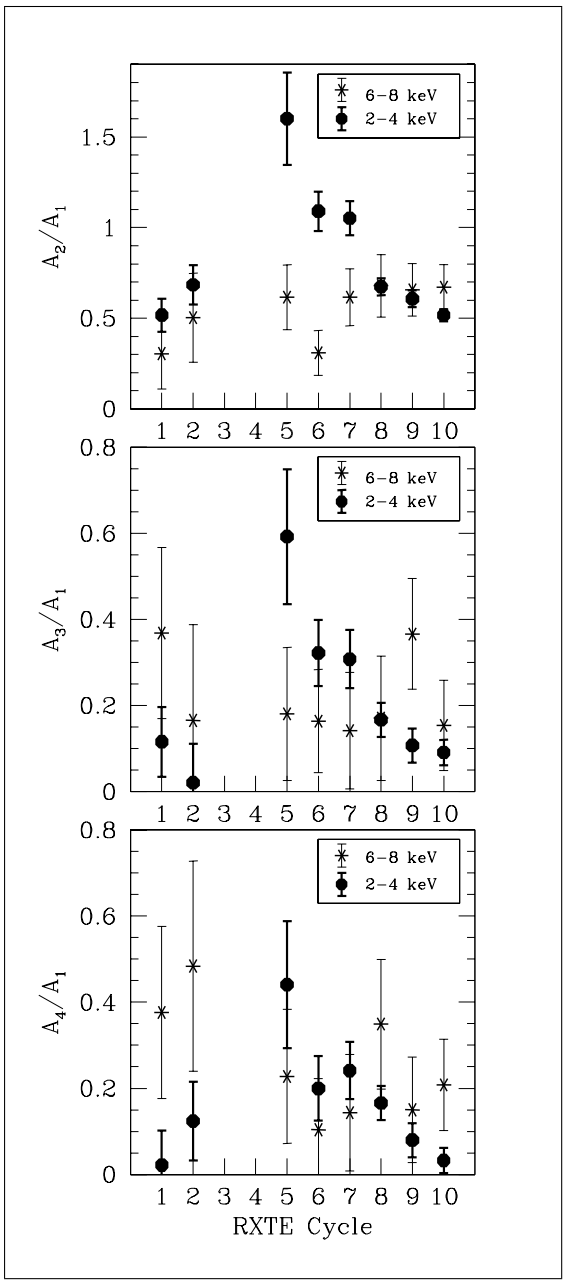

Figure 2.9 Ratios of the Fourier amplitudes of the pulse profiles in two energy bands. *Top:* ratio of the Fourier amplitude of the second harmonic to that of the fundamental. *Middle:* ratio of the Fourier amplitude of the third harmonic to that of the fundamental. *Bottom:* ratio of the Fourier amplitude of the fourth harmonic to that of the fundamental.

Fourier components of the original profile.

The resulting pulsed flux history in counts/s/PCU is shown in the top panel of Figure 2.10. Each point represents one *RXTE* Cycle. The pulsed flux has increased by 36±3% between Cycles 7 and 9. A quick rebinning of the observations shows

that the increase period lasted $\sim$ 2.6 yr (between MJDs 52400 and 53350). We verified that the same trend is detected in PCUs 1−4 individually, and that there are no comparable trends in the long-term light curves of the other 4 AXPs observed as part of this monitoring program.

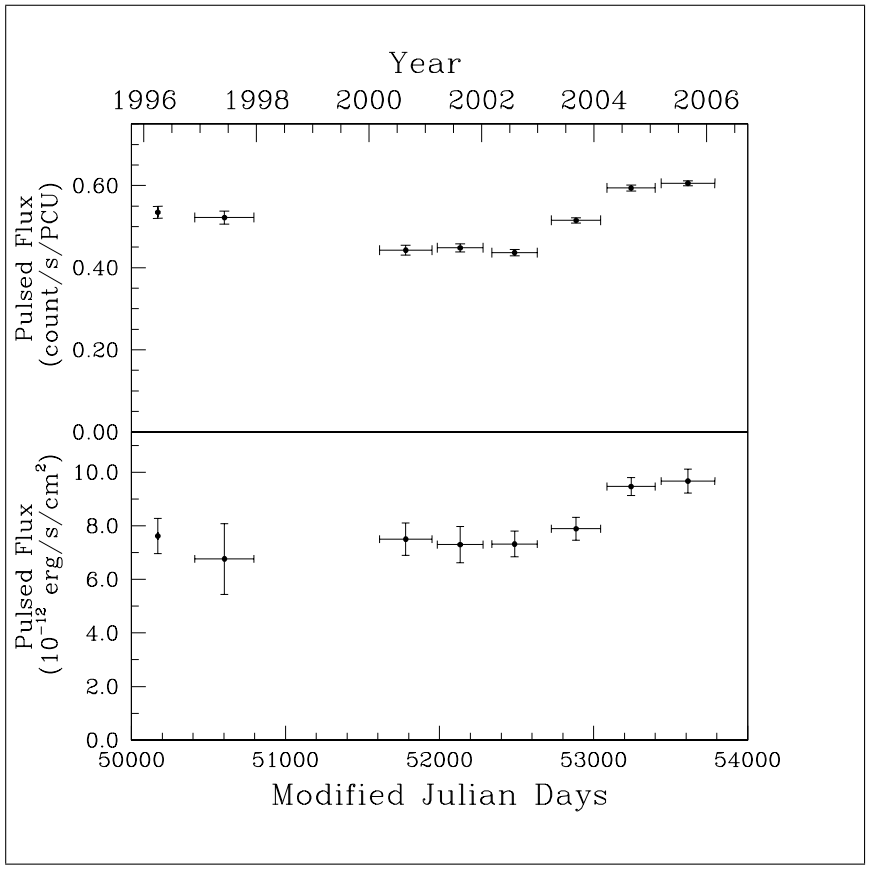

Figure 2.10 *Top:* Pulsed flux evolution of 4U 0142+61 in counts/s/PCU in the 2−10 keV band. Each point corresponds to a full *RXTE* Cycle. *Bottom:* Pulsed flux evolution in erg/s/cm^2 in the 2−10 keV band. See text for details.

We repeated the above procedure of finding the flux for narrower energy bands. There are hints that the long-term increase is present in the 2−4 keV band and not in 6−8 keV but our statistics do not let us confirm this. If the pulsed flux increase is restricted to $<$ 6 keV, this could indicate that the spectrum of the pulsed emission is getting softer. Motivated by this possibility, we performed a detailed spectral analysis of four available archival *XMM* observations. We found that the spectrum is indeed getting softer (Gonzalez et al., 2007).

Note that the method that we used to calculate the pulsed flux, which consisted of calculating the pulsed area under the profile, is more sensitive to noise than are

measurements of the RMS pulsed flux like those used in Woods et al. (2004). Therefore, to reduce the effects of noise, it was necessary to combine the data from entire Cycles in order to obtain each of the pulsed area points reported in the top panel of Figure 2.10, hence the large horizontal error bars. We report measurements of the pulsed area instead of RMS pulsed flux because, while it is true that measurements of the latter are less sensitive to noise, changes in it can be caused by changes in the real pulsed area and *also* by variations in the pulse profile. As a double check, we calculated the RMS pulsed flux for each observation, found the average of the resulting fluxes in each *RXTE* Cycle, and multiplied each average by a conversion factor dependent on the pulse shape, in order to obtain a pulsed area. When we plotted these pulsed areas versus time, we obtained a similar trend to that see in the top panel of Figure 2.10. For further discussion of the various methods used to estimate the pulsed flux see Archibald et al. (2009).

In order to verify that the trend seen in the top panel of Figure 2.10 is not an artifact of the response of the detector, and in order to verify that the relative levels in the pre-gap and the post-gap flux values are not skewed due to an evolution of the response of the detector, we calculated the pulsed flux in erg/s/cm^2 using an additional method that took the evolution of the response into account. For each *RXTE* Cycle, we obtained one phase resolved spectrum (with 16 phase bins across the profile) and one response matrix using the method described above. This time we included PCU 0. Then, we defined the background phase bin to be that where p_{min} lies. We then used the FTOOL `cmppha` to combine the spectra of all phase bins into a single phase-averaged spectrum. Then, using XSPEC, we subtracted the spectrum of the background bin from the combined spectrum of the remaining phase bins, scaling the exposure appropriately. When subtracting the spectrum of the background bin from the spectrum of the remaining bins, we assumed that the resulting spectrum is, to a good approximation, that of the pulsed component of the emission. For each *RXTE* Cycle, we fit the spectrum of the pulsed emission with a model that consisted of a blackbody plus a power law. When doing the fitting we froze the temperature of the blackbody to the value $kT = 0.44$ keV, the power-law photon index to $\gamma = 3.94$ and the column density of neutral hydrogen to $N_h = 0.99 \times 10^{22}$ cm^{-2} . These parameters were obtained from a linked spectral fit of the four archival XMM observations (see Gonzalez et al. 2007). We let the normalizations of the two components of the spectrum vary freely. After the fit was done, we extracted the pulsed flux numbers from the fitted spectrum of the pulsed emission of each *RXTE* Cycle. We multiplied the 1σ error bars

returned by XSPEC by the square root of the reduced chi squared of the spectral fit. This multiplication is equivalent to assuming that the model being fit is the right one to use and that any bad-fit results from an initial underestimation of the error bars of the spectrum that is being fitted. The resulting pulsed flux values in erg/s/cm^2 for each of the *RXTE* Cycles are presented in the bottom panel of Figure 2.10. The trend observed in the pulsed flux is similar to that in the top panel. The observed increase between Cycles 7 and 9 is $\underline{29\pm8\%}$, consistent with that found in the first analysis. However, after having taken the response of the detector into account, the pulsed flux in the pre-gap observations appears to be consistent with the pulsed flux in the first post-gap Cycle.

From the bottom panel of Figure 2.10, the increase in the pulsed flux is $\sim 2.1\times10^{-13}$ erg s^{-1} cm^{-2} in the 2−10 keV band. Assuming a distance of 2.5 kpc (Hulleman, van Kerkwijk, & Kulkarni, 2004), the total luminosity increase in the $\sim$ 2.6-yr period during which the increase happened is $\sim 1.1\times10^{33}$ erg s^{-1}. This increase is of the same order of magnitude as the average energy release rate in the first 1E 1048−5937 flare (Gavriil & Kaspi, 2004). It is also an order of magnitude smaller than the average energy release rate in the first day following the outburst in 1E 2259+586 (Woods et al., 2004). The amount of energy released in the same 2.6-year period due to the increase in the pulsed flux is $\sim 9\times10^{40}$ erg in the 2−10 keV band. This is comparable to the energy released in the second 1E 1048−5937 flare (Gavriil & Kaspi, 2004), and to the energy released in the in the year following the outburst in 1E 2259+586 (Woods et al., 2004).

2.3.4 Combined Pulse Morphology and Pulsed Flux Analysis

In Section 2.3.2, we calculated the Fourier components of the average pulse profiles. This gave us the relative amplitude of the pulse profile harmonics in each *RXTE* Cycle. In Section 2.3.3, we calculated the pulsed flux for every observation. Here, we compute a weighted average of the pulsed flux for each Cycle using the flux points calculated in Section 2.3.3. We then reconstruct the profiles for each of the Cycles from the first six Fourier components (not including the DC), scale them by the average RMS pulsed flux for that Cycle, and add the necessary offset for the lowest point on each curve to be zero. This means that the resulting scaled profiles return the correct pulsed flux. The advantage of this analysis is that we can now trace the evolution of each of the peaks independently. The post-gap scaled profiles in 2−10 keV and in 2−4 keV are

presented in the top panels of Figures 2.11 and 2.12, respectively. We did not include a similar Figure for 6−8 keV because of the poor signal-to-noise ratio in that band. The absolute heights of the peaks in the post-gap Cycles, as well as the absolute height of the dip in between, are plotted in the bottom panels of Figures 2.11 and 2.12. The error bars take into account both the errors on the Fourier components and the errors on the pulsed flux.

In both Figures, there is a hint of increase in the height of the big peak between Cycles 7 and 9. The dip between the peaks appears to be getting shallower more rapidly between Cycles 7 and 9. The difference in the height of the dip over these 3 years is more significant than the difference in the height of either peaks. This indicates that the biggest contribution to the change in the pulsed flux comes from an increase in the emission in the dip, which, in principle, could be caused by the widening of either peak around the dip.

2.4 Discussion

2.4.1 Possible Event in the Gap?

Could a short-time scale energetic event (such as an outburst like that seen in 2002 for 1E 2259+586) have occured sometime within the two-year gap and triggered the pulsed flux and pulse profile changes that we are observing? As discussed above, the possibility of a glitch during the gap was examined by Morii et al. (2005). Here, an examination of our timing, flux, and pulse profile analyses can provide further clues to help answer this question.

From our timing analysis (Section 2.3.1), there is some evidence for a glitch having occured sometime during our gap. Hence, if an outburst did occur, it might have been accompanied by a glitch, as was the case for the 2002 outburst of 1E 2259+586 (Kaspi et al., 2003). If there was a glitch in 4U 0142+61, the unrecovered fractional change in frequency would have been $(7.11\pm0.15)\times10^{-7}$, a factor of 6 smaller than the maximum fractional frequency change of $(4.24\pm0.11)\times10^{-6}$ observed in 1E 2259+586. The fact that the pulsed flux in the first post-gap observations is consistent with that in the last pre-gap observations could be consistent with an outburst in between if any initial flux increase during an outburst had time to die down (see Fig. 2.10). If we assume that the return of the pulse profile to its pre-gap shape is a recovery following an outburst, this would imply a much longer time scale for the pulse profile relaxation phase than for

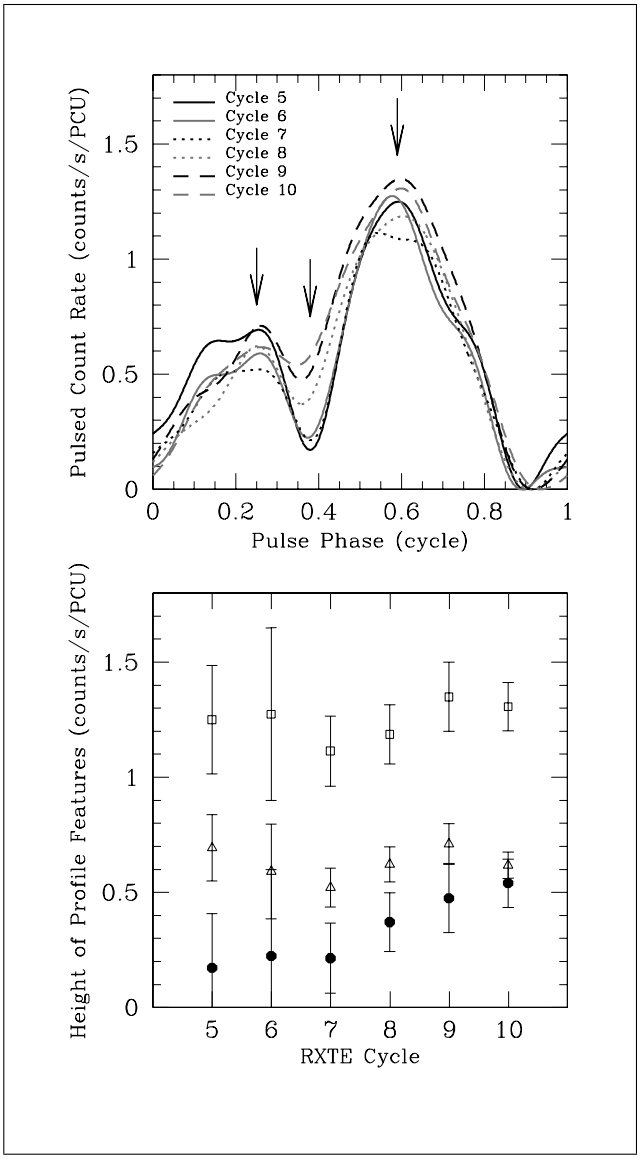

Figure 2.11 *Top:* Superposed post-gap average pulse profiles in 2−10 keV (with six Fourier components included), scaled to give the appropriate average pulsed flux for each *RXTE* Cycle. *Bottom:* The evolution of the heights of three different features in the pulse profiles as a function of *RXTE* Cycle. The open triangles represent the maximum heights of the small peak in each Cycle. The open squares represent the maximum heights of the big peak. The filled circles represent the heights of the dip.

the pulsed flux relaxation, the opposite to what was seen following the 1E 2259+586 outburst (Woods et al., 2004). Alternatively, the post-outburst pulse profile relaxation could have been completed during the gap, and the slow return of the post-gap profile to its pre-gap morphology could be attributed to a different phenomenon. This is further discussed in Section 2.4.3. In either case, if there was an event during the

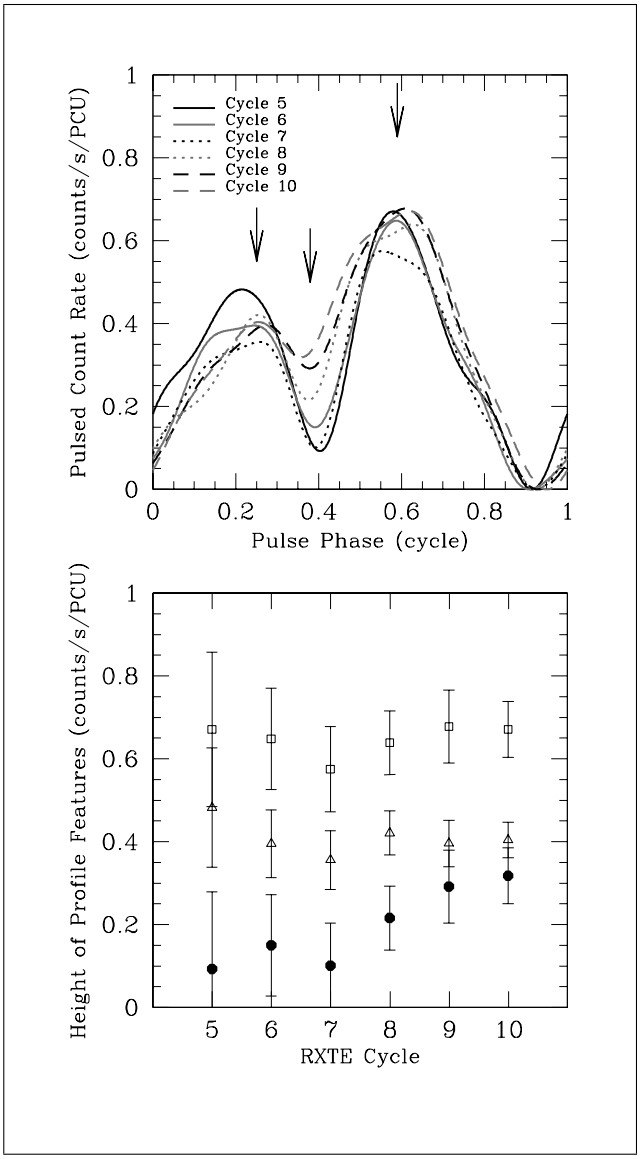

Figure 2.12 See caption for Figure 2.11 but for 2−4 keV.

gap, why the pulsed flux is presently rising is unclear. If the event associated with the putative glitch released energy deep in the neutron-star crust, then the increase could be due to its slow release (eg. Eichler & Cheng 1989; Hirano et al. 1997). Given the size of the observed flux increase and its time scale for release, the initial energy deposition would have had to have been large, $\sim 10^{45}$ erg (Hirano et al., 1997). This is comparable to the observed energy release in giant SGR flares (Hurley et al., 2005).

If we assume that the pulse shape prior to the gap is the "relaxed" pulse shape, the evolution of the harmonic ratios shown in Figure 2.9 supports the possibility of relaxation of the profile following an event in the gap. To shed light on the events in

the gap, we can compare our *RXTE* profiles with those observed with *ASCA* by Morii et al. (2005). In their Figure 4, pulse profiles in 0.5−10 keV for a) September 1994, b) August 1998, and c) combined July and August 1999 profiles are presented. In the 1994 and 1998 observations, the profile consisted of two peaks, with the trailing peak being the smallest, with the dip between the peaks being higher than the lowest bin in the profiles. The shape of the 1998 profile is in agreement with the *RXTE* pre-gap average pulse profiles for Cycle 2 (see Fig. 2.6). In the 1999 *ASCA* profile, the amplitude of the trailing peak was *higher* than that of the leading peak. In addition, the difference between the height of the dip and the lowest point in the profile decreased. Interestingly, the changes in the *ASCA* profiles appeared more significant at the lower end of the energy band, as we observe in our *RXTE* data. In 2000, the first *RXTE* Cycle after the gap has a profile in which the trailing peak is once again smaller than the leading peak. The dip between the peaks, however, is still more pronounced than in the pre-gap observations.

Overall, the timing data and the pulse profile data are consistent with some sort of event, possibly a glitch with accompanying sudden pulse profile change, having occured between 1998 August and 1999 July, possibly with the latter's long-term relaxation still ongoing as of early 2006. However, we suggest an alternate explanation for the latter point below.

2.4.2 Brief Review of the Magnetar Model

In the detailed magnetar model proposed by Thompson et al. 2002 (also see Section 1.2.4), the crust of a magnetar is deformed by internal magnetic stresses, thereby twisting the footpoints of the external magnetic field, driving powerful currents in the magnetosphere and twisting the magnetosphere relative to the standard dipolar geometry. These magnetospheric currents resonantly cyclotron scatter seed surface thermal photons. The seed contribution to the thermal component of the spectrum is thought to arise from heat resulting from the active decay of a high internal magnetic field (Thompson & Duncan, 1996; Thompson et al., 2002). The magnetospheric scattering is responsible for the non-thermal component of AXP spectra. Additionally, the surface is back-heated by the currents, resulting in additional thermal emission. Indeed, the persistent emission in AXPs generally has a spectrum that is well described by a two-component model, consisting of a blackbody plus a hard power-law tail, as expected in this model.

Changes in pulsed and/or total X-ray luminosity, spectral hardness, and torque are predicted to have a common physical origin in the Thompson et al. (2002) model and some correlations are expected. Changes in twist angle of the magnetic field, cause, or may be caused by, changes in the magnetospheric current distribution (due either to sudden crustal deformation like in AXP outbursts and SGR giant flares or due to slower crustal deformations as may be taking place in the AXP flares; Gavriil & Kaspi 2004). Larger twists generally correspond to harder persistent X-ray spectra and higher magnitudes of the spin-down rates, as is observed when comparing the harder SGR spectra to those of the softer AXPs (Marsden & White, 2001). A similar trend might be expected for a single magnetar exhibiting luminosity variations: a higher luminosity should correspond to a larger twist, hence harder spectrum, as has been reported for 1RXS J170849.0−400910 (Rea et al. 2005; Campana et al. 2007). A higher luminosity should also in general correspond to a larger magnitude of the spin-down rate. However, decoupling between the torque and the luminosity can occur because the torque is most sensitive to the current flowing on a relatively narrow bundle of field lines that are anchored close to the magnetic pole. For a single source, whether an X-ray luminosity change will be accompanied by a torque change depends on where in relation to the magnetic pole the source of the enhanced X-rays sits.

The Thompson et al. (2002) model can also explain properties of the pulse profiles of magnetars. According to the model, several effects can affect the pulse shape, generate subpulses, and/or increase the energy dependence of the pulse profile. In addition, an increase in the twisting angle of the magnetic field increases multiple scattering and increases the optical depth to resonant scattering which can simplify the pulse shape. This is one of the two proposed explanations for the sudden simplification of the pulse profile of SGR 1900+14 after its dramatic giant-flare (Woods et al., 2001), the other explanation being the sudden elimination of the nonaxisymmetric components of the magnetospheric currents (Thompson et al., 2002).

2.4.3 Possible Physical Interpretations for 4U 0142+61

In this paper, we have shown that the pulsed flux of 4U 0142+61 has increased on a time scale of a few years, and we have found simultaneous slow pulse profile evolution in the 2−4 keV band, which may to be recovering from some event that occured prior to 2000 but after 1997, possibly in the interval between 1998 August and 1999 July. We have also found evidence, as first suggested by Morii et al. (2005), that there was

a timing glitch in that same interval, although we cannot confirm its existence. Can the magnetar model explain these observations?

The energy dependence of the pulse profile evolution is puzzling. As described above, in the twisted magnetosphere model of Thompson et al. (2002), the non-thermal emission in an AXP is the result of magnetospheric scattering of surface thermal photons. If the surface emission angular pattern were changing, therefore, the non-thermal angular pattern should as well. That we do not observe comparable pulse profile changes in the 6−8 keV band for 4U 0142+61 is thus puzzling. One possibility is that the seed thermal emission is not changing appreciably, but the scattering currents in the outer regions of the magnetosphere, where the cyclotron energy is lower, are changing, while the inner currents are not. This could arise if there is evolution in the field configuration closer to the magnetic poles, with relatively little closer to the magnetic equator. Why variations in the field configuration should be geographically localized, however, is unclear.

The increase in the pulsed flux over a similar time scale as that of the profile evolution is apparently accompanied by a softening of the spectrum (Gonzalez et al., 2007). As discussed above, the putative 1998/1999 glitch may have deposited a large amount of energy in the crust, with it only starting to be radiated away in 2002. The energy released would have had to have been large, $\sim 10^{45}$ erg (Hirano et al., 1997). Such a thermal energy release could be influencing the pulse profile as well, although some change in profile would be expected in the hard band too, which is not observed. Moreover, such an increase has not been observed following the glitches in 1E 2259+586 or 1RXS 170849.0−400910, although this could be a result of smaller total energy releases.

Alternatively, the increase in pulsed flux seen in 4U 0142+61 between 2002 and 2005 could be explained by the twisted magnetosphere model. In this framework, there are two possibilities: *a)* a slow *in*crease in the twist of the magnetic field lines in the magnetosphere, or, *b)* a slow *de*crease in the twist angle.

In the first possibility, the observed increase in the pulsed flux could be an extreme case of the 1E 1048−5937 flares, i.e. a slow twisting of the magnetic field lines in the suggested interpretation of Gavriil & Kaspi (2004). This explanation is only valid if the total flux, which remains to be determined with an imaging telescope, is increasing as well. How this would be related to the putative 1998/1999 event is unclear; any flux enhancement that occured then would have had to have largely decayed away by 2000. In any case, for an increase in the twist angle, one expects a spectral hardening

(Thompson et al., 2002). We do not observe this. Also for an increase in the twist angle, at least naively, the twisted magnetosphere model predicts an increase in torque as the flux rises (Thompson et al., 2002). From Table 2.2, the post-gap ephemeris $\ddot{\nu}$ is positive, meaning $\dot{\nu}$ is increasing, i.e. the magnitude of the pulsar's spin-down rate is decreasing, the opposite of what is expected for a flux increase, unless the magnetospheric currents causing the torque are flowing only in the small polar cap region. Finally, if the slow increase in pulsed flux were caused by a slow magnetospheric twisting, the decrease in the size of the Fourier components of order higher than unity in the low energy band could be interpreted as a simplification of the pulse profile due to an increase in the scattering in the magnetosphere. However, the most extreme case of a pulse profile simplification, which was reported in SGR 1900+14, happened equally in all bands following a dramatic increase in the scattering after a giant flare (Woods et al. 2001, Thompson et al. 2002). The phenomenon that we have observed, by contrast, is restricted to the softer energies.

In the previous paragraph, we mentioned that the increase in the pulsed flux and the gradual changes in the pulse profile may indicate stress build-up caused by an increase in the twist angle in the magnetosphere. The pulse profiles of Cycles 2 and 10 are very similar, indicating that the pulse profile of Cycle 2 may also be showing signs of the same kind of stress build-up. Under these assumptions, if an event occured in the gap following Cycle 2, it is reasonable to expect a similar event to follow after Cycle 10. Indeed, in 2006 April, less than 2 months after the end of Cycle 10, the pulsar appears to have entered an extended active phase: a single burst accompanied by a pulse profile change was detected from the pulsar on April 6 (Kaspi, Dib, & Gavriil, 2006). A series of four bursts was later detected on June 25 (Dib et al., 2006) and a larger burst was detected on 2007 February 07 (Gavriil et al., 2007a). For a detailed paper on these events, see Chapter 3. If they are indeed due to a stress release following several years of slow magnetospheric twist, then the causes of the softening of the spectrum and of the decrease in the magnitude of the pulsar's spin-down are unclear.

The second possibility in the framework of the twisted magnetosphere model, is that the observed increase in the pulsed flux is accompanying a slow *de*crease in the twist angle of the magnetic field lines in the magnetosphere. This explanation is only valid if the total flux is decreasing. If the total flux were falling with the pulsed fraction rising, the observed spectral softening could be consistent with naive *un*twisting expectations as would the decreasing spin-down rate. Indeed an anti-correlation between total flux and pulsed fraction was observed by Tiengo et al. (2005) for 1E 1048.1−5937,

supporting this possibility. However, the problem of why the pulse profile is evolving at low, but not high energies, remains.

2.4.4 Other Wavelengths

4U 0142+61 is truly a multi-wavelength AXP. It is known to pulsate in the optical band (Kern & Martin, 2002; Dhillon et al., 2005) and it has been detected in the near-IR (Hulleman et al., 2004), in the mid-IR using *SPITZER* (Wang, Chakrabarty, & Kaplan, 2006), and in hard X-rays (Kuiper et al., 2006; den Hartog et al., 2006).

The origin of the emission at these other wavelengths remains unclear, although some models have been proposed. In hard X-rays, Thompson & Beloborodov (2005) argue that the emission is either due to bremsstrahlung photons emitted by a thin surface layer, or is due to synchrotron emission originating from the region in the magnetosphere where the electron cyclotron energy is in the keV range. The near-IR and optical emission is thought to be magnetospheric (Eichler, Gedalin, & Lyubarsky, 2002), while the mid-IR emission is suggested to be due to a passive fall-back disk (Wang et al., 2006).

Looking for correlations between the X-rays and the emission in other wavelengths may serve as tests of emission models, as correlations between X-ray and near-IR fluxes have sometimes been observed. For example, a correlation in the decays of the X-ray and near-IR fluxes in 1E 2259+586 was observed following the 2002 outburst (Tam et al., 2004); a similar correlation was reported for XTE J1810−197 (Rea et al., 2004b). However, in other instances, the two fluxes were not correlated, as for 1E 1048−5937 (Gavriil & Kaspi 2004, Mereghetti et al. 2004, and Durant, van Kerkwijk, & Hulleman, 2004). In 4U 0142+61, reported variations in the IR are not seen contemporaneously in our X-ray data, and are on time scales much shorter than that of the X-ray variation reported here (Hulleman et al., 2004; Durant & van Kerkwijk, 2006b).

Wang et al. (2006) observed mid-IR emission from 4U 0142+61 which they argue is associated with a passive fall-back disk irradiated by the central X-ray pulsar. If this is the case, then if 4U 0142+61's X-ray flux is increasing, one expects a corresponding increase in the disk emission. It is thus important to establish the behaviour of the total flux, in addition to that of the pulsed flux reported on here.

The possible presence of a disk suggests that if a sudden, impulsive outburst occured in the gap, the energy released must have been significantly smaller than the disk

binding energy, after accounting for the disk thickness. For a central pulsar mass of $M_{psr} \sim 1.4 M_\odot$, a uniform disk of mass $M \sim 3 M_\oplus$, and inner and outer radii $R_1 \sim 3 R_\odot$ and $R_2 \sim 10 R_\odot$ (Wang et al., 2006) the disk binding energy is $\sim 4 \times 10^{42}$ erg. Since the X-ray luminosity of the source ($\sim 10^{35}$ erg/s) integrated over a period > 5000 yr is much larger than the binding energy of the observed disk, one must assume that when the source is not undergoing an outburst, the disk is in an equilibrium state where the rate of energy absorption is balanced by the rate of disk emission. Assuming this equilibrium cannot hold on the time scale of a sudden outburst, then IR observations of the disk provide an upper limit of $(4 \times 10^{42}/f)$ erg on the energy released in a possible outburst in the gap, where f is the fraction of the solid angle occupied by the thickness of the disk. For $f = 0.01$, this upper limit is three orders of magnitude larger than the total energy released during the flares of 1E 1048−5937 (Gavriil & Kaspi, 2004). It is also five orders of magnitude larger than the energy released during the first day of the 1E 2259+586 outburst (Woods et al., 2004). Thus, an event in the gap of either the magnitude of the flares or that of the outburst occuring could have affected the disk but seems unlikely to have disrupted it. For $f = 0.01$, the upper limit is also of the same magnitude as the energy released in either of the SGR 1900+14 or the SGR 0526−66 giant flares (Mazets et al., 1999b). This suggests that there have been no events of the magnitude of the giant SGR flares since the putative disk's formation. Given that we have witnessed 3 giant SGR flares each from a different source since 1979, and none from AXPs, this suggests that AXPs do not exhibit giant flares. This would suggest an interesting distinction between SGRs and AXPs: if the two are evolutionary linked, the AXP phase must come first, unless a debris disk can reform following a giant flare.

The mid-IR emission has also been interpreted as an active fall-back disk in which the pulsar is accreting in a propeller mode. In this case, the dipole field strength of the pulsar is typical of conventional radio pulsars, ie. $\sim 10^{12}$ G (Ertan et al., 2007), although the surface field strength is in the magnetar range, owing to higher order multipoles. In this model, the X-rays arise from propeller accretion. Without detailed models of the spectra and of the pulse shapes expected in this model, we cannot interpret our observations in this framework. Nevertheless, one might expect a torque change with luminosity in this model. For 4U 0142+61, as noted in Section 2.4.3, the magnitude of the torque is decreasing while the pulsed flux is increasing. If propeller accretion is occuring, then the total flux should be decreasing; this can be checked (Gonzalez et al., 2007). We note that evidence against such a torque/luminosity

correlation has been presented by Gavriil & Kaspi (2004) for a different AXP.

2.5 Summary

Our continuing *RXTE* monitoring program has revealed a possibly new AXP variability phenomenon: 4U 0142+61 exhibited a slow but steady increase in its pulsed flux between 2002 May and 2004 December, such that it has risen 36±3% over 2.6 years in the 2−10 keV band. This is accompanied by a softening of the spectrum (Gonzalez et al., 2007). Quasi-simultaneously, the pulse profile, which comprises two peaks having different spectra, has been evolving since 2000. In particular, the dip of emission between the two peaks has been rising since 2002, as if it is returning to its pre-2000 morphology in which there was no clear distinction between the peaks. The profile evolution translates to a reduction of the power in the Fourier harmonics of order higher than one since 2000. This is in contrast with the pulsed flux which seems to be moving *away* from the pre-2000 value. The evolution in the pulse profile is seen in the 2−4 keV band but not in the 6−8 keV band, presenting an interesting puzzle to the twisted magnetosphere model for magnetars. Intriguingly, Morii et al. (2005) have suggested the pulsar suffered a glitch just before 2000 on the basis of a single discrepant *ASCA* period measurement. Our phase-coherent timing using *RXTE* demonstrates that a glitch is plausible but not necessary to explain the data, but our pulse profile evolution analysis provides new evidence for such an event having occured.

Physical interpretations that described well other observed long-term changes in AXP emission (such as outburst afterglow or flux flares caused by an increased twist in the magnetosphere) do not explain all the phenomena that we have observed. Most of our observations could be explained by the twisted magnetosphere model if the total flux of 4U 0142+61 is actually decreasing. This would indicate a slow *un*twisting in the magnetosphere. Alternatively, if the total flux is increasing, a slow *increase* in the twist angle in the magnetosphere can account for the pulse profile simplification and for the post-Cycle 10 events, but the changes in the spin-down rate and the softening of the spectrum would remain unexplained. Finally, the data could be explained by energy release following an energy deposition, perhaps due to a glitch that occured in the crust of the star sometime during the post Cycle 2 gap, although the energy deposited would have had to have been large. No matter what, the absence of profile evolution at high energies remains a puzzle.

Chapter 3

The 2006−2007 Active Phase of Anomalous X-ray Pulsar 4U 0142+61

In the previous Chapter (Chapter 2) we studied the properties of AXP 4U 0142+61 as they slowly evolved from 2000 to 2006 February. In 2006 March, the source entered an active phase in which several of these properties changed. The changes were accompanied by several short X-ray bursts. This Chapter is based on excerpts from the manuscript "The 2006−2007 Active Phase of Anomalous X-ray Pulsar 4U 0142+61: Radiative and Timing Changes, Bursts, and Burst Spectral Features", submitted to *the Astrophysical Journal* in 2009 April (reference: Gavriil, Dib, & Kaspi, 2009b). Specifically, the Chapter is based on the parts of the manuscript that describe the changes in the pulsed flux, pulse profile, and the timing properties of 4U 0142+61 after the entry into the active phase. The parts of the manuscript where we studied the temporal and spectral properties of the observed bursts are not included. The original abstract is below.

After at least 6 years of quiescence, Anomalous X-ray Pulsar (AXP) 4U 0142+61 entered an active phase in 2006 March that lasted several months and included six X-ray bursts as well as many changes in the persistent X-ray emission. The bursts, the first seen from this AXP in >11 years of *Rossi X-ray Timing Explorer* monitoring, all occurred in the interval between 2006 April 6 and 2007 February 7. The burst

durations ranged from $8-3\times10^3$ s. The first five burst spectra are well modeled by blackbodies, with temperatures $kT \sim 2-6$ keV. However, the sixth burst had a complicated spectrum that is well characterized by a blackbody plus three emission features whose amplitude varied throughout the burst. The most prominent feature was at 14.0 keV. Upon entry into the active phase the pulsar showed a significant change in pulse morphology and a likely timing glitch. The glitch had a total frequency jump of $(1.9\pm0.4)\times10^{-7}$ Hz, which recovered with a decay time of 17 ± 2 days by more than the initial jump (recovery fraction ~ 1.07), implying a net spin-down of the pulsar. We discuss these events in the context of the magnetar model.

3.1 Introduction

Anomalous X-ray Pulsars (AXPs) are isolated neutron stars that are described in Section 1.2.3, and in Appendix C. Their observed 2-10 keV X-ray luminosities ($\sim 10^{33} - 10^{35}$ erg s^{-1}) cannot be accounted for by their available spin-down energy. It is now widely accepted that AXPs are magnetars – young isolated neutron stars powered by their high magnetic fields (Thompson & Duncan, 1995b; Thompson & Duncan, 1996).

Thus far, only the magnetar model predicts the existence the bursts observed from SGRs and AXPs (Thompson & Duncan, 1995b). The internal magnetic field exerts stresses on the crust which can lead to large scale rearrangements of the external field, which we observe as giant flares. If the stress is more localized, then it can fracture the crust and displace the footpoints of the external magnetic field which results in short X-ray bursts. The highly twisted internal magnetic field also slowly twists up the external field; and magnetospheres of magnetars may therefore be globally twisted (Thompson et al., 2002). Reconnection in this twisted magnetosphere has also been proposed as an additional mechanism for the short bursts (Lyutikov, 2002).

In addition to bursts, AXPs and SGRs exhibit pulsed and persistent flux variations on several time scales. An hours-long increase in the pulsed flux has been seen to follow a burst in AXP 1E 1048.1−5937 (Gavriil et al., 2006a). On longer time scales, AXPs can exhibit abrupt increases in flux which decay on several-week time scales. These occur in conjunction with bursts and have been suggested as being due to thermal radiation from the stellar surface after the deposition of heat from bursts. Such flux enhancements have been observed in SGRs (e.g. Woods et al. 2001) as well as in AXPs (e.g. in AXP 1E 2259+586, Woods et al. 2004). AXP 1E 1048.1−5937 exhibited three unusual flux 'flares'. In the first two, the pulsed flux rose on week-long time scales and subsequently decayed back on time scales of months (Gavriil & Kaspi, 2004; Tam et al., 2008a). These variations have been tentatively attributed to twists implanted in the external magnetosphere from stresses on the crust imposed by the internal magnetic field. AXPs XTE J1810−197, 1E 1547.0−5408, and the AXP candidate AX J1845–0258 have also exhibited large flux variations (Ibrahim et al., 2004; Halpern et al., 2008; Gotthelf & Vasisht, 1998; Tam et al., 2006), however it is not clear whether these were of the abrupt rise type as in 1E 2259+586 or the slow-rise type as in 1E 1048.1−5937. CXO J164710.2−455216 showed a clear abrupt rise (Muno et al., 2007). 1RXS J170849.0−400910 has been argued to have flux variations associated

with timing events (Israel et al., 2007). Finally, AXP 4U 0142+61 has exhibited the longest time scale flux variations thus far, in which the pulsed flux increased by 29±8% over a period of 2.6 years (Dib et al. 2007a, Chapter 2, Gonzalez et al. 2007).

4U 0142+61 is an 8.7-s AXP. It has a period derivative of $\dot{P} = 0.2 \times 10^{-11}$, implying a surface dipole magnetic field of 1.3×10^{14} G. 4U 0142+61 was monitored by *RXTE* in 1997 and from 2000 to 2007. Gavriil & Kaspi (2002) showed that 4U 0142+61 generally rotates with high stability. Morii et al. (2005) reported a possible timing glitch in 1999 on the basis of an *Advanced Satellite for Cosmology and Astrophysics* (*ASCA*) observation in which the value of the frequency was marginally discrepant with the frequency as reported by Gavriil & Kaspi (2002). Dib et al. (2007a) showed that the glitch may have occurred but is not required by the existing data. Dib et al. (2007a) also reported on the evolution of the properties of 4U 0142+61 from 2000 March to 2006 April (see Chapter 2). In particular they reported stable timing, and an evolution of the pulse profile in 2−4 keV where the dip between the two peak was rising between 2000 and 2006. They also reported a 29±8% increase in the pulsed flux between 2002 May and 2004 December. As of 2006 March, in the published flux history of this source, there had been no reports of any X-ray activity such bursts or flares, as described above for other AXPs.

Here we report on the first detection of bursts from AXP 4U 0142+61, making this the sixth AXP for which this phenomenon has been observed. We also report that the source appears to have entered an active phase in 2006 March in which almost every aspect of the emission changed. Our observations are described in Section 3.2. Our burst, pulsed morphology, pulse phase, pulsed flux, and timing analysis are presented, respectively, in Sections 3.3.1, 3.3.2, 3.3.3, 3.3.4, and 3.3.5. In Section 3.4, we discuss the possible origins of this behaviour and the implications for the magnetar model.

3.2 Observations

4U 0142+61 has been monitored with *Rossi X-ray Timing Explorer* (*RXTE*) in 1997 and from 2000 to 2007. It has been monitored bi-monthly since 2005 March, with a typical observation length of ∼5 ks. On 2006 March 23, the source entered an active phase where many pulsed flux, spectral, and pulse profile changes were observed. We detected 6 bursts in three observations after the entry into the active phase. After each burst detection, several *RXTE* target-of-opportunity (ToO) observations were made in addition to the regular monitoring.

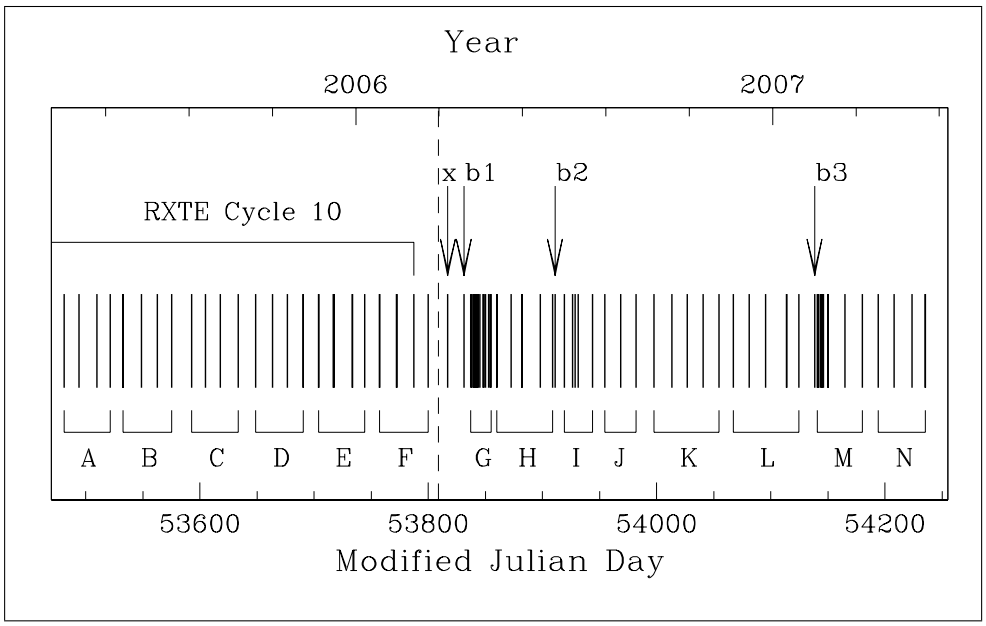

Figure 3.1 Epochs of the *RXTE* observations of 4U 0142+61 analyzed in this Chapter (see Section 3.3.2). Each observation is represented by a vertical line. The dashed line marks the entry of the source into the active phase. An "x" marks the first observation where the pulse profile was significantly different from the long-term average. "b1", "b2", and "b3" mark the observations containing bursts. To the left of the dotted line, the letters refer to groups of observations having similar total integration times. To the right, the letters refer to groups of observations having similar pulse profiles.

Here, we present a detailed analysis of the three observations containing bursts (see Table 3.1). We also present an analysis of 91 other observations spanning the 2005 March 21 to 2007 May 15 time period (MJD 53481 to MJD 54235, Observation IDs 91070-05-04-00 to 92006-05-32-00). 32 of these observations were prior to the entry into the active phase, and the remaining 59 observations were after. This long-term analysis was performed in order to track the evolving pulsed flux and timing properties of the source.

Figure 3.1 shows a timeline of the 94 analyzed observations. Note that two segments of any observation that was split counted as separate observations if the segments were given different observation IDs. The ranges of epochs with an increased density of observations contain the ToO observations. Prior to the active phase, the groups of observations referred to by capital letters in the Figure have similar total integration times. The groups of observations in the active phase have similar pulse profiles. These groups will be referred to in Sections 3.3.2 and 3.3.5.

Table 3.1. Observations containing bursts.

Observation ID	MJD	Date	Number of Bursts	Number of Active PCUs
92006-05-03-00	53831	04/06/2006	1	3*
92006-05-09-01	53911	06/25/2006	4	3
92006-05-25-00	54138	02/07/2007	1	2

*One PCU switched ON and another one OFF partway through the observation, but the total number of active PCUs stayed constant throughout the observation.

3.3 Analysis and Results

All data presented here are from the Proportional Counter Array (PCA, Jahoda et al. 1996) aboard *RXTE* (see Section 1.4). The data were collected in either `GoodXenonwithPropane` or `GoodXenon` mode which record photon arrival times with $\sim$1-μs resolution and bins them with 256 spectral channels in the $\sim$2–60 keV band.

3.3.1 Burst Detection

For each monitoring observation of 4U 0142+61, using software that can handle the raw telemetry data, we generated 31.25-ms lightcurves using all Xenon layers and events in the 2–20 keV band. These lightcurves were searched for bursts using our automated burst search algorithm introduced in Gavriil et al. (2002) and discussed further in Gavriil et al. (2004). In an observation on 2006 April 6, we detected a significant burst, and four more bursts were detected in a single observation on 2006 June 25. The sixth and most energetic burst was detected on 2007 February 7. The bursts were significant in each active PCU. See Table 3.1 for the number of active PCUs in each burst observation, as well as for the burst observation epochs.

3.3.2 Pulse Profile Changes

Many AXP outbursts are accompanied by significant pulse profile changes (e.g. Kaspi et al. 2003). To search for these in 4U 0142+61, for each observation, we generated 64-bin pulse profiles using the method described in Dib et al. (2007a) (Chapter 2). We

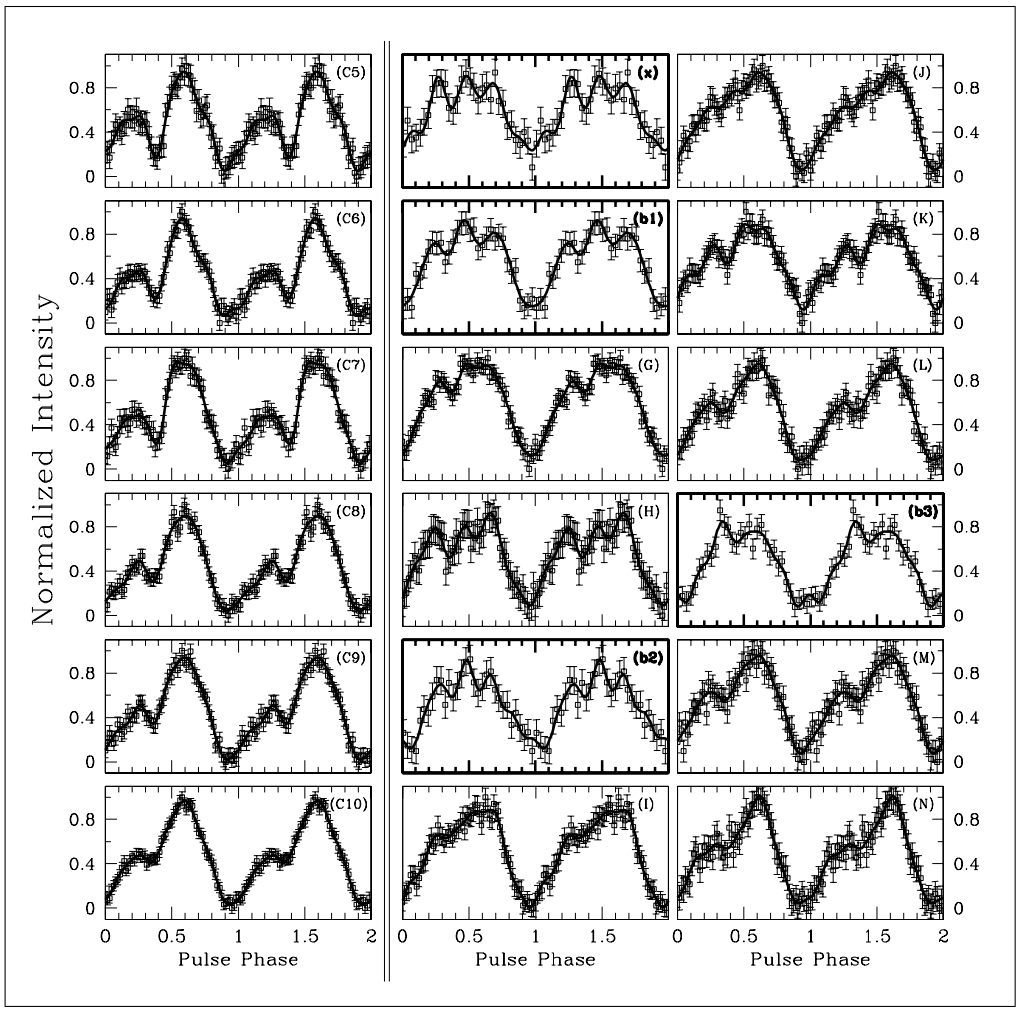

Figure 3.2 Pulse profile evolution of 4U 0142+61. Left-most column: normalized average 2−10 keV pulse profiles in the 6 years prior to the entry into the active phase in chronological order (panels from Dib et al. 2007a, Chapter 2). Middle and right-most columns: normalized, averaged 2−10 keV pulse profiles for each of the data groups marked by a letter in Figure 3.1, after the entry into the active phase. The 4 plots with bold labels correspond to the observations marked with "x", "b1", "b2", and "b3" in Figure 3.1.

then aligned the profiles with a high signal-to-noise template using a cross-correlation procedure in the Fourier domain. Then, for each group of observations in the active phase, we summed the aligned profiles, extracted the DC component from the summed profile, and scaled the resulting profile so that the value of the highest bin is unity and the lowest bin is zero.

The resulting pulse profiles are shown in Figure 3.2 in chronological order. The panels in the left-most column are from Dib et al. (2007a) (Chapter 2) and show pulse

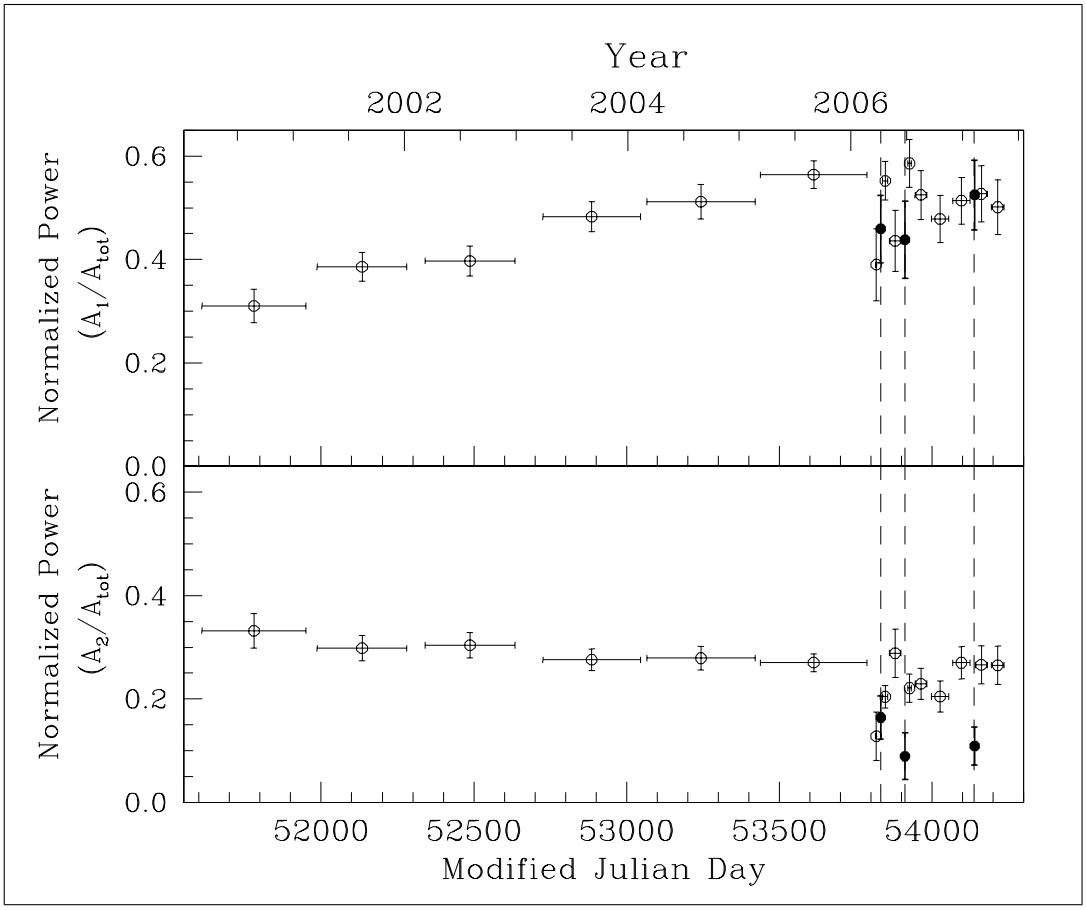

Figure 3.3 Top: evolution of the power in the fundamental Fourier component of the pulse profile of 4U 0142+61 in the 2−10 keV band. Bottom: Evolution of the power in the second harmonic. In both panels, the points with large horizontal error bars are from Dib et al. (2007a) (Chapter 2). The remaining points are obtained from groups of observations after the entry into the active phase. The three bold points correspond to the observations with bursts. The three dashed lines correspond to burst epochs.

profiles in the 6 years prior to the entry into the active phase. Notice the slow change in the height of the dip between the peaks. The panels in columns 2 and 3, marked with the corresponding letter in the top right corner, show pulse profiles for each of the data groups in the active phase that were marked with a letter in Figure 3.1. The 4 plots in bold correspond to the observations marked with "x", "b1", "b2", and "b3" in Figure 3.1.

The pulse profile evolution can be described as follows: prior to the active phase, features in the double peaked pulse profile were evolving on a time scale of several years (see panels C6 to C10 corresponding to *RXTE* Cycles 6 to 10). Then, in the first observation of the active phase (panel x), the pulse profile became suddenly triple-

peaked. It was also triple-peaked in the following observation (panel b1), in which a burst occurred. It remained multi-peaked for the following two groups of observations (panels G and H). Then, an observation with multiple bursts occurred (panel b2). In that observation, also having a triple-peaked pulse profile, the middle peak was taller than the other two. Following this observation, the pulse profile seemed to be slowly recovering back to its double-peaked long-term shape (panels I, J, K, and L). Another burst observation interrupted this evolution seven months later (panel b3). In that observation, a large burst was detected. In the pulse profile of that observation, the left-most peak was significantly taller than usual. The event that caused this change had apparently no effect on the following observation which occurred 2 days later: the profile went back to being double-peaked (panels M and N). To summarize, the pulse profile became multi-peaked at the beginning of the active phase. Following the second observation with bursts, the profile started to recover to its double-peaked shape. The evolution was only temporarily interrupted for the duration of the third observation with bursts. The behaviour of the pulse profile in the 2−4 keV band and 4−10 keV bands was similar.

Note that from Figure 3.2 alone we can compare the sizes of the peaks to each other, but we cannot track the evolution of the heights of each peak separately. In order to do that, we must scale the pulse profile of each group of observations by the average pulsed flux of that group. This analysis is presented in Section 3.3.4.

We also performed an analysis of the Fourier components of the pulse profiles. The results are shown in Figure 3.3. The variations in the power of the fundamental Fourier component are shown in panel 1, and that of the second harmonic in panel 2. Note how the amplitude of the fundamental varied monotonically prior to, but not during, the active phase. Also note how the power in the second harmonic was already back to its pre-active-phase level before the last burst occurred.

3.3.3 Burst Rotational Phases

An important factor in understanding the origin of the bursts is the rotational phase at which they occur. The phases of the bursts are shown in Figure 3.4. For each burst observation we created at 31.25-ms time resolution lightcurve and folded it using our timing solution (see Section 3.3.5). We then phase-aligned these folded profiles by cross-correlating them with the long-term pulse profile template. Our phase-aligned folded profiles are shown in Figure 3.4 (histograms in the last row). Superposed on

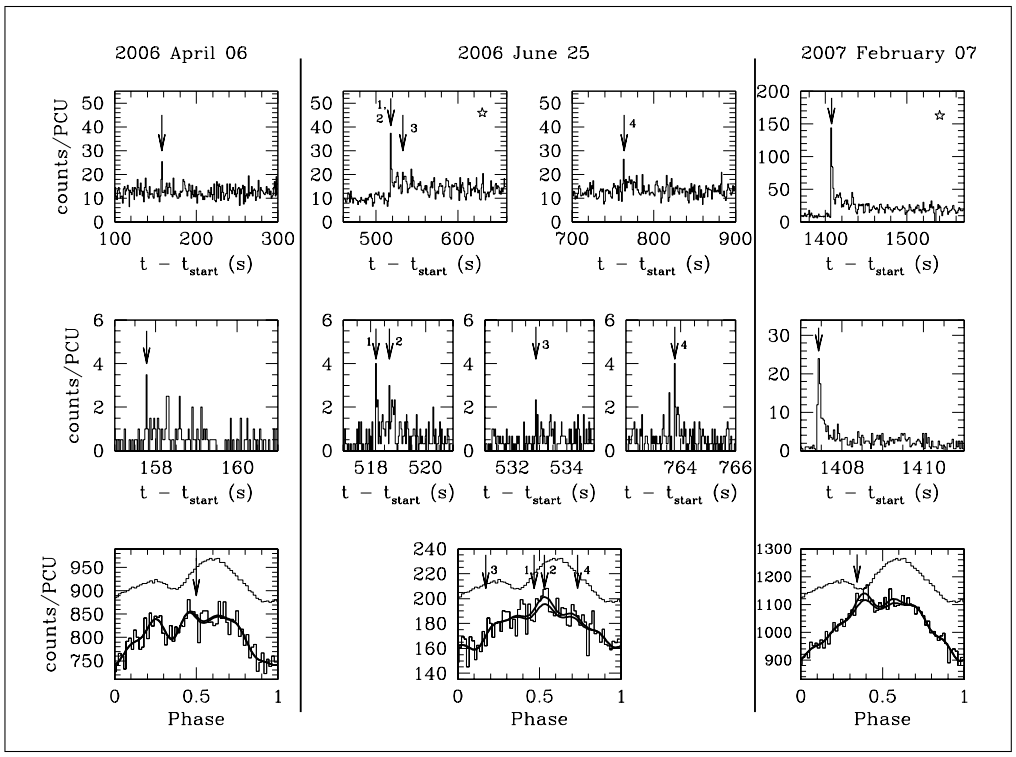

Figure 3.4 Phase analysis of the 6 detected bursts. Each column corresponds to an observation in which bursts were detected. Top row: 200-s segments of the time series containing the bursts in the 2−20 keV band. The time resolution is 1 s. Middle row: 4-s segments of the time series containing the bursts. The time resolution 31.25 ms. Bottom row: aligned folds of the burst observations shown below the scaled long-term average profile. The folded counts are presented as histograms. Superposed on each histogram are two curves. The top curve is made of the 5 Fourier harmonics that best fit the histogram. The bottom curve is made of the best-fit 5 harmonics after the removal of the 4 seconds centered on each burst. The arrows indicate the phases of each burst.

each folded profile are two curves. The top curve is made of the 5 Fourier harmonics that best fit the histogram. The bottom curve is made of the best-fit 5 harmonics after the removal of the 4 seconds centered on each burst. Note how the two curves in a given plot are similar, demonstrating that the additional peaks in the profiles are not due to the burst. The first three bursts occurred near the middle 'new" peak in the profile. Burst 5 occurred near the old tall peak of the profile (see Fig. 3.2). The phase of burst 6 corresponds again to a new peak in the profile, this time located where the previous small peak used to be. The coincidences of several bursts with new, transient profile features that are present even when the actual burst data are removed are suggestive of lower-level transient emission from the same physical location, with

the burst being the extreme of this emission's luminosity distribution.

3.3.4 Pulsed Flux Analysis

Short-Term Pulsed Flux Analysis

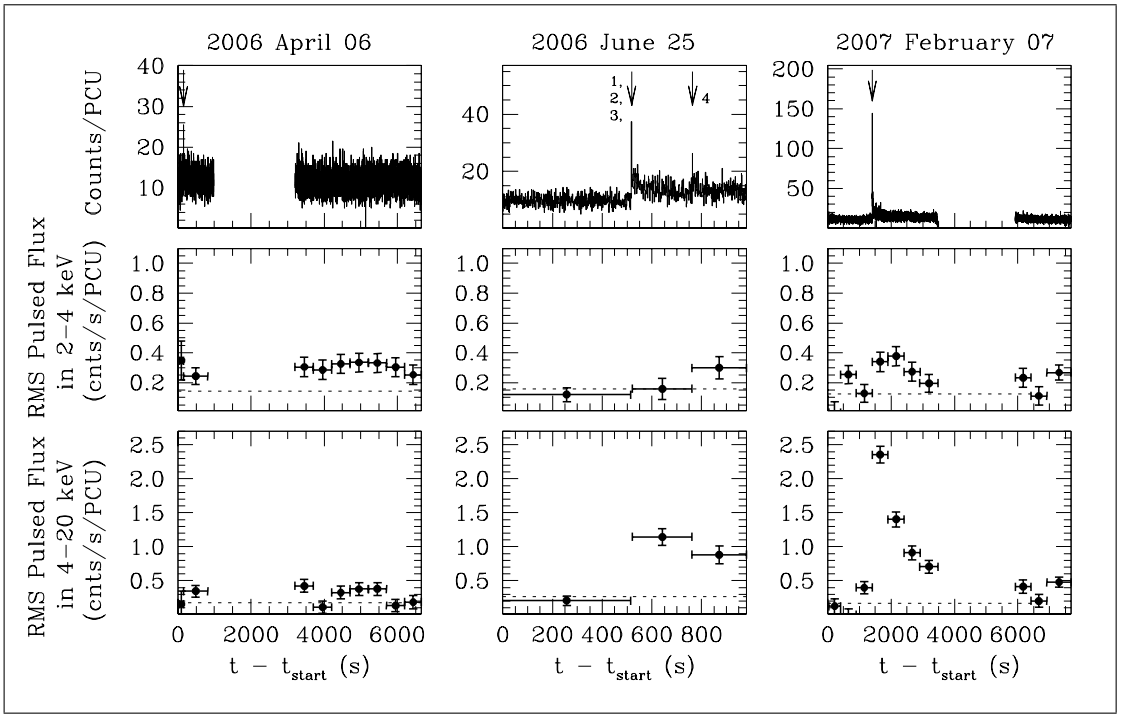

Figure 3.5 RMS pulsed flux within the observations containing bursts. Each column corresponds to one observation. In each column we show, descending vertically, the 1-s resolution lightcurve with the bursts indicated, the 2–4 keV RMS pulsed flux, and the 4–20 keV RMS pulsed flux. The dotted line in each of the pulsed flux plots shows the average of the pulsed fluxes obtained after segmenting and analyzing the time series of the observation immediately prior to the one shown.

Previous AXP bursts are often accompanied by short-term pulsed flux enhancements (e.g. Gavriil et al. 2006a). To search for these, for each of the three observations containing bursts, we made two barycentered time series in count rate per PCU, one for the 2−4 keV band and the other for 4−20 keV. We included only photons detected by PCUs that were on for the entire duration of the observation. The time resolution was 31.25 ms. We removed the 4 s centered on each burst from each time series. Then, we broke each time series into segments of length ∼500 s. For each segment, we calculated the pulsed flux using two different methods.

First, we calculated the RMS pulsed flux using

$$F_{\rm RMS} = \sqrt{2\sum_{k=1}^{n}((a_k{}^2 + b_k{}^2) - (\sigma_{a_k}{}^2 + \sigma_{b_k}{}^2))}, \quad (3.1)$$

where a_k is the $k^{\rm th}$ even Fourier component defined as $a_k = \frac{1}{N}\sum_{i=1}^{N} p_i \cos(2\pi ki/N)$, σ_{a_k} is the uncertainty of a_k, b_k is the $k^{\rm th}$ odd Fourier component defined as $b_k = \frac{1}{N}\sum_{i=1}^{N} p_i \sin(2\pi ki/N)$, σ_{b_k} is the uncertainty of b_k, i refers to the phase bin, N is the total number of phase bins, p_i is the count rate in the $i^{\rm th}$ phase bin of the pulse profile, and n is the maximum number of Fourier harmonics to be taken into account; here n=5 for consistency with Dib et al. (2007a) (Chapter 2) and Gonzalez et al. (2007).

While least sensitive to noise compared to other pulsed flux measurement methods, the RMS method returns a pulsed flux number that is affected by pulse profile changes (Archibald et al., 2009)[1]. To confirm our pulsed flux results, we also used an area-based estimator to calculate the pulsed flux:

$$F_{\rm Area} = a_0 - p_{\rm min}, \quad (3.2)$$

where $a_0 = \frac{1}{N}\sum_{i=1}^{N} p_i$, and $p_{\rm min}$ is the average count rate in the off-pulse phase bins of the profile, determined by cross-correlating with a high signal-to-noise template, and calculated in the Fourier domain after truncating the Fourier series to 5 harmonics. The results are shown for $F_{\rm RMS}$ in Figure 3.5 for $F_{\rm RMS}$ ($F_{\rm AREA}$ gives consistent results). Note the significant increase in the 4−20 keV pulsed flux in the 2006 June observation following the cluster of bursts. This increase is not present in 2−4 keV. Also note the significant rise and subsequent decay of the pulsed flux following the large 2007 February burst. The pulsed flux was sufficiently enhanced in these two observations that one can see individual pulsations by eye in Figure 3.4 in the two panels marked with a star, containing the raw burst lightcurves with 31.25-ms time resolution.

Long-Term Pulsed Flux Analysis

For each of the 94 analyzed observations, we created a pulse profile (in units of count rate per PCU) using the same procedure as in Section 3.3.2. Then we calculated the pulsed flux for each observation using Equations 3.1 and 3.2. Data from PCU 0 were omitted because the long-term trend in the pulsed counts is not the same as that

[1]This is because, for the same area under the curve, the RMS pulsed flux is different for different profile shapes.

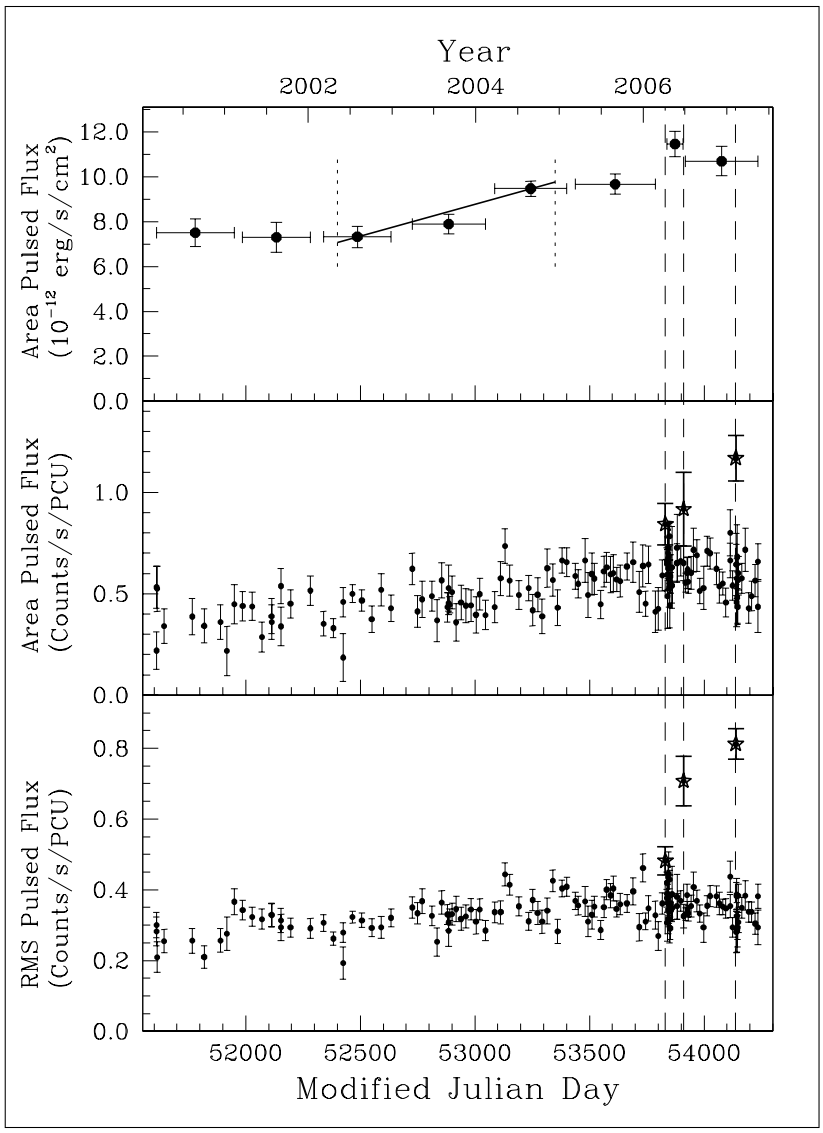

Figure 3.6 Long-term pulsed flux time series in 2−10 keV for 4U 0142+61. Panel 1: area pulsed flux in erg s^{-1} cm^{-2} for combined observations. The solid line marks the 29±8% increase reported in Dib et al. (2007a) (Chapter 2). Panel 2: area pulsed flux in counts/s/PCU for individual observations. Panel 3: RMS pulsed flux in counts/s/PCU for individual observations. All panels: the dashed lines mark the burst epochs. The points marked with stars are the pulsed fluxes of the observations containing bursts.

in the remaining PCUs, presumably due to the loss of its propane layer. Data from PCU 1 were omitted after the loss of its propane layer as well, on MJD 54094.

We extracted pulsed fluxes in the 2−4 keV and 4−20 keV bands using both the RMS and area pulsed flux method because of the numerous pulse profile changes around the times of the bursts. There is no evidence of a long-term change in the pulsed flux associated with the bursts except, possibly, for a hint of an increase in the

2−4 keV band roughly midway between the second and third observations containing bursts. We also note that the 4−20 keV pulsed flux of two of the observations containing bursts are significantly larger than the long-term average. Removing the bursts from these observations does not change this result.

We performed the same analysis for individual observations in 2−10 keV for an extended period of time. This is shown in panels 2 and 3 of Figure 3.6. This plot is an update to Figure 10 of Dib et al. (2007a) (Figure 2.10).

In order to verify that trends seen in panels 2 and 3 of Figure 3.6 are not an artifact of the evolution of the response of the detector, we calculated the pulsed flux in erg s^{-1} cm^{-2} using a method that took the evolution of the response into account. The method is described in Dib et al. (2007a) and takes into account spectral fits obtained from imaging data (in this case *XMM* data, see Gonzalez et al. 2007) to convert counts to energy for each combined set of observations. For this analysis, we used data from all PCUs; however, data from PCU 1 were excluded after the loss its propane layer. Data from PCU 0 were included because the response matrices used took into account the loss of its propane layer.

The results are shown in panel 1 of Figure 3.6. The first 6 points, corresponding to *RXTE* Cycles 6−10, are from Dib et al. (2007a) (Chapter 2). The second to last point is obtained by combining all observations that occurred between bursts 1 and 2, but omitting observations containing bursts. The observations that we included took place during the exponential recovery of the possible glitch (see Section 3.3.5). The last point in panel 1 was obtained by combining the observations that occurred after burst 2, but again omitting those containing bursts. The observations we included took place after the end of the exponential recovery of the possible glitch (see Section 3.3.5).

In the first of the two data points in the active phase, the pulsed flux in erg s^{-1} cm^{-2} is 18±8% larger than in the pre-active phase. This is consistent with the increase reported in Gonzalez et al. (2007) in the same energy range. A hint of this increase can be seen in panel 2 although it appears less significant. This discrepancy can be accounted for by the fact that the spectrum changed: Gonzalez et al. (2007) reported a temporary increase in the spectral hardness in an *XMM* observation of 4U 0142+61 immediately following the bursts.

Combined Pulse Morphology and Pulsed Flux Analysis

In Section 3.3.2, we calculated the Fourier components of the aligned average pulse profiles. This gave us the relative amplitude of the pulse profile harmonics in each group

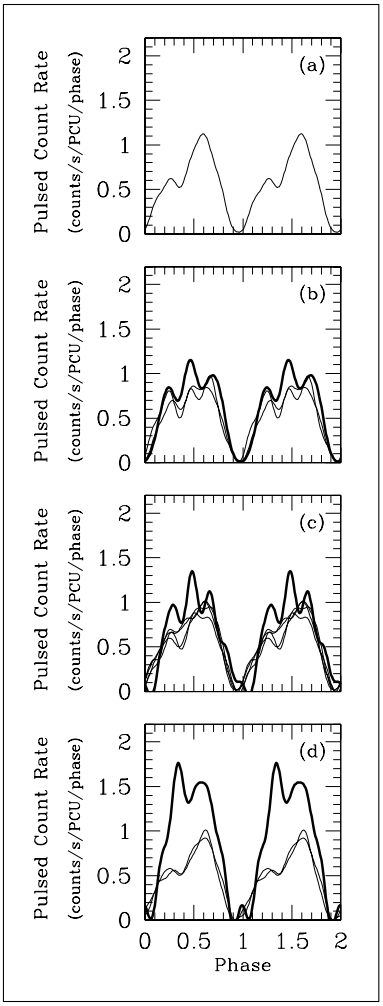

Figure 3.7 Average pulse profile per observation in the 2−10 keV band in several groups of observations reconstructed from the first five Fourier components, and scaled to return the appropriate pulsed flux. *(a)* average scaled pulse profile for observations in *RXTE* Cycle 10, the last *RXTE* Cycle before the active phase. *(b)* Bold curve: scaled pulse profile of the observation containing burst 1. Thin curves: average scaled pulse profile for each of the groups of observations that followed burst 1 (groups G and H in Figure 3.1). *(c)* Bold curve: scaled pulse profile of the observation containing bursts 2, 3, 4, and 5. Thin curves: average scaled pulse profile for each of the groups of observations that followed the bursts (groups I, J, K, and L in Figure 3.1). *(d)* Bold curve: scaled pulse profile of the observation containing burst 6. Thin curves: average scaled pulse profile for each of the groups of observations that followed burst 6 (groups M, and N from Figure 3.1).

of observations marked with a letter in Figure 3.1. In Section 3.3.4, we calculated the pulsed flux for every observation. Here, we compute a weighted average of the pulsed flux for each group of observations using the flux points calculated in Section 3.3.4.

We then reconstruct the profiles for each of the groups from the first five Fourier components (not including the DC), scale them by the average RMS pulsed flux for that group, and add the necessary offset for the lowest point on each curve to be zero. This means that the resulting scaled profiles return the correct pulsed flux. The advantage of this analysis is that we can now trace the evolution of each of the peaks independently.

The results are presented in Figure 3.7. In panel (a), we show the average scaled pulse profile per observation for observations in the year preceding the active phase. The profile is double-peaked. In panel (b), we show in bold the scaled profile for the observation containing burst 1. We also show the scaled profiles in each of the groups of observations that followed the burst. The profiles are triple-peaked. In panel (c), we show in bold the scaled profile for the observation containing bursts 2, 3, 4, and 5. We also show the scaled profiles in each of the groups of observations that followed the bursts. Note how the increase in the pulsed flux in the observation containing the bursts is not only a consequence of the appearance of the new peak, but a result of the increase in size of all three peaks. Also note the evolution of the pulse profile back to being double-peaked. In panel (d), we show in bold the scaled profile for the observation containing burst 6. We also show the scaled profiles in each of the groups of observations that followed the burst. Note again how the pulsed flux increase is due to both peaks increasing in size.

3.3.5 Timing Analysis

Many AXP outbursts and active phases are accompanied by interesting timing anomalies (e.g. Kaspi et al. 2003; Woods et al. 2004; Israel et al. 2007, Chapter 5). Next we consider the timing behaviour of 4U 0142+61, which, as we show, also exhibits interesting evolution at the start of the active phase.

For all our *RXTE* observations of 4U 0142+61, photon arrival times at each epoch were adjusted to the solar system barycenter using the position obtained by Patel et al. (2003) from *Chandra* data. They were then binned with 31.25-ms time resolution. In the timing analysis presented below, we included only the events in the energy range 2.5−9 keV, to maximize the signal-to-noise ratio of the pulse.

Each barycentric binned time series was epoch-folded using an ephemeris determined iteratively by maintaining phase coherence; see below. Resulting pulse profiles, with 64 phase bins, were cross-correlated in the Fourier domain with a high signal-

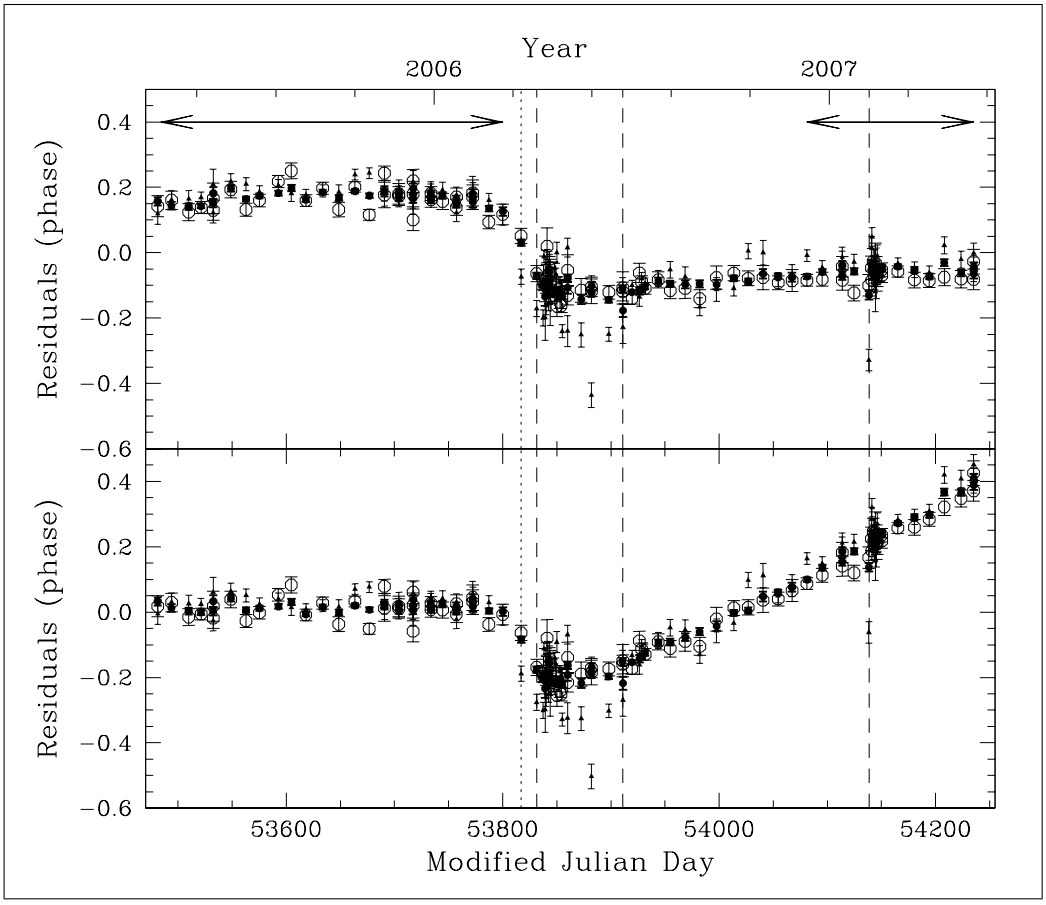

Figure 3.8 Top: Timing residuals for all three sets of TOAs. Bold circles: timing residuals obtained using the first set of TOAs obtained by cross correlation in the Fourier domain. Empty circles: residuals obtained using the second set of TOAs obtained by aligning the off-pulse regions of the pulse profiles. Triangles: residuals obtained using the third set of TOAs obtained by aligning the tallest peak of the pulse profiles. The linear ephemeris used to produce all three sets of residuals is that which best fit the first set of TOAs in the regions indicated with the horizontal arrows (with an arbitrary phase jump in between). Bottom: Timing residuals for the same three sets of TOAs. The linear ephemeris used is that which best fit the first set of TOAs in the pre-active phase region. Both panels: the dotted line indicates the epoch of the first observation of the active phase. The dashed lines indicate the burst epochs.

to-noise template created by adding phase-aligned profiles from all observations. The cross-correlation returned an average pulse time of arrival (TOA) for each observation corresponding to a fixed pulse phase. The pulse phase ϕ at any time t can be expressed as a Taylor expansion,

$$\phi(t) = \phi_0(t_0) + \nu_0(t - t_0) + \frac{1}{2}\dot{\nu}_0(t - t_0)^2 + \frac{1}{6}\ddot{\nu}_0(t - t_0)^3 + \ldots, \qquad (3.3)$$

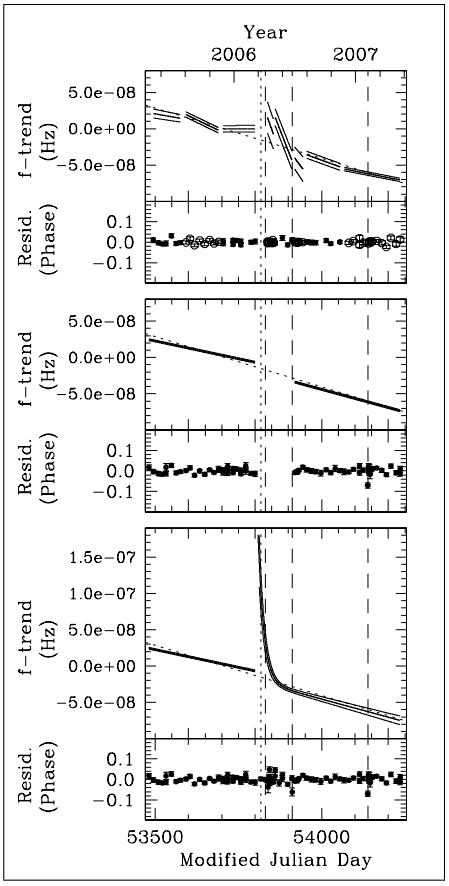

Figure 3.9 Panel 1: Frequency vs. time plot of local linear ephemerides with uncertainties. The linear trend corresponding to the local ephemeris directly before the active phase is subtracted from all local ephemerides. Panel 2: Timing residuals after subtracting the ephemerides shown in panel 1. Panel 3: Frequency vs. time plot (with uncertainties) of the best-fit linear ephemerides in the pre-active phase region and in the post-burst 2 region. The same trend as in panel 1 was subtracted. Panel 4: Timing residuals after subtracting the ephemerides shown in panel 3. Panel 5: Frequency vs. time plot (with uncertainties) of the best-fit long-term ephemeris which includes a glitch at MJD 53809 followed by a fast exponential recovery. The same trend as in panel 1 was subtracted. Panel 6: Timing residuals after subtracting the ephemeris shown in panel 5. All Panels: The dotted line marks the entry into the active phase. The dashed lines mark the burst epochs.

where $\nu \equiv 1/P$ is the pulse frequency, $\dot{\nu} \equiv d\nu/dt$, etc., and subscript 0" denotes a parameter evaluated at the reference epoch $t = t_0$. To obtain ephemerides, the TOAs were fitted to the above polynomial using the pulsar timing software package `TEMPO`[2] (also see Section 1.1.9).

As explained above, our first set of TOAs was obtained by aligning the folded

[2]See http://www.atnf.csiro.au/research/pulsar/tempo.

observations with a template profile using a cross-correlation procedure. In order to determine to what extent this set of TOAs was affected by the pulse profile changes that took place in the active phase, we generated two additional sets of TOAs (sets 2 and 3).

For set 2, we made the assumption that the location of the off-pulse, determined by finding the minimum in the pulse profile after applying Von Mises smoothing (Archibald et al., 2009), is not affected by the pulse profile changes. We then generated TOAs by aligning the off-pulse regions of the folded observations with the off-pulse region of the template and extracting phase differences. The last set of TOAs (Set 3) was obtained after aligning the tallest peak of each smoothed pulse profile with that of the long-term template.

Timing residuals for all three sets of TOAs are shown in Figure 3.8 using two different ephemerides. The linear ephemeris used in the top panel is that obtained by fitting the first set of TOAs in the regions indicated by the horizontal arrows, with a phase jump in between. The linear ephemeris used in the bottom panel is the ephemeris that best fit the first set of TOAs prior to the active phase. The same long-term trend is present in the first two sets of timing residuals, with more scatter in the second set. The difference in phase between each bold circle and the corresponding empty circle represents our uncertainty in determining a fiducial point on the pulsar. In the third set of residuals, the outlier points represent the observations where the largest peak was no longer the right-most peak. Apart from the outliers, the same trend seen in the other two sets of residuals is present in the third set.

From here on, we assume that the presence of the same trend in our three sets of residuals is an indication that the TOAs in the first set were not significantly affected by the pulse profile changes. We therefore have used the first set of TOAs in the remainder of this Section.

Using the above assumption, the results of the timing analysis are shown in Figure 3.9. The results of a segmented timing analysis are in panels 1 and 2. The results of a long-term timing analysis are in panels 3, 4, 5, and 6 of the same Figure.

For the segmented timing analysis, we used the 70 TOAs that had the smallest uncertainties and omitted the TOAs of the 3 burst observations as well as the TOA of the first observation in the active phase. We then divided the data into segments of similar pulse profiles. For each data segment we found a linear ephemeris using `TEMPO`[3]. We plotted the resulting ephemerides in panel 1 of Figure 3.9 with the uncertainties

[3]For the segmented timing analysis we ran `TEMPO` in mode 1.

returned by TEMPO. The timing residuals are shown in panel 2. Notice how the slope between bursts 1 and 2 is more negative than the long-term average.

We then fit a linear trend through all the pre-burst observations, and another linear ephemeris through the post-burst observations after the pulse profile had started to return to the double-peaked shape. We did not include the TOA corresponding to the last observation containing bursts. The results are plotted in panel 3 of Figure 3.9 with uncertainties, with the residuals in panel 4. Notice the difference in the slope in the two regions. In particular, extrapolating the two ephemerides to a point between their times of validity makes it seem like a sudden spin-down, i.e. an "anti-glitch" occurred.

Finally, we included all the TOAs and did one global fit. In order to provide a good fit to the TOAs at the onset of the active phase, we had to assume that a glitch occurred on MJD 53809, with the glitch model consisting of a permanent change in ν and $\dot{\nu}$ and a frequency change $\Delta\nu_d$ that recovered exponentially on a time scale τ_d, i.e.,

$$\nu = \nu_0(t) + \Delta\nu + \Delta\nu_d e^{-(t-t_g)/\tau_d} + \Delta\dot{\nu}\ (t - t_g), \tag{3.4}$$

where $\nu_0(t)$ is the frequency evolution pre-glitch given by $\nu_0(t) = \nu(t_0) + \dot{\nu}(t - t_0)$, $\Delta\nu$ is a instantaneous unrecovered frequency jump, $\Delta\nu_d$ is the frequency increase that decays exponentially on a time scale τ_d, t_g is the glitch epoch determined by setting the phase jump to zero, and $\Delta\dot{\nu}$ is the post-glitch change in the long-term frequency derivative. The values of the fit parameters are listed in Table 3.2.

From Table 3.2, we can see that the total sudden change in frequency which happened at the onset of the active phase ($\Delta\nu_{tot} = \Delta\nu + \Delta\nu_d$) is positive, and $\Delta\nu_d$ decayed exponentially. At the end of the decay, the net effect of the recovered glitch was a negative $\Delta\nu$. That is, the data suggest that after ν_d had decayed, there remained net spin-*down* relative to the undisturbed ephemeris from before the active phase.

The fit parameter $\Delta\nu_d$, from which we conclude a sudden spin-up, is controlled primarily by the first few TOAs in the active phase. It is therefore possible that it is affected by pulse profile changes. However, as shown in Figure 3.8, the TOAs in the active phase were not significantly contaminated by pulse profile changes. Also, the segmented analysis shown in Figure 3.9 clearly indicates an initial spin-up.

In contrast to $\Delta\nu_d$, the fit parameter $\Delta\nu$, from which we conclude a net spin *down*, is primarily controlled by the TOAs outside of the active phase, which were certainly not affected by pulse profile changes (Figure 3.9, panel 3).

Table 3.2. Spin and Glitch Parameters for 4U 0142+61 in the Active Phase[a]

Parameter	Value
MJD start	53481.268
MJD end	54235.319
TOAs	93[b]
ν (Hz)	0.1150920955(12)
$\dot{\nu}$ (10^{-14} Hz s^{-1})	$-2.661(9)$
Epoch (MJD)	53809.185840
Glitch Epoch (MJD)	53809.185840
$\Delta\nu$ (Hz)	$-1.27(17)\times10^{-8}$
$\Delta\dot{\nu}$ (Hz s^{-1})	$-3.1(1.2)\times10^{-16}$
$\Delta\nu_d$ (Hz)	$2.0(4)\times10^{-7}$
t_d (days)	17.0(1.7)
RMS residual (phase)	0.0168

[a]Numbers in parentheses are TEMPO-reported 1σ uncertainties.

[b]A single TOA was omitted due to the very poor signal to noise ratio in the corresponding observation.

We therefore conclude that the pulsar likely suffered a spin-up glitch near or at the start of the radiatively active phase, but that the glitch over-recovered' such that long-term, its net effect is a spin-*down* of the pulsar.

3.4 Discussion

In this paper, we have described the timing, pulse profile, and pulsed flux behaviour of 4U 0142+61, during its 2006-2007 active phase, the first such episode yet studied from this source. Specifically we have shown that in addition to a sudden departure from a slow, systematic evolution of the source's pulsed flux and pulse profile, this AXP also suffered a significant timing event that is best described as a sudden spin-up glitch, followed by a large decay of the frequency jump such that the net effect was a slow-*down* with $\Delta\nu/\nu \simeq -8 \times 10^{-8}$. Interestingly, the pulsed X-ray flux showed no

significant change apart from immediately following bursts, in contrast to other AXP radiative outbursts (e.g. Kaspi et al. 2003; Tam et al. 2008a; Ibrahim et al. 2004; Muno et al. 2007). Further, we have reported on six SGR-like bursts from the source that occurred during this period.

3.4.1 The SGR-Like Bursts from 4U 0142+61

Five of the six bursts reported here for 4U 0142+61 had fast-rise-slow-decay profiles, with tails much longer than the rise times. These morphologies are similar to the class of AXP bursts labeled as "Type B" by Woods et al. (2005). Type B AXP bursts have also been characterized by arriving preferentially at pulse maximum, and are seen more often in AXPs compared with SGRs (Woods et al., 2005; Gavriil et al., 2006a). They were suggested as being due to a sudden rearrangement of magnetic field lines anchored in the crust following a crustal fracture (Thompson & Duncan, 1995b), as opposed to reconnection events in the upper magnetosphere (*e.g.* Lyutikov 2002), argued as more likely for the shorter, symmetric "Type A" bursts that show no preference for pulse maximum. However, it is interesting that in the 4U 0142+61 bursts, in spite of their B-type morphology, no clear preference for arrival at or near pulse maximum was seen (see Figure 3.4). This may blur somewhat the distinction between the putative types, although the morphological distinction remains clear.

It is also notable that the vast majority of bursts seen from three of the four AXPs from which bursts have yet been detected, 1E 1048.1−5937, XTE J1810−197 and now 4U 0142+61, had long tails following fast rises. The exception to-date is 1E 2259+586 for which, during its 2002 outburst, the minority (roughly one dozen out of 80) of the bursts seen were of this form, the majority being of Type A, similar to those classically seen in SGRs, and suggested by Woods et al. (2005) to be magnetospheric. A possible hint regarding the origin of the different types may lie in that 1E 2259+586 was mid-outburst when its bursts were observed, whereas the other sources' bursts all occurred in the days/months following the commencement of an active period, presumably as the pulsar recovered from a major event, rather than mid-event.

3.4.2 The Net Spin-Down Event in 4U 0142+61

The timing glitch reported on in Section 3.3.5 had recovery fraction, defined as $Q \equiv \Delta\nu_d/(\Delta\nu_d + \Delta\nu)$, equal to 1.07 ± 0.02. $Q > 1$ implies that the net frequency change after the transients have decayed is negative (see panel 3 of Figure 3.9 and Table 3.2).

Indeed, the net $\Delta\nu/\nu$ observed is $-1.1 \pm 0.1 \times 10^{-7}$. Such a $Q > 1$ has not previously been reported in any AXP but has been seen following magnetar-like radiative behaviour in one high-B rotation-powered pulsar (Livingstone et al., 2009). Note that Morii et al. (2005) reported a candidate glitch in 1999 from this source. If such a glitch occurred, based on the ephemerides reported in Dib et al. (2007a) (Chapter 2), the fractional frequency change, after any recovery, would have been $+1.9(2)\times10^{-7}$–$8.6(2)\times10^{-7}$ depending on the glitch epoch, but manifestly positive.

In the standard model for glitches in rotation-powered pulsars, the neutron-star crust contains superfluid neutrons that rotate faster than the bulk of the surrounding matter (see Anderson & Itoh 1975; Anderson et al. 1982; Alpar et al. 1984a; Alpar & Pines 1993). This is argued to be a result of the fact that the external magnetic torque acts on the crust and coupled core components only, with the uncoupled superfluid unaffected. The superfluid's angular momentum resides in quantized vortex lines whose density is proportional to angular velocity. The vortex lines are suggested to be pinned to crustal nuclei, and suffer strong forces due to the angular velocity lag that builds between crust and superfluid. A glitch in this picture is a sudden unpinning and outward motion of vortex lines, with a transfer of angular momentum from superfluid to crust. In a magnetar, unpinning may occur due to the strong internal magnetic field as it deforms the crust plastically or cracks it violently (Thompson & Duncan, 1996).

In the 4U 0142+61 event we describe in Section 3.3.5, if the standard glitch model is roughly correct and applies here, then some regions of the stellar superfluid were originally spinning *slower* than the crust. Then the transient increase in frequency would be a result of transfer of angular momentum first from a more rapidly rotating region, with a subsequent angular momentum drain from the crust to a more slowly rotating region. As argued by Thompson et al. (2000), regions of slower-rotating superfluid can occur in magnetars, because the superfluid vortex motions are governed not by spin-down-related forces, but by advection across the stellar surface by the deforming crust. Those authors show that the number of vortex lines per unit surface area of crust can increase or decrease depending on the crustal motion relative to the stellar rotation axis. They invoke this possibility to explain a possible "anti-glitch" seen in SGR 1900+14. However, that event was orders of magnitude larger than what we have observed in 4U 0142+61, with $\Delta\nu/\nu \sim 10^{-4}$ (Thompson et al., 2000), and also was likely associated with the extremely energetic flare seen on 1998 August 27 (Mazets et al., 1999b).

Independent evidence for slow crustal deformations in 4U 0142+61 that could result

in the regions of slower-rotating superfluid required to explain the spin-down may come from the long-term flux and pulse profile evolution previously reported for this source by Dib et al. (2007a) (Chapter 2) and shown again here in Figures 3.6 and 3.2. Although such variations could also be magnetospheric in nature, possibly due to twisting of the magnetic field (*e.g.* Thompson et al. 2002; Beloborodov & Thompson 2007), problems with this interpretation exist, as discussed by Dib et al. (2007a). For example, if magnetospheric, it is puzzling that most if not all of the changes in pulse profile are seen below 4 keV, with none above 6 keV. On the other hand, slow evolution of the surface emission (*e.g.* Özel & Guver 2007), hence structure, is perhaps more consistent with low-energy evolution. It remains to be seen if detailed modeling can reproduce the sort of slow pulse profile changes we have observed, quite apart from the sudden appearance of new peaks, hence greater harmonic structure, near bursts. We note that the latter has also recently been seen during periods of activity in 1E 1048.1−5937 (Tam et al., 2008a).

Previously Kaspi et al. (2000) noted that the existence of AXP glitches having properties comparable to those seen rotation-powered pulsars was not in itself evidence for AXPs being magnetars. This is because the standard glitch model applies regardless of the mechanism by which the crust slows down; in principle a glitch can occur in an accretion-powered neutron star, since in this case too there should develop a crust/superfluid angular velocity lag. However only in the context of magnetars has the possibility of more slowly rotating superfluid been suggested (Thompson et al., 2000). The net spin-down in 4U 0142+61 may thus add to the already large amount of evidence against any accretion-powered origin for 4U 0142+61.

3.4.3 The Active Phase of 4U 0142+61 and Other AXP Outbursts

In many ways, the 2006-2007 active phase of 4U 0142+61 is similar to other phases of activity seen in AXPs: it was punctuated by short bursts, pulse profile changes were seen, and it was accompanied by a significant rotational anomaly. However the 4U 0142+61 activity is unique in one interesting way: the pulsar did not suffer a large, long-lived pulse flux increase at the beginning of the phase. Indeed its pulsed flux (Fig. 3.6), apart from very near bursts, has remained relatively stable. We note that observations with focusing X-ray telescopes may reveal some phase-averaged flux variations (see Gonzalez et al. 2007); indeed pulsed fraction has been shown to be inversely correlated with total flux in 1E 1048.1−5937 (Tiengo et al., 2005; Tam

et al., 2008a), rendering pulsed flux variations smaller relative to total variations. Still, for 4U 0142+61, such a correlation would have to conspire to render the pulsed flux steady. This seems unlikely, however only focusing telescope observations can rule this out.

Other AXP radiative outbursts have been suggested as arising from large magnetospheric twists, with associated magnetospheric currents returning to the stellar surface and heating it, resulting in increased X-ray emission from the source (e.g. Thompson et al. 2002; Beloborodov & Thompson 2007; Beloborodov 2008). Such twists are thought to represent a release of magnetic energy and helicity from the internally wound-up magnetic field.

On the assumption that the pulsed flux is a reasonable proxy for the total flux for 4U 0142+61, here, we find no clear evidence for significantly increased X-ray emission on time scales longer than a few minutes. Thus any large-scale magnetospheric twist scenario is problematic. As originally showed by Thompson et al. (2002), the X-ray luminosity due to returning currents reheating the surface in a significantly twisted magnetosphere in general are comparable to that produced from internal processes; this is clearly not observed in the 2006-7 active period of 4U 0142+61.

Instead, for this source, long-term evolution of the crust, driven presumably internally by field decay, and resulting in multiple unstable configurations though without any large scale magnetospheric twists, could result in sudden cracking and local rearrangements. This could be accompanied by bursts and profile changes, as well as with vortex line shifting. Why such surface motion does not produce significant magnetospheric twists is, however, puzzling, given that field lines are thought to be anchored in the crust; perhaps only for large motions do field lines become sufficiently twisted for enhanced X-ray emission to be produced.

Dib et al. (2008a) showed that other AXP glitches have been unaccompanied by radiative changes. For example, AXP 1E 1841−045 has glitched multiple times yet its pulsed flux remains very steady. Such radiatively "silent" glitches may be a result of internal activity that does not result in significant twisting of outer magnetosphere field lines, where as radiatively 'loud" glitches could be those for which the magnetosphere is impacted. We note in fact that thus far, the data are consistent with *all* AXP radiative outbursts being accompanied by timing anomalies. This may also be true of SGRs, though in those cases, timing anomalies are harder to establish because of the difficulty in achieving phase-coherent timing in quiescence.

3.5 Summary and Conclusions

We have reported on anomalous X-ray pulsar 4U 0142+61 entering an active phase which was preceded by a long-term increase in pulsed flux. The active phase, which commenced in 2006 March, consisted of a timing anomaly that can be described as a net "anti-glitch", that is, a net spin-down following an initial spin-up that decayed on a time scale of 17 days. Following the glitch, we detected six bursts from the pulsar, the first ever observed from this source. Despite 10 yr of *RXTE* monitoring, the bursts all occurred in the narrow time span between 2006 April 6 and 2007 February 7. The pulse profile of the source changed from double- to triple- peaked near the bursts, and underwent considerable evolution otherwise. At the burst epochs the relative intensity of the three peaks significantly varied. The pulse profile is now relaxing to its pre-active phase morphology. Most aspects of 4U 0142+61's emission changed during the active phase, with the notable exception of the pulsed flux (except near bursts). This argues against this event being associated with a sudden magnetospheric twist, as has been invoked for other AXP activity, and is suggestive of crustal evolution driven internally by the large magnetic field, though without significant magnetospheric twisting. We suggest that other, radiatively silent AXP glitches have a similar origin, whereas radiatively loud AXP timing events occur when the crustal motions cannot avoid significant twisting of the magnetic field lines.

Chapter 4

Glitches in the Anomalous X-ray Pulsars RXS J170849.0−400910 and 1E 1841−045

This chapter is based on the manuscript "Glitches in Anomalous X-Ray Pulsars", published in *the Astrophysical Journal* in 2008 February (reference: Dib, Kaspi, & Gavriil, 2008a). In the manuscript, we conduct a long-term study of two sources: RXS J170849.0−400910 and 1E 1841−045. For RXS J170849.0−400910, 2 glitches had been reported in the past. We report on one new glitch and on three possible (candidate) glitches. For 1E 1841−045, we report on 3 large glitches. We also study the pulsed flux evolution and the pulse profile evolution of the two sources, from 1998 to 2007. The original abstract and a few additional notes are below.

We report on 8.7 and 7.6 yr of *Rossi X-ray Timing Explorer (RXTE)* observations of the Anomalous X-ray Pulsars (AXPs) RXS J170849.0−400910 and 1E 1841−045, respectively. These observations, part of a larger *RXTE* AXP monitoring program, have allowed us to study the long-term timing, pulsed flux, and pulse profile evolution of these objects. We report on four new glitches, one from RXS J170849.0−400910 and three from 1E 1841−045. One of the glitches from 1E 1841−045 is among the largest ever seen in a neutron star in terms of fractional frequency increase. With nearly all known persistent AXPs now seen to glitch, such behaviour is clearly generic to this source class. We show that in terms of fractional frequency change, AXPs are

among the most actively glitching neutron stars, with glitch amplitudes in general larger than in radio pulsars. However, in terms of absolute glitch amplitude, AXP glitches are unremarkable. We show that the largest AXP glitches observed thus far have recoveries that are unusual among those of radio pulsar glitches, with the combination of recovery time scale and fraction yielding changes in spin-down rates following the glitch similar to, or larger than, the long-term average. We also observed a large long-term fractional increase in the magnitude of the spin-down rate of 1E 1841−045, following its largest glitch, with $\Delta\dot{\nu}/\dot{\nu} = 0.1$. These observations are challenging to interpret in standard glitch models, as is the frequent occurrence of large glitches given AXPs' high measured temperatures. We speculate that the stellar core may be involved in the largest AXP glitches. Furthermore, we show that AXP glitches appear to fall in two classes: radiatively loud and radiatively quiet. The latter, of which the glitches of RXS J170849.0−400910 and 1E 1841−045 are examples, show little evidence for an accompanying radiative event such as a sudden flux increase or pulse profile change. We also show, however, that pulse profile and pulsed flux changes are common in these AXPs, but do not appear closely correlated with any timing behaviour.

Additional Notes:

- In RXS J170849.0−400910, The last of the three glitch candidates was very close to the end of the data set, making the glitch parameters uncertain. Moreover, timing events similar to this glitch occurred in the subsequent months suggesting that glitch candidate was an episode of large timing noise rather than a glitch.

- In this manuscript we reported two possible sets of parameters for the first glitch from 1E 1841−045. After the publication, and with the help of additional data from *XMM*, we were able to determine that the timing solution that we reported as less likely was the correct one. For a revised analysis of this glitch, see Chapter 6.

- A fourth glitch from 1E 1841−045 was discovered the year after the publication of the manuscript, and is discussed in a later chapter.

4.1 Introduction

The past decade has seen significant progress in our knowledge of the observational properties of Anomalous X-ray Pulsars (AXPs, see Woods & Thompson 2006 and Kaspi 2007 for reviews; also see Section 1.2.3 and Appendix C). From a timing point of view, the presence of binary companions has been practically ruled out (Mereghetti et al., 1998; Wilson et al., 1999), and subsequently their potential for great rotational stability was demonstrated (Kaspi et al., 1999), thereby allowing the discovery that AXPs can exhibit spin-up glitches (Kaspi et al., 2000; Kaspi & Gavriil, 2003; Dall'Osso et al., 2003), and large (factor of $\sim$10) torque variations (Gavriil & Kaspi, 2004). From a radiative point of view, AXPs are now known to show a variety of different variability phenomena, including long-lived flares (Gavriil & Kaspi, 2004), short SGR-like bursts (Gavriil et al., 2002, 2004; Woods et al., 2005), large outbursts (Kaspi et al. 2003; Ibrahim et al. 2004; Israel et al. 2007; Dib et al. 2007b; Tam et al. 2006; Tam et al. 2008a), and slow, low-level flux and pulse profile variability (Dib et al. 2007a; Gonzalez et al. 2007). Spectrally, though previously studied only in the soft X-ray band, AXPs are now seen in the radio band (Camilo et al., 2006), through the mid- (Wang et al., 2006) and near-IR (e.g., Israel et al., 2002; Wang & Chakrabarty, 2002; Hulleman et al., 2004; Tam et al., 2004; Rea et al., 2004a; Durant & van Kerkwijk, 2005), in the optical range (e.g., Kern & Martin, 2002; Dhillon et al., 2005), up to hard X-ray energies (Kuiper et al., 2006). The evidence thus far argues strongly that AXPs, like their close cousins, the Soft Gamma Repeaters, are magnetars – young, isolated neutron stars powered by a large magnetic energy reservoir, with surface fields of $> 10^{14} - 10^{15}$ G (Thompson & Duncan, 1996; Thompson et al., 2002).

In spite of this progress, however, many aspects of AXPs remain mysterious. Particularly so are their variability properties. What is the origin of the variety of different types of variability? Although bursts can be explained as sudden crustal yields, slower evolution (e.g., Gavriil & Kaspi, 2004; Dib et al., 2007a) has been suggested to be due to slow magnetospheric twists (Thompson et al., 2002). Some support for this picture has been argued to come from observed correlations between flux and spectral hardness (Woods et al., 2004; Rea et al., 2005; Campana et al., 2007), although Özel & Guver (2007) argue that such a correlation need not originate uniquely from the magnetosphere and could be purely thermal. At least some radiative variability has been seen to be correlated with timing behaviour. The best example of this occurred in the 2002 outburst of AXP 1E 2259+586 in which the pulsar suffered

a large spin-up glitch apparently simultaneously with a major X-ray outburst (Kaspi et al., 2003; Woods et al., 2004). Israel et al. (2007) describe a similar radiative outburst in AXP CXOU J164710.2−455216, and report a large contemporaneous glitch, as did Dib et al. (2007b) recently for AXP 1E 1048.1−5937. By contrast, AXP RXS J170849.0−400910 exhibited two glitches with no evidence for a corresponding radiative event (Kaspi et al., 2000; Kaspi & Gavriil, 2003) although Dall'Osso et al. (2003) suggested possible low-level pulse profile changes associated with the second glitch. Campana et al. (2007) also suggested that observed flux and spectral changes may be associated with glitches and predicted a third glitch would be observed after mid-2005 on the basis of an observed flux increase and apparently correlated spectral changes.

Here we report on 8.7 and 7.6 yr of monitoring of RXS J170849.0−400910 and 1E 1841−045, respectively, using the Proportional Counter Array (PCA) aboard the *Rossi X-ray Timing Explorer* (*RXTE*). See Appendix C for details about the two sources. We report the discovery of one new glitch and three new glitch candidates in RXS J170849.0−400910 as well as three new glitches in 1E 1841−045, including one of the largest glitches, in terms of fractional frequency increase, thus far observed in any neutron star. We also present pulsed flux time series for RXS J170849.0−400910 and 1E 1841−045 which reveal little or no evidence for correlated changes with glitches, although RXS J170849.0−400910 shows low-level pulsed flux variability at many epochs. We also report a pulse profile evolution analysis which shows that both pulsars' profiles are evolving slowly with time, though in neither case does this evolution show a clear correlation with timing behaviour. These results demonstrate that AXPs RXS J170849.0−400910 and 1E 1841−045 are frequent glitchers. They also demonstrate that although AXP timing glitches can occur simultaneously with significant long-lived radiative enhancements, they need not always do so.

4.2 Observations

The results presented here were obtained using the PCA on board *RXTE* (see Section 1.4). Our 294 observations of RXS J170849.0−400910 and our 136 observations of 1E 1841−045 are of various lengths (see Tables 4.1 and 4.2). Most were obtained over a period of several years as part of a long-term monitoring program, but some are isolated observations (see Figures 4.1 and 4.2).

For the monitoring, we used the `GoodXenonwithPropane` data mode except during

Table 4.1. Summary of *RXTE* Observations of RXS J170849.0−400910

Obs. Cycle	Typical Exp.[a] (ks)	Typical Separation[a] (days)	No. of Obs.[b]	Total Exp.[c] (ks)	First – Last MJD[d]	First Date – Last Date
3	2.5	15	29	75	50825.7−51186.7	01/12/1998−01/08/1999
4	3	24	20	60	51215.7−51614.1	02/06/1999−03/11/2000
5	3	24	13	40	51655.7−52041.5	04/21/2000−05/12/2001
6	3	29	13	40	52049.5−52325.6	05/20/2001−02/20/2002
7	5.5	23	12	65	52366.5−52718.7	04/02/2002−03/20/2003
8	1.8	5	58	105	52745.7−53058.6	04/16/2003−02/23/2004
9	2	5	70	135	53063.1−53429.1	02/28/2004−02/28/2005
10	2	8	47	90	53435.1−53791.6	03/06/2005−02/25/2006
11[e]	2	7	32	60	53799.0−54015.4	03/05/2006−10/07/2006

[a]The exposure and separation are approximate. Note that the PCA effective area changed with time primarily due to the reduction of the a average number of PCUs operational during an integration. This effect is not incorporated in the tabulated integration times.

[b]When the last digits of the observation ID of two successive data sets are different, the two data sets are considered separate observations.

[c]The total exposure does not include Earth occultation periods.

[d]First MJD and Last MJD are the epochs, in Modified Julian Days, of the first and the last observations in a Cycle.

[e]Cycle 11 was not completed when this manuscript was published.

Table 4.2. Summary of *RXTE* Observations of 1E 1841−045

Obs. Cycle	Typical Exp.[a] (ks)	Typical Separation[a] (days)	No. of Obs.[b]	Total Exp.[c] (ks)	First – Last MJD[d]	First Date – Last Date
4	4.5	27	26	120	51224.4−51597.3	02/15/1999−02/23/2000
5	4.5	38	16	70	51644.7−51976.9	04/10/2000−03/08/2001
6	7	27	8	50	52001.6−52300.1	04/02/2001−01/26/2002
7	12	45	7	80	52349.8−52666.0	03/16/2002−01/27/2003
8	4.5	20	17	80	52726.8−53052.9	03/28/2003−02/17/2004
9	4.5	20	19	80	53073.7−53413.3	03/09/2004−02/12/2005
10	5	14	31	130	53440.0−54153.9	03/11/2005−02/22/2007
11[e]	5	14	12	60	53800.9−53970.6	03/06/2006−08/23/2006

[a]The exposure and separation are approximate. Note that the PCA effective area changed with time primarily due to the reduction of the a average number of PCUs operational during an integration. This effect is not incorporated in the tabulated integration times.

[b]When the last digits of the observation ID of two successive data sets are different, the two data sets are considered separate observations.

[c]The total exposure does not include Earth occultation periods.

[d]First MJD and Last MJD are the epochs, in Modified Julian Days, of the first and the last observations in a Cycle.

[e]Cycle 11 not yet completed.

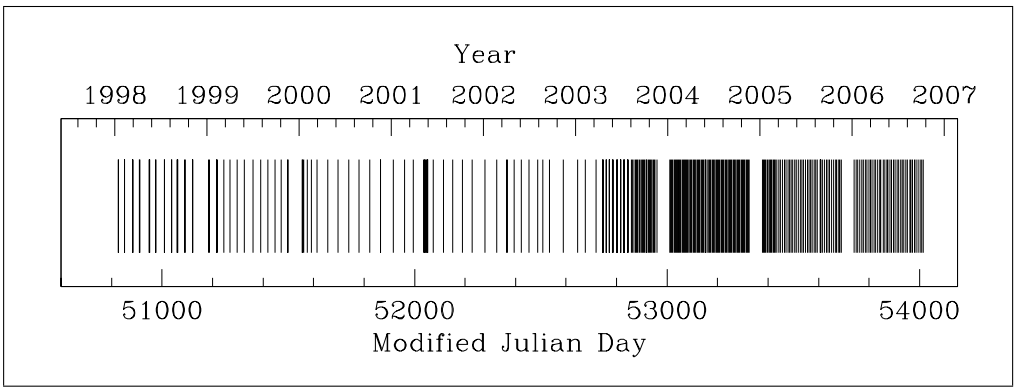

Figure 4.1 Epochs of observations of RXS J170849.0−400910 with *RXTE*. Gaps near the end/start of each year are due to Sun avoidance. See Table 4.1 for details.

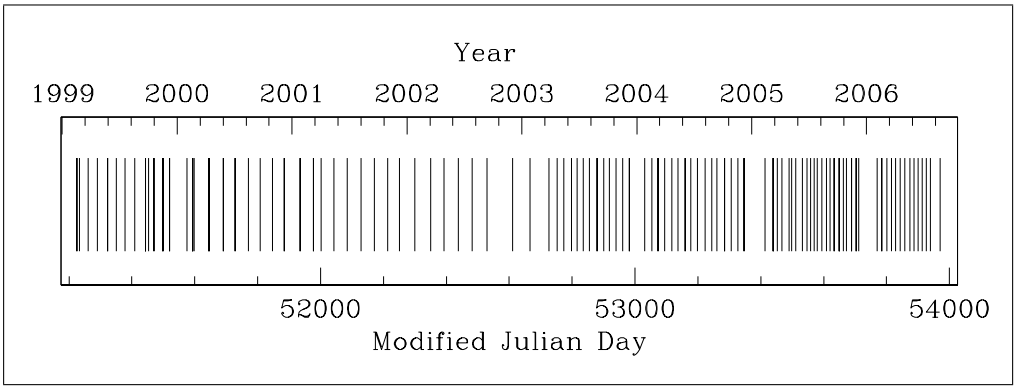

Figure 4.2 Epochs of observations of 1E 1841−045 with *RXTE*. Gaps near the end/start of each year are due to Sun avoidance. See Table 4.2 for details.

Cycles 10 and 11 when we used the `GoodXenon` mode. Both data modes record photon arrival times with 1-μs resolution and bin photon energies into one of 256 channels. To maximize the signal-to-noise ratio, we analysed only those events from the top xenon layer of each PCU.

4.3 Phase-Coherent Timing

Photon arrival times at each epoch were adjusted to the solar system barycenter. Resulting arrival times were binned with 31.25-ms time resolution. In the RXS J170849.0−400910 timing analysis, we included only events in the energy range 2−6 keV, to maximize the signal-to-noise ratio of the pulse. Similarly, for 1E 1841−045 we included events in the energy range 2−11 keV.

Each barycentric binned time series was folded using an ephemeris determined iter-

atively by maintaining phase coherence as we describe below. Resulting pulse profiles, with 64 phase bins, were cross-correlated in the Fourier domain with a high signal-to-noise template created by adding phase-aligned profiles from all observations. The cross-correlation returned an average pulse time of arrival (TOA) for each observation corresponding to a fixed pulse phase. The pulse phase ϕ at any time t can usually be expressed as a Taylor expansion,

$$\phi(t) = \phi_0(t_0) + \nu_0(t - t_0) + \frac{1}{2}\dot{\nu}_0(t - t_0)^2 + \frac{1}{6}\ddot{\nu}_0(t - t_0)^3 + \ldots, \qquad (4.1)$$

where $\nu \equiv 1/P$ is the pulse frequency, $\dot{\nu} \equiv d\nu/dt$, etc., and subscript "0" denotes a parameter evaluated at the reference epoch $t = t_0$. The TOAs were fitted to the above polynomial using the pulsar timing software package `TEMPO`[1] (also see Section 1.1.9).

Note that we also searched for X-ray bursts in each 2–20 keV barycentered, binned time series using the methods described in Gavriil et al. (2004), however no bursts were found in any of our RXS J170849.0−400910 or 1E 1841−045 data sets.

4.3.1 Timing Results for RXS J170849.0−400910

Figure 4.3 and Table 4.3 summarize our results for RXS J170849.0−400910. The pulsar's spin evolution can be characterized by steady spin-down, punctuated by sudden episodes of spin-up, i.e., glitches, in addition to candidate glitch events and apparently random noise. We provide in Table 4.3 pulse ephemerides for inter-glitch ranges labelled as in the top panel of Figure 4.3. Residuals after subtraction of these models are shown in the next panel of Figure 4.3. Overall the models describe the data well. However, particularly when our timing precision was highest (i.e., before 2003), some low-level but significant deviations are seen on time scales of weeks to months. Their origin is unknown but is likely related to "timing noise," commonly seen in other AXPs (e.g., Kaspi et al., 1999; Gotthelf et al., 2002) and ubiquitously in radio pulsars (e.g., Arzoumanian et al., 1994; Hobbs et al., 2004; Livingstone et al., 2005). Note that Dib et al. (2007a) performed simulations which showed that pulse profile changes similar to those observed in this source (see Section 4.4.1) did not result in timing offsets significantly larger than our reported TOA uncertainties. Hence, the features in the timing residuals reported here are not a result of pulse profile changes.

In addition to the two previously reported glitches (which we have reanalysed, finding results consistent with those already in the literature; see Kaspi et al. 2000;

[1]See http://www.atnf.csiro.au/research/pulsar/tempo.

Table 4.3. Long-Term Spin Parameters for RXS J170849.0−400910[a]

Parameter	Ephemeris A Spanning MJD 50826−51418	Ephemeris B Spanning MJD 51446−51996	Ephemeris C Spanning MJD 52036−52960	Ephemeris D Spanning MJD 53010−53325	Ephemeris E Spanning MJD 53377−53548	Ephemeris F Spanning MJD 53556−53631	Ephemeris G Spanning MJD 53638−54015
MJD start	50826.078	51446.610	52035.655	53010.094	53377.133	53555.734	53638.033
MJD end	51418.374	51995.680	52960.186	53325.061	53547.811	53631.161	54015.487
TOAs	39	19	74	69	29	13	49
ν (Hz)	0.090913818(2)	0.090906071(3)	0.090906089(3)	0.090892731(13)	0.090887608(18)	0.090885281(8)	0.090884082(9)
$\dot{\nu}$ (10^{-13} Hz s^{-1})	−1.583(3)	−1.574(2)	−1.565(6)	−1.40(5)	−1.19(8)	−1.70(2)	−1.58(3)
$\ddot{\nu}$ (10^{-22} Hz s^{-2})	−1.4(3)	0.36(9)	−8.9(1.8)	−44(11)	−131(23)	–	−8(7)
$d^3\nu/dt^3$ (10^{-28} Hz s^{-3})	−0.056(9)	–	1.5(3)	5.5(1.6)	15(3)	–	1.4(9)
$d^4\nu/dt^4$ (10^{-35} Hz s^{-4})	–	–	−1.4(3)	−3.1(1.0)	–	–	−0.8(6)
$d^5\nu/dt^5$ (10^{-43} Hz s^{-5})	–	–	7.4(1.5)	–	–	–	–
$d^6\nu/dt^6$ (10^{-50} Hz s^{-6})	–	–	−1.8(4)	–	–	–	–
$\Delta\nu_d$[b](Hz)	–	–	$36(3)\times10^{-08}$	–	–	–	–
t_d[b](days)	–	–	43(2)	–	–	–	–
Epoch (MJD)	51445.3846	52016.48413	52016.48413	52989.8475	53366.3150	53549.15095	53635.6772
RMS residual (phase)	0.0079	0.0150	0.0154	0.0132	0.0142	0.0112	0.0154

[a]Numbers in parentheses are TEMPO-reported 1σ uncertainties.

[b]Parameters held fixed at values determined from local glitch fits as shown in Table 4.4.

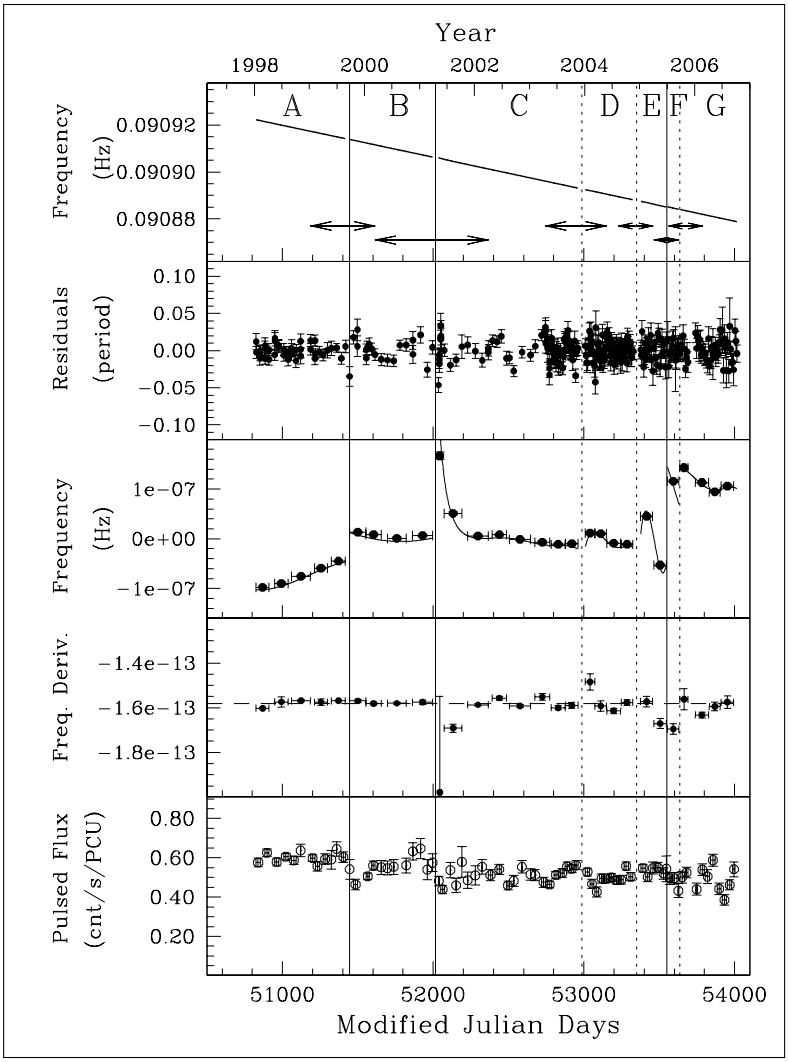

Figure 4.3 Spin and pulsed flux evolution in RXS J170849.0−400910. Panels are described from top to bottom. *Top:* Frequency evolution, with inter-glitch intervals indicated for correspondence with ephemerides given in Table 4.3. Arrows indicate intervals for which glitch ephemerides were obtained (see Table 4.4). *Next:* residuals, after subtraction of the best-fit models given in Table 4.3 (with arbitrary inter-interval phase offsets subtracted). The increased scatter after MJD 52600 is due to a decrease in typical integration time and an increase in monitoring frequency. *Next:* Solid curve: frequency evolution of the models shown in Table 4.3 after removal of the linear trend defined by the frequency and frequency derivative from interval C as measured by fitting only those parameters. Data points: measured frequencies in independent sub-intervals after subtraction of the extrapolation of the same linear trend. *Next:* Evolution of the frequency derivative in sub-intervals, when fitting locally for only ν and $\dot{\nu}$. *Bottom:* Pulsed flux in the 2–10 keV range. *All panels:* Unambiguous glitch epochs are indicated with solid vertical lines. Candidate glitch epochs are indicated with dashed vertical lines.

Kaspi & Gavriil 2003; Dall'Osso et al. 2003), we have identified a third unambiguous glitch that occurred near MJD 53551 (2005 June 30). Note that the exact glitch epoch is unknown due to our non-continuous monitoring; we report an epoch for which the phase jump is zero. This is because a non-zero phase jump at the time of the glitch would suggest an unphysically large torque on the star. This third glitch had fractional frequency jump $\Delta\nu/\nu = 2.7 \times 10^{-6}$, and no obvious recovery. This glitch amplitude is intermediate between those of the previous two observed glitches, and the lack of recovery is similar to what was seen in the first glitch, but in marked contrast with the second glitch, as is clear from Figure 4.4. A sudden change in post-glitch spin-down rate for the third glitch is difficult to constrain, because of a possible additional glitch that occurred not long after, as we describe below. Indeed glitch-induced long-term changes in $\dot{\nu}$ aside from that following the first glitch, as described by Kaspi et al. (2000), are difficult to identify given the apparent timing noise processes. Table 4.4 summarizes the parameters of the three certain glitches of RXS J170849.0−400910, assuming a glitch model consisting of a permanent change in ν and $\dot{\nu}$ and a frequency change ν_d that decayed on a time scale of τ_d, i.e.,

$$\nu = \nu_0(t) + \Delta\nu + \Delta\nu_d e^{-(t-t_g)/\tau_d} + \Delta\dot{\nu}\ (t - t_g), \tag{4.2}$$

where $\nu_0(t)$ is the frequency evolution pre-glitch, $\Delta\nu$ is a instantaneous frequency jump, $\Delta\nu_d$ is the post-glitch frequency increase that decays exponentially on a time scale τ_d, t_g is the glitch epoch, and $\Delta\dot{\nu}$ is the post-glitch change in the long-term frequency derivative.

For the second glitch, residuals after subtraction of a simple glitch model with fractional exponential recovery have clear remaining trends, as is clear in Figures 4.3 (second panel) and 4.4 (bottom panel). Systematic trends after simple glitch model subtraction were also reported by Woods et al. (2004) for the 2002 glitch in 1E 2259+586. We also find this in the largest glitch in 1E 1841−045 (see Section 4.3.2). Woods et al. (2004) showed that for 1E 2259+586, the glitch fit was significantly improved by adding an exponential growth term. We have tried fitting this model to the second glitch from RXS J170849.0−400910 but find no improvement, with the preferred growth term consistent with zero.

In addition to the new certain glitch we report above, we find strong evidence for an additional three glitches, each having fractional amplitude similar to the first certain glitch seen in this source. The properties of these candidate glitches are summarized in

Table 4.4. Local Ephemerides of RXS J170849.0−400910 Near Glitch Epochs[a]

Parameter	Ephemeris Near Glitch 1	Ephemeris Near Glitch 2	Ephemeris Near Glitch 3
MJD range	51186.503−51614.187	51614.185−52366.663	53465.392−53631.161
TOAs	22	29	26
Epoch (MJD)	51445.3846	52016.48413	53549.15095
ν (Hz)	0.090913822(2)	0.090906068(2)	0.090885035(9)
$\dot{\nu}$ (10^{-13} Hz s^{-1})	−1.5714(14)	−1.5797(11)	−1.67(2)
Glitch Epoch (MJD)	51445.3846	52016.48413	53549.15095
$\Delta\nu$ (Hz)	$5.1(3)\times10^{-8}$	$2.2(4)\times10^{-8}$	$24.6(9)\times10^{-8}$
$\Delta\dot{\nu}$ (Hz s^{-1})	$-0.8(4)\times10^{-15}$	$-1.1(2)\times10^{-15}$	$-2(2)\times10^{-15}$
$\Delta\nu_d$ (Hz)	–	$36(3)\times10^{-8}$	–
t_d (days)	–	43(2)	–
RMS residual (phase)	0.0102	0.0193	0.0140

[a]Numbers in parentheses are TEMPO-reported 1σ uncertainties.

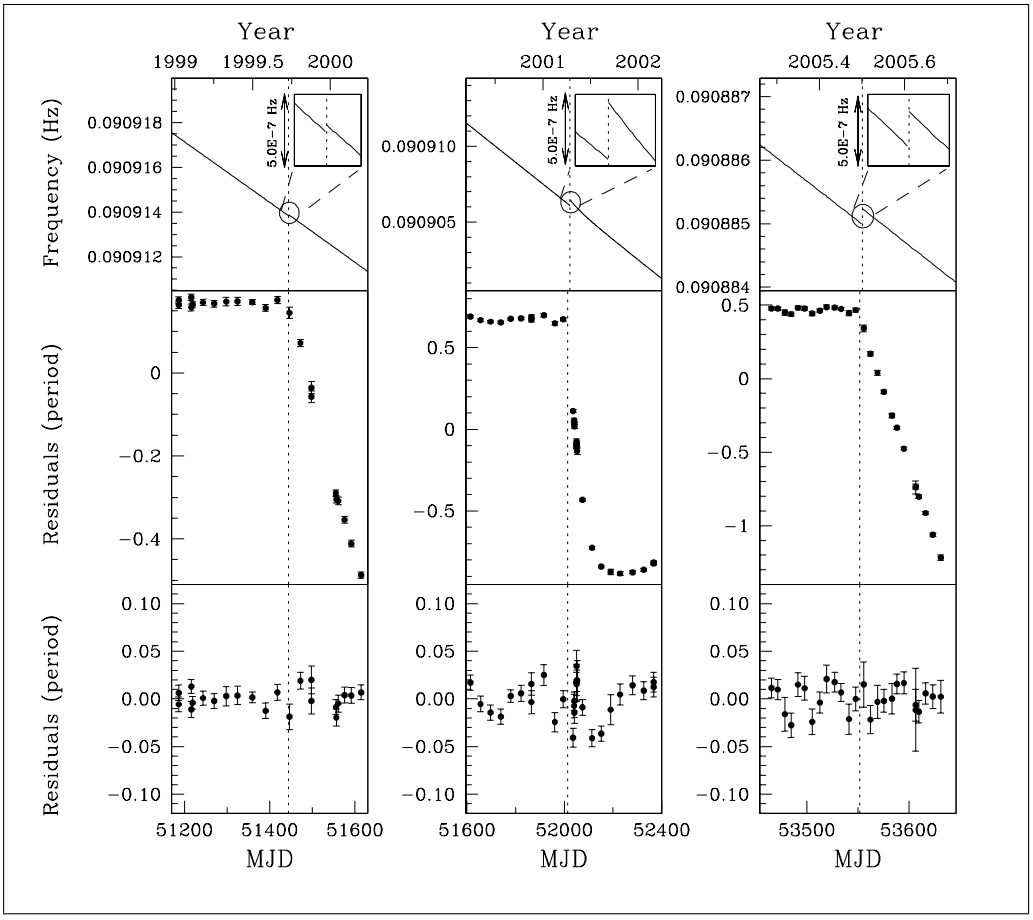

Figure 4.4 The three unambiguous glitches observed in RXS J170849.0−400910. *Top panels:* Frequency evolution around glitch as determined from ephemerides in Table 4.4, with the blow-up inset displaying glitch amplitude on a common scale for comparison. *Middle panels:* Residuals after subtraction of the best-fit pre-glitch ephemeris given in Table 4.4. *Bottom panels:* Residuals after subtraction of best-fit glitch models given in Table 4.4. *All panels:* Dashed vertical lines indicate assumed glitch epochs.

Table 4.5. Timing residuals around the epochs of these glitches are shown in Figure 4.5, in the top panel. Residuals following the subtraction of a glitch model are shown in the middle panel of that Figure. We refer to these as candidates only because a 4-th order polynomial fit to the same data results in similar residuals (bottom panel of Fig. 4.5; Table 4.6) without the need to invoke a sudden event. The distinction between true glitches and timing noise is often difficult to make for small-amplitude glitches, as discussed by Kaspi et al. (2000). One way to distinguish, at least statistically, is that apparent discontinuities attributable to timing noise should not have a preferential direction, i.e., apparent spin-down 'glitches' should be seen too. An examination of the frequency panel in Figure 4.3 reveals apparent frequency jumps at the candidate

glitch levels in both directions, suggesting one or more of the candidates could indeed be timing noise. Continued monitoring to acquire a larger database of such apparent discontinuities will help clarify this issue.

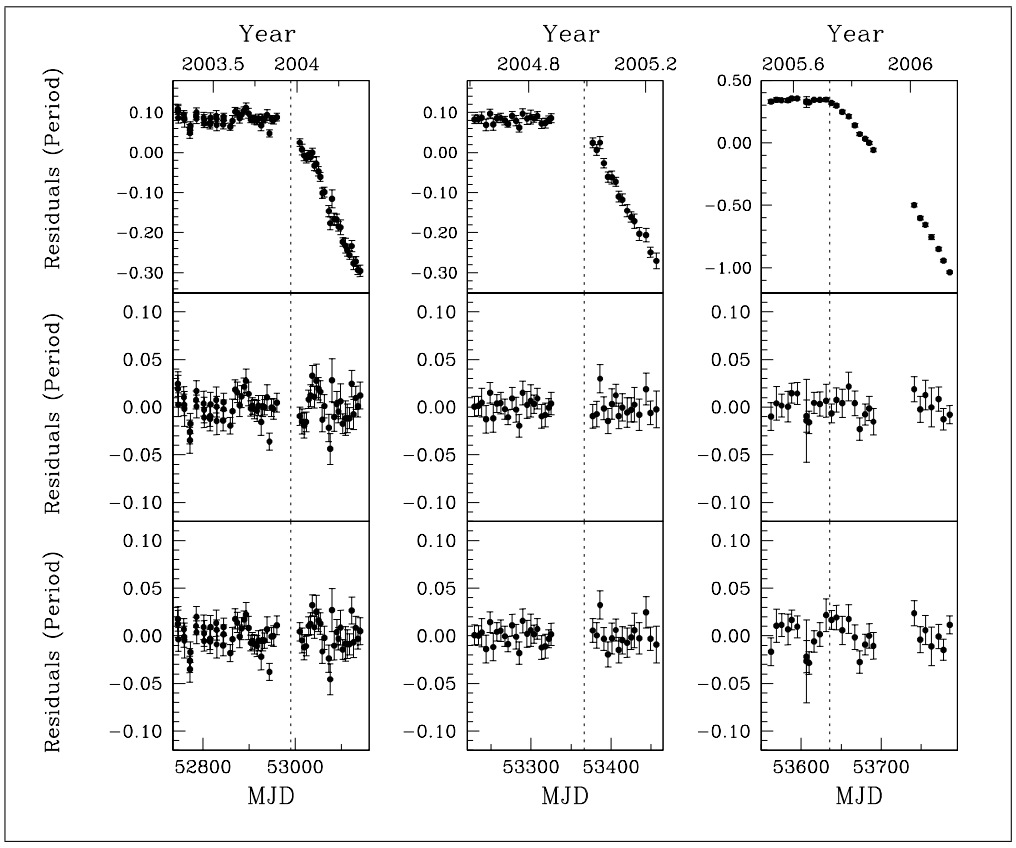

Figure 4.5 The three candidate glitches in RXS J170849.0−400910. *Top panels:* Residuals after subtraction of best-fit pre-'glitch' ephemeris given in Table 4.5. *Middle panels:* Residuals after subtraction of best-fit glitch models given in Table 4.5. *Bottom panels:* Residuals after subtraction of best-fit alternative models given in Table 4.6. *All panels:* Dashed vertical lines indicate assumed glitch epochs.

Subsequent to our submission and posting of this paper, Israel et al. (2007) posted the results of a similar analysis of a subset of these same data. Some of their results are consistent with ours, however others differ. They reported two glitches, the first of which corresponds to our second candidate glitch (Table 4.5). For that glitch, the reported fit parameters are similar though not identical to ours. Their second glitch corresponds to our third glitch in Table 4.4. For that glitch, the reported frequency jump at the glitch epoch was similar to ours but the jump in frequency derivative was significantly different. We find that this difference is due to their inclusion of more post-glitch TOAs when fitting the glitch. We did not include these TOAs because

Table 4.5. Local Ephemerides of RXS J170849.0−400910 Near Candidate Glitch Epochs[a]

Parameter	Ephemeris Near Candidate 1	Ephemeris Near Candidate 2	Ephemeris Near Candidate 3
MJD range	52745.790−53140.604	53229.271−53456.688	53562.209−53785.652
TOAs	78	38	28
Epoch (MJD)	529898475	53366.3150	53635.6772
ν (Hz)	0.0908927493(18)	0.090887617(5)	0.090884020(8)
$\dot{\nu}$ (10^{-13} Hz s^{-1})	−1.5842(15)	−1.570(7)	−1.67(2)
Glitch Epoch (MJD)	529898475	53366.3150	53635.6772
$\Delta\nu$ (Hz)	$2.8(4)\times10^{-8}$	$5.2(6)\times10^{-8}$	$6.7(3)\times10^{-8}$
$\Delta\dot{\nu}$ (Hz s^{-1})	0[b]	$-1.9(1.3)\times10^{-15}$	$6.0(5)\times10^{-15}$
$\Delta\nu_d$ (Hz)	–	–	–
t_d (days)	–	–	–
RMS residual (phase)	0.0153	0.0099	0.0110

[a]Numbers in parentheses are TEMPO-reported 1σ uncertainties.

[b]Entries with the value '0' are consistent with being zero.

Table 4.6. Alternate Ephemerides of RXS J170849.0−400910 Near Candidate Glitch Epochs[a]

Parameter	Ephemeris Near Candidate 1	Ephemeris Near Candidate 2	Ephemeris Near Candidate 3
MJD range	52745.790−53140.604	53229.271−53456.688	53562.209−53785.652
TOAs	75	38	28
Epoch (MJD)	52989.8475	53366.3150	53635.6772
ν (Hz)	0.0908928173(6)	0.0908876402(13)	0.090884059(2)
$\dot{\nu}$ (10^{-13} Hz s^{-1})	−1.556(3)	−1.492(6)	−1.485(16)
$\ddot{\nu}$ (10^{-22} Hz s^{-2})	1.2(4)	4(2)	0[b]
$d^3\nu/dt^3$ (10^{-28} Hz s^{-3})	−0.66(16)	−6.6(1.4)	−19(4)
$d^4\nu/dt^4$ (10^{-35} Hz s^{-4})	−1.0(4)	−18(6)	52(12)
RMS residual (phase)	0.0146	0.0106	0.0152

[a]Numbers in parentheses are TEMPO-reported 1σ uncertainties.

[b]Entries with the value '0' are consistent with being zero.

of a candidate event that occurs shortly thereafter, but which Israel et al. did not report. In addition to this difference, the frequency value reported in their post-glitch ephemeris was initially 42σ away from the value that we measure at the same epoch using our post-glitch ephemeris. This was due to a typographical error which was fixed in a later version of their article.

4.3.2 Timing Results for 1E 1841−045

Figure 4.6 and Table 4.7 summarize the long-term timing behaviour of 1E 1841−045. As for RXS J170849.0−400910, the spin evolution of 1E 1841−045 is well characterized by regular spin-down punctuated by occasional sudden spin-up events, plus timing noise. Ephemerides in Table 4.7 are given for the glitch-free intervals indicated in the top panel of Figure 4.6. As for RXS J170849.0−400910, the long-term timing residuals show some unmodelled trends whose origin is unknown. We consider these trends timing noise, as did Gotthelf et al. (2002) in their analysis of ∼2 yr of data from this object. Note that the ephemeris in Table 4.7 labeled B2 is the same as that labeled B except for the omission of data immediately post-glitch (see caption to Fig. 4.6).

The frequency panel in Figure 4.6 and first panel in Figure 4.7 make clear that 1E 1841−045 suffered a large glitch, with significant recovery, near MJD 52460 (2002 July 5). This epoch is estimated, as for all glitches reported in this paper, by taking the epoch at which the phase jump is zero. Note that for this glitch there were several such epochs and the one we are reporting gives the most conservative frequency jump assuming an exponential recovery. The least conservative possible frequency jump is $\sim$ 50% larger. The glitch fractional amplitude was $\Delta\nu/\nu = 1.6 \times 10^{-5}$ (see Table 4.8), among the largest yet seen from any neutron star. A fraction $Q \equiv \Delta\nu_d/(\Delta\nu_d + \Delta\nu) = 0.64$ of the glitch recovered on a time scale of 43 days. This glitch is thus similar to the second certain glitch seen in RXS J170849.0−400910, and to the 2002 glitch in 1E 2259+586, which also showed significant recoveries on time scales of weeks. Also, like the second glitch of RXS J170849.0−400910, this large glitch in 1E 1841−045 is not well modelled by Equation 4.2, as is clear in the residuals plot in Figure 4.7. Accompanying this frequency glitch was a substantial long-term increase in the magnitude of $\dot{\nu}$, with fractional increase $\Delta\dot{\nu}/\dot{\nu} = 0.0959 \pm 0.0007$. This is discussed further in Section 4.6.1.

Because of the sparsity of the data around the glitch epoch, we found an alternate ephemeris for the period of time covered by ephemeris B (Fig. 4.6, Table 4.7). The

Table 4.7. Long-Term Spin Parameters for 1E 1841−045[a]

Parameter	Ephemeris A Spanning MJD 51225−52438	Ephemeris B Spanning MJD 52460−52981	Ephemeris B2 Spanning MJD 52610−52981	Ephemeris C Spanning MJD 53030−53816	Ephemeris D Spanning MJD 53829−53983
MJD start	51224.538	52460.000	52610.313	53030.093	53828.808
MJD end	52437.712	52981.186	52981.186	53815.842	53983.431
TOAs	53	19	17	54	11
ν (Hz)	0.0849253002(9)	0.084904428(7)	0.084889922(3)	0.084890135(6)	0.084868767(7)
$\dot{\nu}$ (10^{-13} Hz s^{-1})	−2.9940(10)	−3.176(2)	−3.179(2)	−3.354(7)	−2.833(9)
$\ddot{\nu}$ (10^{-22} Hz s^{-2})	3.30(14)	–	–	16.4(4)	–
$d^3\nu/dt^3$ (10^{-29} Hz s^{-3})	0.9(2)	–	–	−2.81(11)	–
$d^4\nu/dt^4$ (10^{-36} Hz s^{-4})	−2.3(2)	–	–	–	–
$d^5\nu/dt^5$ (10^{-43} Hz s^{-5})	1.5(3)	–	–	–	–
$d^6\nu/dt^6$ (10^{-51} Hz s^{-6})	−3(2)	–	–	–	–
$\Delta\nu_d$[b](Hz)	–	$8.1(6)\times10^{-7}$	–	–	–
t_d[b](days)	–	43(3)	–	–	–
Epoch (MJD)	51618.000	52464.00448	52997.0492	52997.0492	53823.9694
RMS residual (phase)	0.029	0.025	0.028	0.033	0.022

[a]Numbers in parentheses are TEMPO-reported 1σ uncertainties.

[b]Parameters held fixed at values determined from local glitch fits as shown in Table 4.8.

Table 4.8. Local Ephemerides of 1E 1841−045 Near Glitch Epochs[a]

Parameter	Ephemeris Near Glitch 1	Ephemeris Near Glitch 2	Ephemeris Near Glitch 3
MJD range	52001.684−52981.186	52773.845−53244.179	53579.360−53970.681
TOAs	30	26	31
Epoch (MJD)	52464.00448	52997.0492	53823.9694
ν (Hz)	0.084903950(2)	0.084889815(3)	0.084868657(4)
$\dot{\nu}$ (10^{-13} Hz s^{-1})	−2.8980(10)	−3.162(3)	−2.872(4)
Glitch Epoch (MJD)	52464.00448	52997.0492	53823.9694
$\Delta\nu$ (Hz)	$4.78(7)\times10^{-7}$	$2.08(4)\times10^{-7}$	$1.18(7)\times10^{-7}$
$\Delta\dot{\nu}$ (Hz s^{-1})	$-2.78(2)\times10^{-14}$	$4(3)\times10^{-16}$	$2(1)\times10^{-15}$
$\Delta\nu_d$ (Hz)	$8.1(6)\times10^{-7}$	–	–
t_d (days)	43(3)	–	–
RMS residual (phase)	0.022	0.015	0.022

[a]Numbers in parentheses are TEMPO-reported 1σ uncertainties.

fit parameters are $\nu = 0.0849041677(17)$ Hz, $\dot{\nu} = -2.852(3) \times 10^{-13}$ Hz s^{-1}, $\ddot{\nu} = -2.47(8) \times 10^{-21}$ Hz s^{-2}, and $d^3\nu/dt^3 = 8.8(7) \times 10^{-29}$ Hz s^{-3} at the reported glitch epoch MJD 52464.00448, with RMS phase residual of 0.019. This ephemeris disagrees with ephemeris B in the shape of the recovery (see dotted curve in panel 3 of Fig. 4.6) but agrees with it after the end of the recovery. Using the parameters of this alternate ephemeris, the change in ν at the glitch epoch would be $2.20(3) \times 10^{-7}$ Hz much smaller than the one reported in Table 4.8. However, we hesitate to interpret the glitch using this ephemeris because of the very unusual and unique shape of the recovery it predicts. Note that this alternate ephemeris also shows a long-term increase in the magnitude of $\dot{\nu}$ after the glitch.

We also report the detection of two additional, smaller glitches, as summarized in Table 4.8 and displayed in Figures 4.6 and 4.7. Neither glitch displays significant recovery, and both are well modelled by a simple permanent frequency jump.

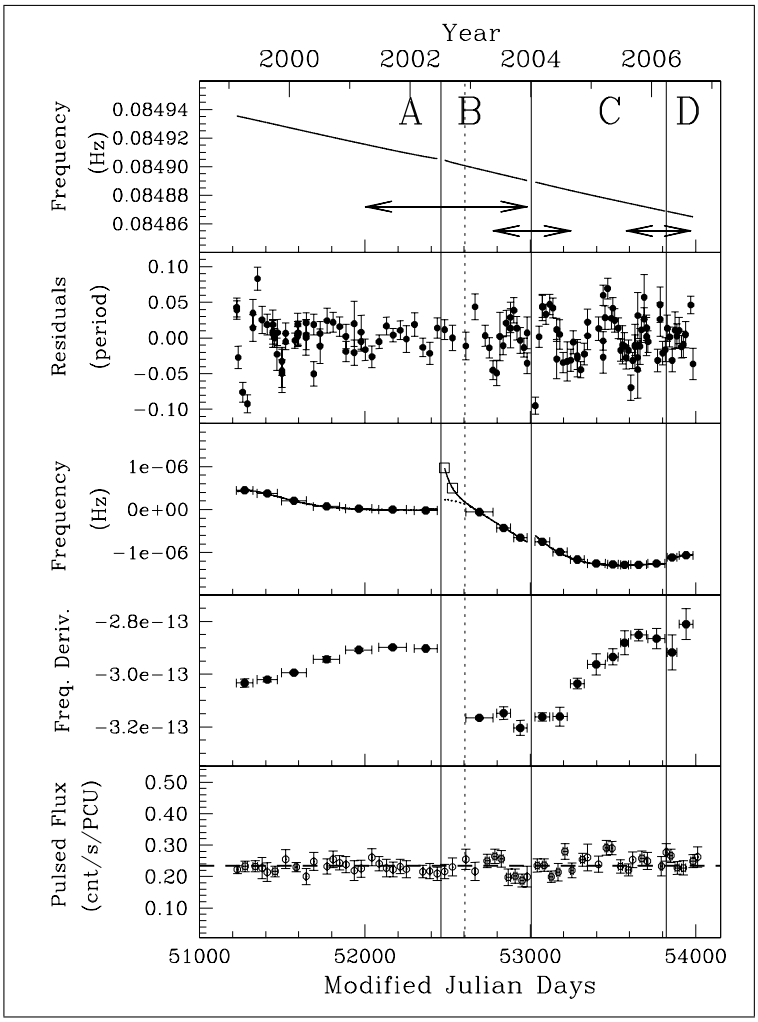

Figure 4.6 Spin and pulsed flux evolution in 1E 1841−045. Panels are described from top to bottom. *Top:* Frequency evolution, with inter-glitch intervals indicated for correspondence with ephemerides given in Table 4.7. Arrows indicate intervals for which glitch ephemerides were obtained (see Table 4.8). *Next:* Residuals, after subtraction of the best-fit models given in Table 4.7. *Next:* Solid curve: frequency evolution of the models shown in Table 4.7 after removal of the linear trend defined by the frequency and frequency derivative from the last year of data before the first glitch, as measured by fitting only those parameters. Dotted curve: alternate glitch recovery (see Section 4.3.2 for details). Filled circles: Measured frequencies in independent sub-intervals after subtraction of the extrapolation of the same linear trend. Unfilled squares: Epochs of the two immediate post-glitch observations (too few for the measurement of an independent frequency but crucial for the phase-coherent analysis). *Next:* Evolution of the frequency derivative in sub-intervals, when fitting locally for only ν and $\dot{\nu}$. *Bottom:* Pulsed flux in the 2–10 keV range. All panels: Glitch epochs are indicated with solid vertical lines. The dashed vertical line indicates the start of ephemeris B2, which does not include the two immediate post-glitch observations (indicated with unfilled squares).

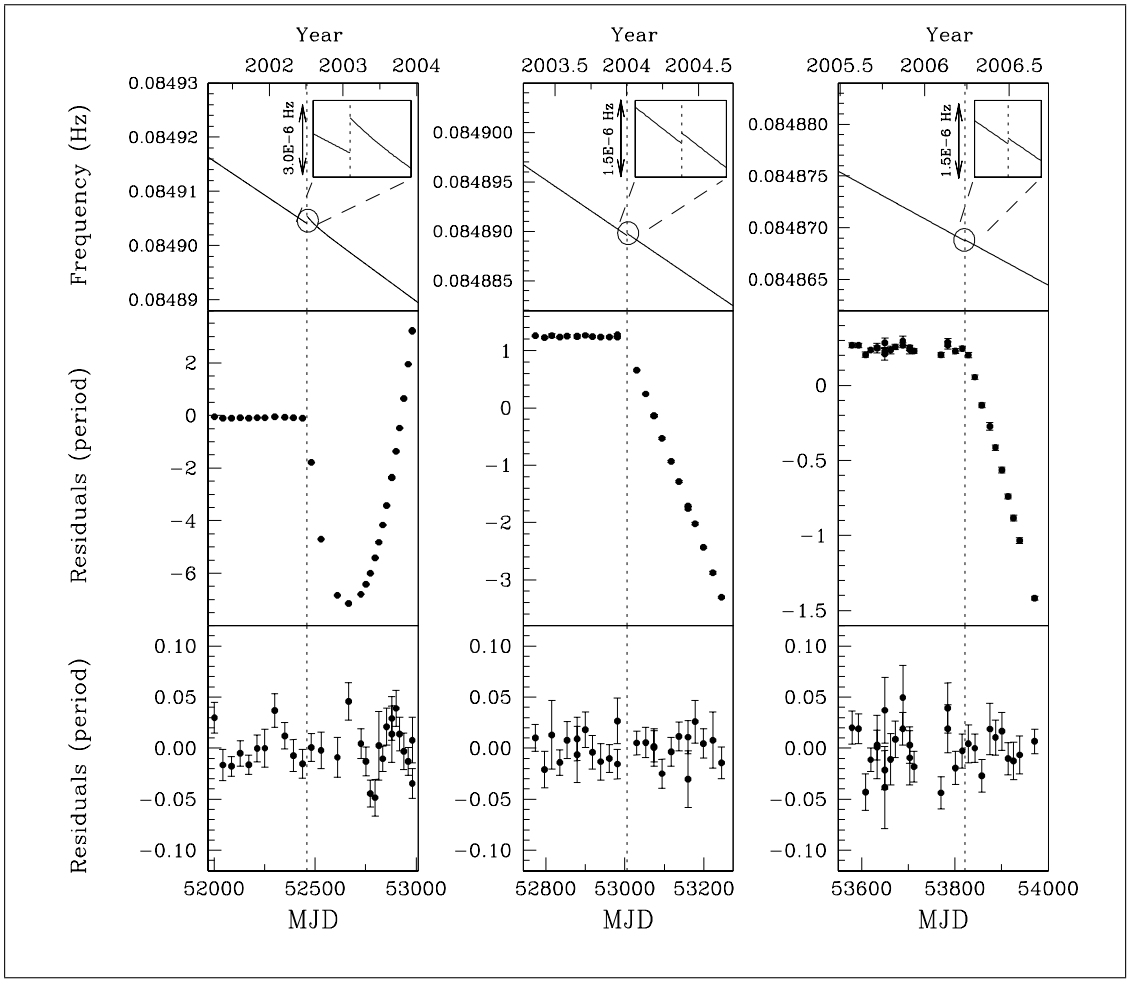

Figure 4.7 The three glitches in 1E 1841−045. *Top panels:* Frequency evolution around glitches as determined from ephemerides in Table 4.8, with the blow-up inset displaying glitch amplitude. *Middle panels:* Residuals after subtraction of the best-fit pre-glitch ephemeris given in Table 4.8. *Bottom panels:* Residuals after subtraction of best-fit glitch models given in Table 4.8. *All panels:* Dashed vertical lines indicate assumed glitch epochs.

4.4 Pulse Profile Changes

Another interesting AXP property we can study thanks to *RXTE* monitoring is the evolution of the pulse profile. We performed a pulse profile analysis on each AXP using FTOOLS version 5.3.1[2]. We used the following steps: for each observation, we ran the FTOOL `make_se` to combine the `GoodXenon` files. We then used the FTOOL `fasebin` to make a phase-resolved spectrum of the entire observation with 64 phase bins across the profile. When we ran `fasebin`, we selected layer 1 of the detector, disregarded the propane photons, and included the photons from PCUS 1, 2, 3, and 4. We omitted PCU 0, for which an independent analysis of AXP 4U 0142+61 revealed spectral modeling irregularities (Dib et al., 2007a). `fasebin` also took care of barycentering the data. For each observation, we then used `seextrct` to make a phase-averaged spectrum for the same set of detector layers and PCUs. The phase-averaged spectrum was then used by the perl script `pcarsp` to make a response matrix.

We loaded the phase-resolved spectra and the response matrices into the X-ray Spectral Fitting Package (XSPEC[3]) and selected photons belonging to three energy bands: 2−10, 2−4, and 4−10 keV. Using XSPEC, we extracted a count-rate pulse profile for each of the energy bands. The profiles included XSPEC-obtained 1σ error bars on each of the phase bins. To obtain a pulse profile in units of count rate per PCU, we divided the overall profile by a PCU coverage factor that took into account the amount of time each PCU was on.

We then aligned the 64-bin profiles with a high signal-to-noise template using a similar cross-correlation procedure to the one used in the timing analysis. Then, for each glitch-free interval, we summed the aligned profiles, subtracted the DC component, and scaled the resulting profile so that the value of the highest bin is unity and the lowest point is zero.

4.4.1 Profile Analysis results of RXS J170849.0−400910

Average profiles for RXS J170849.0−400910 in the three energy bands are presented in Figure 4.8. In a given band, the different profile qualities are due to different net exposure times. Energy dependence is clearly visible to the eye as well as small fluctuations. For example, in the 2–4 keV band, the small peak off the main pulse has clearly fluctuating intensity. This small peak gets larger at higher energy, as seen in

[2]http://heasarc.gsfc.nasa.gov/ftools
[3]http://xspec.gsfc.nasa.gov Version: 11.3.1

the 2–10 keV band. In the 4–10 keV band, the smaller peak seems to blend with the main low-energy peak to yield a broad single peak structure, although fluctuations in that structure are apparent.

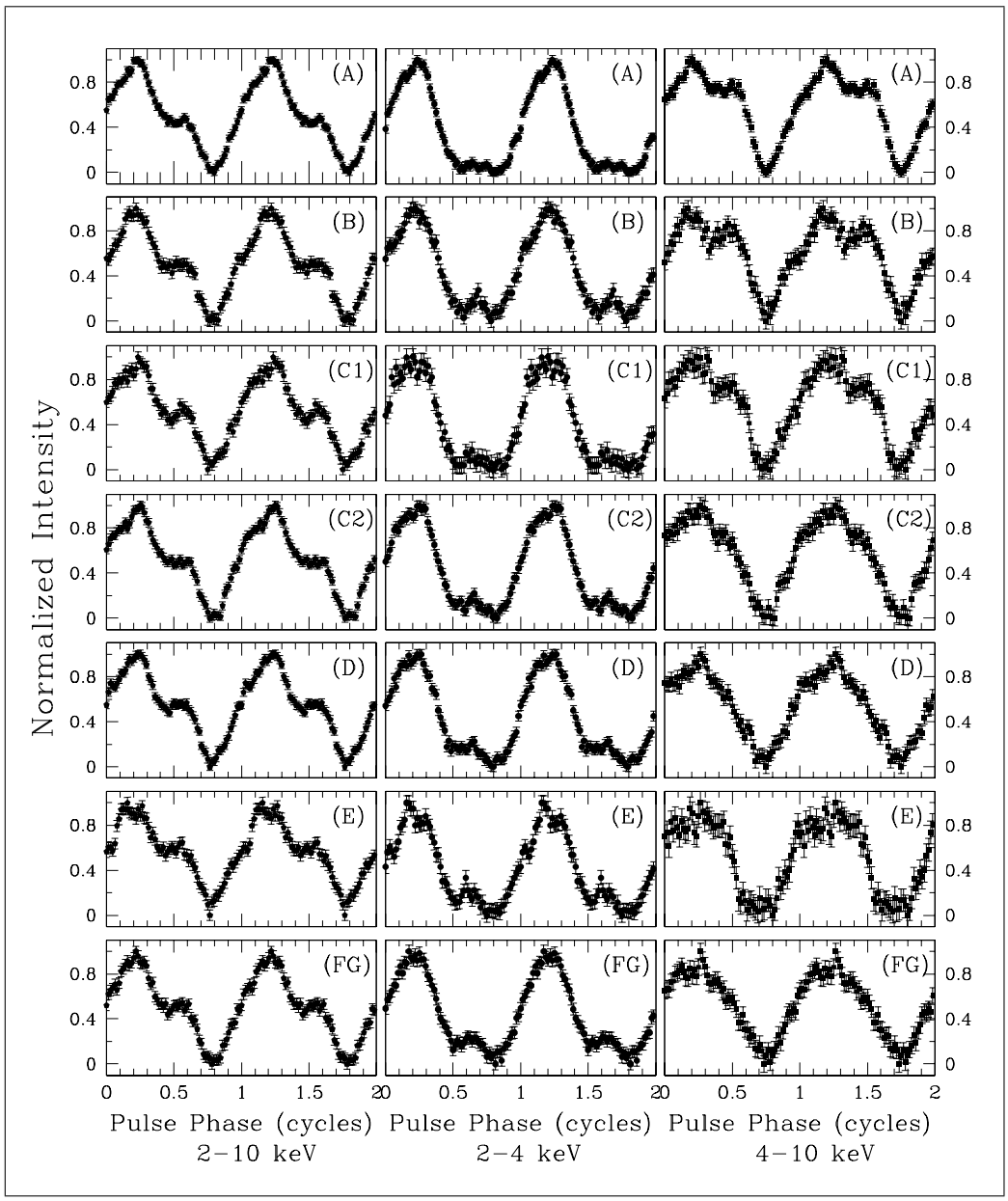

Figure 4.8 Normalized pulse profiles in three energy bands for RXS J170849.0−400910 for the seven glitch-free intervals (with corresponding labels at the top right) defined in the top panel of Figure 4.3. Different data qualities within an energy range are due to different net exposure times. Two cycles are shown for each profile for clarity.

To study these fluctuations quantitatively, we subjected each profile to a Fourier analysis. Figure 4.9 shows the evolution of the first three profile harmonics with time.

Although there are hints of variation in all energy bands, only variations in the hard 4–10 keV band are statistically significant (as determined by the χ^2 statistic from a fit to a constant value); the decline of the second and third harmonics in the hard band have probabilities of 0.0007% and 0.0012%, respectively, of being due to chance. Thus in the hard band the profile is certainly becoming more sinusoidal, in agreement with what is inferred by eye.

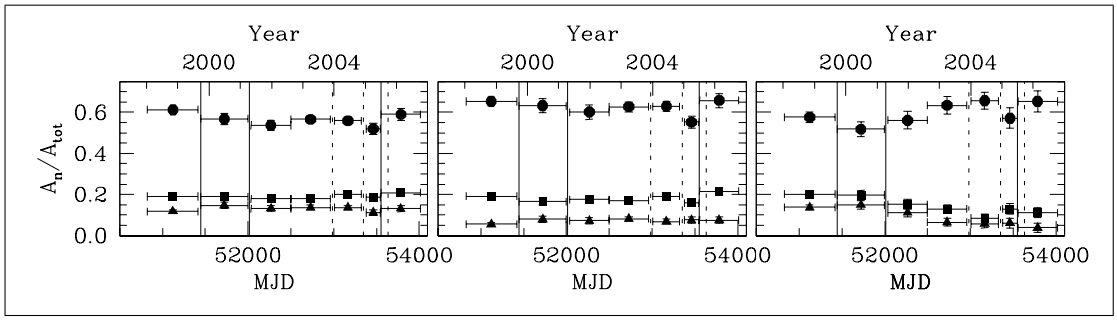

Figure 4.9 *Left panel:* Time evolution of the ratio of the power in the nth harmonic to the total power in the 2–10 keV pulse profile of RXS J170849.0−400910. Circles represent $n = 1$, squares $n = 2$, and triangles $n = 3$. Solid vertical lines indicate epochs of glitches; dashed vertical lines are epochs of candidate glitches. *Middle panel:* Same as left panel but for 2–4 keV. *Right panel:* Same as middle but for 4–10 keV.

The above analysis shows that the profile is changing, but not whether these changes are truly correlated with the glitch epochs, since changes could be occurring throughout. To search for pulse profile changes correlated with glitch epochs, as were claimed by Dall'Osso et al. (2003), we divided glitch-free intervals into several sub-intervals (typically of duration ∼30 days) for which independent profiles were created. The number of sub-intervals was chosen by trading off signal-to-noise ratio for time resolution. These sub-interval profiles were then Fourier analysed. The evolution of the Fourier powers in the first three harmonics in the 2–10 keV profile are shown in the top panel of Figure 4.10.

To determine whether the apparent fluctuations are statistically significant, we fit a constant value to each time series and from the χ^2 of the best fit, found that the probabilities of the fluctuations being due to random noise are 68, 96 and 69% for $n = 1, 2, 3$, respectively. This analysis thus shows no evidence for profile changes associated with the glitch epochs, including the second glitch. However the reduced signal-to-noise ratios in the sub-interval average profiles, required for interesting time resolution, makes us insensitive to subtle profile changes. To search for glitch-correlated pulse profile changes in a different way, for each sub-interval we calculated the reduced χ^2

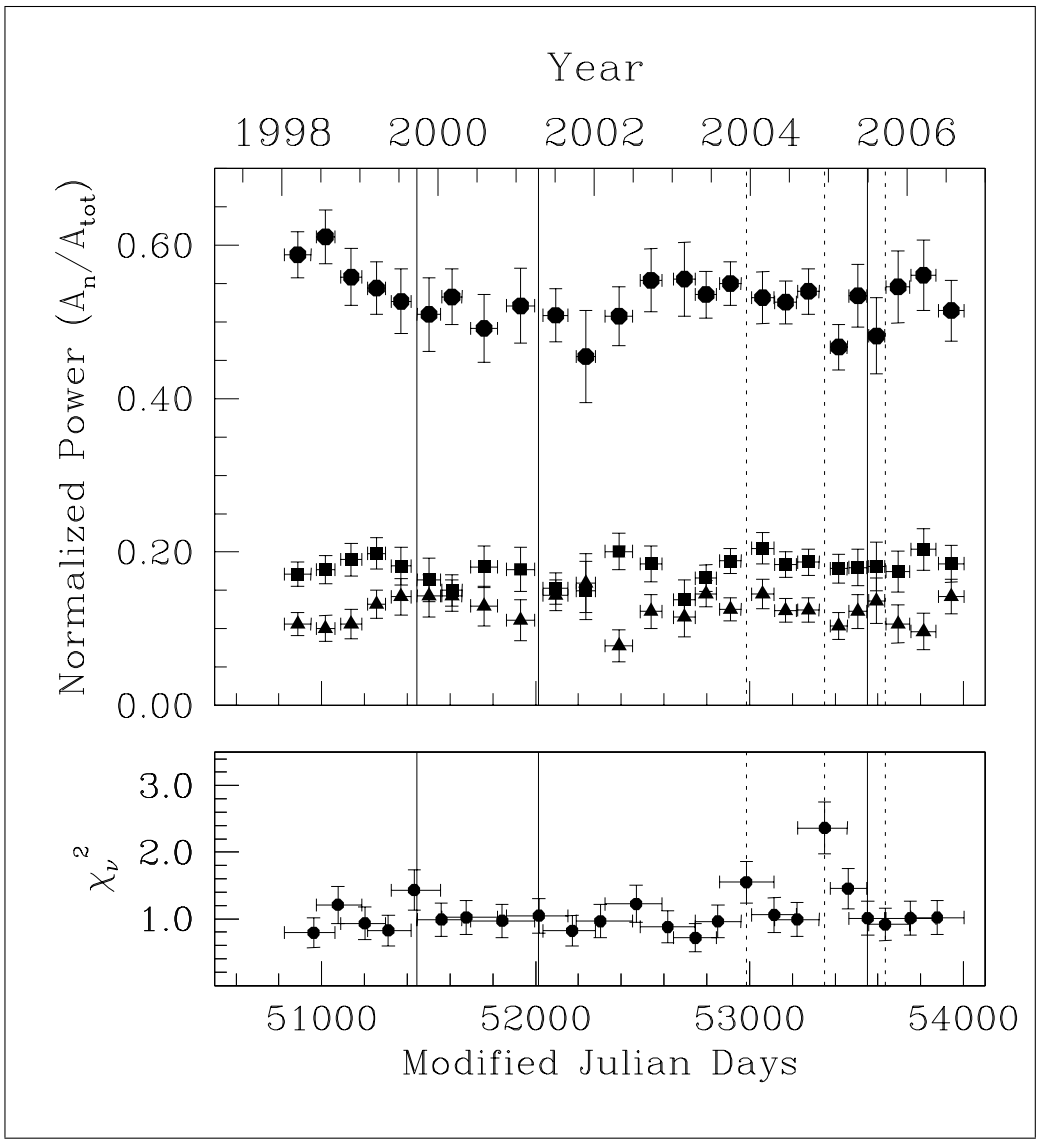

Figure 4.10 *Top panel:* Time evolution of the ratio of the power in the nth harmonic to the total power in the 2–10 keV pulse profile of RXS J170849.0−400910. The circles represent $n = 1$, squares $n = 2$, and triangles $n = 3$. Solid and dashed vertical lines indicate epochs of glitches and candidate glitches, respectively. The probability that the observed fluctuations are due to random noise are 68%, 97% and 69% for $n = 1, 2, 3$, respectively. *Bottom panel:* reduced χ^2 per degree of freedom for successive profile differences (see Section 4.4.1 for details).

of the difference between that sub-interval's average profile and the previous one. The time series of these χ^2 values is shown in the bottom panel of Figure 4.10. There is clearly no evidence for any profile change at the second glitch, or at the third certain glitch. There is some hint of profile changes at the first and second candidate glitches, however a K-S test shows that our χ^2 values as a group have a probability of

39% of originating from χ^2 distribution. Interestingly though, the probability of the single high χ^2 value we measure at the second candidate glitch occurring randomly is only 1.0×10^{-6}; that at the first glitch is 1.7% and at the first glitch candidate is 0.4%. Thus we do find possible evidence in this analysis for glitch-correlated pulse profile changes, though the best evidence for significant changes occurs only at two candidate glitches, i.e., the lowest amplitude events.

4.4.2 Profile Analysis results of 1E 1841−045

Summed profiles for 1E 1841−045 in three energy bands for the five glitch-free intervals defined in the top panel of Figure 4.6 are shown in Figure 4.11. As for RXS J170849.0−400910, some low-level profile fluctuations are suggested, particularly in the relative amplitude of the leading and trailing sides of the large single peak in the 2–10 keV band (though clearly this peak could also be considered the blend of two or more adjacent peaks).

As for RXS J170849.0−400910, we quantify the profile fluctuations of 1E 1841−045 via Fourier analysis. Figure 4.12 shows the evolution of the first three profile harmonics with time in each energy band. Interestingly, in contrast to RXS J170849.0−400910, here the profile changes are most prominent in the soft 2–4 keV band, in which the fraction of power in the fundamental of the profile in interval A2 (see Fig. 4.6) decreased, then slowly relaxed back to the previous range. However, a χ^2 test shows the probability of this behaviour being due to random noise is 18%, too large to exclude.

To look for pulse profile changes correlated with glitches, again, sub-intervals within glitch-free intervals were chosen and summed profiles computed and Fourier analysed. The evolution of the first three harmonics is shown in the top panel of Figure 4.13. Fluctuations are apparent although none is particularly remarkable at any of the glitch epochs, including the first and largest, and the time series for $n = 1, 2, 3$ are all consistent with a constant value. This argues again against correlated profile and timing anomalies in this source thus far. As a confirmation, as for RXS J170849.0−400910, a difference profile was calculated for each sub-interval by subtracting that interval's profile from the preceding one. The χ^2 values of these difference profiles are shown in the bottom of Figure 4.13; no significant features are present.

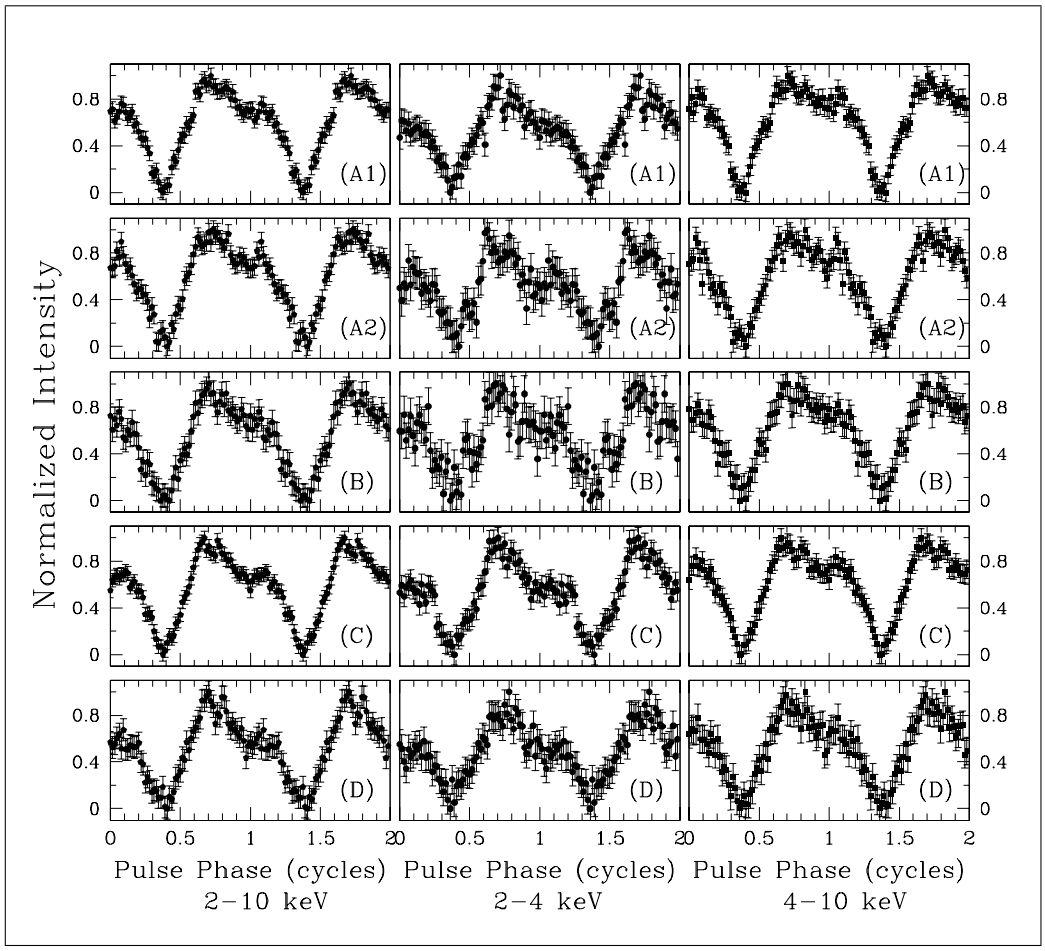

Figure 4.11 Normalized pulse profiles in three energy bands for 1E 1841−045 for the five glitch-free intervals defined in the top panel of Figure 4.6. Different data qualities in each energy range are due to different net exposure times. Two cycles are shown for each profile for clarity.

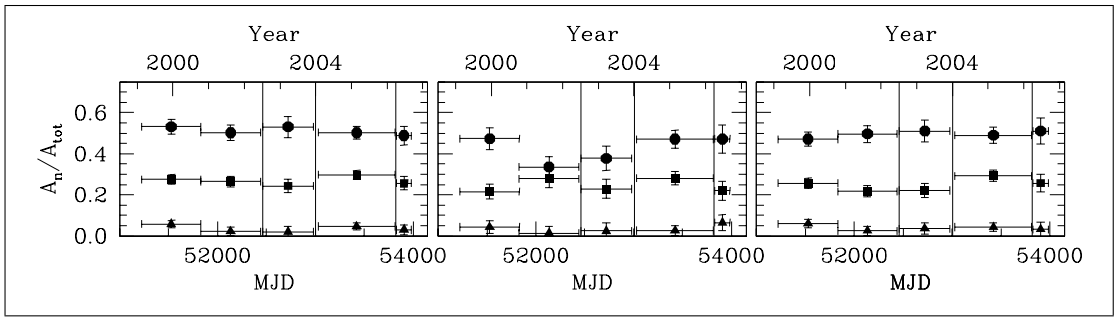

Figure 4.12 *Left panel:* Time evolution of the ratio of the power in the nth harmonic to the total power in the 2–10 keV pulse profile of 1E 1841−045. Circles represent $n = 1$, squares $n = 2$, and triangles $n = 3$. Solid vertical lines indicate epochs of glitches. *Middle panel:* Same as left panel but for 2–4 keV. *Right panel:* Same as middle but for 4–10 keV.

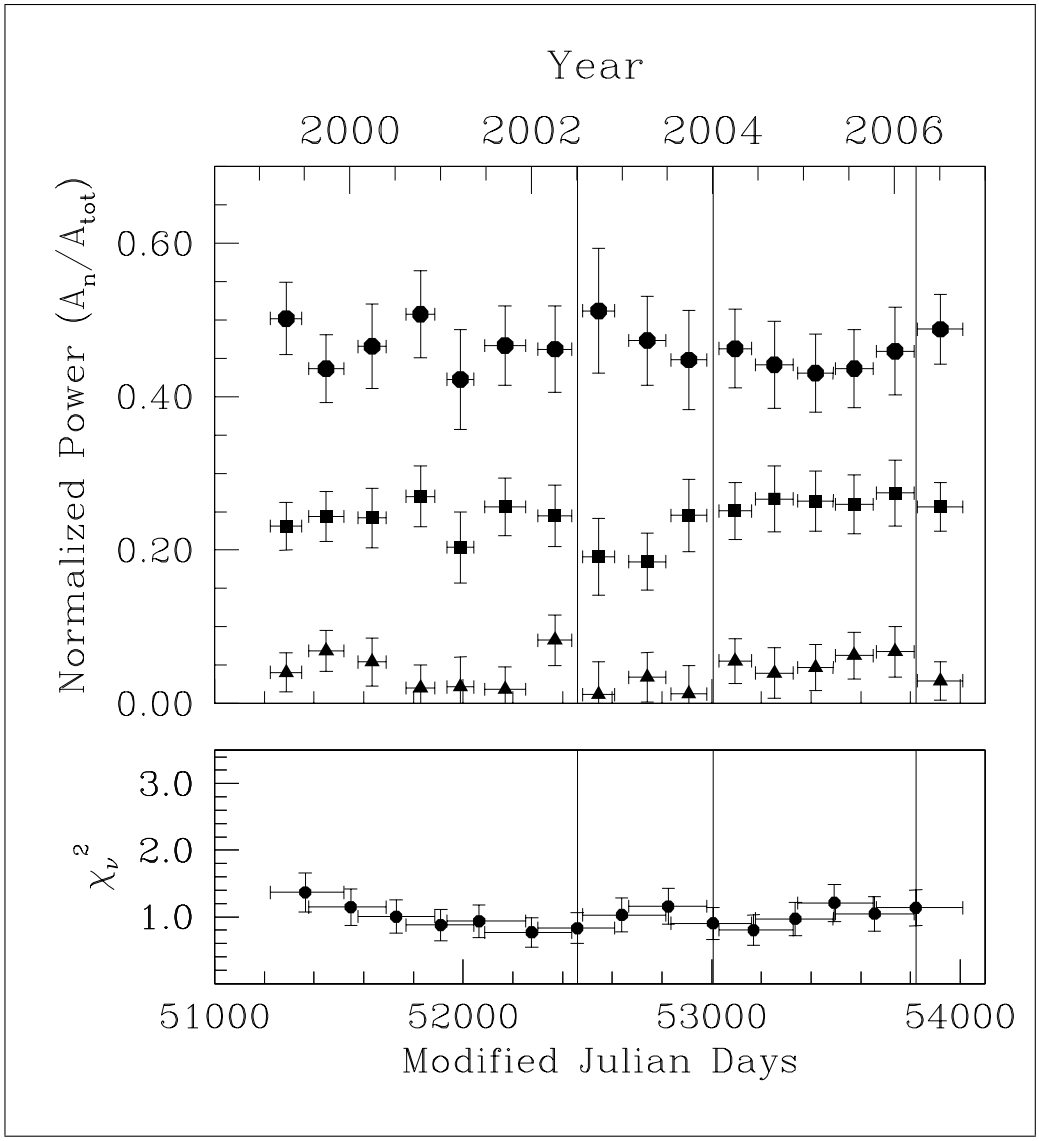

Figure 4.13 *Top panel:* Time evolution of the ratio of the power in the nth harmonic to the total power in the 2–10 keV pulse profile of 1E 1841−045. Circles represent $n = 1$, squares $n = 2$, and triangles $n = 3$. Solid vertical lines indicate epochs of glitches. The probabilities that the observed fluctuations arise from random noise are 99%, 97% and 96% for $n = 1, 2, 3$, respectively. *Bottom panel:* reduced χ^2 per degree of freedom for successive profile differences (see Section 4.4.2 for details).

4.5 Pulsed Flux Time Series

RXTE monitoring also allows the study of the evolution of the pulsed flux of these sources. To obtain a pulsed flux time series for RXS J170849.0−400910 and 1E 1841−045, we did the following. First, for each observation, we used a procedure similar to that described in Section 4.4 to make a count rate per PCU pulse profile (with 64 phase bins across the profile and excluding PCU 0) in the energy range 2–10 keV. The profiles included XSPEC-determined 1σ error bars on the flux value in each of the phase bins.

The pulsed flux for each of the profiles was calculated using the following RMS formula:

$$F = \sqrt{2\sum_{k=1}^{n}((a_k{}^2 + b_k{}^2) - (\sigma_{a_k}{}^2 + \sigma_{b_k}{}^2))}, \tag{4.3}$$

where a_k is the k^{th} even Fourier component defined as $a_k = \frac{1}{N}\sum_{i=1}^{N} p_i \cos(2\pi ki/N)$, $\sigma_{a_k}{}^2$ is the uncertainty of a_k, b_k is the odd k^{th} Fourier component defined as $b_k = \frac{1}{N}\sum_{i=1}^{N} p_i \sin(2\pi ki/N)$, $\sigma_{b_k}{}^2$ is the uncertainty of b_k, i refers to the phase bin, N is the total number of phase bins, p_i is the count rate in the i^{th} phase bin of the pulse profile, and n is the maximum number of Fourier harmonics to be taken into account. We used $n = 6$ for both RXS J170849.0−400910 and 1E 1841−045.

Our method for estimating the pulsed flux F is equivalent to the simple RMS formula $F = \frac{1}{\sqrt{N}}\sqrt{\sum_{i=1}^{N}(p_i - \overline{p})^2}$ (where p_i is the count rate in the i^{th} phase bin of the pulse profile and $\overline{p}$ is the average count rate), except that we have subtracted the variances (to eliminate the upward statistical bias) and only included the statistically significant Fourier components. For a detailed discussion on pulsed flux estimates, see Archibald et al. (2009).

4.5.1 Pulsed Flux Time Series for RXS J170849.0−400910

Our pulsed flux time series for RXS J170849.0−400910 is shown in Figure 4.3 (bottom panel) and again in Figure 4.14. Each data point represents the average of pulsed fluxes measured over ∼1 month. There appear to be frequent low-level pulse flux variations in this source. Although our error estimates on the pulsed fluxes include only statistical uncertainty (i.e., we have made no effort to estimate systematic uncertainties), we are given confidence that the fluctuations seen e.g., near MJD 52000 are real, given how stable the pulsed flux of 1E 1841−045 is in the same time interval (see Section 4.5.2).

There are no large increases in pulsed flux following any of the glitches, unlike

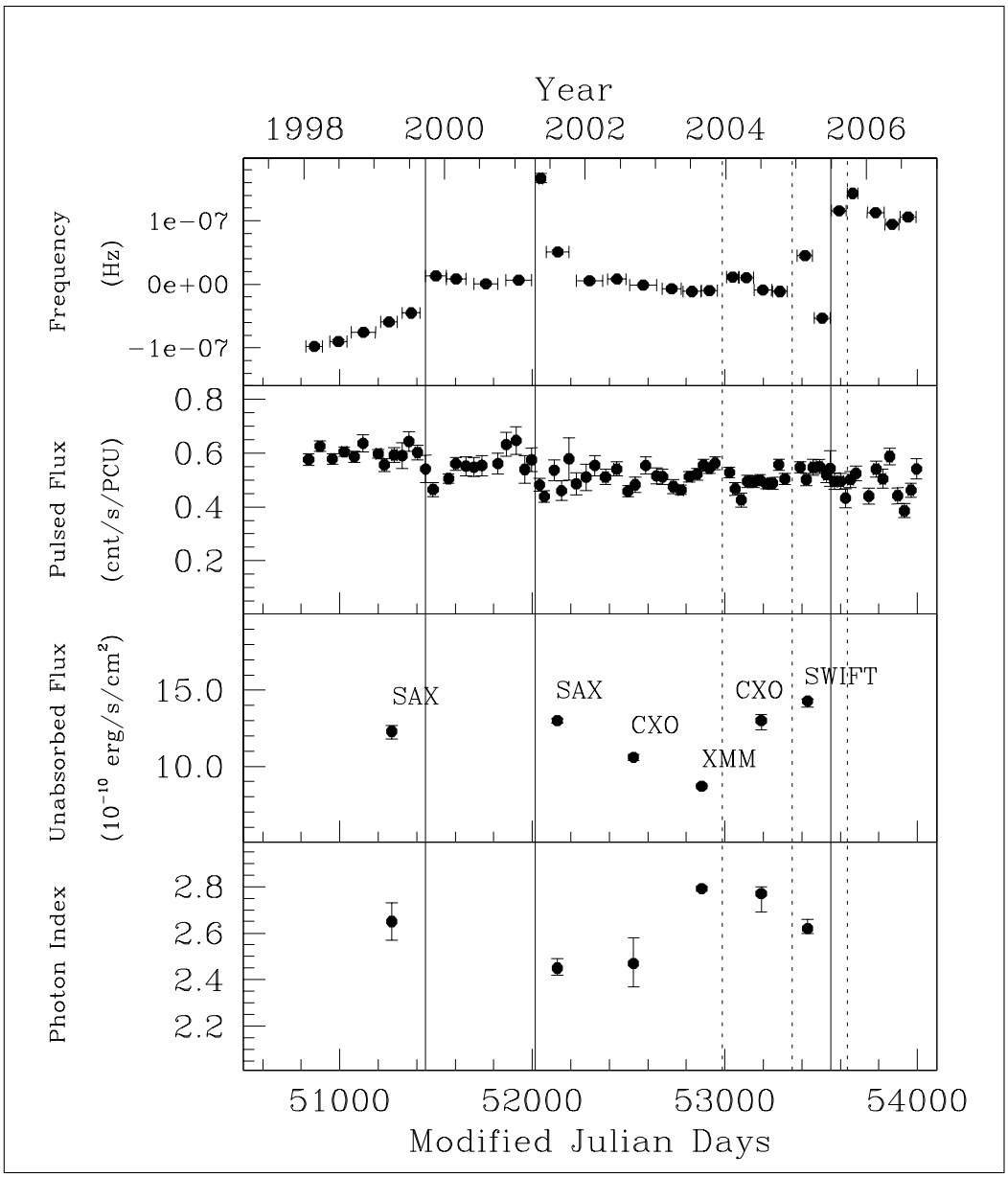

Figure 4.14 Frequency, pulsed flux, reported total unabsorbed flux, and reported photon index as a function of time for RXS J170849.0−400910. Frequency and pulsed flux data are identical to those shown in Figure 4.3. Solid and dashed vertical lines indicate epochs of glitches and glitch candidates, respectively. Unabsorbed phase-averaged 0.5–10 keV fluxes and photon indexes are from Rea et al. (2005) and Campana et al. (2007), and are labelled by observing telescope. That the pulsed flux remains relatively constant while the phase-averaged flux appears to vary by nearly a factor of two (albeit as measured by different instruments) suggests a strong anti-correlation between total flux and pulsed fraction.

what was seen following the 2002 glitch of AXP 1E 2259+586 (Kaspi et al., 2003;

Woods et al., 2004). However, there is a possible pulsed flux enhancement prior to the second glitch, and a dip following it. Given this and the lack of clearly associated pulse profile changes coincident with glitch epochs (see Section 4.4.1), the glitches of RXS J170849.0−400910 appear to be "quiet", in the sense that they seem unaccompanied by significant pulsed radiative change. This is discussed further in Section 4.6.

Figure 4.14 shows phase-averaged fluxes in the 0.5–10 keV band as measured using a variety of focussing X-ray telescopes (Rea et al., 2005; Campana et al., 2007). Interestingly, while the reported phase-averaged flux varies considerably (by a factor of $\sim$1.6), and in concert with the photon index as measured in the conventionally used blackbody/power-law spectral model, the 2–10 keV pulsed flux remains relatively constant. This suggests that the pulsed fraction of RXS J170849.0−400910 is precisely anti-correlated with total flux, in such a way as to keep the pulsed flux near constant. This is discussed further in Section 4.6.

The origin of the apparent low-level pulsed flux variations is not clear, given the apparent lack of correlation with the phase-averaged flux. As shown by Archibald et al. (2009), a changing pulse profile can affect an RMS-based pulsed flux estimator such as that in Equation 4.3. To verify that our measured pulsed fluxes were not influenced by the changing pulse profile of RXS J170849.0−400910 (see Section 4.4), we also found the pulsed flux using an estimator based on the area under the profile (after baseline subtraction), which is, by definition, insensitive to pulse profile changes. With this method, we obtained qualitatively similar results for the pulsed fluxes.

4.5.2 Pulsed Flux Time Series for 1E 1841−045

Our pulsed flux time series for 1E 1841−045 is shown in the bottom panel of Figure 4.6. Each data point represents the average of pulsed fluxes measured over $\sim$1 month. Note the increased scatter after MJD 52700 is due to decreased effective integration time, a result of the reduction in the average number of operational PCUs. The measured pulsed fluxes are consistent with being constant, with their probability of being due to random fluctuations 52%. There is no evidence for any pulsed flux change at the glitch epochs. Thus the glitches of 1E 1841−045 appear to be "quiet", at least in pulsed flux, on time scales comparable to or longer than our sampling time.

4.6 Discussion

4.6.1 AXP Glitches

We have now observed a sufficiently large sample of AXP glitches that we can make meaningful phenomenological comparisons with glitches in radio pulsars, a much better studied phenomenon. Detection of systematic differences in AXP and radio pulsar glitch properties would be interesting as it could signal structural differences between magnetars and conventional radio pulsars.

Figure 4.15 shows the fractional and non-fractional amplitude distributions of radio pulsar and AXP glitches. As is clear from the figure, although the fractional glitch amplitudes of AXPs are generally large by radio pulsar standards, the AXP absolute glitch amplitudes, more directly related to the angular momentum transfer during the glitch, are neither especially large nor especially small. Thus, glitch amplitude in neutron stars is clearly not correlated with frequency as some studies of radio pulsars have suggested (Lyne et al., 2000).

Given the spectacular radiative outburst contemporaneous with the large 2002 1E 2259+586 glitch, we can speculate that larger angular momentum transfers, which occasionally occur in radio pulsars, could result in even more dramatic outbursts in affected AXPs, possibly like those seen in XTE 1810−197 (Ibrahim et al., 2004) and in the AXP candidate AX J1845−0258 (Tam et al., 2006). Indeed a recent X-ray burst observed from CXOU J164710.2−455216 (Muno et al., 2007) has been claimed to be accompanied by a very large ($\Delta\nu/\nu \simeq 6 \times 10^{-5}$, $\Delta\nu \simeq 6 \times 10^{-6}$) glitch (Israel et al., 2007), and AXP 1E 1048.1−5937 recently exhibited a large glitch and flux increase (Dib et al. 2007b, Chapter 5). However the lack of any observed radiative change in 1E 1841−045 around the time of its first observed glitch, which was over a factor of two larger than that in 1E 2259+586 in terms of absolute frequency jump, argues against this idea. Clearly, the data are indicating that AXP glitches, even large ones, can be either radiatively loud or quiet.

Glitch activity has been defined as

$$a_g = \frac{1}{\Delta t} \sum \frac{\Delta\nu}{\nu}, \tag{4.4}$$

where Δt is the total observing span and the sum is over all glitches, and includes decaying components (McKenna & Lyne, 1990). We refer to a_g as fractional activity, since it involves the sum of fractional frequency changes. One can also define an

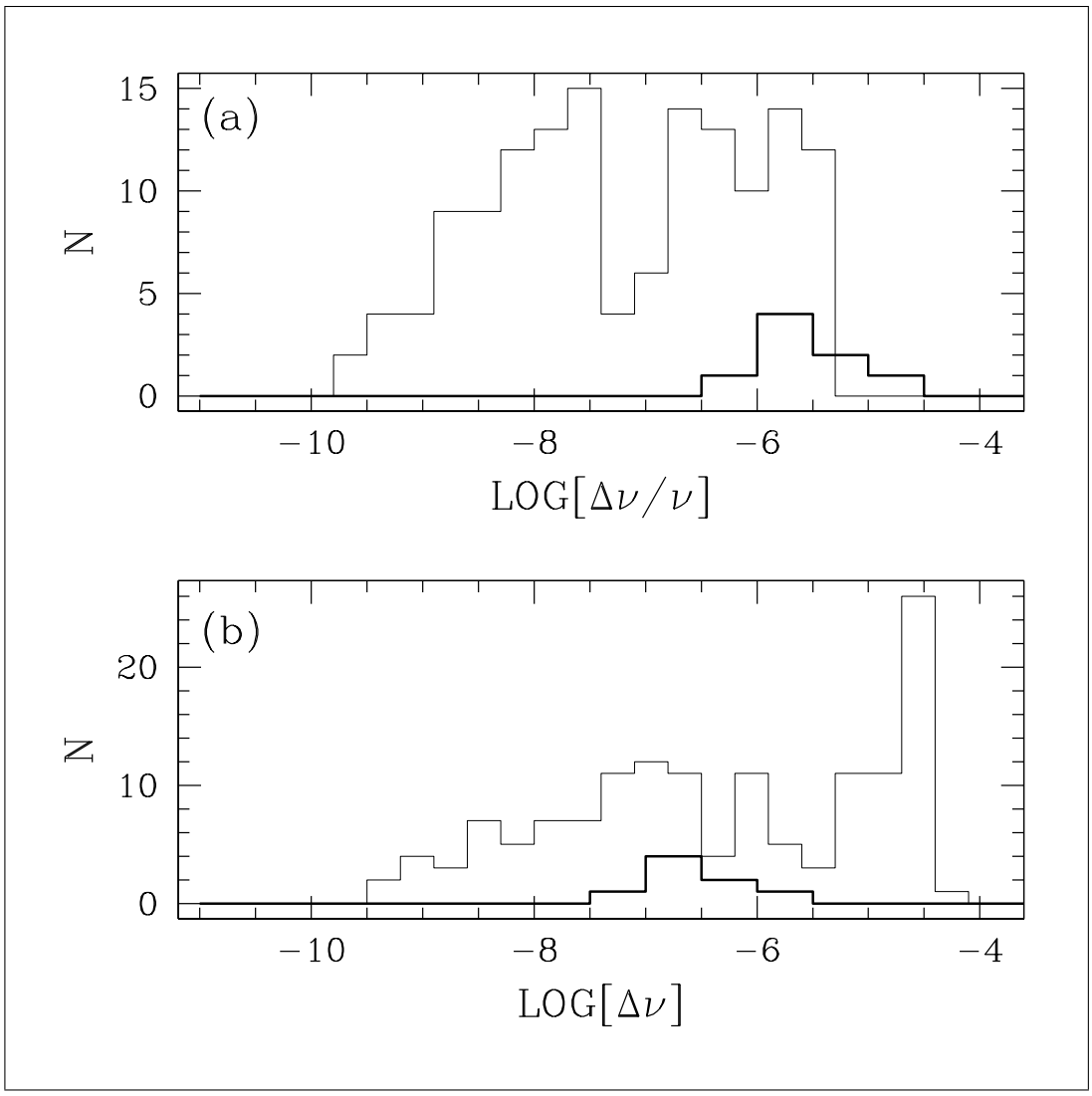

Figure 4.15 Amplitude distribution of AXP glitches (bold line) and radio pulsar glitches (thin line) for (a) fractional frequency jump and (b) absolute frequency jump (in Hz). Radio pulsar glitch amplitudes are from an unpublished catalog kindly supplied by A. Lyne. AXP glitches included here are those listed in Tables 4.4 and 4.8, the 2002 1E 2259+586 glitch (Kaspi et al., 2003; Woods et al., 2004), as well as a recent unpublished 1E 2259+586 glitch (Dib et al., 2008b, 2009a).

absolute glitch activity,

$$A_g = \frac{1}{\Delta t} \sum \Delta\nu, \tag{4.5}$$

where the sum is over the absolute frequency changes (e.g., Wang et al., 2000). The quantities a_g and A_g, introduced for the study of radio pulsars, are approximately interchangeable for those objects, given that the range of frequencies encompassed by glitching radio pulsars is relatively small. By contrast, when considering AXPs and their

much smaller rotation frequencies, a comparison with radio pulsars for a_g and A_g are very different (see, e.g., Heyl & Hernquist, 1999). Also, for establishing the average amount of spin-up imparted to the crust over time, the total frequency increase at each epoch is relevant. However, in some instances, the quantity of interest is the *unrelaxed* portion of the glitch, i.e., the permanent frequency jump only. In general, for radio pulsars, Q is small so this distinction is not important. However for AXPs, given the paucity of glitches we have observed thus far as well as the fact that several, particularly the largest, of these have had large values of Q (e.g., $Q \simeq 1$ for the second glitch seen in RXS J170849.0−400910), the distinction between including the total frequency jump and only the unrelaxed frequency jump is important. We choose here to remain with convention and include the total frequency jump at each epoch when calculating a_g and A_g, although this choice should be kept in mind.

With 8.7 yr of monitoring of RXS J170849.0−400910, we can now reasonably calculate glitch activity parameters for this source using Equations 4.4 and 4.5. If only counting the unambiguous glitches, $a_g = 2.9 \times 10^{-14}$ s^{-1} and $A_g = 2.5 \times 10^{-15}$ s^{-2}. Including candidate glitches only increases these numbers by ∼20%. With three glitches in 7.6 yr, 1E 1841−045 is evidently a very active glitcher as well. Its glitch activity parameters are $a_g = 7.9 \times 10^{-14}$ s^{-1} and $A_g = 6.7 \times 10^{-15}$ s^{-2}. Indeed A_g for 1E 1841−045 is the highest glitch activity seen thus far in any neutron star, radio pulsar or AXP, to our knowledge. We also calculated a tentative glitch activity for AXP 1E 2259+586, for which we have observed two glitches, the well documented one in 2002 (Kaspi et al., 2003; Woods et al., 2004) and a second, smaller glitch that occurred very recently and had fractional amplitude 8.5×10^{-7} and no recovery (Dib et al. 2008b, Dib et al. 2009a, Chapter 6). Using these events and given that we have observed this source with *RXTE* for 9.4 yr, we find $a_g = 1.7 \times 10^{-14}$ s^{-1} and $A_g = 2.4 \times 10^{-15}$ s^{-1}.

We can plot these activities as a function of pulsar age (as estimated via spin-down age $\nu/2\dot{\nu}$) and $\dot{\nu}$; see Figure 4.16. Previous authors have noted interesting correlations on these plots for radio pulsars (e.g., Lyne et al., 2000; Wang et al., 2000); these are seen in our plots as well. Note that upper limits for some radio pulsars of relevant ages fall well below the apparent correlations (e.g., Wang et al., 2000); we choose not to plot those because, as discussed in that reference, a single glitch of average size would bring them roughly in line with the correlation. Note that the radio pulsar outlier at small age and high $\dot{\nu}$ in all plots is the Crab pulsar, long-known to exhibit few and small glitches. We also looked for a trend in a plot of a_g or A_g versus surface

dipolar field (as estimated via $3.2 \times 10^{19}\sqrt{P\dot{P}}$ G) but found none.

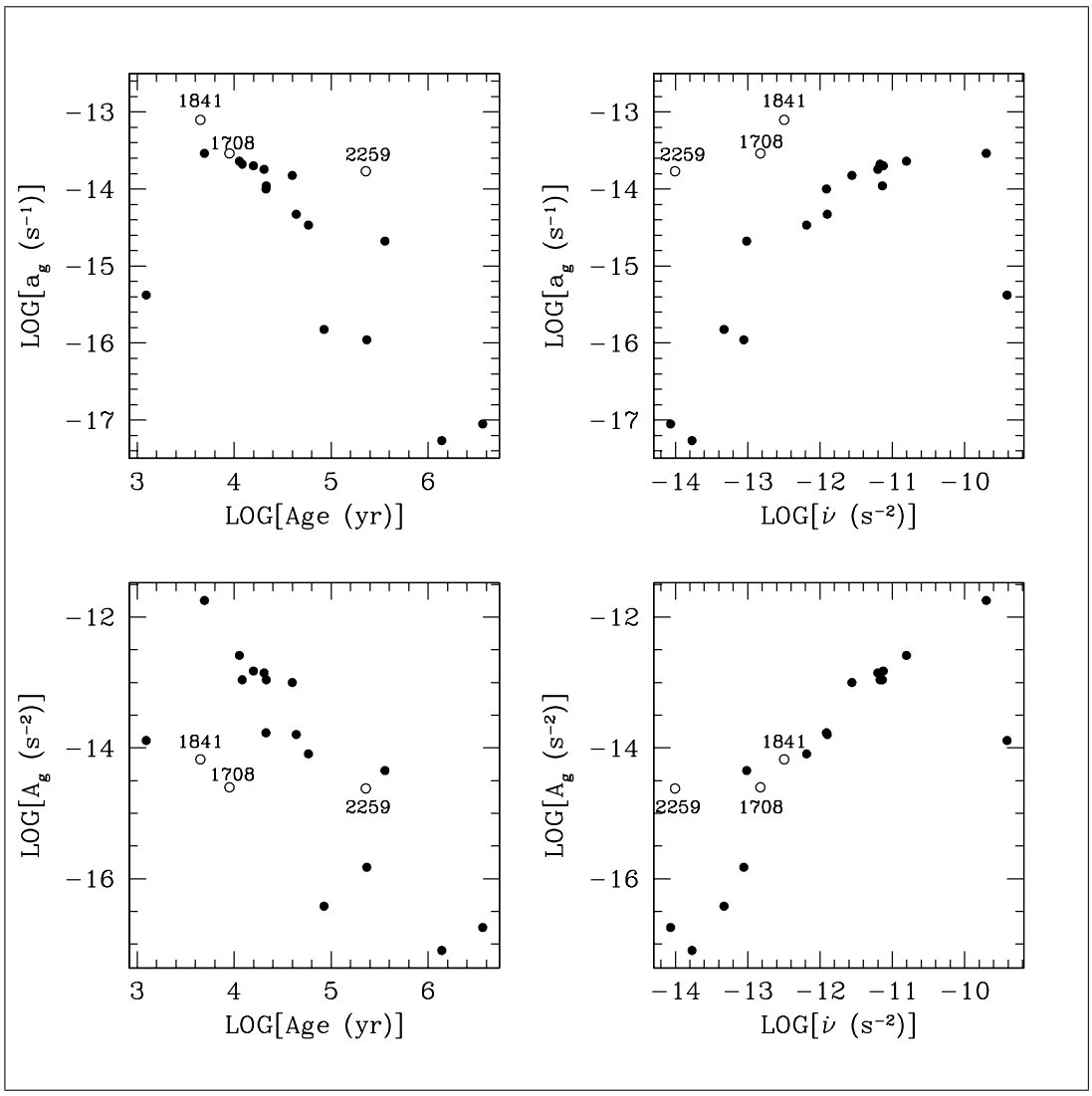

Figure 4.16 Activity parameters versus age (as estimated from $\nu/2\dot{\nu}$) and versus $\dot{\nu}$ for radio pulsars and AXPs. Fractional activity a_g is defined using the sum of the fractional frequency changes, while activity A_g is defined using the absolute frequency jumps. The only radio pulsars included (filled circles) are those having exhibited three glitches or more during continual (e.g., bi-monthly) monitoring, as recorded in the unpublished glitch catalog kindly supplied by A. Lyne. The AXPs included here (open circles) are RXS J170849.0−400910, 1E 1841−045, and 1E 2259+586. The latter has glitched twice, once in 2002 (Kaspi et al., 2003; Woods et al., 2004), and once in 2007 (Dib et al. 2008b, Dib et al. 2009a). Only unambiguous glitches were included for RXS J170849.0−400910; as the candidate glitches are small, including them does not make a qualitative difference.

As a group, the AXPs do not especially distinguish themselves when either activity,

a_g or A_g is plotted versus spin-down age, though they do increase the scatter. This suggests a universal correlation with spin-down age. The same is true of A_g plotted versus $\dot{\nu}$. However, interestingly, the AXPs as a group all stand out on the diagram of a_g versus $\dot{\nu}$ (Fig. 4.16), such that for similar spin-down rates, their fractional glitch activities are much larger than in radio pulsars.

Link et al. (1999) argued that a_g provides a strict lower limit on the fraction of the moment of inertia of the neutron star that resides in the angular momentum reservoir (generally assumed to be the crustal superfluid) tapped during spin-up glitches, I_{res}. They showed that $I_{res}/I_c \geq \nu a_g/|\dot{\nu}| \equiv G$, where I_c is the moment of inertia of the crust and all components strongly coupled to it, and G is a "coupling parameter." For radio pulsars, they argued for a universal G that implies $I_{res}/I_c \geq 0.014$. It is interesting to ask whether this same apparently universal relationship holds for AXPs. Figure 4.17 shows G plotted versus age for radio pulsars and AXPs. As is clear, the Link et al. (1999) relation seems to hold for the radio pulsars, even with increased glitch statistics. Also, AXPs RXS J170849.0−400910 and 1E 1841−045 lie among the radio pulsars, suggesting similar reservoir fractions. However the outlier point, 1E 2259+586, has $G = 0.25$, much larger than the others. Admittedly, for this AXP, a_g is estimated from two glitches only, with the 2002 event greatly dominating, so the values are tentative. Still, the large G, if real, suggests that at least ∼25% of the stellar moment of inertia is in the angular momentum reservoir (see also Woods et al., 2004). We note that the analysis of Link et al. (1999) ignores recovery, important for the 2002 1E 2259+586 glitch, which dominates its a_g. However in the 2002 glitch, the recovery fraction was only ∼19%, so even accounting for recovery, G for 1E 2259+586 is surprisingly high.

As described by Kaspi et al. (2003) and Woods et al. (2004), the 2002 1E 2259+586 glitch was unusual when compared with those of radio pulsars. Specifically the combination of the recovery time scale and the large recovery fraction Q conspired to make the pulsar spin down, for over two weeks post-glitch, at over twice its long-term average spin-down rate. Although spin-down rate enhancements post-glitch are often seen in radio pulsars (e.g., Flanagan, 1990), they usually amount to only a few percent. A remarkably large post-glitch spin-down rate enhancement was seen also in the second glitch of RXS J170849.0−400910 and the first observed glitch of 1E 1841−045, though to a lesser degree than in 1E 2259+586. Of course a much larger increase in spin-down rate post-glitch in RXS J170849.0−400910 or 1E 1841−045 could have been missed due to our sparse sampling.

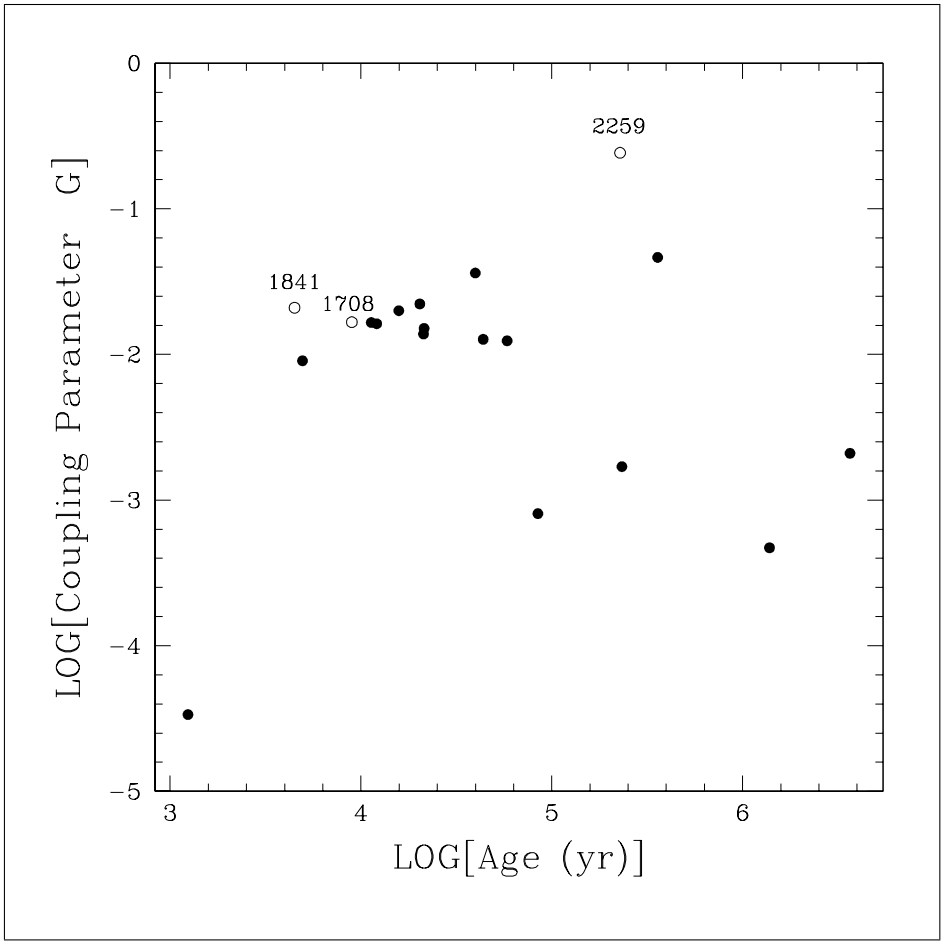

Figure 4.17 "Coupling parameter" G (as defined by (Link et al., 1999); see Section 4.6.1) as a function of spin-down age ($\nu/2\dot{\nu}$). Solid points are radio pulsars with three or more observed glitches, as recorded in the unpublished catalog of A. Lyne. Open circles are AXPs 1E 2259+586, RXS J170849.0−400910, and 1E 1841−045.

One way to quantify the enhanced spin-down more precisely is using Equation 4.2 at $t = 0$, and noticing that the instantaneous spin-down rate at the glitch epoch due to the exponential recovery is given by $\Delta\nu_d/\tau$. Comparing this quantity for the AXP glitches that show recovery with the pre-glitch time-averaged spin-down rate $\dot{\nu}$, we find that for 1E 2259+586 $\Delta\nu_d/\tau = (8.2 \pm 0.6)\dot{\nu}$, $\Delta\nu_d/\tau = (0.64 \pm 0.6)\dot{\nu}$ for RXS J170849.0−400910, and $\Delta\nu_d/\tau = (0.75 \pm 0.08)\dot{\nu}$ for 1E 1841−045, all very large by radio pulsar standards.

The increase in spin-down rate post-glitch, at least for radio pulsars, is generally attributed to a decoupling of a small percentage of the moment of inertia of the star, usually presumed to be part of the crustal superfluid (e.g., Pines & Alpar, 1985), with constant external torque. If the observed AXP recoveries and temporarily enhanced

spin-down rates were interpreted in the same way, it would imply that very large fractions (ranging from 0.4 to 0.9) of the moment of inertia of the star decoupled at the glitch, much larger than the crustal superfluid is reasonably expected to comprise, for any interior equation of state. To avoid this problem, Woods et al. (2004) suggested that a pre-glitch rotational lag between the crust and superfluid might have temporarily reversed at the glitch (see also Alpar et al., 2000). Then the observed larger spin-down rate post-glitch would be due to the crust transferring angular momentum back to the superfluid in order to reestablish equilibrium.

In glitches, the equilibrium angular velocity lag between the crust and more rapidly rotating crustal superfluid is thought to be the origin of glitches. This lag is proposed to develop because the crustal superfluid's angular momentum vortices, in many models (e.g., Alpar et al., 1984b), become pinned to crustal nuclei and hence are hindered from moving outward as the star's crust and associated components are slowed by the external torque. How this lag could reverse is puzzling. Woods et al. (2004) suggested that a twist of magnitude 10^{-2} rad of a circular patch of crust offset in azimuth from the rotation axis could result in sufficient spin-down of the crustal superfluid to account for the properties of the 2002 glitch in 1E 2259+586. They noted further that such a twist also produces X-rays of the luminosity observed in that outburst (Thompson et al., 2002). The absence of any significant radiative changes at the time of largest glitches in RXS J170849.0−400910 and 1E 1841−045 is thus problematic for the crustal twist, and hence lag reversal, model. We note that it has been argued independently that a similar suggested lag reversal between crust and crustal superfluid in the Vela pulsar is unphysical (Jahan-Miri, 2005).

We also note that the large and long-term increase in the magnitude of $\dot{\nu}$ following the large glitch in 1E 1841−045 (see Section 4.3.2) is interesting. Alpar et al. (1993) showed that, ignoring transient terms, $I_{res}/I_c \geq \Delta\dot{\nu}/\dot{\nu}$. For the large 1E 1841−045 glitch, this implies $I_{res}/I_c \geq 0.1$, much larger than has been seen in any radio pulsar.

One possibility that can explain the large G for 1E 2259+586, the large transient increases in the magnitude of $\dot{\nu}$ in all three large glitches, as well as the large extended $\dot{\nu}$ change in the first 1E 1841−045 glitch, is that core superfluid is somehow involved, as it is expected to carry the bulk of the moment of inertia. We note that core glitches have been discussed in the radio pulsar context for some time, albeit for very different reasons. Although Alpar et al. (1984c) argued that the crust and core should be strongly coupled on very short time scales, Jones (1998) found that crustal pinning of superfluid vortices cannot be occurring in neutron stars, because the maximum pinning

force is orders of magnitude smaller than the estimated vortex Magnus force. Donati & Pizzochero (2003) argue that crustal vortex pinning cannot occur for independent reasons. If these authors are correct, pulsar glitches would generally not originate in the crust.

Why would the clearest evidence for core glitches come from AXPs? The interaction between vortices and quantized magnetic flux tubes in a core superfluid could provide resistance to outward motion of vortices (Jones, 1998; Ruderman et al., 1998; Jones, 2002). The interior magnetic field playing a role in vortex pinning as studied by Ruderman et al. (1998) could help explain why such unusual glitch recoveries are seen preferentially in AXPs, which appear to have much larger magnetic fields than conventional radio pulsars. Perhaps the larger field, which implies a higher density of flux tubes, can effectively pin more superfluid vortex lines in a magnetar core; with greater magnetic activity, sudden magnetic reconfigurations would result in large core vortex reconfigurations. We note that Kaspi et al. (2000) and Dall'Osso et al. (2003) argued that the Ruderman et al. (1998) model must be inapplicable to AXPs as that model predicts no glitches for periods greater than ~ 0.7 s. However a more careful reading of Ruderman et al. (1998) reveals that this prediction does not apply for magnetar-strength magnetic fields.

As pointed out by Kaspi et al. (2000), the high temperatures of AXPs, as measured from their X-ray spectra, are at odds with the glitch observations. This is because in the crustal pinning models, the pinning force is highly temperature dependent, such that vortex lines can creep outward much more easily when the temperature is high (e.g., Alpar et al., 1989). This has long been the explanation (e.g., Anderson & Itoh, 1975) for the difference between the Crab and Vela pulsar glitch behaviours: the hotter Crab pulsar glitches less frequently and with smaller frequency jumps because its vortex array can move outward more smoothly. If this were true, AXPs, having measured effective temperatures much higher than the Crab pulsar, should glitch less frequently and with smaller glitch amplitudes than the Crab pulsar, clearly not what is observed. If we abandon the crustal glitch model (at least in AXP glitches) the absence of the expected temperature dependence and the observed universal age correlation could be explained. For example, as discussed by Jones (1998), perhaps relatively smooth outward motion of core vortices could take place before the magnetic flux distribution necessary for impeding them has developed. In this picture, magnetic field distribution, not temperature, is the age-associated property that is a primary factor determining glitch behaviour.

Finally, Campana et al. (2007) argued, on the basis of seven observations of RXS J170849.0−400910 obtained over ∼10 yr, that observed spectral and flux variations were correlated with glitch epoch. They predict, given apparent flux increases seen in mid-2004 and mid-2005, that a glitch should occur soon thereafter (see Fig. 4.14). Indeed as we have shown (see Table 4.4), an unambiguous glitch occurred just following their mid-2005 observation. On the other hand, the first candidate glitch (Table 4.5) occurred when the total flux was very low and apparently declining. Thus, if there is a causal connection between long-term flux variations in RXS J170849.0−400910 and glitches, either this candidate glitch is not a true glitch, or accompanying radiative changes are only relevant to large glitches. The sparsity of the total flux measurements, along with the relatively short time scale of the pulsed flux variations we report in RXS J170849.0−400910, suggest that more dense total flux monitoring could reveal yet unseen fluctuations that are not glitch-associated. The flux variability of RXS J170849.0−400910 is discussed further below.

4.6.2 Radiative Changes

The approximate stabilities of the pulsed fluxes of RXS J170849.0−400910 and 1E 1841−045 (see Section 4.5) are in contrast to those seen for AXPs 1E 2259+586 and 1E 1048.1−5937, both of which have shown large pulsed flux variations (Kaspi et al., 2003; Woods et al., 2004; Gavriil & Kaspi, 2004), and even 4U 0142+61 which has shown a slow pulsed flux increase with time (Dib et al. 2007a, Chapter 2). It is interesting that the phase-averaged flux of RXS J170849.0−400910 has been reported to be highly variable (Rea et al., 2005; Campana et al., 2007 and Fig. 4.14), with changes as large as ∼60% in 2004-2005, while the pulsed flux is not, with maximum contemporaneous change of $< 15\%$. Note that this conclusion holds even when the phase-averaged fluxes, reported in the 0.5–10 keV band, are converted to 2–10 keV, that used for our *RXTE* observations. This suggests an anti-correlation between pulsed fraction and total flux that acts to ensure that the pulsed flux is roughly constant. If so, pulsed flux is not a good indicator of total energy output for RXS J170849.0−400910. A similar anti-correlation between total flux and pulsed fraction has been reported for AXP 1E 1048−5937 (Tiengo et al., 2005; Gavriil et al., 2006a, 2007b), although in that case the pulsed flux does not remain constant (Gavriil & Kaspi, 2004), but follows the phase-averaged flux, just with lower dynamic range (Tam et al., 2008a). For RXS J170849.0−400910, the exactness of the anti-correlation is perhaps surpris-

ing. It could be that all the phase-averaged flux variations are in the 0.5–2 keV band, invisible to *RXTE*. However this would not jibe with the reported correlation of the phase-averaged fluxes with power-law index (Rea et al., 2005; Campana et al., 2007). We also note that in the phase-averaged flux analysis, the equivalent hydrogen column N_H was allowed to vary from observation to observation, rather than being held fixed at a constant. This inconsistency could bias the comparison, though likely not by a large amount. It is tempting to question the relative calibrations of the different instruments used to measure the phase-averaged flux of RXS J170849.0−400910, as the greatest dynamic range is implied by lone *XMM-Newton* and *Swift* observations, and even the two *Chandra X-ray Observatory* observations were obtained with different instruments. Still, admittedly, relative systematic calibration uncertainties are not expected to yield a >50% dynamic range, as is reported. Regular monitoring with a single imaging instrument could settle this issue.

Changes in pulse profile seem to be generic in AXPs and, as discussed above, are not always correlated with glitches, although in some cases, e.g., 1E 2259+586, 4U 0142+61, and possibly RXS J170849.0−400910, they are. Spectrally no clear pattern has emerged. In 1E 2259+586, the pulse profile changes following its 2002 event were broadband (Woods et al., 2004), while in 4U 0142+61 (Dib et al., 2007a) and 1E 1841−045, they appear more prominent at soft energies. In RXS J170849.0−400910, the changes are more apparent in the hard band. In the context of the magnetar model, this hints at crustal motions and surface activity, possibly coupled with magnetospheric activity, with the exact observational manifestation dependent on a variety of factors ranging from viewing geometry to magnetospheric scattering optical depth. Whether ultimately this specific phenomenon will provide insights into the physics of magnetars remains to be seen.

4.7 Summary

We have reported on long-term *RXTE* monitoring of AXPs RXS J170849.0−400910 and 1E 1841−045, which has allowed us to study these sources' timing, pulsed flux, and pulse profile evolutions.

We have discovered four new AXP spin-up glitches, one in RXS J170849.0−400910 and three in 1E 1841−045, plus three new glitch candidates in RXS J170849.0−400910. Nearly all of the "classical" AXPs have now been seen to glitch, clearly demonstrating that this behaviour is generic to the class. Moreover,

in terms of fractional frequency increases, AXPs are among the most actively glitching neutron stars known. Further, unlike radio pulsar glitches, AXP glitches appear to come in two varieties: those that, like radio pulsars, are radiatively quiet in pulsed flux, and those that are, unlike radio pulsars, radiatively loud, including correlated sudden flux increases and pulse profile changes. Thus far there is no clear correlation between AXP glitch size and whether or not it will be radiatively loud or quiet – two of the largest AXP glitches thus far were quiet. We have found a substantial long-term increase in the magnitude of the spin-down rate in the largest glitch from 1E 1841−045, and have also shown that large AXP glitches often have recoveries that are unusual compared with those seen in radio pulsars. Specifically, their spin-down rates in the days and sometimes weeks after a glitch are significantly larger in absolute value than their long-term spin-down rate. This latter effect may indicate a temporary reversal in the crust/crustal superfluid lag at the time of the glitch, or possibly more plausibly, and certainly more intriguingly, glitches of the core, which could explain the transient and extended $\dot{\nu}$ increases, as well as the large G value for 1E 2259+586.

Radiatively, we have found that the pulsed fluxes of RXS J170849.0−400910 and 1E 1841−045 are both fairly steady with time. This is perhaps surprising in light of the large changes in phase-averaged flux that have been reported for RXS J170849.0−400910, and suggests, unless the latter are affected by systematic calibration uncertainties, that pulsed flux for this source, as for AXP 1E 1048.1−5937 (Tiengo et al., 2005), is not a good indicator of AXP X-ray output. Also, the pulse profiles of RXS J170849.0−400910 and 1E 1841−045 both evolve; such evolution appears also to be a generic property of AXPs. However, no clear patterns in AXP pulse profile changes have yet emerged beyond occasional correlation with glitches. Hopefully further monitoring will shed physical light on this phenomenon.

Chapter 5

Monitoring of the Anomalous X-ray Pulsar 1E 1048.1−5937: Long-Term Variability and the 2007 March Event

This chapter is based on the manuscript "Monitoring of the Anomalous X-ray Pulsar 1E 1048.1−5937: Long-Term Variability and the 2007 March Event", published in *the Astrophysical Journal* in 2009 September. (reference: Dib, Kaspi, & Gavriil, 2009b). In the manuscript we conduct a long-term study of the source 1E 1048.1−5937. We focus on the timing anomalies, the pulsed flux changes, and the pulse profile changes near the slow-rise flare of 2001, near the slow-rise flare of 2002, and near the 2007 outburst. The original abstract is below.

After three years of no unusual activity, Anomalous X-ray Pulsar 1E 1048.1−5937 reactivated in 2007 March. We report on the detection of a large glitch ($\Delta\nu/\nu = 1.63(2) \times 10^{-5}$) on 2007 March 26 (MJD 54185.9), contemporaneous with the onset of a pulsed-flux flare, the third flare observed from this source in 10 years of monitoring with the *Rossi X-ray Timing Explorer*. Additionally, we report on a detailed study of the evolution of the timing properties, the pulsed flux, and the pulse profile of this source as measured by *RXTE* from 1996 July to 2008 January. In our timing study, we attempted phase coherent timing of all available observations. We show that in 2001, a timing anomaly of uncertain nature occurred near the rise of the first pulsed flux flare; we show that a likely glitch ($\Delta\nu/\nu = 2.91(9) \times 10^{-6}$) occurred in 2002, near the rise of the second flare, and we present a detailed description of the variations

in the spin-down. In our pulsed flux study, we compare the decays of the three flares and discuss changes in the hardness ratio. In our pulse profile study, we show that the profile exhibited large variations near the peak of the first two flares, and several small short-term profile variations during the most recent flare. Finally, we report on the discovery of a small burst 27 days after the peak of the last flare, the fourth burst discovered from this source. We discuss the relationships between the observed properties in the framework of the magnetar model.

5.1 Introduction

The source 1E 1048.1−5937 is part of the class of sources known as Anomalous X-ray Pulsars (AXPs, see Section 1.2.3). They have generally been characterized by a persistent X-ray luminosity in excess of available spin-down power, although there are exceptions (e.g. AXP 1E 1547.0−5408 in 2006 (Camilo et al., 2007b; Gelfand & Gaensler, 2007)). AXPs are young, isolated pulsars with a large inferred magnetic field ($> 10^{14}$ G). They are detected across the electromagnetic spectrum from the radio (in 2 cases) to the hard X-ray regime. Just like a closely related class of pulsars, the Soft Gamma Repeaters (SGRs), AXPs exhibit a wide range of variability, including but not limited to spectral variability, timing glitches, X-ray bursts, X-ray pulsed and persistent flux "flares", and pulse profile changes. For recent reviews, see Kaspi (2007) and Mereghetti (2008).

The magnetar model (Thompson & Duncan, 1995b; Thompson & Duncan, 1996; Thompson et al., 2002) recognizes the power source of these objects to be the decay of their strong magnetic fields. In this model, the bursts of high-energy emission are thought to occur when the crust succumbs to internal magnetic stresses and deforms. The deformation twists the footpoints of the external magnetic field, driving currents into the magnetosphere and twisting it relative to the standard dipolar geometry. These magnetospheric currents resonantly cyclotron-scatter seed surface thermal photons, giving rise to the non-thermal component of the spectrum, usually fitted to a power-law model below 10 keV. Additionally, the high energy X-ray spectrum of magnetars may be explained by the existence of a plasma corona contained within the closed magnetosphere (Beloborodov & Thompson, 2007).

We have been monitoring 1E 1048.1−5937 with the *Rossi X-ray Timing Explorer* (*RXTE*) since 1997 (see Appendix C for the history of the source). During that time, the AXP has exhibited significant timing and pulsed flux variability. Early regular monitoring showed that the spin-down of 1E 1048.1−5937 was so unstable that phase coherence could be maintained for periods of only a few months at a time (Kaspi et al., 2001). In late 2001, two small bursts were detected from this AXP (Gavriil et al., 2002). The first of the two bursts coincided with the rise of the first of two consecutive slow pulsed flux flares (Gavriil & Kaspi, 2004). The second flare, the longer-lasting of the two, decayed during the second half of 2002, and throughout 2003 and 2004. A third burst was observed from the source during this decay (Gavriil et al., 2006a). While the second pulsed flux flare was ongoing, Mereghetti et al. (2004) and Tiengo

et al. (2005) reported an enhancement in the total flux of the source followed by a decay based on data from X-ray imaging observations. The source was also seen to brighten in the IR at the onset of the second flare (Wang & Chakrabarty, 2002; Israel et al., 2002).

In 2003, during the decay of the second flare, Gavriil & Kaspi (2004) reported order-of-magnitude variations in the spin-down of the pulsar on time scales of weeks to months. In 2004, near the end of the decay of the second flare, the source entered a quiescent period in which the pulsed flux slowly decreased, with much smaller and more monotonic variations in the spin-down. Then, in 2007 March, the source entered a new active phase. Dib et al. (2007b) reported the detection of a sudden spin-up accompanied by pulsed flux increase (hereafter referred to as the third flare) in regular *RXTE* monitoring data. The enhancement in the phase-averaged X-ray and infrared fluxes that accompanied this new flare are discussed in detail in Tam et al. (2008a). Wang et al. (2008) reported on an optical enhancement, and very recently Dhillon et al. (2009) have reported contemporaneous optical pulsations.

Here we present a detailed analysis of all *RXTE* observations of 1E 1048.1−5937 that were taken between 1996 July 03 and 2008 January 09. We report the results of an in-depth analysis of the timing behaviour, pulsed flux changes, and pulse profile variations. These results include but are not limited to those obtained from the analysis of the 2007 March events. We also report on the detection of a fourth small burst on 2007 April 28. Our observations are described in Section 5.2. Our timing, pulsed morphology, and pulsed flux analyses are presented, respectively, in Sections 5.3, 5.4, and 5.5. In Section 5.6, we discuss the most recent burst. Finally, in Section 5.7, we compare the observed properties of 1E 1048.1−5937 to those of the other AXPs, and we discuss the implications of our findings in the framework of the magnetar model.

5.2 Observations

The results presented here were obtained using the proportional counter array (PCA) on board *RXTE* (see Section 1.4).

There are 841 *RXTE* observations of 1E 1048.1−5937 taken between MJD 50294.3 (1996 July 03) and MJD 54474.7 (2008 January 09). We used 821 of them for the analysis presented in this paper. The remaining observations were excluded for various reasons (unusually short observations, pointing errors, or missing files).

The length of the observations varied between 0.75 ks and 45 ks, but most of them

were 2 ks long (see Figure 5.1). The time intervals between the observations are shown in Figure 5.2. The observation frequency varied over the years from once per month to several times per month. Because it was difficult to achieve long-term phase-coherent timing for this source (Gavriil & Kaspi, 2004), in 2002 March, we adopted the strategy of observing it three times every two weeks with three closely spaced observations. The bold vertical line in Figures 5.1 and 5.2 mark when this strategy was implemented. The observing frequency increased to three times per week in 2005 March.

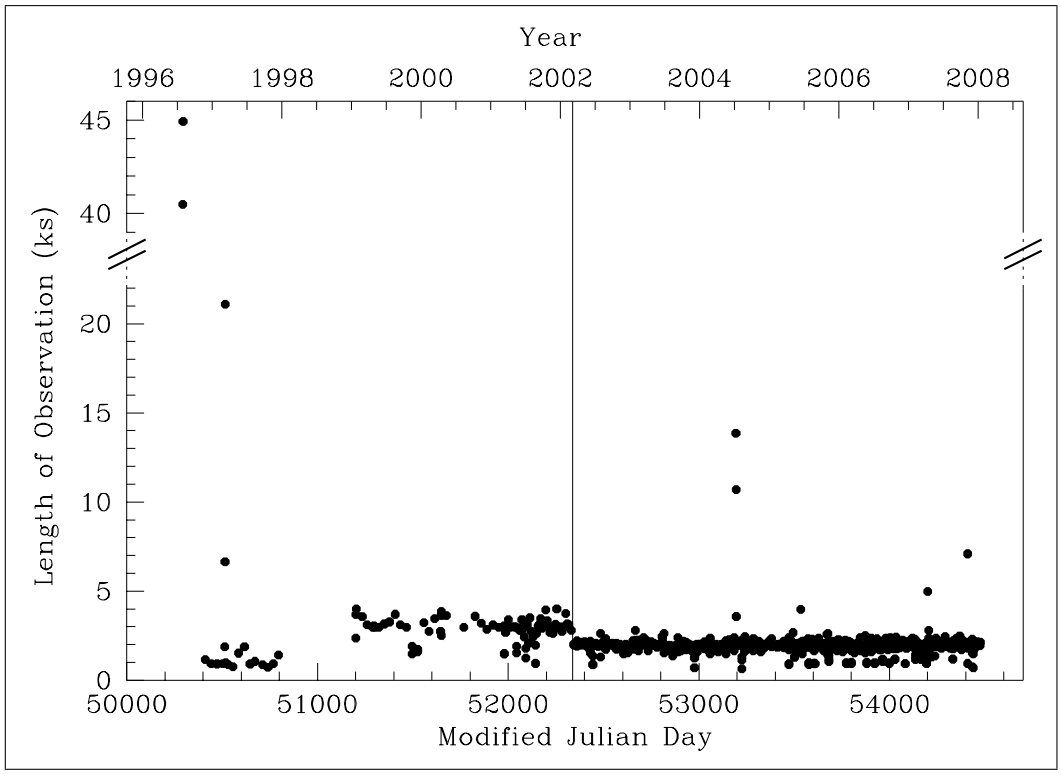

Figure 5.1 Length (on-source integration time) of the *RXTE* observations of 1E 1048.1−5937 used in this paper versus epoch. The solid line indicates when we adopted the strategy of observing the source with sets of three closely spaced observations.

Throughout the monitoring, we used the `GoodXenonwithPropane` data mode to observe this source, except during *RXTE* Cycles 10 and 11 when we used the `GoodXenon` mode. Both data modes record photon arrival times with 1-μs resolution and bin photon energies into one of 256 channels. To maximize the signal-to-noise ratio, we analysed only those events from the top Xenon layer of each PCU.

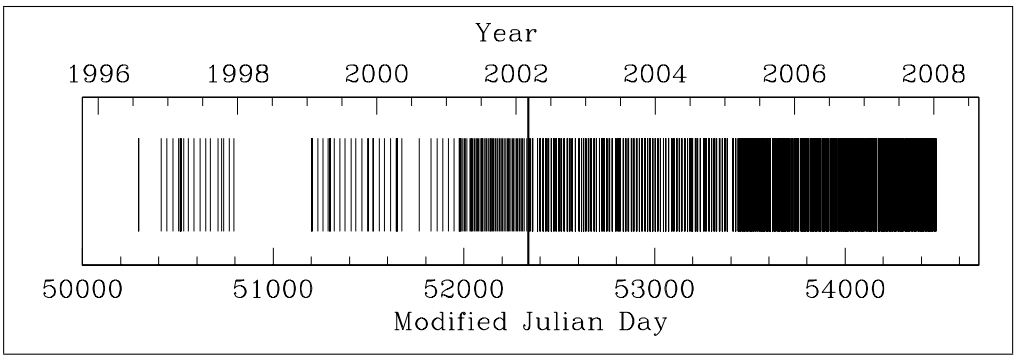

Figure 5.2 Epochs of the observations of 1E 1048.1−5937 used in this paper. The bold line indicates when we adopted the strategy of observing the source with sets of three closely spaced observations.

5.3 Phase-Coherent Timing Study: Analysis and Results

5.3.1 Long-Term Timing

To do the timing analysis, photon arrival times at each epoch were adjusted to the solar system barycenter. Resulting arrival times were binned with 31.25-ms time resolution. In the timing timing analysis, we included only events in the energy range 2−5.5 keV, to maximize the signal-to-noise ratio of the pulse. Each barycentric binned time series was epoch-folded using an ephemeris determined iteratively by maintaining phase coherence as we describe below. When an ephemeris was not available, we folded the time series using a frequency obtained from a periodogram. Resulting pulse profiles, with 64 phase bins, were cross-correlated in the Fourier domain with a high signal-to-noise template created by adding phase-aligned profiles. The cross-correlation returned an average pulse time of arrival (TOA) for each observation corresponding to a fixed pulse phase. The pulse phase ϕ at any time t can usually be expressed as a Taylor expansion,

$$\phi(t) = \phi_0(t_0) + \nu_0(t - t_0) + \frac{1}{2}\dot{\nu}_0(t - t_0)^2 + \frac{1}{6}\ddot{\nu}_0(t - t_0)^3 + \ldots, \qquad (5.1)$$

where $\nu \equiv 1/P$ is the pulse frequency, $\dot{\nu} \equiv d\nu/dt$, etc., and subscript "0" denotes a parameter evaluated at the reference epoch $t = t_0$.

To obtain ephemerides for data prior to 2001, we fitted the TOAs to the above polynomial using the pulsar timing software package `TEMPO`[1]. `TEMPO` also returned an

[1]See http://www.atnf.csiro.au/research/pulsar/tempo.

absolute pulse number associated with each TOA, corresponding to the number of times that the pulsar rotated since the first TOA (also see Section 1.1.9). Since the spin-down of this source was unstable, phase coherence could only be maintained for periods of several months at a time (Kaspi et al., 2001).

After 2002 March 02, we started observing 1E 1048.1−5937 using sets of three closely spaced observations. For data after this date, we adopted a new timing strategy. We broke the list of TOAs into several segments. Each segment lasted between 8 and 16 weeks (4 to 8 weeks after 2005 March), with an overlap between one segment and the next of at least four weeks (2 weeks after 2005 March), except for the week of 2003 April 13 (MJD 52742) where the overlap was of two weeks only, and except at the onset of the flares where there was no overlap. For each two overlapping segments, we used `TEMPO` to fit the TOAs with Equation 5.1 and extract pulse numbers. We then checked that the pulse numbers of the observations present in both segments were the same. This gave us confidence that the two overlapping ephemerides were consistent with each other and that phase coherence was not lost. Combining all overlapping segments between two given dates yielded a time series of absolute pulse number versus TOA. The errors on the TOAs were converted into fractional errors on the pulse numbers. We also used `TEMPO` to fit the TOAs obtained between 2001 and 2002 March 02 with two non-overlapping ephemerides and extracted pulse numbers.

All the pulse numbers obtained using the procedure above were then organized into four different pulse number versus TOA time series: a time series covering the time interval between 2001 and the onset of the first flare (2001 March to 2001 October), a time series covering the interval between the onset of the first flare and that of the second (2001 November to 2002 April), a time series covering the interval between the onset of the second flare and that of the third (2002 May to 2007 March), and a time series covering the interval between the onset of the third flare and the date of the last observation included in this paper (2007 March to 2008 January).

Because of the irregularities in the spin-down of AXP 1E 1048.1−5937, timing solutions spanning long periods of time required the use of very high-order polynomials which tended to oscillate at the end points of fitted intervals. Instead of using these polynomials, we used splines. A spline is a piecewise polynomial function. It consists of polynomial pieces of degree n (here $n = 5$) defined between points called knots. The two polynomial pieces adjacent to any knot share a common value and common derivative values at the knot, through the derivative of order $n-2$ (see Dierckx, 1975 for more details about splines). We fit a spline function through each of the above

time series, weighted by the inverse of the square of the fractional errors on the pulse numbers. To minimize oscillations in the spline due to noise, we set the spline smoothing parameter to allow the RMS phase residual obtained after subtracting the spline from the data points to be twice the average 1σ uncertainty in the pulse phase. The smoothing parameter controls the tradeoff between closeness and smoothness of fit by varying the polynomial coefficients and the spacing between the knots. We found the uncertainties on the spline by adding Gaussian noise to our data points 500 times, with mean equal to the 1σ uncertainty on each data point, fitting each time with a spline, averaging all the splines, and finding the standard deviation at each point.

The derivative of the spline function is the frequency of the pulsar, and the second derivative of the spline function is the frequency derivative of the pulsar.

The results of this timing analysis are presented in Figure 5.3.

The top panel of Figure 5.3 shows frequency versus time. The first horizontal double arrow indicates a time interval in which 1E 1048.1−5937 was not observed with *RXTE*. The second horizontal arrow indicates a time interval in which data were so sparse that multiple phase-coherent timing solutions could be found. The first two plotted curves are ephemerides obtained using `TEMPO` only. They are consistent with the first three ephemerides reported in Kaspi et al. (2001). The remaining plotted curves are ephemerides obtained from taking the derivatives of spline functions. The slope of the diagonal dotted line is the average spin-down of the pulsar. The deviations from the average spin-down are clear to the eye. Note that since the onsets of the first two flares were accompanied by significant pulse profile changes, we did not include the data from the two weeks surrounding each in this Figure (see Sections 5.3.2, and 5.3.3).

The second panel of Figure 5.3 shows the timing residuals for all phase-connected intervals. The RMS residuals for the two intervals fitted with `TEMPO` are 2.4% and 1.9% of a pulse cycle. The RMS residuals for the four intervals fitted with splines are 3.2%, 3.5%, 1.2%, and 2.1% of the pulse cycle. The slow increase in the values of the uncertainties between 2004 and the onset of the third flare reflects a decrease in signal-to-noise that is due both to a decrease in the pulsed flux of the source and to a decrease in the effective number of operational PCUs on board *RXTE*. The uncertainties are smaller after the flare due to the rise in the pulsed flux.

The third panel of Figure 5.3 shows the frequency versus time after having subtracted the long-term average linear trend shown in the top panel. The two early ephemerides were obtained with `TEMPO`. The curves, representing the remaining

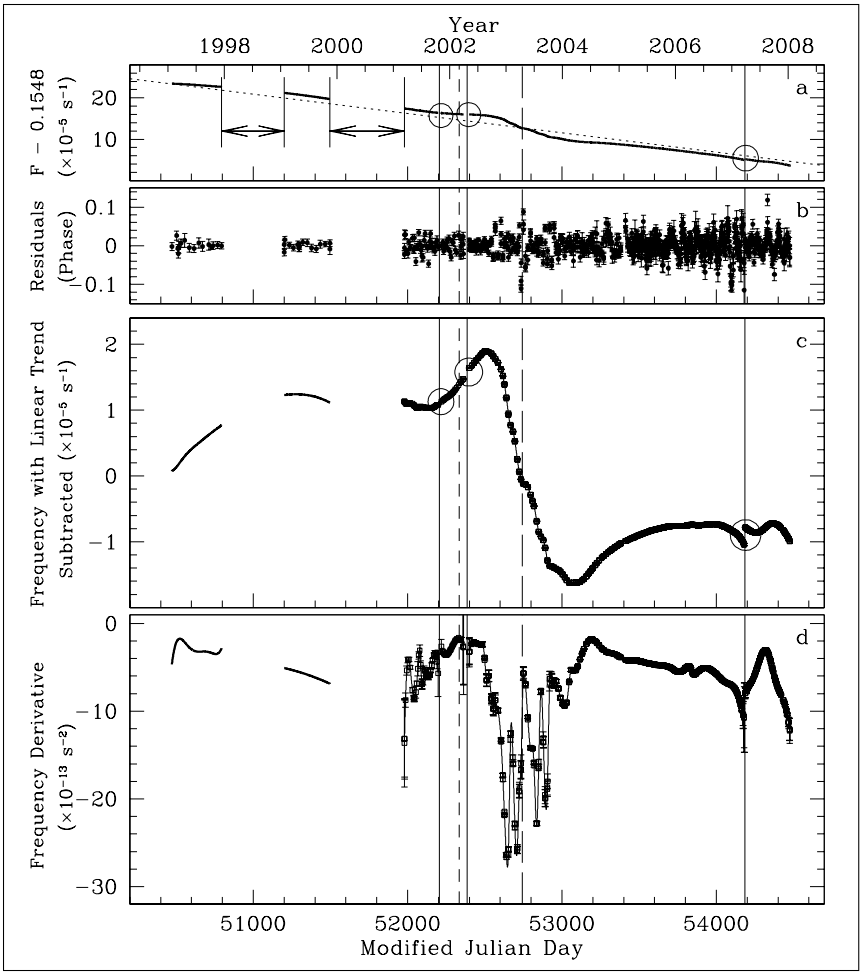

Figure 5.3 Timing properties of AXP 1E 1048.1−5937. (*a*) Long-term evolution of the frequency of 1E 1048.1−5937. The slope of the diagonal dotted line is the average spin-down of the pulsar ($\sim -5.4 \times 10^{-13}$ s^{-2}). The deviations from the average spin-down are clear to the eye. The three circles are centered at the start of the three pulsed flux flares (see Figures 5.10 and 5.16), and mark the location of a timing anomaly, a likely glitch, and a glitch. (*b*) Timing residuals obtained after subtracting the TOAs from the ephemerides plotted in panel a. (*c*) Long-term frequency evolution with the long-term average spin-down subtracted. For the first two plotted curves, the error bars are smaller than the width of the lines. The three circles are centered at the start of the three pulsed flux flares, and mark the location of a timing anomaly and two glitches (see Sections 5.3.2−5.3.4 in the text). (*d*) Long-term evolution of the frequency derivative of the pulsar. *All panels:* The three solid lines indicate the onset of the three pulsed flux flares. The short-dashed line marks the epoch when we started observing the source in sets of three closely spaced observations. The long-dashed line indicates the epoch when the overlap in the partial ephemerides was for a single set of three observations (see Section 5.3.1 for details).

ephemerides, were obtained from derivatives of splines. The points marked as squares are the values of the derivative evaluated at the epochs at which observations were taken. A detailed timing analysis of data inside the circles is done in Sections 5.3.2, 5.3.3, and 5.3.4.

We note in this panel that the spin-down of the pulsar was significantly enhanced starting a few months after the onset of the second flare, a phenomenon which lasted until 2004. In this period of time the pulsar's rotational evolution became much noisier and phase-coherent timing would not have been possible without the availability of sets of three closely spaced observations. Note that Gavriil & Kaspi (2004) previously reported this phenomenon without using long-term phase-coherent timing: they obtained individual frequency measurements by finding the frequency that best fit each three observations.

In the same panel, we can also see that the pulsar then entered a quiescent period in mid-2004 during which the frequency evolution was closer to the long-term average. Note that even though the frequency evolution in the pre-2000 and post-2004 years looks stable, an analysis performed by Archibald et al. (2008) of 1E 1048.1−5937 data between 2004 and 2007 reveals that the amplitude of the timing noise (deviations from a simple spin-down) of this AXP is significantly larger than that seen thus far for any other AXP.

Finally, in 2007 March, the pulsar underwent one of the largest glitches yet observed in an AXP. The frequency jump inside the third circle in Figure 5.3 is clear to the eye. This is discussed in detail in Section 5.3.4.

The fourth panel of Figure 5.3 shows the frequency derivative versus time. The first two plotted curves are obtained with `TEMPO`. The remaining four curves, spanning data from 2001 to 2008, and separated by the solid lines that mark the onset of the three flares, are obtained by taking the second derivative of spline functions. The points marked as squares are the values of that derivative evaluated at the epochs where observations were taken. Note that the large error bars at the beginning and end of each curve reflect the fact that the extremes of the curves are not well constrained by the data.

We note in this panel that, starting a few months after the onset of the second flare, the pulsar underwent frequent and significant variations in its spin-down on time scales of weeks to months. The variations noted in this plot are consistent with those reported by Gavriil & Kaspi (2004) although our analysis here has higher time resolution. This is because in that study, the spin-down was determined in short inter-

vals by calculating the slope of three consecutive frequency measurements, and each frequency measurement was obtained by phase-connecting a group of three closely spaced observations.

More specifically, we note that $\dot{\nu}$ was stable from 29 days preceding the peak of the second flare, until 41 days following the flare, fluctuating around the value $\sim -2.3\times10^{-13}$ s^{-2} with variations on the order of 0.08×10^{-13} s^{-2} every two weeks. Then, from the 41 days to 141 days after the flare, $\dot{\nu}$ dropped an average of 2×10^{-13} s^{-2} every two weeks. The very rapid changes in $\dot{\nu}$ started 141 days after the peak of the flare. From 141 to 196 days after the flare, $\dot{\nu}$ dropped an average of 5.6×10^{-13} s^{-2} every two weeks. $\dot{\nu}$ then fluctuated between -26×10^{-13} s^{-2} and -6×10^{-13} s^{-2} 4 times in the space of 450 days. During this period of unusual activity, there are four significant upward jumps in $\dot{\nu}$. Although none of the measured peak values of $\dot{\nu}$ is positive, spin-up glitches could still have occurred between measurements.

This panel also shows that the frequency derivative stabilized between 2004 and 2007. It then appears to have decreased before the large glitch associated with the third flare. However, this decrease stops in the two weeks preceding the flare (see Section 5.3.4).

After the glitch, $\dot{\nu}$ increased by $\sim 0.33\times10^{-13}$ s^{-2} every week, rising from $\sim -7.7\times10^{-13}$ s^{-2} to -2.9×10^{-13} s^{-2} in $\sim$130 days before starting to fall continuously again at the same rate. A preliminary analysis of the most-recent data shows that in 2008 May, the pulsar appears to have entered a new noisy phase (not shown in the Figure). Weekly variations in $\dot{\nu}$ starting roughly a year after the onset of the third flare are similar to, but a factor of $\sim$2 smaller, than the variations observed starting 141 days after the peak of the second flare. This noisy phase was still ongoing as of 2008 November 17, the date of submission of the manuscript on which this Chapter is based. For a continuation of the data set see Chapter 6.

5.3.2 Timing Around the First Flare

In this Section we describe the analysis of the TOAs in the 14 weeks surrounding the onset of the first flare (MJD 52254 − 52163). We show here that a previously unreported and puzzling timing anomaly occurred and was coincident with the rise of the flare. The results are presented in Figure 5.4.

In panel a, two lines, representing two ephemerides, are plotted. The left ephemeris is obtained by fitting a frequency and a frequency derivative through the pre-flare data,

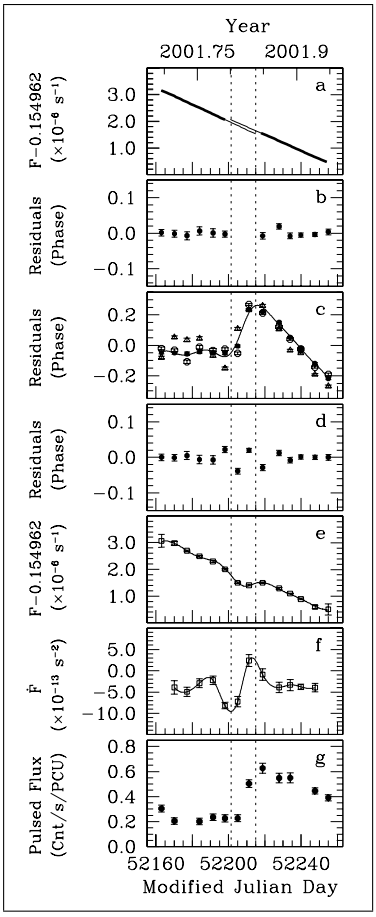

Figure 5.4 Timing properties of AXP 1E 1048.1−5937 near the onset of the first flare (MJD 52254 − 52163). The two dotted lines enclose the data from the week preceding and following the onset of the flare. (*a*) Frequency versus time, showing the TEMPO-obtained pre-flare and post-flare ephemerides, not including the data points between the dotted lines. The lines shown between the double dotted lines are extentions of the pre-flare and the post-flare ephemerides. (*b*) Timing residuals corresponding to panel a. (*c*) Data points: timing residuals for three different sets of TOAs obtained after subtracting the TOAs from the pre-flare ephemeris (see Section 5.3.2 for details). Solid curve: the spline that best fit the pre-flare and post-flare TOAs subtracted from the pre-flare ephemeris. (*d*) Timing residuals obtained after subtracting the original TOAs from the spline. (*e*) Frequency obtained by evaluating the derivative of the spline shown in panel c. (*f*) Frequency derivative obtained by evaluating the second derivative of the spline shown in panel c. (*g*) The 2−10 keV RMS pulsed flux of the pulsar near the onset of the first flare.

excluding the data between the dotted lines. The right ephemeris is obtained by fitting the same parameters through the post-flare data, again excluding the data between the dotted lines. If we extend both ephemerides toward each other, it appears that a spin-up glitch of size $\Delta\nu \sim 1 \times 10^{-7}$ s^{-1} occurred near the onset of the flare. The residuals obtained from the two fits are presented in panel b.

In Section 5.4, we show that the pulsar underwent pulse profile changes near the onset of the flares. Because we could not be certain that our TOAs, obtained by cross-correlating the profiles of the individual observations with a long-term template, were not affected by pulse profile changes, we created two additional sets of TOAs. The first additional set was obtained by aligning the tallest peak in the each profile with the tallest peak in the template, and extracting a phase offset The second additional set was obtained by aligning the lowest point in each profile with the lowest point in the template.

In panel c, we subtracted all three sets of TOAs from the pre-flare ephemeris and plotted the residuals. The points marked with solid circles represent the residuals obtained from the original set of TOAs. The points marked with empty circles and empty triangles represent the residuals obtained from the two additional sets of TOAs. While the scatter in the residuals corresponding to the additional sets of TOAs is large, note how all three sets of residuals follow the same trend, indicating that it is unlikely to be caused by pulse profile changes. However, it cannot be ruled out that the trend is caused by the motion of the active region. The difference in phase between each solid circle and the corresponding empty circle and empty triangle represents our uncertainty in determining a fiducial point on the pulsar. Also note that subtracting a full phase turn from all post-flare residuals, which would yield a different timing solution, would require a non-zero phase jump to have occured near the onset of the flare, which would imply an unphysically large torque on the star.

Assuming the pulse numbers on which the residuals in panel c are based are correct, we fit the pulse arrival times from the 14 weeks surrounding the start of the flare with a spline. The spline subtracted from the pre-flare ephemeris is the curve shown in panel c. The residuals after subtracting the TOAs from the spline are shown in panel d. These residuals are clearly not featureless.

The first derivative of the obtained spline, which is the frequency of the pulsar, is shown in panel e. Notice the anomalous "dip" in frequency surrounding the onset of the flare. The rapidly changing frequency derivative is shown in panel f. The RMS pulsed flux is shown for reference in panel g (see Section 5.5 for more details on how

the pulsed flux is calculated). Notice how the dip in the frequency of the pulsar started before the rise in the pulsed flux.

To summarize, a timing anomaly occurred near the onset of the first flare. Careful analysis shows that it is not consistent with a simple spin-up glitch, but with a gradual slow down lasting 2−3 weeks, followed by a recovery. The rotational event appears to have preceded the flux event.

5.3.3 Timing Around the Second Flare

In this Section we describe our analysis of the TOAs in the 28 weeks surrounding the onset of the second flare (MJD 52282 − 52485). We have discovered that a likely spin-up glitch occurred during the week when the pulsed flux started rising. We found this glitch while we were trying to fit all available data with short simple overlapping ephemerides and encountered a discontinuity. The results are presented in Figure 5.5.

Once again, because of pulse profile changes around the start of the flare, we generated two additional sets of TOAs by correlating the highest and lowest points of the individual pulse profiles with the long-term template and extracting phase differences. The residuals after subtracting all three sets of TOAs from the pre-flare ephemeris are shown in panel a of Figure 5.5. Once again, the scatter in the residuals obtained from the additional sets of TOAs is larger than that obtained from the standard TOAs, but all three sets follow the same trend.

The trend in the residuals shown in panel a indicates that a glitch oaccurred. However, due to the finite resolution of the data (sets of three closely spaced observations obtained every two weeks, starting in 2002 March), which is particularly problematic given the extreme timing noise of this source, a rapid non-instantaneous variation cannot be ruled out. The curvature following the glitch is due to a change in the frequency derivative rather than glitch recovery. Because the largest pulse profile changes occurred in the week the pulsed flux started rising (see Section 5.5), there is large scatter in the three standard TOAs obtained then. Because of this scatter, it was not possible to determine if the glitch occurred before or after the pulsed flux started to rise. The glitch epoch was MJD 52386.0 ± 1.5. The dates of the first three observations having a larger pulsed flux than the pre-flare long-term average are MJD 52385.5, 52386.6, and 52386.7. The change in the frequency at the time of the glitch was $\Delta\nu = 4.51(14) \times 10^{-7}$ s^{-1} ($\Delta\nu/\nu = 2.91(9) \times 10^{-6}$). The change in frequency derivative was $\Delta\dot{\nu} = -4.10(15) \times 10^{-14}$ s^{-2}.

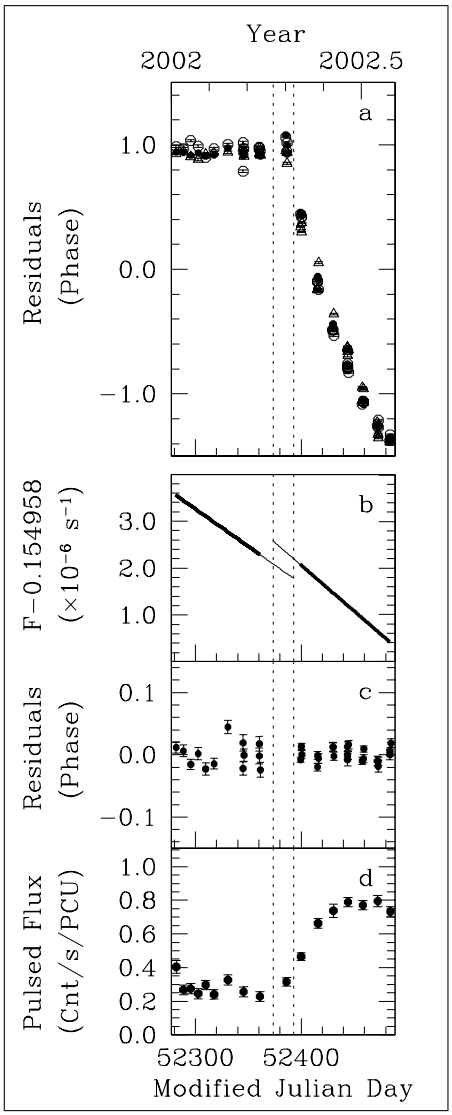

Figure 5.5 Timing properties of AXP 1E 1048.1−5937 near the onset of the second flare (MJD 52282 − 52485). The two dotted lines enclose the data from the week when the pulsed flux started rising. (*a*) Timing residuals for three different sets of TOAs obtained after subtracting the TOAs from the pre-flare ephemeris (see Section 5.3.3 for details). (*b*) Frequency versus time obtained from the original set of TOAs showing the `TEMPO`-obtained pre-flare and post-flare ephemerides, not including the data points between the dotted lines. (*c*) Timing residuals corresponding to panel b. (*d*) The 2−10 keV RMS pulsed flux of the pulsar near the onset of the second flare.

The pre-flare and post-flare ephemerides are shown in panel b of Figure5.5. Note the difference in slope between them. The residuals are shown in panel c. The pulsed flux is shown for reference in panel d. Each pulsed flux data point is the average of the pulsed flux values obtained from three closely spaced observations.

To summarize, a glitch, or a very rapid change in the frequency, as well as a significant change in the frequency derivative, occurred during the week the second pulsed flux flare started rising. Because of the large uncertainty on the glitch epoch, which is due to the pulse profile changes near the onset of the flare, it is not possible to determine which happened first, the rise in the pulsed flux, or the frequency jump.

5.3.4 Timing Around the Third Flare

In this Section we report on our analysis of the TOAs in the 14 weeks surrounding the onset of the third flare (MJD 54131 – 54223). We show that a large spin-up glitch occurred coincident with the rise of the pulsed flux. The results are presented in Figure 5.6.

We first plotted the pre-flare and post-flare ephemerides in panel a. The pre-flare ephemeris consists of a frequency and three frequency derivatives. The post-flare ephemeris consists of a frequency and a single frequency derivative. The residuals are shown in panel b. Note how in panel a, the pre-flare curve appears to flatten in the two weeks preceding the glitch, indicating that the frequency derivative was becoming less negative. This argues that it is important to choose data as close to the glitch as possible when fitting for the glitch parameters.

In panel c, we show the pre-glitch and the post-glitch timing residuals after subtracting the TOAs from an ephemeris that includes the frequency and frequency derivative that best fit the pre-glitch data. The observed trend in the residuals clearly indicates that a large glitch occurred. To obtain the glitch parameters, we performed two different fits with `TEMPO`.

For the first fit, we included data from the 14 weeks surrounding the glitch epoch. We subtracted the TOAs from an ephemeris consisting of the best-fit ν, $\dot{\nu}$, and discrete jump in ν and $\dot{\nu}$ at the glitch epoch. The timing residuals for the first fit are shown in panel d. For the second fit, we included data from the 6 weeks surrounding the glitch epoch. We subtracted the TOAs from an ephemeris consisting of the same set of parameters. The timing residuals for the second fit are shown in panel e. As expected, the best-fit jump in $\dot{\nu}$ at the glitch epoch was significantly larger for the first fit than

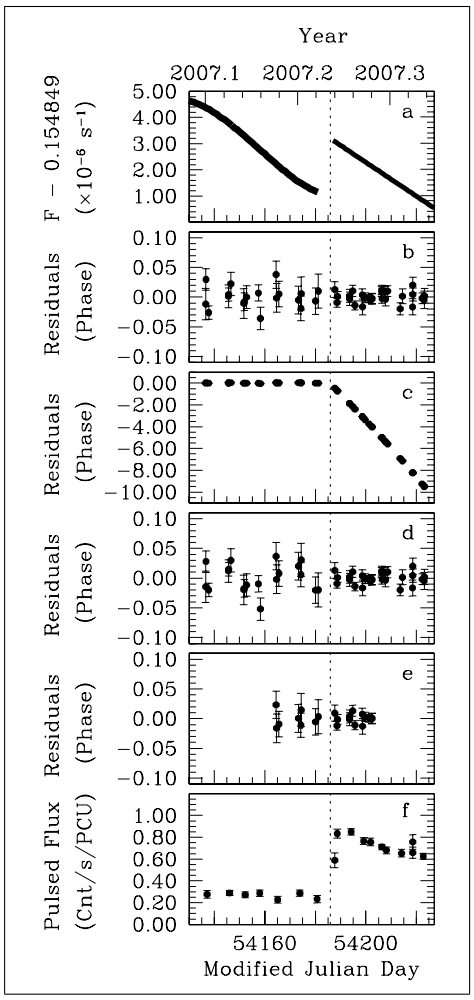

Figure 5.6 Timing properties of AXP 1E 1048.1−5937 near the onset of the third flare (MJD 54131 − 54223). The dotted line marks the epoch of a large glitch (see Section 5.3.4 for details). (*a*) Frequency versus time of the pre-flare and post-flare ephemerides. The pre-flare ephemeris consists of a frequency and three frequency derivatives. Notice how the curve is flatter in the two weeks preceding the flare. The post-flare ephemeris consists of a frequency and a single frequency derivative. (*b*) Timing residuals corresponding to panel a. (*c*) Residuals obtained after subtracting pre-flare and post-flare TOAs from a pre-flare ephemeris consisting of a frequency and frequency derivative. The change in the slope marks the occurrence of the glitch. (*d*) Timing residuals obtained after fitting a glitch through the data for the 14 weeks surrounding the glitch. The RMS phase residual is 1.6%. (*e*) Timing residuals obtained after fitting a glitch through the data for the 6 weeks surrounding the glitch. The RMS phase residual is 0.98%. (*f*) The 2−10 keV RMS pulsed flux of the pulsar near the onset of the third flare (see Section 5.3.4 for details).

for the second fit ($1.76(8)\times10^{-13}$ s^{-2} versus $6(4)\times10^{-14}$ s^{-2}). This is because of the rapid change in the frequency derivative in the few weeks preceding the glitch.

Table 5.1. Local ephemeris of 1E 1048.1−5937 near the 2007 glitch[a]

Parameter	Value
MJD range	54164.545−54202.475
TOAs	21
Epoch (MJD)	54185.912956
ν (s^{-1})	0.15484969(6)
$\dot{\nu}$ (s^{-2})	$-8.2(5)\times10^{-13}$
Glitch Epoch (MJD)	54185.912956
$\Delta\nu$ (s^{-1})	$2.52(3)\times10^{-6}$
$\Delta\dot{\nu}$ (s^{-2})	$6(4)\times10^{-14}$
RMS residual (phase)	0.0098

[a]Numbers in parentheses are TEMPO-reported 1σ uncertainties.

From the second fit, the total frequency jump observed at the glitch epoch was $\Delta\nu = 2.52(3) \times 10^{-6}$ s^{-1} ($\Delta\nu/\nu = 1.63(2) \times 10^{-5}$)[2]. The glitch epoch, determined by setting the phase jump to zero at the time of the frequency jump, is MJD 54185.912956 (2007 March 26). For a complete list of the fit parameters, see Table 5.1.

The pulsed flux is shown for reference in panel f of Figure 5.6. Each plotted pulsed flux data point is the average of the pulsed flux values obtained from three closely spaced observations, except in two instances (see Section 5.5). The date of the last pre-flare observation was MJD 54181.32. The date of the first observation with a large pulsed flux is MJD 54187.67. As explained in Section 5.5, it is difficult to determine if the pulsed flux of the latter observation is lower than the pulsed flux peak, due to noise. Once again, we cannot determine whether the glitch occurred before or after the pulsed flux started rising.

To summarize, a large glitch occurred on MJD 54185, two days before the first observation having a large pulsed flux. The change in the frequency derivative at the time of the glitch was not significant, but it was preceded by three weeks where the magnitude of $\dot{\nu}$ was decreasing, which followed a rapid decrease that lasted several

[2]This is different from the value in Dib et al. (2007b) because of a typographical error: the authors reported the value of $\Delta\nu$ instead of reporting the value of $\Delta\nu/\nu$.

weeks. Because of the possibility that the pulsed flux of the first observation after the onset of the flare is consistent with the peak of the flare, we were not able to determine which happened first, the rise in the pulsed flux, or the glitch.

5.4 Pulse Profile Study: Analysis and Results

Tam et al. (2008a) reported pulse profile changes in 1E 1048.1−5937 from imaging data near the third flare. In this Section we confirm their findings and report on additional pulse profile changes near the first two flares.

We performed a first pulse profile analysis using FTOOLS version 5.3.1[3]. Data from PCU 0 were included in the analysis up to 2000 May 12, when it lost its propane layer. Data from PCU 1 were included in the analysis up to 2006 December 25, when it lost its propane layer. We used the procedure described in detail in Dib et al. (2007a) (Chapter 2) to extract a pulse profile for each observation in the 2−10 keV band. We used 64 phase bins. When a local ephemeris was not available, we folded the data at a pulsar period extracted from a periodogram. We verified that the results of the folding are not very sensitive to the precise period used. We then aligned the 64-bin profiles with a high signal-to-noise template using a cross-correlation procedure similar to that described in Section 5.3.1.

1E 1048.1−5937 was monitored with *RXTE* from 1997 to 2008. To do the first pulse profile analysis, we divided this time span into many segments, shown with letters at the bottom of Figure 5.7.

For each time interval, we summed the aligned profiles, subtracted the DC component from the summed profile, and scaled the resulting profile so that the value of the highest bin is unity and the lowest point is zero. The results are presented in Figure 5.7 with the time intervals marked in the top left corner of each profile. The different profile qualities are due to the segments having different total exposure, and to changes in the pulsed flux of the pulsar.

To look for pulse profile changes on a smaller time scale, we performed a second pulse profile analysis. We extracted a pulse profile for each observation in the 2−10 keV band using all available PCUs to maximize the signal to noise. We used 32 phase bins. We aligned the obtained profiles with the high signal-to-noise template and subtracted the respective average from each of the aligned profiles and from the template. For each observation, we then found the scaling factor that minimized the reduced χ^2 of

[3]http://heasarc.gsfc.nasa.gov/ftools

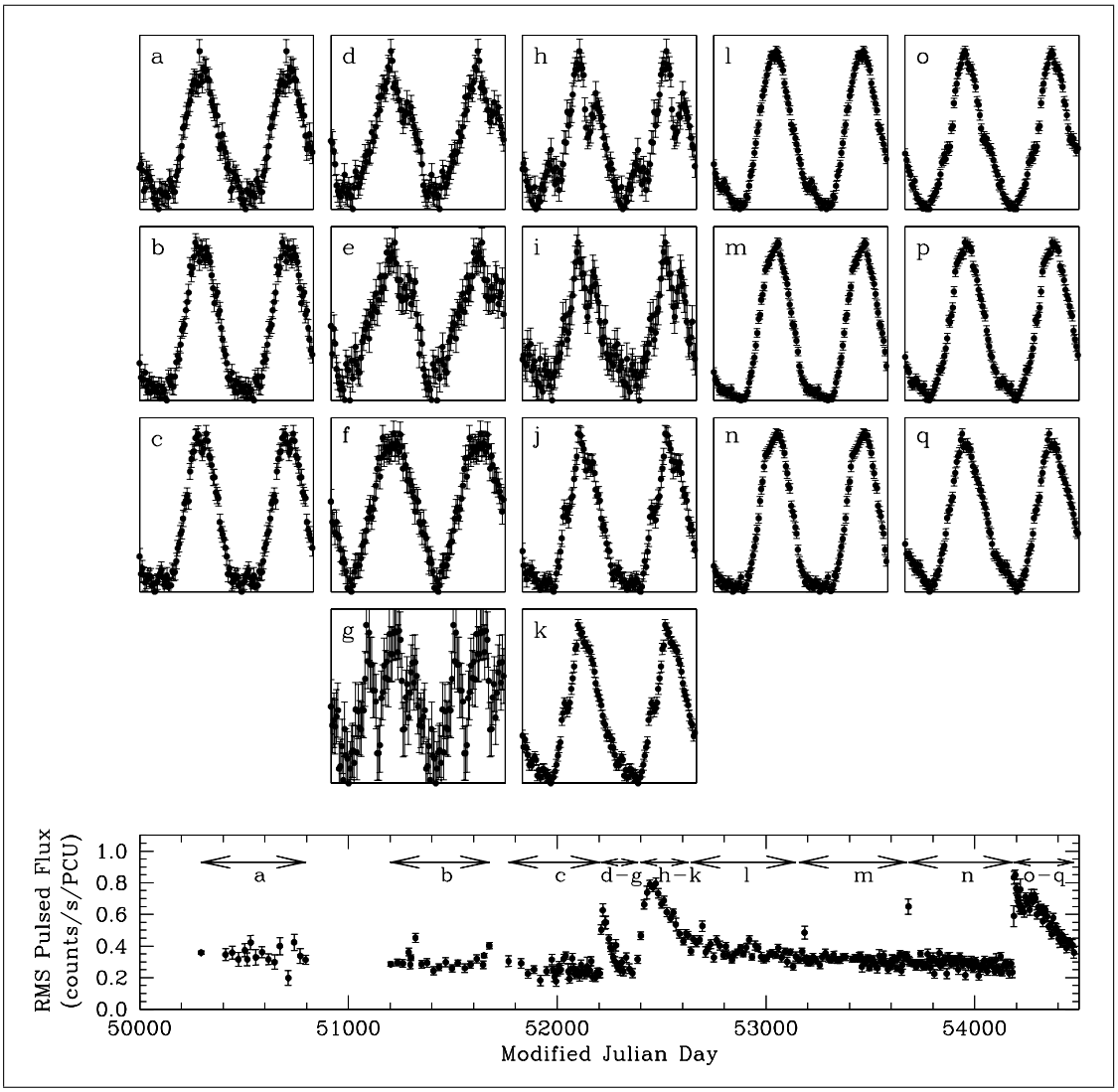

Figure 5.7 Normalized 2−10 keV pulse profiles of 1E 1048.1−5937 from 1997 to 2008. The letter shown in the top-left corner of each plot refers to the time segments marked by arrows in the bottom plot, where the 2−10 keV RMS pulsed flux is shown for reference.

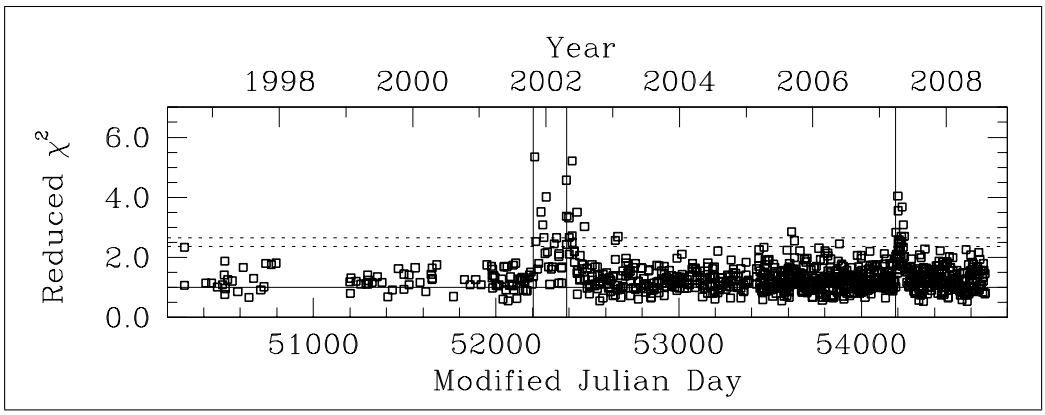

Figure 5.8 Reduced χ^2 statistics versus time, calculated after subtracting the scaled and aligned profiles of the individual observations from a high signal-to-noise template. The solid vertical lines indicate the onsets of the flares. The solid horizontal line indicates a reduced χ^2 of 1. The lower dotted line corresponds to the 2 σ significance level. The upper dotted line corresponds to the 3 σ significance level.

the difference between the scaled profile and the template. The obtained reduced χ^2 values are plotted in Figure 5.8.

Figure 5.7 shows for the first time that the broad pulse profile of 1E 1048.1−5937 developed a small side-peak during the rise and the fall of the first flare (segments d and e). The rise of the second flare (segments g and h) was marked by large profile changes in which the pulse profile was clearly multi-peaked. The pulse profile slowly returned to its long-term average shape while the flare was decaying (segments i, j, and k). There were no significant pulse profile changes in the following three years of quiescence (segments l, m, and n), although the profiles in segments m and n seem to have triangular peaks, more so than in segments b, c, and l. Figure 5.8 confirms the pulse profile changes near the first two flares, and additionally suggests that small occasional profile changes may occur in individual observations throughout segments a, b, c, l, m, and n, but only at the $\sim$2−3σ level.

It appears from Figure 5.7 that the pulse profiles in segments o, p, and q, corresponding to the decay of the third flare, were stable and presented no significant deviations from the long-term average on long time scales. However, Figure 5.8 shows that many significant pulse profile changes occurred on short time scales during the decay of the third flare. The changes are clearly visible in the pulse profiles of individual observations having a high signal-to-noise ratio (particularly long observations, or observations with a large numbers of operational PCUs). An example of two such profiles is presented in Figure 5.9. The top profile is obtained from a 6 ks-long observation

taken on 2007 April 09 (14 days after the glitch epoch) with two operational PCUs. The second profile is obtained from a 2 ks-long observation taken on 2007 May 03 (38 days after the glitch epoch). These short-term pulse profile changes are similar to the ones reported in Tam et al. (2008a). They were seen mostly in the first two months following the onset of the flare, and occurred less often in the next months, although this may be partially due to the reduction in signal-to-noise due to the pulsed flux falling. Several months after the flare small occasional profile changes may be present, but only at the $\sim 2\sigma$ level.

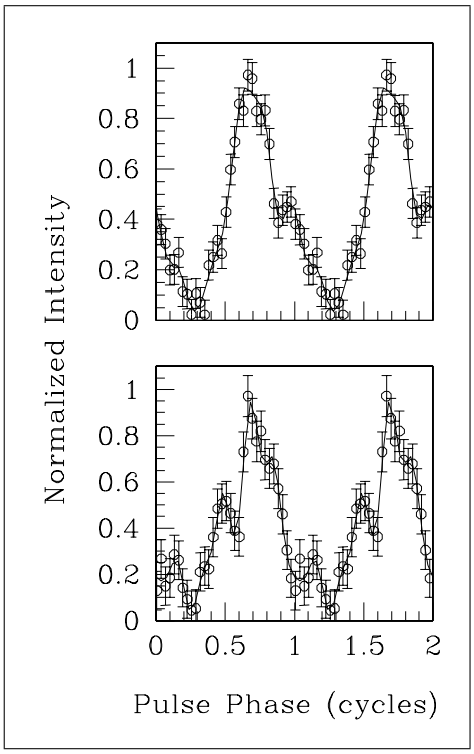

Figure 5.9 Normalized 2−10 keV pulse profiles from two observations taken during the decay of the third flare. The first observation was taken on 2007 April 09 (14 days after the glitch epoch). The second observation was taken on 2007 May 03 (38 days after the glitch epoch). The multiple peaks in the profile are obvious.

5.5 Pulsed Flux Study: Analysis and Results

To obtain a pulsed flux time series for 1E 1048.1−5937, for each observation, we created a pulse profile (in units of count rate per PCU) using the same procedure as in Section 5.4. Data from PCUs 0 and 1 were excluded after the loss of their respective propane layers, because an independent analysis of data from PCU 0 of AXP

4U 0142+61 revealed spectral modeling irregularities after the loss of the propane layer (Dib et al., 2007a). Pulse profiles were generated in three bands: 2−4 keV, 4−10 keV, and 2−10 keV. For each folded profile, we calculated the RMS pulsed flux,

$$F_{RMS} = \sqrt{2\sum_{k=1}^{n}((a_k{}^2 + b_k{}^2) - (\sigma_{a_k}{}^2 + \sigma_{b_k}{}^2))}, \tag{5.2}$$

where a_k is the $k^{\rm th}$ even Fourier component defined as $a_k = \frac{1}{N}\sum_{i=1}^{N} p_i \cos(2\pi ki/N)$, $\sigma_{a_k}{}^2$ is the variance of a_k, b_k is the odd $k^{\rm th}$ Fourier component defined as $b_k = \frac{1}{N}\sum_{i=1}^{N} p_i \sin(2\pi ki/N)$, $\sigma_{b_k}{}^2$ is the variance of b_k, i refers to the phase bin, N is the total number of phase bins (here N=64),, p_i is the count rate in the $i^{\rm th}$ phase bin of the pulse profile, and n is the maximum number of Fourier harmonics used; here n=5.

We verified using an independent pulsed flux estimator calculated from the area under the pulse (i.e. insensitive by definition to pulse shape, Archibald et al. 2009) that the trends seen in the RMS pulsed flux of 1E 1048.1−5937 are not a consequence of changes in the pulse profile. The results of the pulsed flux analysis are presented in Figure 5.10.

In the top panel, we show the pulsed flux results in the 2−10 keV band. For observations taken before 2002 March 02 (date marked with a dashed line), we plotted the pulsed flux values obtained from individual observations. After 2002 March 02, we plotted the average of the pulsed flux values of each set of three closely spaced observations, with the exception of 4 observations. The 4 observations are indicated with arrows located along the bottom of the panel. The first observation, on 2004 June 29, was not averaged with its neighbors because a burst occurred within the observation (Gavriil et al., 2006a). The second, on 2005 November 08, is an observation with an anomalously high pulsed flux. The third, on 2007 March 28, is the first observation that is part of the most recent pulsed flux flare. The fourth observation, on 2007 April 28, also contained a burst. In each of these cases, we have singled out the abnormal observation, and averaged the other two that were part of the same set. Each of these exceptions is discussed below and in Section 5.6.

Also in the top panel, the pulsed flux time series obviously has significant structure. The most obvious features are the three long-lived flares. Gavriil & Kaspi (2004) estimated the peak flux of the first flare to occur at MJD 52218.8 ± 4.5, with a rise time of 20.8 ± 4.5 days and a fall time of 98.9 ± 4.5 days. They estimated the peak flux of the second flare to occur at MJD 52444.4 ± 7.0, with a rise time of 58.3 ± 7.0 days and a fall time greater than 586 days. In fact, we can see in the first panel that

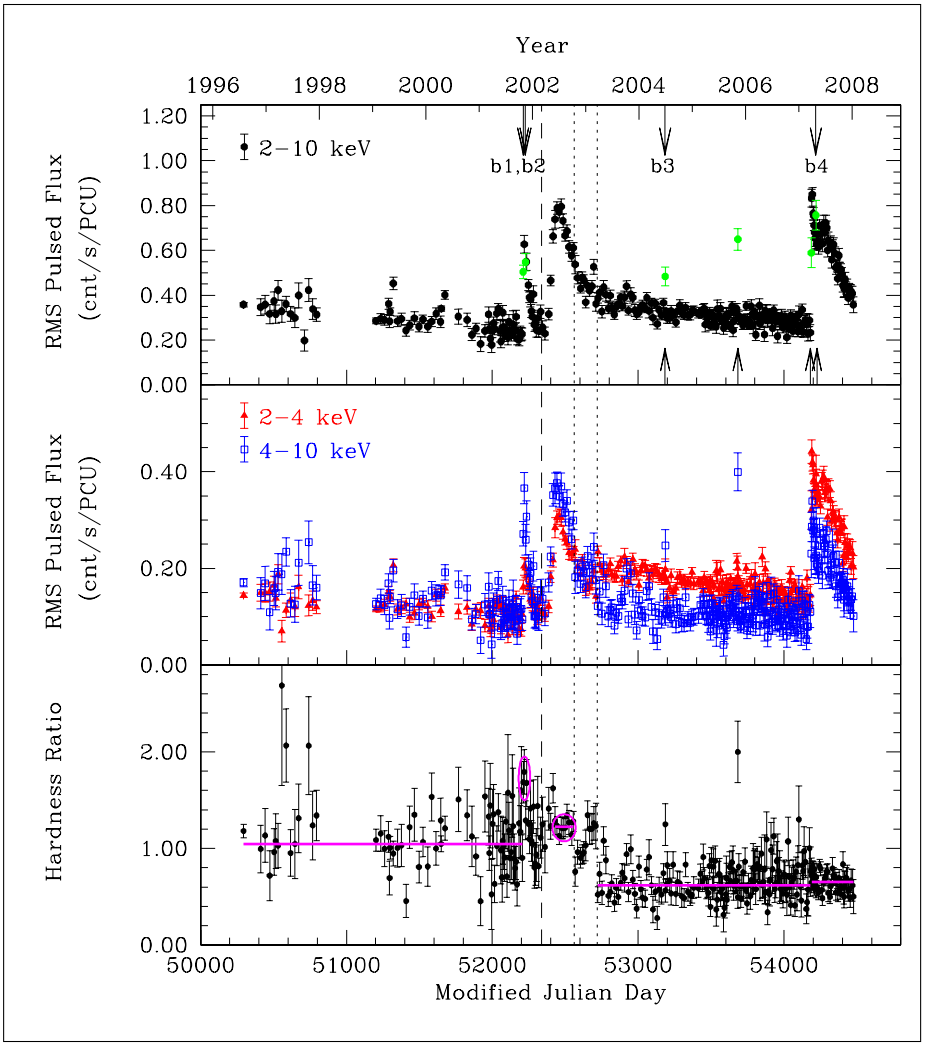

Figure 5.10 *Top:* Pulsed flux time series in the 2−10 keV band. For observations taken after 2002 March 02, we plotted the average of the pulsed flux values of each three closely spaced observations, with the 4 exceptions indicated by arrows along the bottom of the panel. All observations containing bursts are indicated by arrows along the top of the panel. All points indicated with an arrow are also coloured in green. *Middle:* Pulsed flux time series in the 2−4 keV band (red triangles) and in the 4−10 keV band (blue squares). *Bottom:* Hardness ratio computed from the pulsed flux in the energy range (4−10 keV)/(2−4 keV). The hardness ratios near the peaks of the first two flares are marked with two magenta circles. *All panels:* The dashed line indicates the epoch when we started observing the source with sets of three closely spaced observations. The left dotted line marks the location when the hardness ratio dropped, 342 days after the peak of the second flare. The right dotted line marks the location when the hardness ratio drops further, 500 days after the peak of the second flare.

the second flare continued to decay slowly, and that the pulsed flux had not returned to its pre-flares value by the time the third flare occurred. However, the pulsed flux in the year prior to the flares was low compared to the previous years, making it unclear what the real quiescent flux level is.

Here we estimate the peak pulsed flux of the third flare to have occurred at MJD 54191.6 $\pm$ 3.1, with an upper limit on the rise time of 7.3 days. The three observations obtained in the last week before the flare all had a pulsed flux consistent with quiescence. The three observations obtained 7 days later all had a significantly higher pulsed flux. The first of these three observations, occurred 1.75 days after the determined glitch epoch and had a lower pulsed flux than the second observation. The two observations were separated by 22 hours. It is possible that the first observation is part of the rise of the flare, which would imply a resolved rise with a rise time significantly smaller than 7 days. However the value of the pulsed flux for that observation before the binning is less than 3σ away from that of the following observation, and the scatter in the unbinned data near the start of the flare is large. We also estimate the fall time of that flare to be greater than 288 days (date of the last observation included in this paper) since the pulsed flux had not returned to its pre-flare value.

We estimate that the three flares had peak pulsed fluxes of 2.32 $\pm$ 0.15, 2.90 $\pm$ 0.07, and 3.13 $\pm$ 0.10 times the quiescent pulsed flux for the 2$-$10 keV band. By "quiescent pulsed flux" we mean the average pulsed flux from the year preceding the first flare and from the year preceding the third flare.

An anti-correlation between the total flux and the pulsed fraction has been reported for this source (Tiengo et al., 2005). Tam et al. (2008a) used imaging observations from 1E 1048.1$-$5937 to derive the following anti-correlation in the 2$-$10 keV band:

$$F_{tot} = A \times (F_{RMS}/a)^{1/(1+b)}, \tag{5.3}$$

where F_{tot} is the total flux of the source in erg/s/cm^2, F_{RMS} is the RMS pulsed flux in counts/s/PCU, a and b are constants (a=1.53, b=$-$0.46), and A is a constant scaling factor ($A\sim$125). Note that there were no imaging observations obtained in a data mode suitable for extracting pulsed fractions from near the peaks of the first two flares; the parameters in the above equation were obtained on the basis of the third flare only. This information allows us to scale our pulsed fluxes to estimate the total energy released in each flare, assuming that the relation for the third flare holds for the first two as well. Assuming a distance of 2.7 kpc (Gaensler et al., 2005), and assuming roughly

linear decays (see Section 5.7.1), we find a total energy release of $\sim 4.4\times 10^{40}$ erg for the first flare, $\sim 3.1\times 10^{41}$ erg for the second, and $\sim 3.9\times 10^{41}$ erg for the third, all in the 2−10 keV band. For a distance of 9 kpc (Durant & van Kerkwijk, 2006a), these numbers become $\sim 4.8\times 10^{41}$ erg, $\sim 3.5\times 10^{42}$ erg, and $\sim 4.3\times 10^{42}$ erg.

In the middle panel of Figure 5.10, we show the pulsed flux results in 2−4 keV (red triangles) and in 4−10 keV (blue squares). Note that in the years between flares 2 and 3 there are two data points with a significantly high pulsed flux in the 4−10 keV band. The corresponding dates are 2004 June 29 (MJD 53185) and 2005 November 08 (MJD 53682). The observation corresponding to the first point contains the third burst detected from this source. Gavriil et al. (2006a) reported a pulsed flux increase immediately following the burst, and a slow decay within the 2 ks-long observation (see Section 5.6). We did not detect a burst within the observation corresponding to the second point, and we found no evidence for a decay in the pulsed flux within the 1.5 ks-long observation. See Section 5.7.6 for more discussion.

In the bottom panel, we show the ratio of the two pulsed flux time series $H \equiv$ (4−10 keV/2−4 keV). The weighted average hardness ratio for the years preceding the first flare is marked with a magenta horizontal line with $H = 1.04\pm0.02$. The hardness ratios near the peaks of the first two flares are marked with two magenta circles and have $H = 1.6\pm0.1$ and $H = 1.22\pm0.03$, respectively. The hardness ratio for the 4 years preceding the third flare is also marked with a magenta horizontal line with $H = 0.62\pm0.01$. Finally, the hardness ratio after the onset of the third flare is marked with another magenta horizontal line at $H = 0.65\pm0.01$. It is clear from the middle and bottom panels that the pulsed emission from 1E 1048.1−5937 had a harder spectrum near the peaks of the first two flares compared to the pulsed emission preceding the flares. It is also clear that 342 days after the peak of the second flare (first vertical dotted line), this ratio dropped. It dropped again 500 days after the peak of the second flare (second vertical dotted line) to a value smaller than the pre-flares value, a value that was maintained until the onset of the third flare. We verified that these changes in the hardness ratio do not coincide with the epochs of gain change of *RXTE*, nor do they coincide with the dates of loss of the propane layers of PCUs 0 and 1. We also verified that there are no similar changes at the same epochs in the other monitored AXPs.

5.5.1 Comparison of RXTE and CXO-observed Spectral Changes

Note that the hardness ratios reported above are obtained from the pulsed flux of *RXTE*. Any changes in the hardness ratio of the total flux, as observed by an imaging instrument, might not necessarily be reflected in the behaviour of the pulsed hardness ratio if the pulsed and persistent spectra are different. Tam et al. (2008a) reported a significant increase in the hardness ratio obtained from *Chandra X-ray Observatory* (*CXO*) data at the onset of the third flare. The hardness ratio was defined as $(S+H)/(S-H)$ where S and H are countrates in the $1-3$ keV and $3-10$ keV bands, and it increased by $\sim$14% at the onset of the flare. With *RXTE*, we observe a small increase ($\sim$5%) in the (4−10 keV)/(2−4 keV) pulsed hardness ratio when we compare the pre-flare and the post-flare data. In order to verify that these two results are consistent, we used the *CXO* data to simulate *RXTE* pulsed hardness ratios at the epochs of six *CXO* observations that occurred near *RXTE* observations.

To do the simulations, we used the X-ray spectral fitting package `XSPEC`[4] v12.3.1. We loaded the spectra of the *CXO* observations and fit them with the models described in Tam et al. (2008a). Then we loaded the *RXTE* response matrices for nearby *RXTE* observations, and extracted *RXTE* count rates in the 2−4 keV and 4−10 keV bands. We then multiplied the simulated *RXTE* countrates by the *CXO* pulsed fractions in the appropriate bands (see Figure 5.11) to extract *RXTE* pulsed fluxes. Taking the ratio of the pulsed fluxes yielded a simulated hardness ratio. The results are presented in the top panel of Figure 5.11.

The resulting simulated *RXTE* hardness ratios were within 2σ of the observed *RXTE* hardness ratios. We attribute the small difference mainly to two factors. First, in multiplying the simulated *RXTE* countrates by the *CXO* pulsed fractions, we assumed that the *CXO* pulsed fractions are the same as the *RXTE* pulsed fractions, which cannot be measured. This assumption does not hold when the pulsed and unpulsed spectra are different. In fact, the ratio of these two quantities is changing since the pulsed spectrum is evolving differently from the unpulsed spectrum. We know this because the dependence of pulsed fraction on energy is changing (bottom panel of Figure 5.11). The discrepancy between the simulated and observed results could also be partly attributed to the fact that the models used to fit the spectra and to generate the simulated data did not fit the original data perfectly.

[4] http://xspec.gsfc.nasa.gov

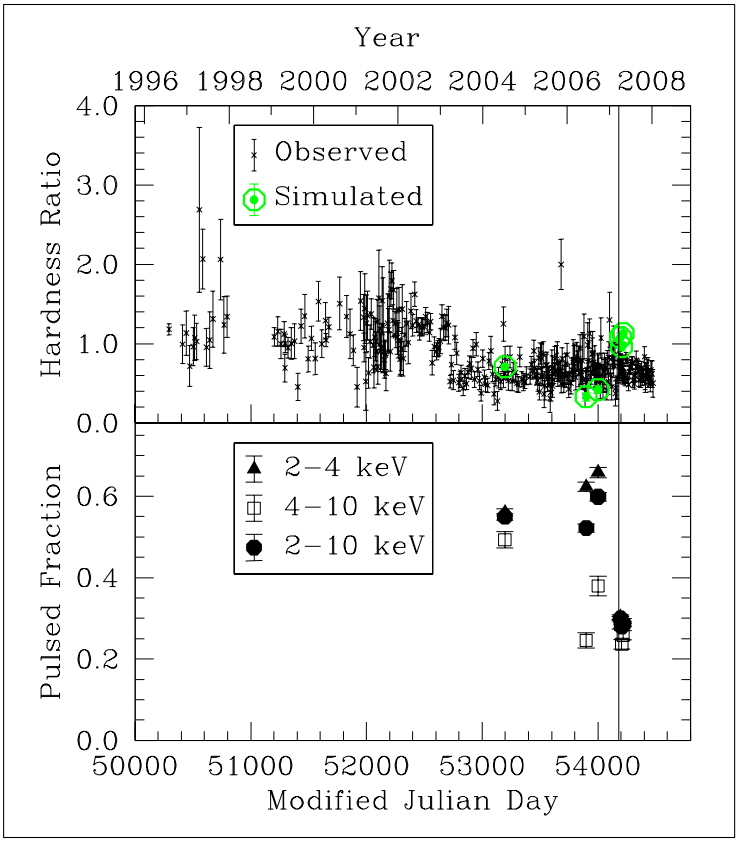

Figure 5.11 A comparison of *RXTE* and *CXO* spectral changes. *Top:* Small crosses: *RXTE* hardness ratio computed from the pulsed flux in the energy range (4−10 keV)/(2−4 keV). Green circles: hardness ratio computed from simulated *RXTE* pulsed fluxes at the epochs of five *CXO* observations (see Section 5.5.1 for details). *Bottom:* Pulsed fractions for the 5 *CXO* observations surrounding the onset of the third flare. *Both panels:* the solid line indicates the onset of the flare.

5.6 A New Burst

Searching for bursts is part of our regular AXP monitoring routine. For each observation of 1E 1048.1−5937, we generated 31.25 ms lightcurves using all Xenon layers and events in the 2–20 keV band. These lightcurves were searched for bursts using the algorithm introduced in Gavriil et al. (2002) and discussed further in Gavriil et al. (2004). Four bursts have been detected from this source. The first two bursts occurred on 2001 October 29 and 2001 November 14 (Gavriil et al., 2002). One of these bursts was coincident with the rise of the first pulsed flux flare, and the other with its fall (see Figure 5.10). The third burst occurred on 2004 June 29, 740 days following the peak of the second pulsed flux flare (Gavriil et al., 2004). Here, we report on the

detection of a fourth burst[5], which occurred on 2008 April 28, 27 days after the peak of the third flare.

5.6.1 Burst Properties

To analyse the burst, we created event lists in FITS[6] format using the standard FTOOLS[7]. For consistency with previous analyses of SGR/AXP bursts, we extracted events in the 2-20 keV band, and reduced them to the solar system barycenter. We subtracted the instrumental background using the model background lightcurve generated by the FTOOL `pcabackest`. The model background lightcurve generated by `pcabackest` only has 16-s time resolution. We therefore fit the simulated background lightcurve to a fourth order polynomial and subtracted this model from our high-time-resolution lightcurves. Using the resulting light curve, we then subtracted an additional background determined from a 300-s long interval ending 100-s before the burst. The final background-subtracted burst lightcurve is shown in Figure 5.12. The burst temporal properties, namely peak time (t_p), peak flux (f_p), rise time (t_r), T_{90}, which is the time from when 5% to 95% of the total burst counts have been collected, and T_{90} fluence were determined using the methods described in Gavriil et al. (2004). The peak flux and T_{90} fluence were then determined in units of erg/s/cm^2 and erg/cm^2, respectively, assuming a power-law spectrum (see below). The burst properties are listed in Table 5.2. The burst rise time, 955 ms, calculated using a linearly rising model, is longer by a factor of $\sim$45 than the longest rise time seen from this source to date. The peak flux calculated over a 64-ms time interval (or over the rise time interval) is the lowest of all four bursts. The total burst fluence is within the range of fluences observed for the other bursts from this source.

A burst spectrum was extracted using all the counts above 2 keV within the T_{90} interval. The spectrum was then grouped so as to have at least 20 counts per bin after background subtraction. The bin above $\sim$40 keV was ignored because it had insufficient counts even after grouping. A response matrix was created using the FTOOL `pcarsp`. The burst spectrum, background spectrum, and response matrix were then read into XSPEC. The spectrum was fit to a photoelectrically absorbed blackbody, and to a photoelectrically absorbed power-law. In both cases, because of *RXTE*'s

[5]The burst search routine also returned several candidate bursts with a significance several orders of magnitude smaller than those reported for the published bursts. We do not report on the analysis of these putative bursts here.

[6]http://fits.gsfc.nasa.gov

[7]http://heasarc.gsfc.nasa.gov/docs/software/ftools/

Table 5.2. Burst Timing and Spectral Properties

Temporal Properties	
Burst day (MJD)	54218
Burst start time (fraction of day)	0.578621(6)
Burst rise time, t_r (ms)	955^{+80}_{-115}
Burst duration, T_{90} (s)	111.2^{+26}_{-19}
Fluxes and Fluences	
T_{90} fluence[a] (counts/PCU)	445±15
T_{90} fluence[a] ($\times 10^{-10}$ erg cm^{-2})	68.9±2.3
Peak flux for 64 ms[a] ($\times 10^{-10}$ erg s^{-1} cm^{-2})	24.2±5.4
Peak flux for t_r ms[a] ($\times 10^{-10}$ erg s^{-1} cm^{-2})	15.9±1.1
Spectral Properties	
Power law:	
Power law index	$0.37^{+0.20}_{-0.19}$
Unabsorbed power law flux ($\times 10^{-11}$ erg s^{-1} cm^{-2})	$4.64^{+0.44}_{-0.44}$
Reduced χ^2/degrees of freedom	1.80/18
Blackbody:	
kT (keV)	$4.9^{+0.7}_{-0.6}$
Unabsorbed Blackbody flux ($\times 10^{-11}$ erg s^{-1} cm^{-2})	$5.01^{+1.32}_{-1.34}$
Blackbody Radius[b](km)	$0.014^{+0.006}_{-0.004}$
Reduced χ^2/degrees of freedom	1.20/18

[a]Fluxes and fluences are calculated in the 2–20 keV band.

[b]Assuming a distance of 9.0 kpc to the source (Durant & van Kerkwijk, 2006a).

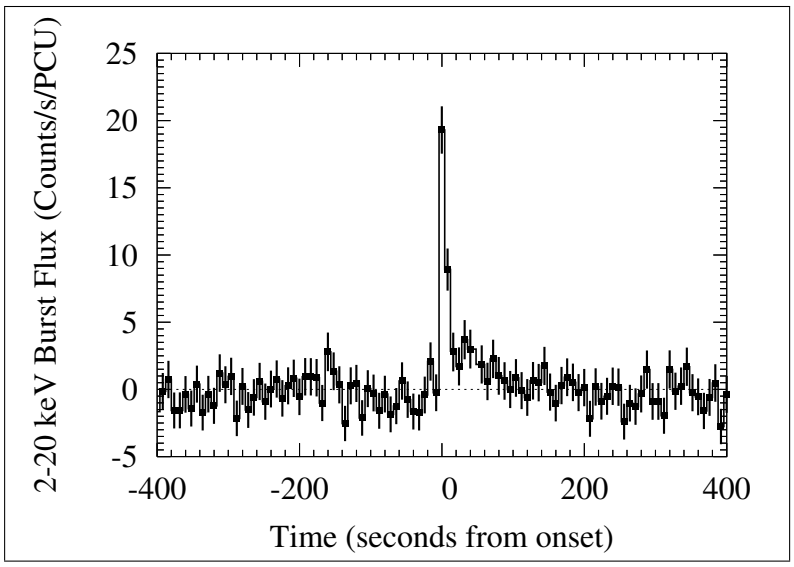

Figure 5.12 Background subtracted 2−20 keV burst light curve binned with 8 s time resolution.

lack of response below 2 keV, we held the column density fixed to the value found by Tam et al. (2008b) ($N_H = 0.97 \times 10^{22}$ cm^{-2}). The power-law model was a poor fit. The blackbody was a better fit but not exceptional, with a 25% probability that the deviations from the model are due to random noise only, given the number of degrees of freedom (see Table 5.2). Two component-models such as two blackbodies or a blackbody plus power-law did not improve the fits. Two other bursts from this source exhibited spectral features at ∼14 keV. To determine whether the burst exhibited any spectral features that might have been smeared out by extracting a spectrum over the burst's long T_{90} interval, we repeated the above procedure for the first few seconds of the burst (see Fig. 5.13 for spectral fits of the first 3 s of the burst). There was indeed excess at $\sim$ 14 keV when fitting the spectrum of the burst with a simple continuum model (see Fig. 5.13). To establish the veracity of the feature we performed the following Monte Carlo simulations.

We generated 1000 simulated spectra having the same count rate and exposure as our data and a photoelectrically absorbed blackbody shape. The simulated spectrum was created using the kT value found from the best fit line+gaussian model. We then added Poisson noise to our simulated spectra, fit them with a simple photoelectrically absorbed blackbody model, and calculated a χ^2 value. Next, we added a spectral line to our fitting model and refit the data. To prevent the fit from falling into a local minimum, when doing the fitting, we stepped the central energy of the line from 2 keV to 40 keV in steps of 0.1 keV, but allowed the width and normalization of the line to

vary. We found 17 cases out of 1000 for which the addition of a line induced a change in χ^2 that was greater than or equal to that found from adding a line to the model used to fit the real data. Thus, we place a significance of 99.983% on the line which is equivalent to a 2.1-σ detection. This is not a highly significant detection, nor is it as significant as the other lines seen from this source (Gavriil et al., 2002; Gavriil et al., 2006a), however, it is highly suggestive that given there have been only four bursts seen from this source, two of which have shown similar features at comparable energies.

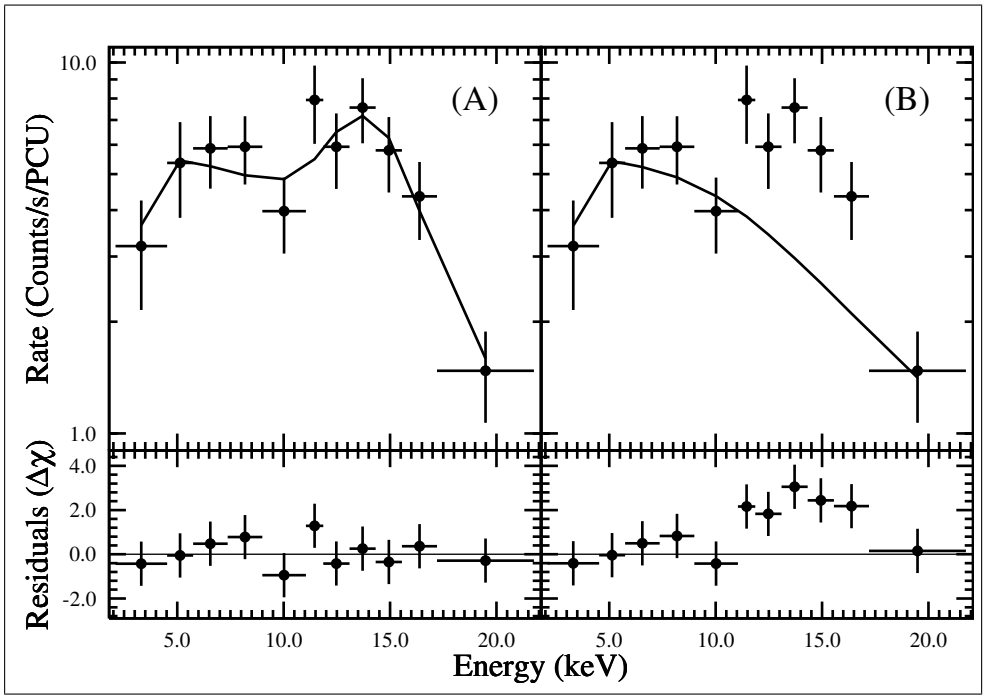

Figure 5.13 Spectral fits of the first 3 seconds of the new burst. (*a*) Photoelectrically absorbed power-law plus Gaussian model. (*b*) Photoelectrically absorbed power-law model.

5.6.2 Short-Term Pulsed Flux Variability and Burst Phases

We show the 2−20 keV lightcurves of the 4 seconds surrounding each of the 4 bursts discovered from 1E 1048.1−5937 in the top panels of Figure 5.14. Each column corresponds to a burst. For each of the observations containing bursts, we made three barycentric time series in count rate per PCU, for the 2−4, 4−20, and 2−20 keV bands. The time resolution was 31.25 ms. We removed the 4 s centered on each burst from each time series. Then, we broke each time series into six segments.

Table 5.3. Spectral Fit to the First 3 seconds of the New Burst

Parameter	Value			
	Power-Law	Power-Law + Gaussian	Blackbody	Blackbody + Gaussian
Index/Temperature (keV)	$\sim$0.44	$0.71^{+0.28}_{-0.23}$	$6.12^{+0.80}_{-0.66}$	$5.26^{+0.99}_{-0.99}$
Continuum Flux[a]	$5.63^{+0.46}_{-2.65}$	$4.49^{+0.60}_{-0.68}$	$6.55^{+0.34}_{-0.77}$	$5.44^{+1.40}_{-1.24}$
Line Energy (keV)	···	$14.61^{+0.50}_{-0.52}$	···	$14.88^{+0.60}_{-0.57}$
Line Width (keV)	···	$1.81^{+0.73}_{-0.60}$	···	$1.35^{+0.68}_{-0.83}$
Line Flux[a] ($\times 10^{-10}$ erg s^{-1} cm^{-2})	···	$2.70^{+0.74}_{-0.79}$	···	$1.91^{+1.00}_{-0.75}$
Reduced χ^2/degrees of freedom	2.49/11	1.08/8	1.71/11	1.04/8

[a]Fluxes are unabsorbed and calculated in the 2–20 keV band, in units of $\times 10^{-10}$ erg s^{-1} cm^{-2}.

For each segment, we calculated the RMS pulsed flux. The results are presented in the middle panels of Figure 5.14. A similar analysis was performed for burst 3 by Gavriil et al. (2004). Note the significant increase in the 4−20 keV pulsed flux in the observations containing the first, third, and last bursts following the onset of the bursts, while the pulsed flux remained constant in the 2−4 keV band in those same events.

To determine the phase of each burst, we folded each observation at the best-fit frequency and found when, relative to the folded profile, the burst peak occured. We then aligned each of the folded profiles with a high signal-to-noise long-term average profile. The pulse phases are shown in the bottom panels of Figure 5.14. In each panel, the histogram at the bottom is a fold of the entire observation. The smooth curve is obtained from the best-fit 5 harmonics. The histogram at the top is the long-term average. The first, second, and fourth folded profiles have a different shape from the long-term average; they occured during flares. Note how the first three bursts occur near the peak of the profile (burst phases 0.58±0.02, 0.64±0.02, and 0.66±0.02 relative to the template shown in the Figure), but the last burst is further from the peak (burst phase 0.43±0.02 relative to the template shown in the Figure).

5.7 Discussion

5.7.1 Pulsed Flux Variations

The goal of continued systematic *RXTE* monitoring of AXPs is to flesh out the phenomenological phase space of these intriguing objects. In this regard, 1E 1048.1−5937 has not disappointed us. It has shown a surprisingly diverse range of behaviours in practically every observational property. This includes its rotational evolution, in which we have seen several different timing anomalies – with two likely spin-up glitches – in addition to remarkable timing "noise", for lack of a better term. Its radiative evolution has been equally eventful, with 3 large, long-lived pulsed flux increases and multiple bursting episodes, as well as spectral changes and pulse profile changes. Understanding the physical origin of all this behaviour is clearly very challenging; likely the best physical insights will come from considering multiple studies such as ours, for many different objects. Nevertheless here we consider what these phenomena may be telling us about the physics of magnetars.

Several AXPs have exhibited pulsed flux variations on long time scales.

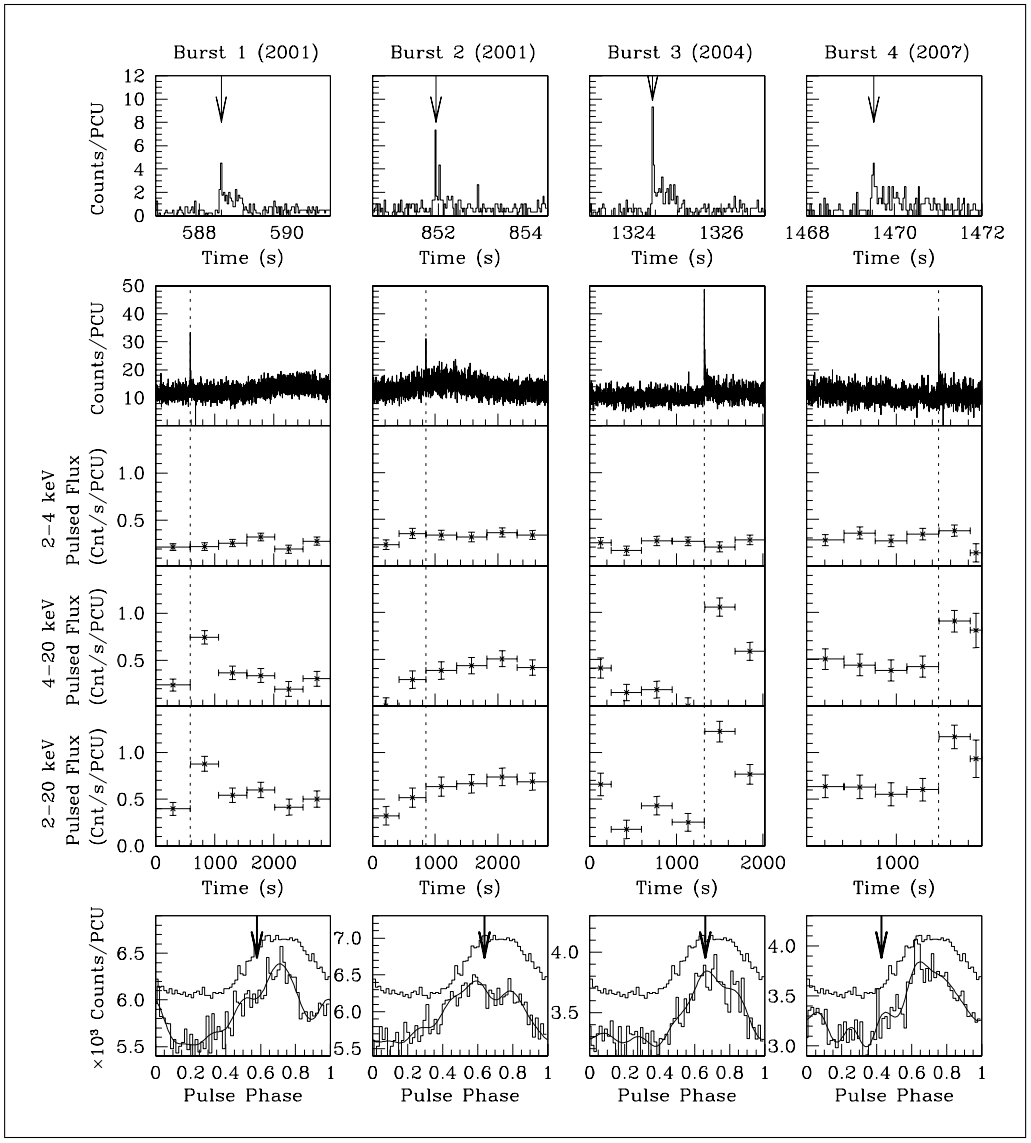

Figure 5.14 Short-term pulsed flux variability near the bursts, and burst phases. Each column corresponds to an observation in which a burst was detected. In each column: *Top:* a 4-s long time series with 31.25 ms time resolution showing the burst. The peak of the burst is indicated with an arrow. *Middle:* time series of the entire observation with 1-s time resolution, followed by the RMS pulsed flux in three different bands. We excluded the 4 s surrounding the burst for this pulsed flux analysis. *Bottom:* A fold of the entire observation shown below the scaled long-term average profile. The phase at which the burst occured is marked with an arrow. This phase corresponds to the time bin indicated with an arrow in the top plot.

RXS J170849.0−400910 exhibited low-level pulsed flux variations on time scales of weeks to months (Dib et al., 2008a). 4U 0142+61 exhibited a pulsed flux increase by 29±8% over a period of 2.6 years (Dib et al. 2007a, Chapter 2). 1E 2259+586

exhibited an abrupt increase in the pulsed (and persistent) flux which decayed on time scales of months to years (Woods et al., 2004). This abrupt increase occured in conjunction with bursts, and the decay is thought to be due either to thermal radiation from the stellar surface after the deposition of heat from bursts (eg. Lyubarsky et al. 2002), or the result of the slow decay of a magnetospheric "twist" (Thompson et al., 2002). This outburst was accompanied by a glitch. XTE 1810−197 and candidate AXP AX J1845−0258 also exhibited an increase in the pulsed flux although the rise time is unclear (Ibrahim et al., 2004; Torii et al., 1998; Tam et al., 2006).

The long-term pulsed flux behaviour of AXP 1E 1048.1−5937 is different from that of any other AXP: in the first two flares exhibited by 1E 1048.1−5937, the pulsed flux rose on week-long time scales and subsequently decayed back on time scales of months to years (Gavriil & Kaspi, 2004). It is unclear whether the third flare had a resolved rise (see Section 5.5). Although small bursts sometimes occured during these events (see Section 5.6), the afterglow of these small bursts cannot explain the overall flux enhancement, and in the absence of evidence for large bursts prior to the flare, we can attribute the flares to twists implanted in the external magnetosphere from stresses on the crust imposed by the internal magnetic field.

Based on the idea that a plasma corona is contained within the closed magnetosphere, Beloborodov & Thompson (2007) offer a prediction for the behaviour of the luminosity of the source after a magnetospheric twist occurs. Assuming that a large flux enhancement is caused by a twist, that the emission from the heated crust is small compared to the magnetospheric emission of twisted magnetic flux tubes, and assuming no additional twists introduced after the original twist, Equation 17 of Beloborodov & Thompson (2007) predicts that the luminosity will decay linearly, and is proportional to $-\phi^2 \times (t - t_0)$, where ϕ is the voltage between two footpoints of a magnetic field line and $t - t_0$ is the time since the start of the decay of the luminosity. ϕ is induced by the current that accompanied the gradual untwisting of the magnetic field. Its minimum value is that needed for the creation of electron positron pairs. It is proportional to the local magnetic field.

Using Equation 5.3 and our pulsed flux time series, we produced a total flux time series for 1E 1048.1−5937 (Figure 5.15). We then fit a linear decay to the first few months of data after each of the three flares. Including data beyond that would have made the fits worse, indicating that we can attribute at most the first part of the decay to a linear twist relaxation. The second part could perhaps be attributed to crust afterglow following some internal heat deposition (see Section 5.7.3). The slopes of the lin-

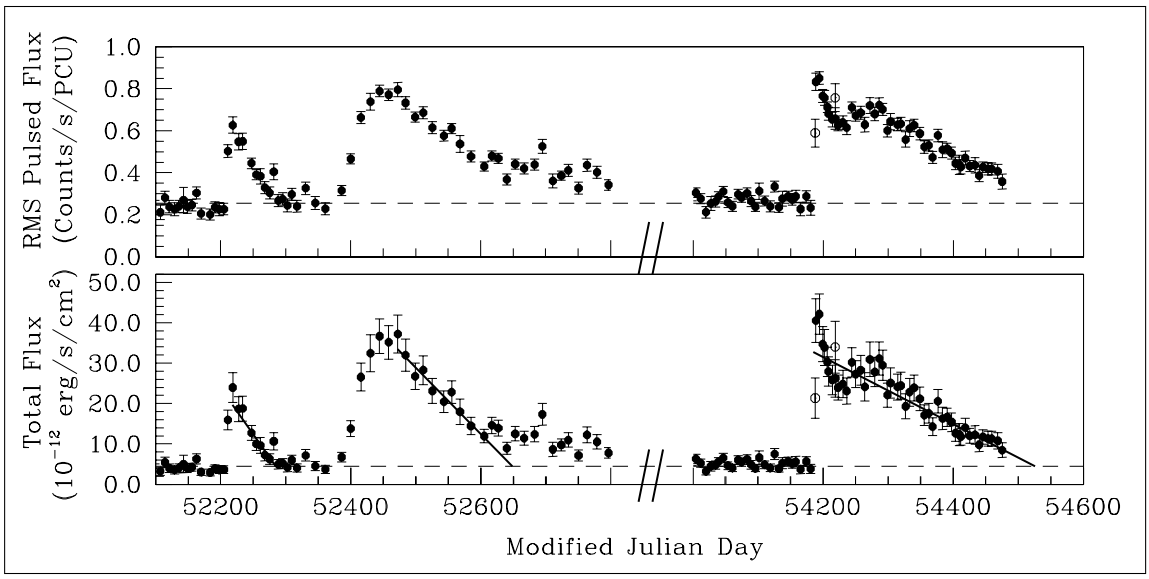

Figure 5.15 *Top:* Pulsed flux in the 2−10 keV near the three flares. *Bottom:* Simulated total 2−10 keV unabsorbed flux, estimated from the *RXTE* pulsed flux and from the power-law correlation between the pulsed fraction and the total flux described by Tam et al. (2008a). The solid lines in the bottom plot are linear decays fit to the first few months of data after each of the flares.

ear fits had the values $-0.23(3)\times10^{-12}$ erg/s/cm^2/day, $-0.164(13)\times10^{-12}$ erg/s/cm^2/day, and $-0.083(5)\times10^{-12}$ erg/s/cm^2/day, with reduced χ^2 values of 0.72, 0.38, and 0.91, respectively. The fits were good, as predicted by Beloborodov & Thompson (2007), but the three slopes significantly differed from each other, suggesting, in the context of this model, that different flux tubes (with different values of local magnetic fields) were twisted in each event.

5.7.2 Timing Behaviour

In addition to flux variability, regularly monitored AXPs also exhibit different kinds of timing variability. In RXS J170849.0−400910, the frequency derivative fluctuates by ∼8% about its long-term average ∼1.58 $\times10^{-13}$ s^{-2} on a time scale of months (Dib et al., 2009a), except at the second detected glitch which had an exponential recovery (Kaspi & Gavriil, 2003). The frequency derivative of 1E 1841−045 varies by ∼10% on a time scale of many years, except at the first detected glitch where $\dot{\nu}$ suddenly dropped by ∼10% (Dib et al., 2008a). It slowly dropped further before slowly recovering. The frequency derivative of 4U 0142+61 also fluctuates by ∼3% around its long-term average on a time scale of months to years, except at the onset of the

2007 active phase where it suddenly dropped (Chapter 3). It then slowly recovered. The frequency derivative of 1E 2259+586 also fluctuates about its long-term average, except at the first detected glitch which had an exponential recovery (Woods et al., 2004).

The episode of extreme variations in $\dot{\nu}$ of 1E 1048.1−5937 is not seen in any other AXP. In 2002 and 2003, $\dot{\nu}$ varied by $\sim 5.6\times10^{-13}$ s^{-2} every two weeks (time between consecutive sets of three observations), oscillating between -26×10^{-13} s^{-2} and -6×10^{-13} s^{-2} 4 times in the span of 450 days.

When trying to understand the origin of these variations, it is useful to look for correlation between the timing properties and the flux of the pulsar. Figure 5.16 is a plot of the timing and radiative behaviours of 1E 1048.1−5937.

Earlier we suggested that the flux variations in 1E 1048.1−5937 may be due to twists implanted in the external magnetosphere from stresses on the crust imposed by the internal magnetic field. In the magnetar model, the twisting drives currents into the magnetosphere. The persistent non-thermal emission of AXPs is explained in this model as being generated by these currents through magnetospheric Comptonization (Thompson et al., 2002). Changes in X-ray luminosity, spectral hardness, pulse profile, and torque changes have a common origin in this model.

Gavriil & Kaspi (2004) looked for correlations between the $\dot{\nu}$ and the pulsed flux near the first two flares and reported only a marginal correlation. They suggested that the lack of correlation was because the torque is most sensitive to the current flowing on a relatively narrow bundle of field lines anchored close to the magnetic poles (Thompson et al., 2002). Therefore, whether an X-ray luminosity change will be accompanied by a $\dot{\nu}$ change depends on where in relation to the magnetic pole the source of enhanced X-rays is.

Earlier we suggested that the different decay slopes of the three different flares might indicate that different flux tubes, with different values of local magnetic field, were twisted in each event (Beloborodov & Thompson, 2007). Therefore, even if there was no correlation between $\dot{\nu}$ and the pulsed flux in the case of the early flares, if the flux tubes involved in the third flare were closer to the poles, one might expect a correlation to occur in that flare. From Figure 5.16, this does not appear to be the case. Note that correlations between the luminosity and torque are also expected in accreting scenarios, and are not observed here.

An interesting observation is that episodes of rapid $\dot{\nu}$ variations appear to follow the second and third flares (see Section 5.5). Bi-monthly variations in $\dot{\nu}$ changed

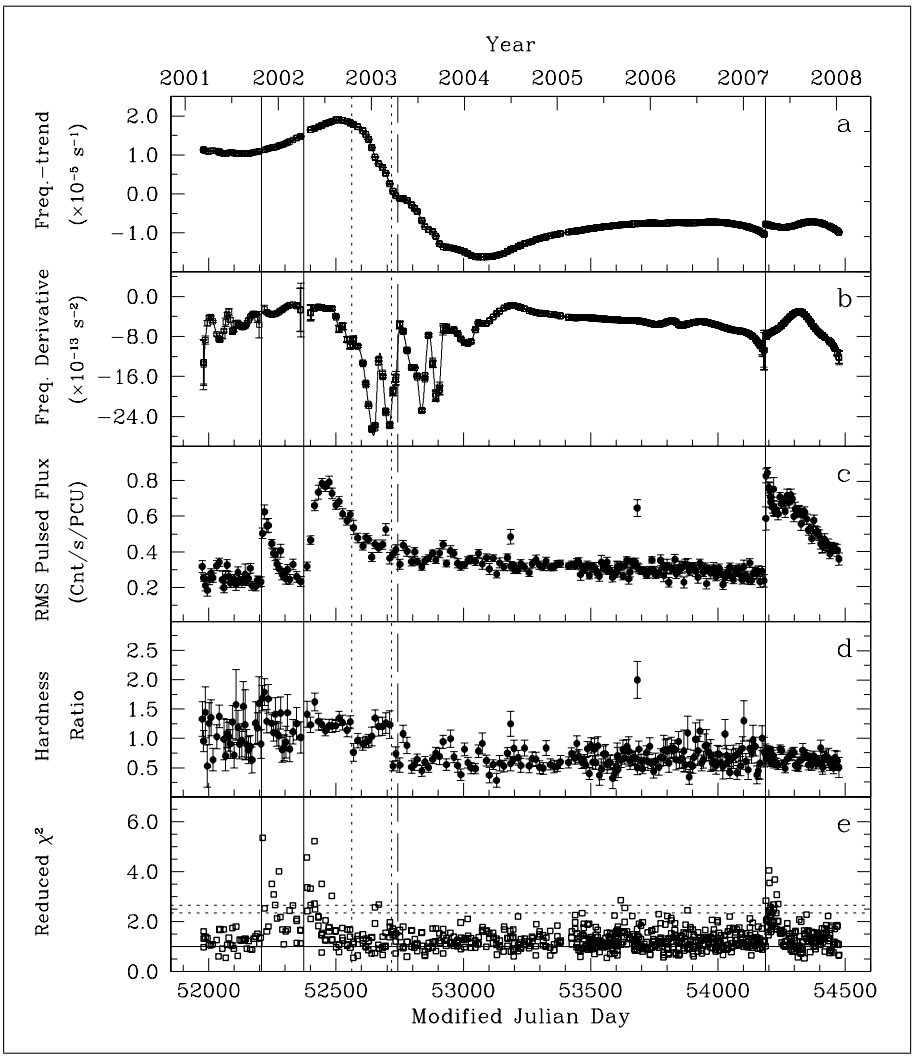

Figure 5.16 Evolution of the different properties of 1E 1048.1−5937. (*a*) Frequency as a function of time, with the long-term average spin-down subtracted. (*b*) The frequency derivative as a function of time. (*c*) The 2−10 keV RMS pulsed flux as a function of time. (*d*) The hardness ratio as a function of time, computed from the pulsed flux in the energy range (4−10 keV)/(2−4 keV). (*e*) Reduced χ^2 statistics as a function of time, calculated after subtracting the scaled and aligned profiles of the individual observations from a high signal-to-noise template. *All panels:* The three solid lines mark the onset of the three flares. The line with the long dashes marks the location where the ephemerides used to obtain the splines overlapped for a short period of time only. The two dotted lines mark epochs where the hardness ratio dropped, and maintained a lower value for the following weeks relative to the values preceding the drop.

from 0.08×10^{-13} s^{-2} near the second flare to 2×10^{-13} s^{-2} 41 days after the same flare, to 5.6×10^{-13} s^{-2} 141 days after the flare. Similarly, weekly variations in $\dot{\nu}$ changed from 0.33×10^{-13} s^{-2} near the third flare to 0.6×10^{-13} s^{-2} 350 days after the flare, to 1.4×10^{-13} s^{-2} 395 days after the flare. This might only be a coincidence, however Beloborodov & Thompson (2007) predict that the impact of a twist in the magnetosphere on the spin-down may appear with a delay of $\sim$2 years. This is because the time scale of the twist spreading to the light cylinder is large due to the resistivity to the currents of the corona contained within the closed magnetosphere.

5.7.3 Glitches

In many glitch models, the superfluid in the crust is spinning faster than the crust, but on average over long times, they have the same $\dot{\nu}$. The superfluid cannot spin down because its angular momentum vortices are pinned to crustal nuclei and hence cannot move outward (see, for example, Alpar et al. 1989). For various reasons, for example, torques on the crust, internal starquakes and thermal agitations, unpinning of the vortex lines may happen in some locations. The vortices could then move outward, and the superfluid angular frequency can decrease and approach that of the crust. At that moment, angular momentum is transferred from the superfluid to the crust, and a glitch occurs. For example, Link & Epstein (1996) argued that starquakes due to magnetic stresses at the core/crust boundary in normal rotation-powered pulsars could deposit energy that then results in sudden spin-ups; such events seem even likelier to occur in magnetars, consistent with their ubiquitous glitching (Kaspi et al., 2000; Kaspi & Gavriil, 2003; Dall'Osso et al., 2003; Dib et al., 2008a; Israel et al., 2007).

The glitch coincident with the third pulsed flux flare of 1E 1048.1−5937 is the largest yet seen in the five regularly monitored AXPs, and has one of the largest fractional frequency increases in any pulsar, including rotation-powered sources. This event was not accompanied by a significant change in $\dot{\nu}$. In fact, in the months preceding the glitch, $\dot{\nu}$ became more and more negative, until three weeks prior to the glitch, when it started decreasing in magnitude, reaching a value not far from the one it adopted after the glitch. It is unclear if this behaviour is somehow related to glitch; perhaps it caused the unpinning of the vortices. Unfortunately, the relation between what is usually considered to be timing noise and the behaviour of the superfluid inside is not well understood.

What is clear, however, is that this glitch was associated with a radiative event:

the third pulsed (and persistent) flux flare. Above, we suggested this flare may be due to a twist in the magnetosphere. The twist originates in a tangle of field lines below the surface of the star. Because of the internal magnetic stresses inside, a piece of crust above the tangle is twisted, twisting the footpoints of the external magnetic field. Eventually this twist propagates outward. It is possible that some vortices that are pinned to the crust get mechanically dislodged when the crust is being twisted, causing a glitch, or that energy deposition during this event raises the temperature such that pinning is affected, as in the Link & Epstein (1996) picture.

In fact, we note that every observed AXP flare or outburst thus far has been accompanied by a timing event. In the case of 1E 2259+586, CXOU J164710.2−455216, and the third flare of 1E 1048.1−5937, the event was a glitch (Woods et al. 2004, Israel et al. 2007, and Section 5.3.4). For 4U 0142+61 and for the second flare of 1E 1048.1−5937, the event was a sudden change in $\dot{\nu}$ possibly accompanied by a glitch (Sections 3.3.5 and 5.3.3). For the first flare of 1E 1048.1−5937 the event was a timing anomaly of uncertain nature (Section 5.3.2). It is possible that all these timing events were caused by some unpinning of superfluid vortices, which in turn was caused by crustal movement due to a twist propagating outward.

Note however that the converse is not true: many AXP glitches appear to be radiatively silent, such as the second glitch observed from 1E 2259+586, and all 4 glitches of AXP 1E 1841−045 (Chapter 4, Dib et al. 2009a). There is no evidence of pulsed flux changes associated with the glitches of RXS J170849.0−400910, however there are claims of an association between variations in the total flux of the source and the glitch epochs (Figure 4.14, also see Campana et al. 2007 and Israel et al. 2007). Why do we not see any released energy in the case of the "silent" glitches? Perhaps it is released deep in the star and some, or all, of it goes into the core. Perhaps when some energy reaches the surface, the delay between the energy release and the start of the associated increase in flux as well as the actual rise time of that increase are related to how deep below the surface this energy was released (see, for example, Cumming & Macbeth 2004, Brown & Cumming 2009). Since the rise time of the flux events associated with the "loud" glitches is never longer than a few months, one could speculate that any energy release that would have caused a larger rise time goes directly into the core.

Indeed, perhaps the radiative events accompanying some glitches are not due to a twist of the footpoints of the external field following crustal cracking. Perhaps the sudden unresolved increases in the flux, like that seen in the 2002 event from

1E 2259+586, are due to a twist propagating from the inside by breaking the crust (possibly combined with a thermal energy release due to the glitch), while the slow resolved increases in the flux, like those seen in the first two flares of 1E 1048.1−5937, are due to a local thermal energy release following a glitch.

5.7.4 Pulse Profile Changes

In Section 5.4, we showed that the largest pulse profile changes happen near the flares. In 1E 1048.1−5937, these changes always involve an increase in the harmonic content of the profiles. This suggests that these changes are not due to a surface disturbance (hot spot), since the effects of this on the profile would probably be smeared due to general relativistic light bending (Dedeo et al., 2001). Instead, they may be due to a local event in the magnetosphere.

Beloborodov & Thompson (2007) argued that it might take several years for the twist to propagate from the surface of the star to the light cylinder. Once the twist reaches the light cylinder, the torque affects the star almost immediately, and variations in $\dot{\nu}$ are observed. In this picture, early on, the twist is in the lower magnetosphere, and much later it is in the upper magnetosphere. A twist in the lower magnetosphere where the fields are very strong affects the properties of the local plasma, modifying its emission as well as the emission that is scattered from the surface below. In this case one might expect noticeable pulse profile changes. A twist that has reached the light cylinder where the fields are weaker affects the properties of the local plasma less, and affects the emission from the lower magnetosphere less. In this case one might expect the pulse profile changes to be much smaller. Thus, that we are seeing the pulse profile changes only at the beginning of the flares is consistent with the picture in Beloborodov & Thompson (2007).

If significant pulse profile changes *had* been observed at the time of the large $\dot{\nu}$ variations, this could have meant that the pulsed flux flares and the subsequent large $\dot{\nu}$ variations are independent. In this case, the $\dot{\nu}$ changes would be due either to a low magnetospheric twist (accompanied by pulse profile changes) which propagates quickly to the light cylinder, causing the torque changes; but why the onset of this twist would not be accompanied by a visible energy release is unclear. Alternatively, the $\dot{\nu}$ changes may not be due to torques at the light cylinder, but to internal events which cause the crust to crack and the lower magnetosphere to twist itself. In this case too it would be unclear why no bursting activity or energy release was seen, and

the unobserved pulse profile changes would be puzzling.

5.7.5 Long-Term Spectral Changes

In Section 5.5 we show that the hardness ratio of 1E 1048.1−5937, obtained from the pulsed flux, dropped significantly 9 months after the peak of the second flare, while the pulsed flux was still decaying, and while the large $\dot{\nu}$ variations were ongoing. Unfortunately, there are no imaging observations of the source around that time, and we cannot verify if the drop in the pulsed hardness ratio was accompanied by a drop in the hardness ratio of the persistent emission. Assuming that it was, this softening may be related to the magnetospheric twist that caused the flares. Indeed in the Thompson et al. (2002) model, spectral hardness is correlated with the luminosity. The hardness ratio is expected to gradually drop when the flux decays. However, the decrease seen here was sudden, not gradual. Also, this does not explain why the hardness ratio was not lower prior to the onset of the flares. Alternatively, this correlation of the softening with the flux decay can also be a consequence of changes in the effective temperatures of the outer layers of the star (Özel & Guver, 2007), and the twisted magnetosphere model need not be invoked here.

5.7.6 Bursts

1E 1048.1−5937 is more active than the other AXPs we monitor in multiple regards. With *RXTE* monitoring over the past ∼10 years, it is the only one which exhibited three large flux flares, it is the only AXP which exhibited extreme variations in $\dot{\nu}$, and the glitch observed in conjunction with the third flare is the largest observed among these AXPs. In addition, 1E 1048.1−5937 has shown four bursts, at different epochs. Other AXPs, such as RXS J170849.0−400910 and 1E 1841−045, have shown none, even though the combined *RXTE* on-source time of these two sources is the same as that of 1E 1048.1−5937.

Since three of the observed bursts were followed by an enhancement in the 4−10 keV pulsed flux, it is possible that the high pulsed flux of the observation taken on 2005 November 08 (see Section 5.5) was due to a burst that occured just before the observation. We detected no evidence for a change in pulsed flux during this observation. Since it was the first in the weekly set of three closely spaced observations, the decay time scale of the putative burst could be such that the decay is not noticeable within the observation, given the size of our pulsed flux uncertainties. The observa-

tion that followed this one occured 18 hours later and its pulsed flux was consistent with the long-term average. We verified that there were no *SWIFT* triggers from the location of 1E 1048.1−5937 in the week preceding the anomalous observation.

The four bursts observed from 1E 1048.1−5937 were associated with different flaring events. Bursts 1 and 2 occured near the peak of the first flare. Burst 3 occured two years after the peak of the second flare, while the pulsed flux was still decaying. Burst 4 occured a month after the peak of the third flare. Bursts 1, 2, and 3 occured near pulse maximum. All four bursts had millisecond rise times. Bursts 1, 3, and 4, had long decay tails (51 s, $>$ 700 s, and 128 s), with a pulsed flux enhancement in the tails. The falltime for burst 2 was 2 s. An apparent feature near 13 keV has been observed in the spectra of the first, and third bursts (Gavriil et al., 2002, 2004), and an apparent feature near 15 keV has been observed in the spectrum of the most recent burst. Note that apparent features near 13 keV have also been observed in the tail of one of the bursts in AXP XTE J1810−197 (Woods et al., 2005), and in the spectrum of the largest burst detected in AXP 4U 0142+61 (Gavriil et al., 2009b). So far the presence of these features is not well understood.

Woods et al. (2005) suggest that there are two types of magnetar bursts. Type A bursts are short, symmetric, and occur uniformly in pulse phase. Type B bursts have long tails, thermal spectra, and occur preferentially at pulse maximum. They also noted that Type B bursts occur preferentially in SGRs (although AXP 1E 2259+586 emitted both kinds of bursts during its 2002 outburst), and Type A bursts occur primarily in AXPs.

Woods et al. (2005) argue that type A bursts are due to reconnections in the upper magnetosphere, and that type B bursts are due to crustal fracture followed by a rearrangement of the magnetic field lines outside the surface. They explain that a magnetospheric origin would lend itself to more isotropic emission having no preference for a particular pulse phase, while the crust fracture model would naturally produce a phase dependence of the burst emission for a localized active region on the crust. The tendency of the bursts to occur near pulse maximum is consistent with the strain in the crust causing the cracking being highest in the regions where the field is the strongest: at the polar caps. Furthermore, Thompson et al. (2002) have argued that the SGRs, with their strong non-thermal spectral components, undergo more reconnection events. Therefore, if the type A bursts are really due to magnetospheric events, then it makes sense that they occur more in SGRs.

None of the bursts observed from 1E 1048.1−5937 is of the symmetric type. All

four bursts had a long tail with pulsed flux enhancement, except in burst 2 where the tail was very short, but still $\sim$ 300 times longer than the rise time. Therefore all four are probably bursts of Type B. However, burst 4 did not occur near pulse maximum. This does not necessarily mean that the above interpretation of Types A and B bursts is wrong; rather, for this burst, perhaps the crustal cracking did not occur near the polar cap, or near the hot spot that usually yields the pulse.

Note that a similar situation occured for AXP 4U 0142+61. Six bursts were detected from this AXP during the 2006 active phase (Gavriil et al. 2009b, Chapter 3). None of them was a short and symmetric Type A burst: they all had tails, although in two cases the tails were shorter than 10 s. Burst 1 occured at pulse maximum. Bursts 2 to 5 all occured within a single observation, and two of them did not occur near pulse maximum. Presumably some global event had caused the crust to crack at many places. Not only did burst 6 not occur at pulse maximum, but it occured where a temporary new peak in the profile appeared. Here, just like for burst 4 of 1E 1048.1−5937, a large crack could have appeared away from the usual location of the emission.

5.8 Summary

We have presented a long-term study of the timing properties, the pulsed flux, and the pulse profile of AXP 1E 1048.1−5937 as measured by *RXTE* from 1996 to 2008. We showed that the onset of the 2001 pulsed flux flare was accompanied by a timing anomaly and by significant pulse profile changes. The timing anomaly was consistent with a gradual slow down lasting 2−3 weeks followed by a recovery. We showed that the onset of the 2002 pulsed flux flare was accompanied by a likely glitch of size $\Delta\nu/\nu = 2.91(9) \times 10^{-6}$, by a large change in $\dot{\nu} = -4.10(14) \times 10^{-14}$, and by significant pulse profile changes. We use the term "likely" because, while the trend in the timing residuals indicates that a glitch occured, due to the finite resolution of the data, which is particularly problematic given the extreme timing noise of this source, a rapid non-instantaneous variation cannot be ruled out. Both of these flares had few-weeks-long rise time. Several months after the peak of the second flare, and while the pulsed flux was still decaying, the source underwent extreme $\dot{\nu}$ variations lasting $\sim$450 days. Then the source entered a period of relative timing quiescence in which no radiative changes were observed except for occasional low-level pulse profile changes. The source reactivated in 2007 and a third pulsed flux flare was

observed. The rise time of that flare was < 7.3 days. It is unclear whether the rise was resolved. Contemporaneous imaging observations showed that the persistent flux rose also. The onset of this flare was accompanied by a very large spin-up glitch ($\Delta\nu/\nu = 1.63(2) \times 10^{-5}$) and by many significant but short-lived pulse profile changes. In total, four short non-symmetric bursts have been observed in this source to date.

The three pulsed flux flares can be attributed to twists implanted in the external magnetosphere from stresses on the crust imposed by the internal magnetic field. Beloborodov & Thompson (2007) postulated the presence of a plasma corona within the closed magnetosphere and predicted a linear decay in the flux following the initial rise due to the twist. The first part of the decay of the observed flares can be well fit with a linear trend, but not the entire decay. Alternatively, the flares can be attributed to an internal heat release associated with the contemporaneous timing events, although the pulse profile changes seen contemporaneously with the flares likely have a magnetospheric origin. All three flares were accompanied by either a timing anomaly or a glitch. This can be due to a disturbance in the superfluid vortex lines caused by the crustal disturbance at the time the twist was implanted. The extreme timing noise observed several months after the peak of the second flare may be attributed, in the Beloborodov & Thompson (2007) picture, to the twist associated with the flare finally having reached the light cylinder, although it is hard to understand the magnitude and the time scale of the variability in this picture. Finally, all four bursts observed in this source can be attributed to the crustal cracking that occured when the twist propagated from the inside of the star to the lower magnetosphere.

A coherent physical picture explaining the variety of behaviours observed in this fascinating source, as well as in other AXPs, has yet to emerge, however we hope through continued detailed studies such as the one presented here, one will be forthcoming soon. Thus far, the framework of the magnetar model appears most promising to us.

Chapter 6

Summaries and Conclusions

The Rossi X-ray Timing Explorer (RXTE) has been operational since 1995 December. The AXP monitoring program began in 1997. When the program was initiated, it became for the first time clear that high precision is possible to achieve with AXP timing. Ever since its start, the project has provided a wealth of information about the behaviour of AXPs both in quiescence and in outburst. In this Chapter I summarize the pulsed flux, pulse profiles, and the timing histories of the five monitored AXPs.

Summary plots covering the time period between the start of the monitoring program until 2008 July (Figures 6.1, 6.2, 6.3, 6.4, and 6.5) are presented for each of the five monitored AXPs in Sections 6.1, 6.2, 6.3, 6.4, and 6.5, respectively. The same method was used to analyse the data and obtain the plots for AXPs 1E 2259+586, 4U 0142+61, RXS J170849.0−400910, and 1E 1841−045. The analysis and the plot for 1E 1048.1−5937 were done differently because of the unusual spin-down variations that this source presents. In Section 6.6, I summarize the pulse profile changes seen in the monitored AXPs. In Section 6.7, I review all AXP glitch parameters and comment on the association between glitches and radiative outbursts, a central topic in this thesis. Finally, in Section 6.8, I present a final discussion.

6.1 1E 2259+586: Timing Properties and Pulsed Flux Evolution

6.1.1 1E 2259+586: Preparing the Summary Plot

To generate the summary plot for AXP 1E 2259+586 (Figure 6.1), the following was done. First an overall trend of the form described in equation 6.1 was chosen,

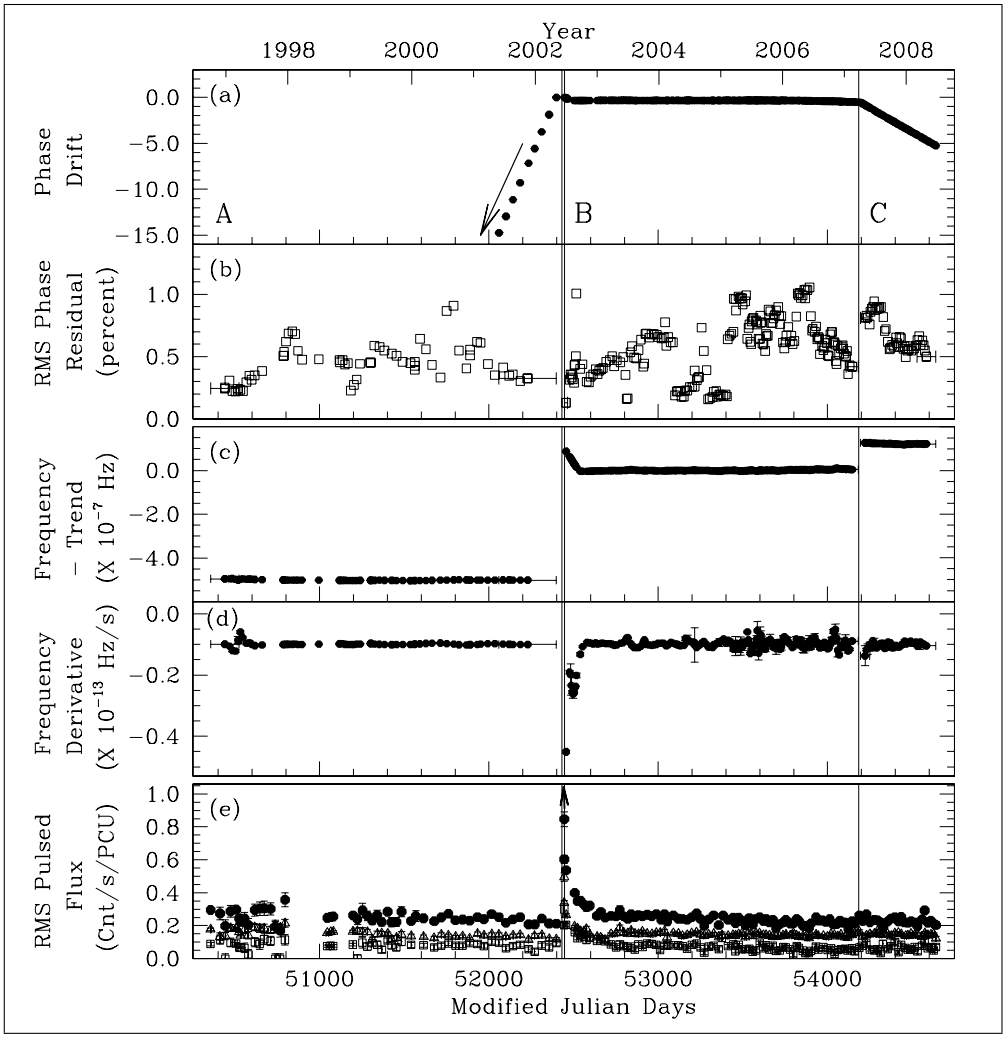

Figure 6.1 Summary Plot for AXP 1E 2259+586. *(a)* phase drift. Each data point corresponds to an individual observation. *(b)* RMS phase residual. The RMS phase residual for each set of TOAs is comparable in size to the typical TOA uncertainty, indicating a good fit. *(c)* frequency of 1E 2259+586 as a function of time with a linear trend subtracted. *(d)* frequency derivative of 1E 2259+586 as a function of time. *(b, c, and* d*):* each data point corresponds to one of the overlapping segments of TOAs. The first and last point of each of the three data sets (marked with "A", "B", and "C") have horizontal error bars that show how long one of the overlapping segments of TOAs is. *(e)* RMS pulsed flux in three different energy bands (solid circles: 2−10 keV, empty triangles: 2−4 keV, empty squares: 4−10 keV). For more details, See Section 6.1. *All panels:* the first two vertical lines (separated by only a few days) indicate the location of the first glitch. They enclose the first observation of the 2002 June outburst, as well as the following two observations which were taken in an unusual data mode. The last vertical line indicates the location of the second glitch exhibited by this source.

$$\nu = \nu_0 + \dot{\nu}(t - t_0), \tag{6.1}$$

where ν is the frequency, $\nu_0 = 0.143287534382$ s^{-1} is the frequency at the reference epoch t_0 = MJD 52400.0, and $\dot{\nu} = -0.099116178052 \times 10^{-13}$ s^{-2} is the frequency derivative of the pulsar. These parameters were obtained from fitting a linear ephemeris to the TOAs corresponding to observations taken between mid-2003 and the end of 2005, a glitch-free and relatively noise-free period. The timing noise in this interval, estimated by eye, was lower than in the pre-glitch interval.

The trend in phase corresponding to the trend in frequency described in Equation 6.1 is given by

$$\phi = \phi_0 + \dot{\phi}(t - t_0) + \frac{\ddot{\phi}}{2}(t - t_0)^2, \tag{6.2}$$

where $\dot{\phi} = \nu_0$, $\ddot{\phi} = \dot{\nu}$, and ϕ_0 is arbitrarily chosen.

The TOAs of AXP 1E 2259+586 (one TOA per observation) were then divided into *three data sets* (indicated with letters "A", "B", and "C" in Figure 6.1), separated by two glitches. For each data set, the following was done.

First, the TOAs were fed into `TEMPO` along with the ephemeris given in Equation 6.1. `TEMPO` returned a list of pulse numbers, each pulse number corresponding to an individual TOA. This number was then subtracted from the pulse phase predicted from Equation 6.2 for that TOA. The resulting phase residuals were plotted in panel a of Figure 6.1 (one data point per observation). During the time periods when the points in panel a form a horizontal line, the pulsar is spinning according to the ephemeris given in Equation 6.1. A line with a slope indicates that ν_0 is off but that the $\dot{\nu}$ of the pulsar is that given in Equation 6.1. A curve indicates that both ν_0 and $\dot{\nu}$ are off, or that the pulsar was spinning down according to a non-linear ephemeris.

To generate panels b, c, and d of Figure 6.1, each *data set* was divided into many *overlapping segments of TOAs*. Each segment contained 11 TOAs. Any two neighbouring segments shared all TOAs but one. For each segment we fitted a linear ephemeris consisting of ν, $\dot{\nu}$, and a reference epoch. For each segment `TEMPO` returned an RMS phase residual. The phase residuals are plotted in panel b. The best-fit ν values are plotted in panel c, after subtracting the trend given by Equation 6.1. The best fit $\dot{\nu}$ values are plotted in panel d. In panels b, c, and d, each data point corresponds to one of the overlapping segments of TOAs.

The RMS pulsed flux time series (panel e of Figure 6.1) was obtained, in three

different bands, using Equation 3.1. Then, for each band, the RMS pulsed flux was binned every 15 days, except for the first few days of the 2002 June outburst. The results are presented in panel e. The arrow indicates that the average RMS pulsed flux for the first observation in the 2002 June outburst has a value of 1.53 count/s/PCU, larger than the top vertical limit of the graph.

6.1.2 1E 2259+586: Monitoring Results

Brief Comparison to other AXPs: 1E 2259+586 is referred to by the number "1" on the P-$\dot{P}$ diagram in Figure 1.2. It is the AXP with the smallest $\dot{\nu}$. The inferred magnetic field of 1E 2259+586 ($B \sim 0.59 \times 10^{14}$ G) is the smallest in any AXP, and smaller than that of at least two rotation-powered pulsars (Section 1.2.6). It is also one of the two softest AXPs, with a power-law index of ~ -4 (Woods et al., 2004). It is associated with SNR CTB 109. The results of the RXTE *monitoring of 1E 2259+586 are presented in Figure 6.1 and summarized below.*

Timing: Panels c and d of Figure 6.1 show that this AXP is the least noisy of all five monitored AXPs (see Figures 6.2, 6.3, 6.4, and 6.5 for comparison). This is confirmed by the fact that it is generally easy to find a phase-connected timing solution when doing the data analysis, and by preliminary measurements of red noise amplitudes in AXPs done in Archibald et al. (2008). This AXP has exhibited two glitches in 12 years of monitoring.

The first glitch happened in 2002 June. The sudden jump in frequency at the time of the glitch as well as the subsequent recovery are clearly visible in panel c of Figure 6.1. Woods et al. (2004) showed that the recovery can be fit with a combination of exponentials, and that the recovery fraction was ~ 0.2. Extrapolating their model leads to a factor of ~ 9.2 enhancement in the frequency derivative at the time of the glitch clearly visible in panel d of Figure 6.1 (see Sections 4.6.1 and 6.7 for further discussion). This glitch was accompanied by a very large outburst (see below).

The second glitch from 1E 2259+586 happened in 2007 March. The sudden frequency jump at the time of the glitch was smaller than that at the first glitch as can be seen from panel c of Figure 6.1. There were no contemporaneous changes in the frequency derivative or the pulsed flux.

Pulsed Flux: The first glitch was accompanied by a very large outburst. The associated enhancement in the pulsed flux can be clearly seen in panel e of Figure 6.1.

Woods et al. (2004) determined that the glitch epoch preceded the first *RXTE* observation of the outburst by a few hours. They showed that at the beginning of that observation, the pulsed flux in the 2−10 keV band (measured in count/s/PCU) was a factor of $\sim$ 17 times its pre-outburst value, and that the total flux of the source rose by a factor of $\sim$ 10. Observations with imaging instruments also showed spectral changes at the time of the outburst. The long-term decay in the flux was studied by Zhu et al. (2008).

Pulse Profile Changes: The 2002 June outburst was accompanied by large pulse profile changes which complicated the timing analysis (see Section 6.6).

Bursts: There were $\sim$ 80 bursts detected from this source, all in the first observation of the 2002 June outburst (Gavriil et al., 2004).

6.2 4U 0142+61: Timing Properties and Pulsed Flux Evolution

6.2.1 4U 0142+61: Preparing the Summary Plot

To generate the summary plot for AXP 4U 0142+61 (Figure 6.2), we followed the same steps as those used in Section 6.1.1 to generate the summary plot for 1E 2259+586. The differences between the two analyses are:

- The chosen linear trend in frequency to be subtracted had the following parameters: $\nu_0 = 0.115097137564$ s^{-1} at reference epoch $t_0 =$ MJD 52400.0, and $\dot{\nu} = -0.265907228464\times10^{-13}$ s^{-2}. These parameters were obtained from fitting a linear ephemeris to the TOAs corresponding to observations taken between the year 2000 and the start of 2006, a long glitch-free period.

- The TOAs were divided into *three data sets* (indicated with letters "A", "B", and "C" in Figure 6.2). Data set "A" corresponds to the observations before the gap, data set "B" corresponds to the observations after the gap but before the active phase, and Data set "C" corresponds to the observations taken after the entry into the active phase. Each *data set* was then divided into *overlapping segments of TOAs*.

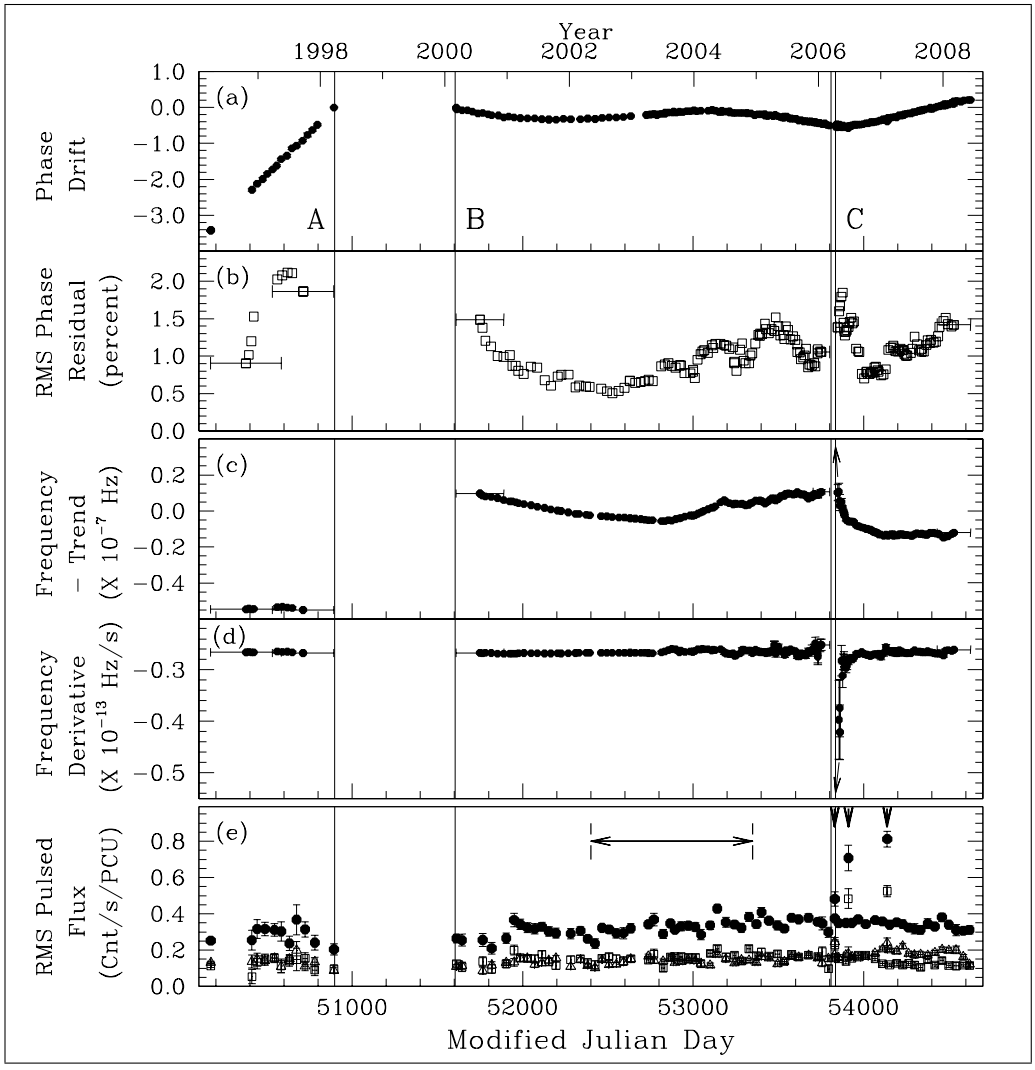

Figure 6.2 Summary Plot for AXP 4U 0142+61. *Individual panels:* same as Figure 6.1. *All panels:* the first two vertical lines enclose a 2-year period with no *RXTE* observations of 4U 0142+61. It is likely that the pulsar suffered a glitch sometime in this gap (see Chapter 2). The next two vertical lines (separated by only a few days) enclose the first observation of the active phase that the source entered in 2006 March. It is likely that the pulsar suffered a glitch at the onset of this active phase (see Chapter 3).

- Each of the *overlapping segments of TOAs* contained 11, 13, or 17 TOAs depending on how often the source was observed.
- For each band, the RMS pulsed flux was binned every 30 days, except for the three observations containing bursts and marked with an arrow in panel e.

6.2.2 4U 0142+61: Monitoring Results

Brief Comparison to other AXPs: 4U 0142+61 is referred to by the number "2" on the P-$\dot{P}$ diagram in Figure 1.2. It is the AXP with the second smallest $\dot{\nu}$. It is the monitored AXP with the second smallest inferred magnetic field ($B \sim 0.589 \times 10^{14}$ G). It is also the monitored AXP with the second softest spectrum (power-law index ~ -3.7) after 1E 2259+586 (Göhler et al., 2005). 4U 0142+61 was studied in Chapters 2 and 3. The results of the RXTE *monitoring of 4U 0142+61 are presented in Figure 6.2 and summarized below.*

Timing: The level of timing noise seen in panels c and d of Figure 6.2 is larger than that seen in AXP 1E 2259+586 (Figure 6.1) but smaller than that seen in the other monitored AXPs (Figures 6.3, 6.4, and 6.5). This AXP has exhibited two likely glitches in 12 (interrupted) years of monitoring.

The first candidate glitch was claimed by Morii et al. (2005) based on frequency measurements in *ASCA* observations taken in 1998 and 1999. Panel c of Figure 6.2 shows that indeed a frequency jump in the 1998−2000 observing gap is likely, although a slow increase in the frequency is also possible (see Chapter 2).

From the beginning of 2000 to the beginning of 2006, the pulsar did not exhibit any large changes in the timing parameters, although some radiative changes were observed (see below).

The second candidate glitch likely occurred in 2006 March at the onset of the active phase described in Chapter 3. The active phase consisted of a timing anomaly that can be described by a net spin-down following an initial spin-up (see the boundary of the "B" and "C" data sets in panels c and d of Figure 6.2), although the magnitude of the spin-up is uncertain because the glitch parameters are very dependent on a single observation and because of the pulse profile fluctuations that occurred during the active phase. Following the spin-up, six bursts were detected (see below).

Pulsed Flux: In Chapter 2, we showed that between 2002 May and 2004 December, the pulsed flux of 4U 0142+61 increased very slowly by 29±8% (after taking the response of the detector into account, and when the flux is measured in erg/cm^2). This period of time is indicated by a double-ended arrow in panel e of Figure 6.2. The pulsed flux was also enhanced during the three observations where bursts were detected (marked with three arrows in panel e of Figure 6.2).

An interesting feature in panel e which has not been investigated yet is the apparent

spectral change that occurred a few weeks before the last observation containing bursts: the empty triangles (pulsed flux data points in the 2−4 keV band) and the empty squares (pulsed flux data points in the 4−10 keV band) suddenly split, indicating a softening in the *pulsed* spectrum (*to be investigated in future work!*).

Pulse Profile Changes: From 2000 to 2006 the pulsar showed a slow evolution in the 2−4 keV pulse profile where the dip between the two peak was rising (Chapter 2). Additional pulse profile changes were seen during the active phase, which made extracting the timing parameters difficult (Chapter 3).

Burst: Six bursts were detected from the pulsar in three observations in the active phase (marked with three arrows in panel e of Figure 6.2).

6.3 1RXS J170849.0−400910: Timing and Pulsed Flux Evolution

6.3.1 1RXS J170849.0−400910: Preparing the Summary Plot

To generate the summary plot for AXP 1RXS J170849.0−400910, (Figure 6.3), we followed the same steps as those used in Section 6.1.1 to generate the summary plot for 1E 2259+586. The differences between the two analyses are:

- The chosen linear trend in frequency to be subtracted had the following parameters: $\nu_0 = 0.090900015529$ s^{-1} at reference epoch $t_0 =$ MJD 52459.0, and $\dot{\nu} = -0.58123165\times10^{-13}$ s^{-2}. These parameters were obtained from fitting a linear ephemeris to the TOAs corresponding to observations taken between the year 2000 and mid-2005.

- The TOAs were divided into *five data sets* three data sets (indicated with letters "A", "B", "C", "D", "E", and "F/G" in Figure 6.2). Data set "A" corresponds to the observations before the first glitch. Data set "B" corresponds to the observations between the first and the second glitch. Data set "C" corresponds to the observations between the second glitch and the Sun-constraint observing gap in 2003 December. Data set "D" corresponds to the observations between the 2003 December and the 2004 December Sun-constraint observing gaps.

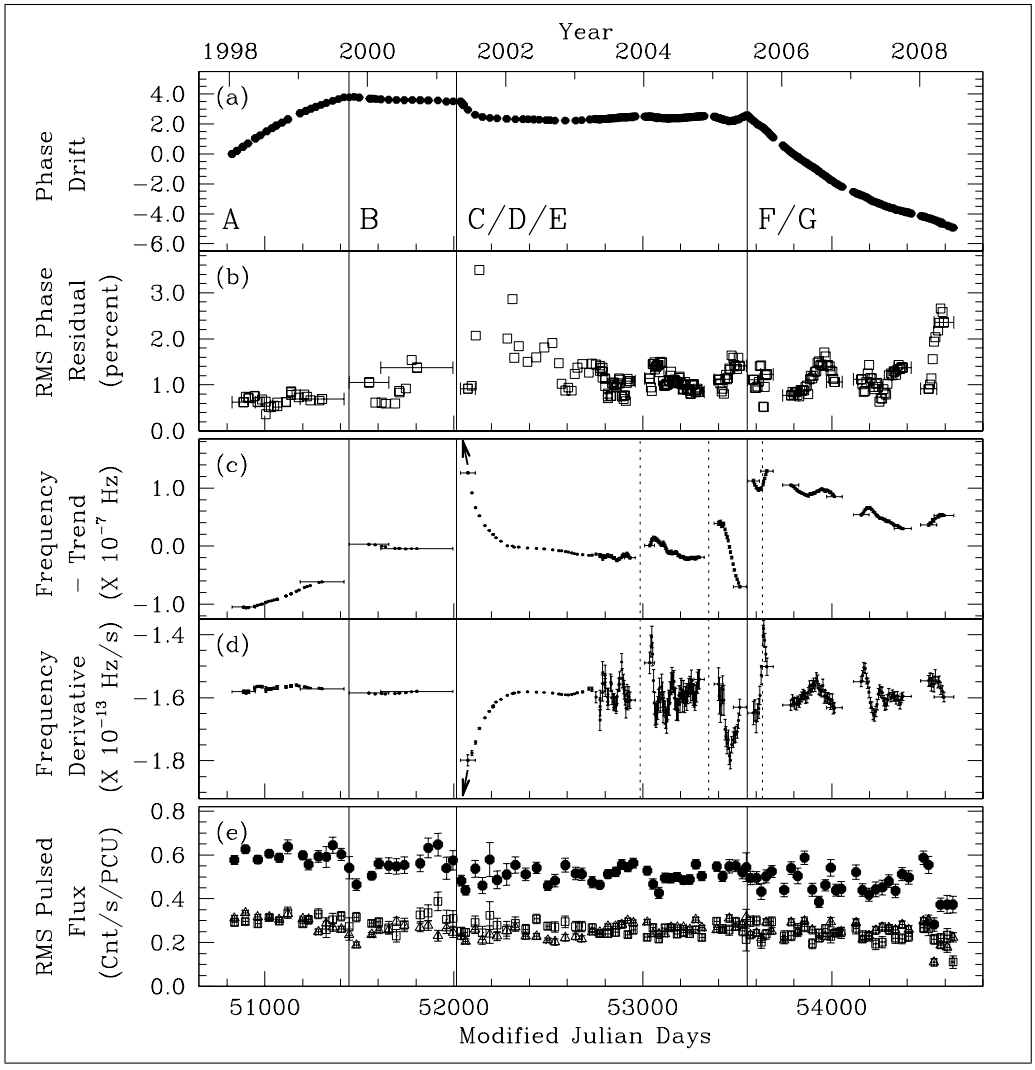

Figure 6.3 Summary Plot for AXP 1RXS J170849.0−400910. *Individual panels:* same as Figure 6.1. *All panels:* the three solid vertical lines mark the location of three glitches. The first two dotted lines mark the location of two candidate glitches, although the second was labelled "glitch" by Israel et al. (2007). The event corresponding to the third dotted line was classified as a candidate glitch in Chapter 4, however continued monitoring shows that similar events often occur, indicating that this event may be better classified as large noise.

Data set "E" corresponds to the observations between the 2004 December Sun-constraint observing gap and glitch 3. Data set "F/G" corresponds to the observations between glitch 3 and the end of the data analysed for this thesis. Each *data set* was then divided into *overlapping segments of TOAs*.

- Each of the *overlapping segments of TOAs* contained 11 or 13 TOAs depending on how often the source was observed.

- For each band, the RMS pulsed flux was binned every 30 days, except for the three observations containing bursts and marked with an arrow in panel e.

6.3.2 1RXS J170849.0−400910: Monitoring Results

Brief Comparison to other AXPs: 1RXS J170849.0−400910 is referred to by the number "3" on the P-$\dot{P}$ diagram in Figure 1.2. Its inferred magnetic field is $B \sim 3.19\times10^{14}$ G. 1RXS J170849.0−400910 and 1E 1841−045 are the AXPs with the longest periods ($P \sim$11.0 for 1RXS J170849.0−400910). They also both have an X-ray luminosity[1] *(calculated from the observed flux and from the estimated distance) that is at least an order of magnitude larger than that of all other non-transient AXPs. This AXP was studied in Chapter 4. The results of the* RXTE *monitoring of 1RXS J170849.0−400910 are presented in Figure 6.3 and summarized below.*

Timing: In 2003 March the observing cadence changed from 12 observations per year to 56 observations per year, and again to 70 observations per year in 2004 March. This made us more sensitive to timing noise on smaller time scales. Panels c and d of Figure 6.3 show that this source is indeed very noisy on weeks-to-months time scale. Several glitches were detected from this source in 11 years of monitoring (Chapter 4).

The first glitch occurred in 1999. The second glitch occurred on 2001 and was followed by a quasi-exponential recovery, as can be seen from panels c and d of Figure 6.3. Immediately after the second glitch, the frequency derivative was enhanced by a factor of 1.64±0.06 (see Sections 4.6.1 and 6.7 for further discussion). In 2003 December and in 2004 December there were two events which we classified in Chapter 4 as "candidate glitches" because it was impossible to determine whether the frequency rose slowly or abruptly since the events happened during an observing gap (see panel c). In 2005 June, a large glitch occurred. Then, in 2005 December the noise level was particularly high which lead us to consider September 21 as a location for another candidate glitch (third dotted line in Figure 6.3). A linear ephemeris fit before and after this date shows that a glitch is possible, however an polynomial of order 4 can also fit the data near that epoch (Chapter 4).

Pulsed Flux: As far as the pulsed flux is concerned, there appears to be no radiative changes at the location of the glitches and the glitch candidates. Although, It appears from panel e of Figure 6.3 that there is a significant scatter in the pulsed flux data

[1] Luminosity from the online magnetar catalog.

points. An example of this is the dip in the pulsed flux in 2008 (which recovered subsequent to the writing of this thesis). When the unbinned pulsed flux time series is plotted (not shown) there appears to be local trends in the pulsed flux. The reason for this scatter is unknown (*to be investigated in future work!*)

Campana et al. (2007) claimed large changes in the total flux of the source based on a few observations done with imaging instruments (Figure 4.14). However this is controversial due to the sparsity of the data and due to the method used to do the spectral fitting (Gavriil et al., 2009a).

Pulse Profile Changes: Dall'Osso et al. (2003) claimed pulse profile changes in this source near the second glitch. In Chapter 4 we did not find evidence for this (see Figure 4.10), and we calculated the probability of a pulse profile change having occurred in the 2−10 keV band at the first glitch to be 0.4%, and at the first candidate glitch to be 1.7%, and at the second candidate glitch to be (1.0×10^{-6})% (also see Section 6.6).

Burst: There were no significant bursts detected from this source.

6.4 1E 1841−045: Timing Properties and Pulsed Flux Evolution

6.4.1 1E 1841−045: Preparing the Summary Plot

To generate the summary plot for AXP 1E 1841−045, (Figure 6.3), we followed the same steps as those used in Section 6.1.1 to generate the summary plot for 1E 2259+586. The differences between the two analyses are:

- The chosen linear trend in frequency to be subtracted had the following parameters: $\nu_0 = 0.084903788106$ s^{-1} at reference epoch $t_0 =$ MJD 52460.0, and $\dot{\nu} = -2.962178444\times10^{-13}$ s^{-2}. These parameters were obtained from fitting a linear ephemeris to the TOAs corresponding to observations taken between 1999 and mid-2002, a long glitch-free period.
- The TOAs were then divided into *four data sets* (indicated with letters "A", "B", "C", and "D" in Figure 6.4), separated by the four glitches detected from this source. Each *data set* was then divided into *overlapping segments of TOAs*.

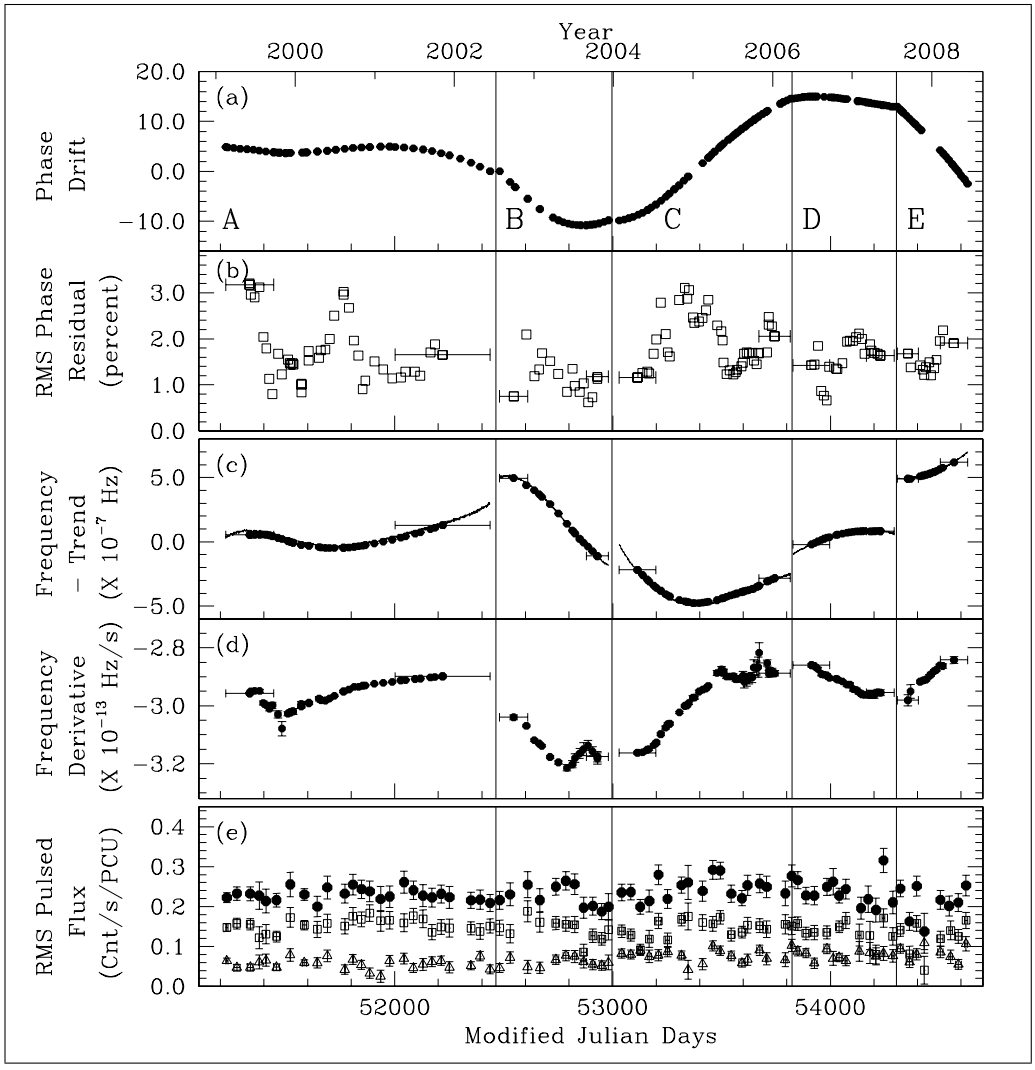

Figure 6.4 Summary Plot for AXP 1E 1841−045. *Individual panels:* same as Figure 6.1. In *(c)*, The curves running through the data points are polynomial fits that stop at the last observation before a glitch and start again at the first observation after a glitch (see Section 4.3.2). *All panels:* the 4 vertical lines mark the epochs of the 4 glitches detected from this source.

- Each of the *overlapping segments of TOAs* contained 5−11 TOAs depending on how often the source was observed.

- For each band, the RMS pulsed flux was binned every 30 days, except for the three observations containing bursts and marked with an arrow in panel e.

6.4.2 1E 1841−045: Monitoring Results

Brief Comparison to other AXPs: 1E 1841−045 is referred to by the number "4" on the P-$\dot{P}$ diagram in Figure 1.2. Its inferred magnetic field is B $\sim$ 4.84×10^{14} G. 1RXS J170849.0−400910 and 1E 1841−045 are the AXPs with the longest period (P $\sim$11.78 for 1E 1841−045). They also both have an X-ray luminosity[2] (calculated from the observed flux and from the estimated distance) that is at least an order of magnitude larger than that of all other non-transient AXPs. 1E 1841−045 has the hardest spectrum of all five monitored AXPs with a power-law index of ~ -2.0 (Morii et al., 2003). 1E 1841−045 is associated with SNR Kes 73. This AXP was studied in Chapter 4. The results of the RXTE *monitoring of 1E 1841−045 are presented in Figure 6.4 and summarized below.*

Timing: 1E 1841−045 was observed twice per month since 2005 March, and less frequently before that. Because it is observed less frequently than 1RXS J170849.0−400910, we are not sensitive to timing noise on as small a time scale as we are for 1RXS J170849.0−400910. But it is still possible to see from panels c and d in Figure 6.4 that the source is noisy. In 1RXS J170849.0−400910, the frequency derivative seems to be continuously varying (on time scales of weeks to months) around the long-term $\dot{\nu}$ (panel d of Figure 6.3), but it does not spend years away from the long-term $\dot{\nu}$. In 1E 1841−045, because the frequency derivative spends years away from the long-term $\dot{\nu}$ (panel d of Figure 6.4), it is difficult to determine what the long-term $\dot{\nu}$ is. The timing-noise spectrum of 1E 1841−045 is thus different from that of 1RXS J170849.0−400910 (*to be investigated in future work!*).

This source has exhibited four large glitches since the start of the monitoring program (marked by the vertical lines in Figure 6.4). The frequency jumps are clearly visible in panel c (see Sections 4.6.1 and 6.7 for a discussion of glitch sizes).

The first glitch was initially thought to have a quasi-exponential recovery (Chapter 4). However, after the publiation of the manuscript on which Chapter 4 is based, and with the help of two additional observations from *XMM*, we were able to determine that the correct timing solution near the glitch epoch was one that we had reported in Chapter 4 as an alternate unlikely solution. The combined *XMM* and *RXTE* analysis will be presented in Dib et al. (2009a). Panels a, b, c, and d of Figure 6.4 are consistent with the revised analysis and include the data points corresponding to the *XMM* observations.

[2]Luminosity from the online magnetar catalog.

Pulsed Flux: There were no observed significant changes in the pulsed flux of this source (panel e of Figure 6.4) neither at glitch epochs, nor in glitch-free intervals. If one assumes that the pulsed fraction is also constant, this means that the total flux of the source is constant as well. Zhu et al. (2009) investigated this possibility by studying imaging observations of the source and found that the total flux is not varying. However this is a preliminary result.

Pulse Profile Changes: There were no significant pulse profile changes detected from this source.

Bursts: There were no significant bursts detected from this source.

6.5 1E 1048.1−5937: Timing Properties and Pulsed Flux Evolution

6.5.1 1E 1048.1−5937: Preparing the Summary Plot

To generate the summary plot for AXP 1E 1048.1−5937 (Figure 6.5), the following was done. First an overall trend of the form described in equation 6.1 was chosen, where ν is the frequency, $\nu_0 = 0.155009326241$ s^{-1} is the frequency at the reference epoch t_0 = MJD 51000.0, and $\dot{\nu} = -5.424845132570\times10^{-13}$ s^{-2} is the frequency derivative of the pulsar. These parameters correspond to the long-term average linear ephemeris.

The TOAs of AXP 1E 1048.1−5937 (one TOA per observation) were then divided into *six data sets* (indicated with letters "A", "B", "C", "D", "E", and "E" in and "D" in Figure 6.5), separated by timing anomalies/glitches or gaps in the data. Then, for each data set the frequency as a function of time, frequency derivative as a function of time, and timing residuals were found by fitting splines through the data points (for complete details, see Section 5.3.1). The results are shown in panels b, c, and d of Figure 6.5, with the overall linear trend in frequency described above subtracted from panel c.

The RMS pulsed flux time series (panel e of Figure 6.5) was obtained using Equation 3.1. When several observations were obtained within 24 hours of each other, their

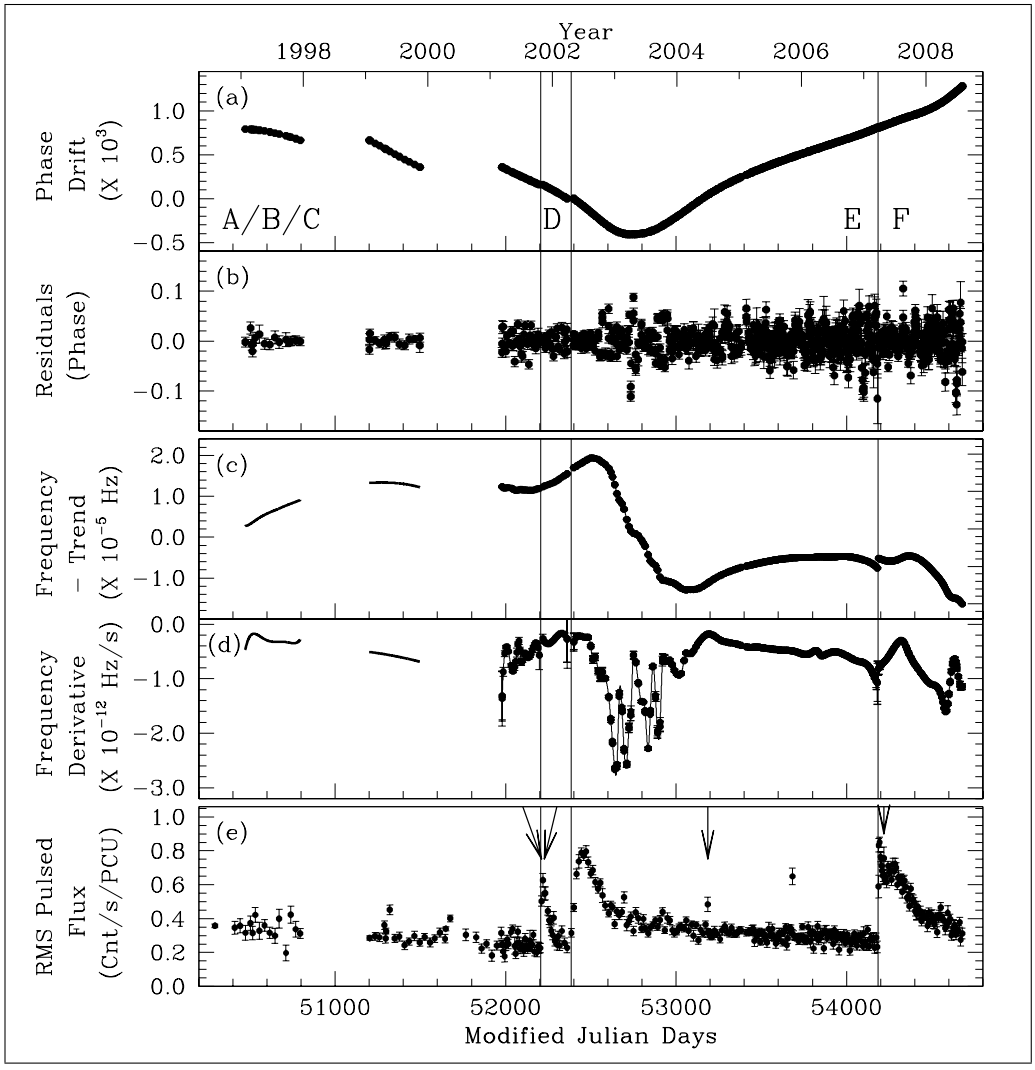

Figure 6.5 Summary Plot for AXP 1E 1048.1−5937. *(a)* phase drift relative to a long-term linear ephemeris. *(b)* Timing residuals obtained after subtracting the TOAs from the ephemerides plotted in panel c. In both panels *a* and *b* each data point corresponds to an individual observation. *(c) Curve:* frequency of 1E 1048.1−5937 as a function of time with a linear trend subtracted, obtained from spline-fitting. *Data points:* the spline evaluated at the epoch of the observations. *(d) Curve:* frequency derivative of 1E 1048.1−5937 as a function of time, obtained from spline fitting. *Data points:* the spline evaluated at the epoch of the observations. For more details, see Section 6.5, Section 5.3.1, and the caption to Figure 5.3. *(e)* RMS pulsed flux in the 2−10 keV band. The 2−4 keV and the 4−10 keV bands are not shown here because of overcrowding but can be seen in Figure 5.10. *All panels:* The first vertical line marks the location of a timing anomaly. The second vertical line marks the location of a glitch candidate. The third vertical line marks the location of a large glitch.

pulsed flux was averaged except when bursts were detected (arrows in panel e) or at

the onset of pulsed flux flares.

6.5.2 1E 1048.1−5937: Monitoring Results

Brief Comparison to Other AXPs: 1E 1048.1−5937 is referred to by the number "5" on the P-$\dot{P}$ diagram in Figure1.2. Its inferred magnetic field is $B \sim 2.66 \times 10^{14}$ G. It is the monitored AXP with the largest $\dot{\nu}$ (although not the largest $\dot{P}$). It is also by far the noisiest monitored AXP and the monitored AXP that has exhibited the most radiative changes (see below). When not in outburst, it also has the smallest luminosity[3] (calculated from the observed flux and from the estimated distance) of all five monitored AXPs. This AXP was studied in Chapter 5. The results of the RXTE *monitoring of 1E 1048.1−5937 are presented in Figure 6.5 and summarized below.*

Timing: 1E 1048.1−5937 is the noisiest of all monitored AXPs: it is difficult to find a phase-connected solution describing the timing properties of this source even outside periods of unusual activity. As can be seen from panels c and d of Figure 6.5, from the beginning of 2001 to the beginning of 2004, and particularly during 2003, timing the source was even more difficult due to a level of noise in the frequency derivative never before reported in a pulsar. In Section 5.7 we speculated whether this noise episode was related to the pulsed flux flares that occurred the preceding year. But our discussion was inconclusive. The source seems to have entered a new noisy episode in 2008 and a comparison between the two episodes of noise might shed light on the cause of the noise (*to be investigated in future work!*)

A close examination of the timing behaviour revealed that a timing anomaly occurred at the onset of the first pulsed flux flare and that a glitch candidate occurred at the onset of the second pulsed flux flare. The event was classified as a glitch candidate because a rapid non-instantaneous variation cannot be ruled out (Sections 5.3.2 and 5.3.3). The largest glitch detected from a monitored AXP occurred in 2007 at the onset of the third pulsed flux flare of the source (third vertical line in Figure 6.5). Note that there was a turn-over in the frequency derivative before the glitch which is difficult to see in panel d (however see Figure 5.6).

Pulsed Flux: The source exhibited two slow-rise pulsed flux flares in 2002 and in 2003 (panel e of Figure 6.5). No other AXP has showed a similar type of behaviour. In 2007, the source exhibited a third rise in pulsed flux but it was difficult to determine

[3]Luminosity from the online magnetar catalog.

how fast the pulsed flux rose due to the uncertainty on the pulsed flux in the first post-glitch observation. In all three cases it was not possible to determine whether the timing event coincident with the flare occurred before or after the the pulsed flux started to rise. All three pulsed flux flares were accompanied by rise in the overall flux of the source (Tiengo et al., 2005; Tam et al., 2008a). Tiengo et al. (2005) and Tam et al. (2008a) also reported an anti-correlation between the total flux of this source and the pulsed fraction.

1E 1048.1−5937 also exhibited variations in the pulsed flux on a much shorter time scale: the pulsed flux was enhanced (and slowly fell) within the 4 observations in which bursts occurred (marked with arrows in panel e of Figure 6.5). The spectrum in these 4 observations was harder than average. The pulsed flux was also enhanced and the spectrum was harder in one observation in 2006 but no evidence for a burst of for a slow pulsed flux decay was found within the observation. Since many AXP bursts are accompanied by an enhancement in the pulsed flux which decays within a few hours, searching for enhancements in the pulsed flux on short time scales might lead to evidence for bursts that the burst-search routine has missed (*to be investigated in future work!*)

Long-term overall changes in the hardness of the spectrum also occur and they are associated with the outbursts (see Section 5.5).

Pulse Profile Changes: The source exhibited pulse profile changes at the onset of all three slow-rise pulsed flux flares. In all three cases the central peak developed one to several small side peaks (see Sections 5.4 and 6.6).

Bursts: Four bursts were detected from this source. The first two happened near the peak of the first slow-rise pulsed flux flare. The second happened during the decay of the second flare, and the last happened during the decay if the third flare. In addition, our burst-search routine detected several bursts (from this source and from the other sources) with much lower significance. It is unknown whether these very narrow bursts originate from the AXPs, from something else in the field of view, or if they are instrumental (*to be investigated in a future work!*)

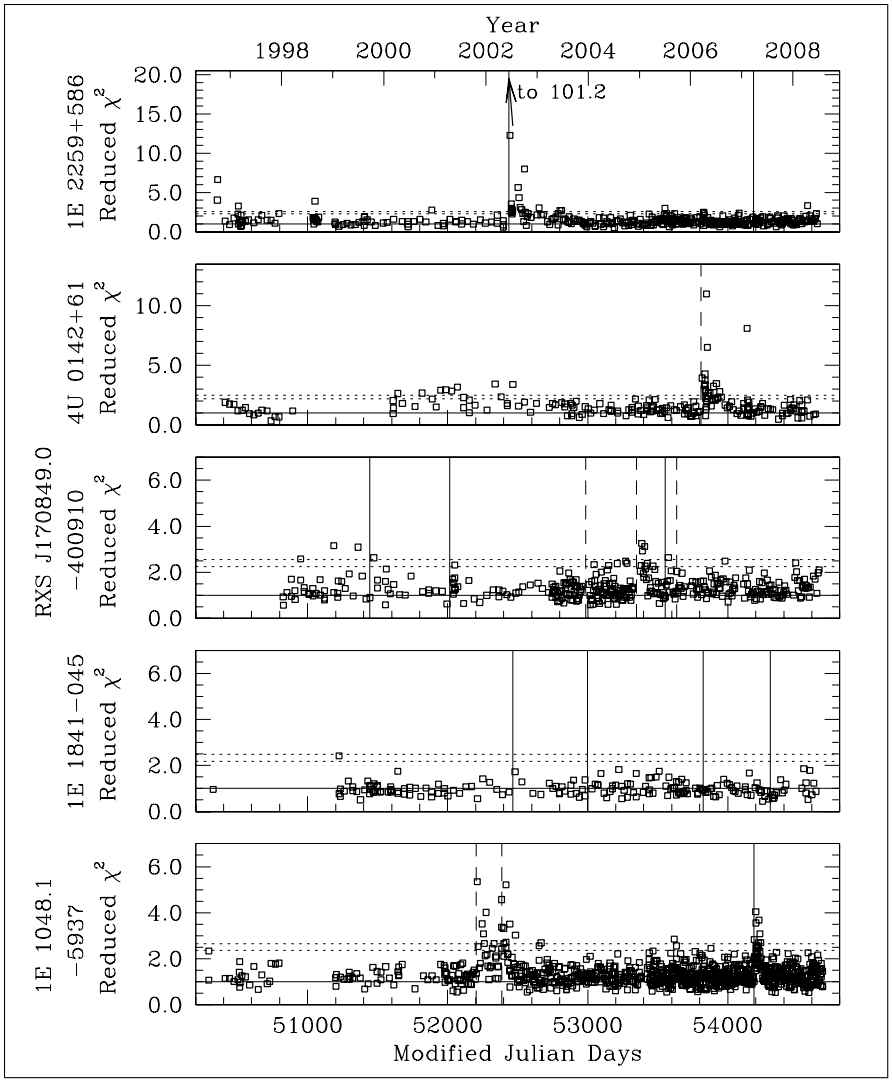

Figure 6.6 Reduced χ^2 statistics versus time, calculated after subtracting the scaled and aligned profiles of the individual observations from a high signal-to-noise template for each AXP. The following energy bands were used. 1E 2259+586: 2.5−9.0 keV band, 4U 0142+61: 2.5−9.0 keV band, 1RXS J170849.0−400910: 2.0−6.0 keV band, 1E 1841−045: 2.0−11.0 keV band, and 1E 1048.1−5937: 2.0−10.0 keV. The solid vertical lines indicate the location of glitches, and the dashed vertical lines indicate the locations of glitch candidates. Some of these glitches/glitch candidates were accompanied by an increase in the pulsed flux (see Sections 6.1, 6.2, 6.3, 6.4, and 6.5). *All panels:* The solid horizontal line indicates a reduced χ^2 of 1. The lower dotted line corresponds to the 2 σ significance level, after having taken the number of trials into account. Any point on this line indicates that the difference between the pulse profile of the corresponding observation and the long-term average profile is significant on the 2 σ level. The upper dotted line corresponds to the 3 σ significance level.

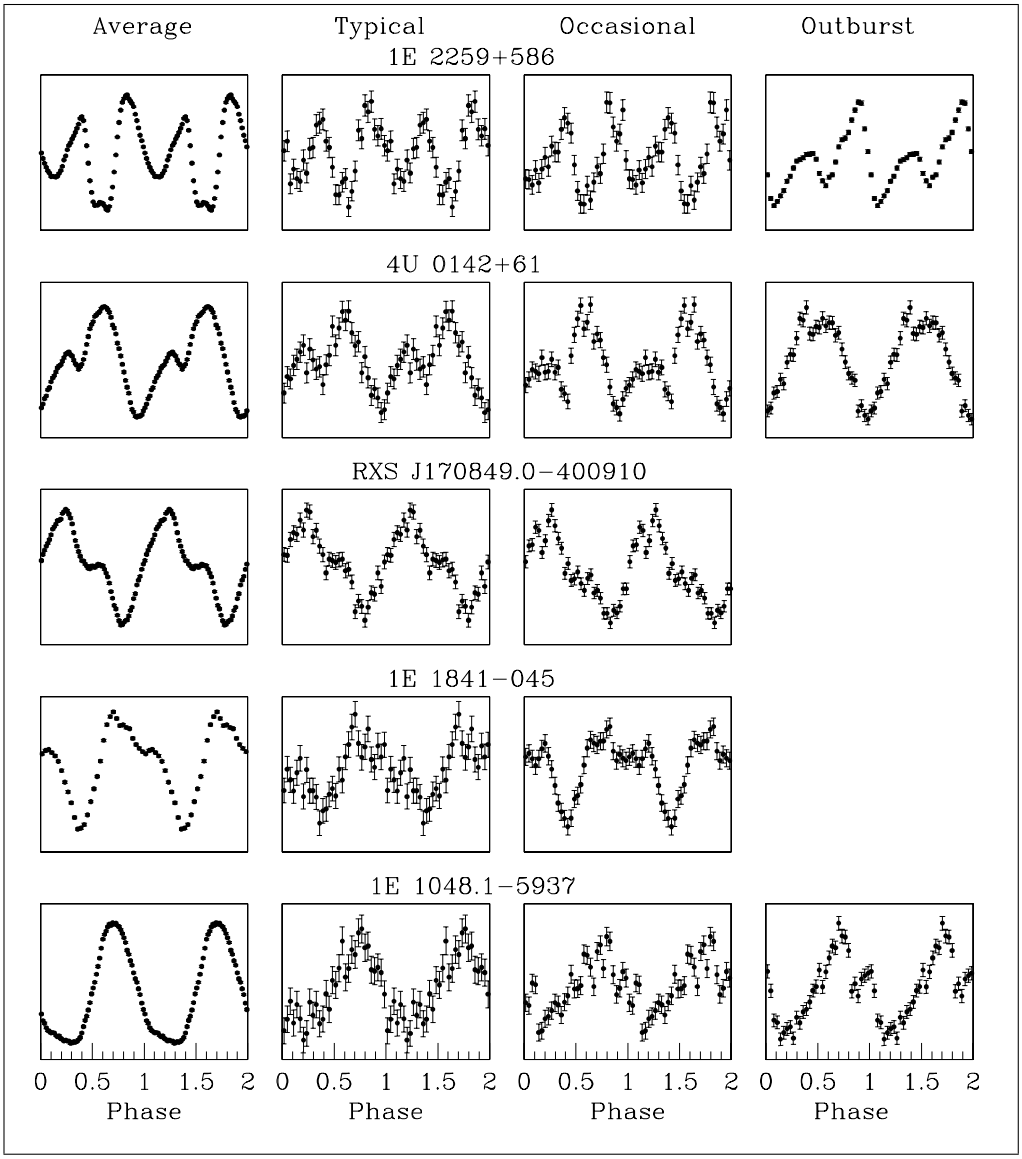

Figure 6.7 Pulse profiles from each of the five monitored AXPs in the following energy bands. 1E 2259+586: 2.5−9.0 keV band, 4U 0142+61: 2.5−9.0 keV band, 1RXS J170849.0−400910: 2.0−6.0 keV band, 1E 1841−045: 2.0−11.0 keV band, and 1E 1048.1−5937: 2.0−10.0 keV band. *Left-Most Column:* the long-term average pulse profile. *Second Column:* typical pulse profiles from five typical observations, the deviation from the long-term average profile is $\sim 1\ \sigma$ in all five cases (see Figure 6.6). *Third Column:* five unusual pulse profiles obtained outside periods of outburst. the deviations from the long-term average profiles are, from top to bottom, 2.1 σ, 3.4 σ, 3.1 σ, 1.7 σ, and 2.9 σ. *Right-Most Column:* pulse profiles of three AXPs in outburst. the deviations from the long-term average profiles are, from top to bottom, 101.2 σ, 8.1 σ, and 5.3 σ. AXPs 1RXS J170849.0−400910 and 1E 1841−045 did not go into outburst while being monitored by *RXTE*.

6.6 The Pulse Profiles of the Monitored AXPs

Pulse profile changes were seen on several occasions from AXPs over the duration of the *RXTE* monitoring program. 1E 2259+586 exhibited large pulse profile changes at the onset of the 2002 June outburst where the two peaks in the profile swapped amplitude (Woods et al., 2004). 4U 0142+61 exhibited slow pulse profile changes between 2000 and 2006 in the 2−4 keV band where the dip between the two peaks seemed to be slowly rising (Chapter 2). It also exhibited pulse profile changes at the onset of the 2006 active phase (Chapter 3). 1RXS J170849.0−400910 showed hints of pulse profile changes near two glitch candidates (Chapter 4). The pulse profile of 1E 1048.1−5937 developed side peaks near the onset of all three pulsed flux flares (Chapter 5). In the literature there also are other examples of magnetars (AXPs and SGRs) exhibiting pulse profile changes. The most dramatic example of this is the simplification of the profile of SGR 1900+14 after its dramatic giant-flare (Woods et al., 2001).

Pulse profiles were analysed in the individual Chapters and were discussed in Sections 2.4, 3.4, 4.6, and 5.7. In addition to the analysis presented in the individual chapters, we did the following. We extracted a pulse profile for each observation in each AXP using all available PCUs to maximize the signal to noise. We used 32 phase bins. We aligned the obtained profiles with the high signal-to-noise template and subtracted the respective average from each of the aligned profiles and from the template. For each observation, we then found the scaling factor that minimized the reduced χ^2 of the difference between the scaled profile and the template. The obtained reduced χ^2 values are plotted in Figure 6.6. Examples of typical and of unusual pulse profiles for each of the AXPs are presented in Figure 6.7.

The results presented in the Figure confirm our findings: the largest pulse profile changes occurred at the onset of the outburst of 1E 2259+586, the flares of 1E 1048.1−5937, and the active phase of 4U 0142+61. In addition, there seems to be occasional pulse profile variations on the 2−3 σ level in all AXPs. A careful look at the corresponding observations shows that there is some correlation between the length of the observation and the significance of the pulse profile deviation from the long-term average profile. This suggests that the pulse profile of the AXPs may be continuously changing on a level that we usually cannot detect because our signal-to-noise ratio is too low.

To understand the pulse profiles of magnetars better, Fernández & Thompson

(2007) attempted Monte Carlo simulations of the resonant scattering in the magnetosphere of thermal seed photons supplied by single-temperature blackbody emission from the stellar surface. From this, they constructed pulse profiles for arbitrary orientations of the spin axis, magnetic axis, and line of sight, using a self-similar, twisted dipole field geometry. They found that their calculations generally reproduce X-ray pulse profiles that are characteristic of the AXPs: single or multiple peaks, with sinusoidal shapes and sometimes the presence of narrow sub-pulses, which depended on the orientation of the spin and magnetic axes of the neutron star.

In addition to the location of the hot spots on the surface, and to the orientation of the rotation and magnetic axes with respect to each other and to the line of sight, the Thompson et al. (2002) model specifies that several other parameters can contribute towards a certain pulse shape and can sometimes alter it by generating subpulses or changing the energy dependence of the pulse profile. These parameters include an anisotropy in the optical depth in the twisted magnetosphere due to particle resonant scattering, an aspherical shape of the resonant surface, Doppler beaming of the scattered radiation resulting from the bulk motion of the charge carriers, and resonant scattering by non-axisymmetric currents (even for an axisymmetric magnetic field); this latter effect, happens when the deformations in the neutron star crust that generate the currents have azimuthal structure. Furthermore, an increase in the twisting angle in the magnetosphere increases multiple scattering, and increases the optical depth to resonant scattering which can simplify the pulse shape.

From the above, there appears to be no lack of reasons for a continuous or a sudden change in the pulse profile of AXPs, but on a case-by-case basis it is very difficult to determine which of these effects is responsible for the observed changes, especially because the geometry of the spin and the magnetic axes is not very well constrained. So while in principle studying pulse profile changes can lead to a better understanding of the structure of the surface and of the magnetosphere, so far studying the pulse profiles of the monitored AXPs has not lead to a significant breakthrough.

6.7 AXP Glitches Revisited

In Table 6.1, I present a summary of the glitch parameters for all the glitches that occurred in the five monitored AXPs since the start of the monitoring program.

Table 6.1. Glitches Observed in the Monitored Anomalous X-ray Pulsars*,⋆

Glitch Number	MJD Range[a]	Glitch Epoch (MJD)	$\Delta\nu$[b] (Hz)	$\Delta\nu/\nu$[c]	$\Delta\dot{\nu}$[d] (Hz/s)	τ[e] of Exponential Recovery (day)	Associated Radiative Events[f]	References
AXP 1E 2259+586, $P \sim 6.98$ s, $\nu \sim 0.1432865$ Hz, $\dot{\nu} \sim -0.0991\times10^{-13}$ Hz/s, B[g]$\sim 0.59\times10^{14}$ G.								
Glitch 1[h]	51623−52900	52443.130000	$\sim4.95\times10^{-7}$ (long-term) + $\sim1.13\times10^{-7}$ (recovered)	$4.24(11)\times10^{-6}$	$+2.18(25)\times10^{-16}$	A few months[h]	Bursts, pulsed and total flux enhancements, large profile changes	Woods et al. (2004) Kaspi et al. (2003)
Glitch 2	54085−54256	54184.732924	$1.27(4)\times10^{-7}$	$8.8(3)\times10^{-7}$	0[i]	—	—	Dib et al. (2008b)
AXP 4U 0142+61, $P \sim 8.69$ s, $\nu \sim 0.115094$ Hz, $\dot{\nu} \sim -0.265\times10^{-13}$ Hz/s, B $\sim 0.92\times10^{14}$ G.								
Candidate-glitch 1[j]	50170−52340	50898−51605	$(6.7(3)-8.1(3))\times10^{-8}$	$(5.8(2)\text{-}7.0(2))\times10^{-7}$	$-2.4(3)\times10^{-16}$	—	Possible profile changes	Morii et al. (2005) Chapter 2†
Candidate-glitch 2[k]	53481−54235	53809.185840	$-1.27(17)\times10^{-8}$ (long-term) $+2.0(4)\times10^{-7}$ (recovered)	$1.6(4)\times10^{-6}$	$-3.1(1.2)\times10^{-16}$	17.0(1.7)	Bursts, short-term pulsed flux increase[l], pulse profile changes	Chapter 3†
AXP RXS J170849.0−400910, $P \sim 11.00$ s, $\nu \sim 0.090896$ Hz, $\dot{\nu} \sim -1.58\times10^{-13}$ Hz/s, B $\sim 3.2\times10^{14}$ G.								
Glitch 1	51186−51614	51445.384600	$5.1(3)\times10^{-8}$	$5.6(3)\times10^{-7}$	$-8(4)\times10^{-16}$	—	—	Kaspi et al. (2000) Chapter 4†
Glitch 2	51614−52366	52016.484130	$2.2(4)\times10^{-8}$ (long-term) $+3.6(3)\times10^{-7}$ (recovered)	$4.2(2)\times10^{-6}$	$-1.1(2)\times10^{-15}$	43(2)	Possible profile changes	Kaspi & Gavriil (2003) Dall'Osso et al. (2003) Chapter 4†
Candidate-glitch 1[m,q]	52745−53140	52989.847500	$2.8(4)\times10^{-8}$	$3.1(5)\times10^{-7}$	0[i]	—	—	Chapter 4†
Candidate-glitch 2[m,n,q]	53229−53456	53366.315000	$5.5(8)\times10^{-8}$	$6.0(8)\times10^{-7}$	$-1.9(1.3)\times10^{-15}$[o]	—	Possible profile changes	Chapter 4† Israel et al. (2007)
Glitch 3	53465−53631	53549.150950	$2.46(9)\times10^{-7}$	$2.71(10)\times10^{-6}$	$-2(2)\times10^{-15}$[p]	—	—	Chapter 4† Israel et al. (2007)
AXP 1E 1841−045, $P \sim 11.78$ s, $\nu \sim 0.08487$ Hz, $\dot{\nu} \sim -2.96\times10^{-13}$ Hz/s, B $\sim 4.8\times10^{14}$ G.								
Glitch 1[r]	52300−52610	52453.132194	$2.91(10)\times10^{-7}$	$3.43(12)\times10^{-6}$	$-1.28(12)\times10^{-14}$	—	—	Chapter 4†, unpublished work
Glitch 2	52773−53244	52997.049200	$2.08(4)\times10^{-7}$	$2.45(4)\times10^{-6}$	$+4(3)\times10^{-16}$	—	—	Chapter 4†
Glitch 3	53579−53971	53823.969400	$1.17(7)\times10^{-7}$	$1.38(9)\times10^{-6}$	$+2(1)\times10^{-15}$	—	—	Chapter 4†
Glitch 4	54209−54348	54304.150312	$4.6(3)\times10^{-7}$	$5.5(4)\times10^{-6}$	$-2.1(1.4)\times10^{-14}$	—	—	Dib et al. (2008b)
AXP 1E 1048.1−5937, $P \sim 6.46$ s, $\nu \sim 0.1549$ Hz, $\dot{\nu} \sim -5.43\times10^{-13}$ Hz/s[s], B $\sim 2.7\times10^{14}$ G.								
Candidate-glitch 1[t]	52281−52485	52386.0(1.5)	$4.51(14)\times10^{-7}$	$2.91(9)\times10^{-6}$	$-4.10(15)\times10^{-14}$	—	Onset of second pulsed (and total) flux flare, large profile changes	Chapter 5†
Glitch 1	54164−54202	54185.912956	$2.52(3)\times10^{-6}$	$1.63(2)\times10^{-5}$	$-6(4)\times10^{-14}$	—	Onset of third pulsed (and total) flux flare, some profile changes	Chapter 5† Dib et al. (2008b) Tam et al. (2008a)

*Numbers in parentheses are TEMPO-reported 1σ uncertainties.

*See Appendix E for the text of the tablenotes "a" to "t".

†Chapter 2: Dib et al. (2007a), Chapter 3: Gavriil et al. (2009b), Chapter 4: Dib et al. (2008a), Chapter 5: Dib et al. (2009b).

In Chapter 4 we pointed out that detection of systematic differences in AXP and rotation-powered pulsar glitch properties would be interesting, as it could signal structural differences between magnetars and conventional pulsars. Figure 6.8 *a* and *b* is an update to Figure 4.15, and it shows the fractional and absolute amplitude distributions of radio pulsar and AXP glitches. The observation we made in Chapter 4 remains unchanged: although the fractional glitch amplitudes of AXPs are generally large by radio pulsar standards, the AXP absolute glitch amplitudes, more directly related to the angular momentum transfer during the glitch, are neither especially large nor especially small. Note however that in the three noisiest AXPs, it is difficult to distinguish between small glitches and timing noise and this could bias the number of AXP glitches towards the large amplitude.

Also potentially interesting is how often AXPs glitch compared to rotation-powered pulsar glitches. The small studied sample shows that AXPs glitch once to four times per decade. From the glitch database in Peralta (2006), it appears that pulsars as slow as the AXPs do not glitch as often. However this may be due to the long-period pulsars not being observed regularly.

Another interesting question is whether the waiting time between any two glitches in an AXP is correlated with the size of the subsequent glitch. This question is directly related to the glitch mechanism. Recall from Section 4.6 that in the standard glitch model, some angular momentum vortices inside the superfluid are pinned to the crustal nuclei, and cannot propagate outward and communicate their momentum to the crust except during glitches (Anderson & Itoh, 1975; Jones, 1998; Link & Epstein, 1996). Melatos et al. (2008) postulated that the angular momentum vortices are a self-organized critical system, that is, a system that is discrete, interaction dominated, that adjusts internally via erratic, spatially connected avalanches of local, impulsive, threshold-activated relaxation events, exactly like a sand pile. In these systems, the time between one avalanche and the next is independent of the size of the avalanches. The one exception to this is if a significant fraction of the sand pile all fell apart, in which case you would expect a longer wait until the next avalanche (Bak et al., 1987). Melatos et al. (2008) studied the waiting time in the 9 pulsars that glitched most frequently and showed that except in 2 cases where the glitches happened almost periodically, there was no correlation between the waiting time and the size of the next glitch, supporting the hypothesis that angular momentum vortices constitute a self-organized critical system. This idea is difficult to test in AXPs because of the very

small sample of glitches. However, from Figures 6.3 and 6.4, there does not seem to be a correlation between the waiting time and the size of the following glitch.

Another quantity for which it is interesting to compare AXPs to rotation-powered pulsars is the change in the frequency derivative immediately after a glitch. Unfortunately, because of the large timing noise in AXPs, this parameter is difficult to measure, except in the case of the glitches followed by a recovery (Glitch 2 in RXS J170849.0−400910, glitch 1 in 1E 2259+586, and candidate glitch 2 in 4U 0142+61, see Table 6.1). Figure 6.8 shows the instantaneous $\Delta\dot{\nu}/\dot{\nu}$ for rotation-powered pulsar glitches in Table 1.2 of Peralta (2006) when $\dot{\nu}$ is listed and has a negative sign. The arrows show the value of this parameter for two AXP glitches plus a candidate that were followed by a recovery. The AXP values are significantly large compared to those in rotation-powered pulsars, even compared to those of the Vela pulsar whose enhancement in $\dot{\nu}$ is measured *minutes* after the glitch epoch. In Section 4.6 we estimated the size of the fraction of the moment of inertia involved in the angular momentum reservoir in AXPs to be much larger than the 1% usually calculated for rotation-powered pulsars. We suggested that a fraction of the stellar core may be involved. Whether this interpretation of the enhanced $\dot{\nu}$ is true or not, the unusual recoveries definitely point to an underlying difference between AXPs and rotation-powered pulsars.

When studying glitches, it is difficult to relate measured properties such as the size of the glitch, the size of jump in $\dot{\nu}$, and the recovery fraction to internal parameters such as the internal magnetic field or the internal temperature. As pointed out by Kaspi et al. (2000) and in Section 4.6, the high temperatures of AXPs, as measured from their X-ray spectra, are at odd with the glitch observations. This is because in the crustal pinning models, the pinning force is highly temperature dependent, such that vortex lines can creep outward much more easily when the temperature is high (*e.g.* Alpar et al. 1989) leading to smaller and less frequent glitches, not what is observed. It is possible however that the surface temperatures are not necessarily telling us about the interior.

The above is not the only observation that is difficult to explain. It became clear from *RXTE* monitoring of AXPs that some AXP glitches are radiatively silent and some are not (see Section 4.6). After further investigation, it appears clear that all radiative events in AXPs are accompanied by some sort of timing event, but that the converse is not true (see Section 5.7). In rotation-powered pulsar glitches, accompanying radiative events are not seen. How does the above tie-in with the idea of

pinned angular momentum vortices? In the Melatos et al. (2008) picture, avalanches happen spontaneously. The silent glitches can be thought of as these avalanches. However, Link & Epstein (1996) postulated that the vortices need a trigger to propagate outward, such as an internal starquakes. It could be that the internal twists in the magnetic field, as they try to propagate outward, cause crustal motion, which provides the trigger specified by Link & Epstein (1996). In this picture the twist propagating outward causes both the radiative change (by heating the crust locally and by introducing a new twist in the magnetosphere), and the radiatively loud glitch (by providing the trigger necessary for the release of angular momentum vortices).

A completely different explanation for the "silent" versus "radiatively loud" glitches links the amount of energy released immediately after the glitch to the depth at which the glitch occurred. A third possibility is that all glitches are associated with a local twist, and whether we detect radiative changes or not depends on the geometry: if the bundle of twisted field lines never points towards us, then the only observable effect of this is the change in frequency.

6.8 Final Discussion and Conclusions

The AXPs were recognized as a class in 1995 (Mereghetti & Stella, 1995; Stella et al., 1996). Observationally, they are different from ordinary pulsars because of their anomalously high luminosity. Their large P and $\dot{P}$ imply an external dipolar magnetic field $\sim 10^{14}$ G (see Section 1.1.6). Their spectra are traditionally fit to a blackbody (kT $\sim$0.5 K) with a power-law tail. The magnetar model postulated that the source of power of these objects is magnetic energy, rather than accretion. One of the early goals of the AXP monitoring program with *RXTE* was to show that these pulsars are isolated and stable enough for phase-coherent timing. Shortly after the start of the program, the presence of a binary companion was ruled out (*e.g.* Kaspi et al. 1999).

But several questions remain: Did the monitoring program help understand what internally differentiates the AXPs from the rotation-powered pulsars? What is the implication of this to the progenitors and birth rates of magnetars? Does the wealth of accumulated observational information help in constraining the parameters of the magnetar model? What do all the external parameters measured with *RXTE* and other instruments (spin and glitch parameters, strength of timing noise, pulsed flux, total flux, spectral parameters) tell us about the internal parameters of the pulsar such that the internal temperature, the internal magnetic field, and the internal composition.

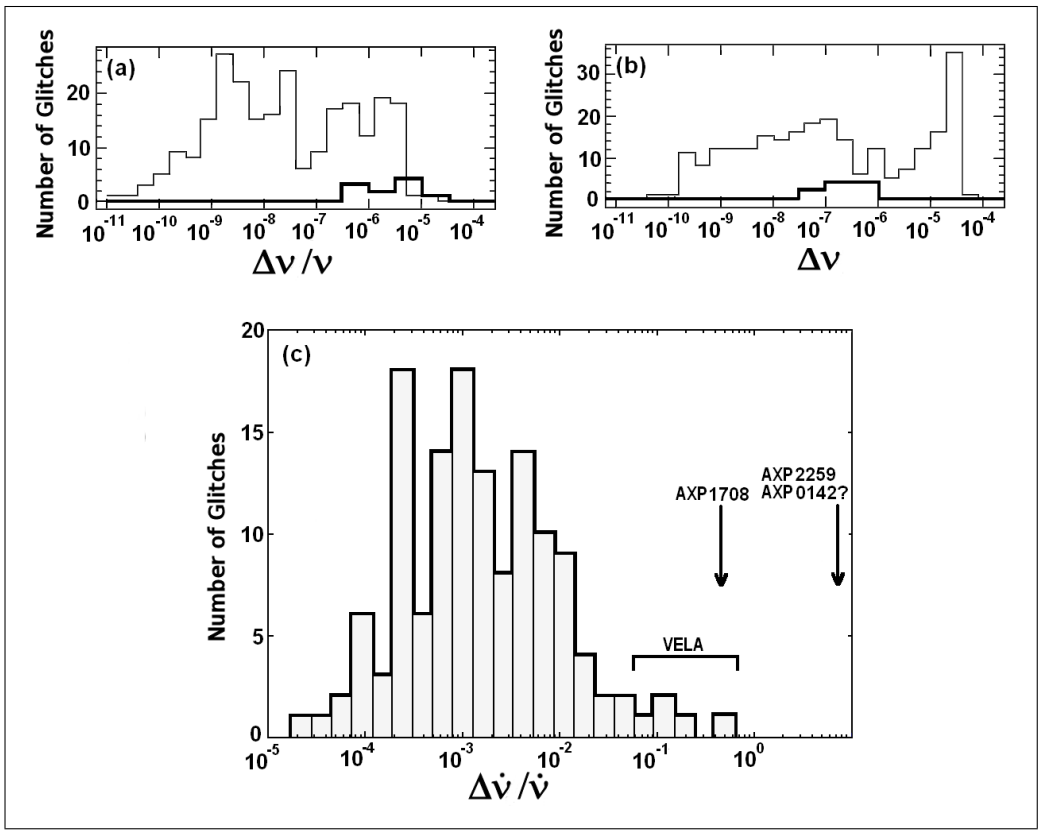

Figure 6.8 Amplitude distribution of AXP glitches (bold line) and radio pulsar glitches (thin line) for *(a)* fractional frequency jump and *(b)* absolute frequency jump (in s^{-1}). Rotation-powered pulsar glitch amplitudes are from Table 1.2 in Peralta (2006). AXP glitches included here are those listed in Table 6.1. *(a and b)* are an update of the panels in Figure 4.15. *(c)* Instantaneous $\Delta\dot{\nu}/\dot{\nu}$ at the glitch epoch for the 115 rotation-powered pulsar glitches that are followed by a negative jump in $\dot{\nu}$ in Table 1.2 of Peralta (2006). $\Delta\dot{\nu}/\dot{\nu}$ for the AXP glitches that had a quasi-exponential recovery are indicated by arrows. See Section 6.7 for more details.

And what do the external parameters tell us about the geometry of the individual AXPs?

It is very difficult to provide specific answers to the above questions and to extract conclusions because in the decade and a half during which these objects have been extensively studied, every AXP behaved mostly differently from every other AXP, and to complicate matters, no AXP underwent the same kind of outburst twice. One thing that we can say is that the theoretical model that attempts to describe the AXPs (and the SGRs) is not a simple one since it has to accommodate all the observed behaviour. In that sense the bank of accumulated observations can serve as a test for the model: if the predictions of the model contradict the observations, the model has to be modified

or eliminated.

The question of what differentiates AXPs from ordinary rotation-powered pulsars is a complicated one. It might be easier to start by asking this: if the monitored AXPs are all a part of the same class why do they behave so differently from each other? To summarize their behaviour: 1E 2259+586 is the AXP with the lowest inferred magnetic field. It has very little timing noise. One major radiative outburst was detected from this source in 2002. The outburst was accompanied by several bursts. There is evidence that a similar event happened in 1990 (Iwasawa et al., 1992). 4U 0142+61 is the AXP with the second-lowest field. It entered an active phase in 2006 in which a few bursts were detected. RXS J170849.0−400910 and 1E 1841−045 have a large inferred magnetic field compared to that of 1E 2259+586. They are the "silent" AXPs: no radiative outburst has been detected from either. Both have exhibited several glitches (discussed in Section 6.7). Both have an X-ray luminosity larger than those of all non-transient AXPs. 1E 1048.1−5937 also has a large inferred magnetic field compared to 1E 2259+586. It is a very noisy source, particularly in 2003 when it underwent large and rapid spin-down variations. It exhibited three pulsed flux flares, the first two had resolved rise times. So why do they behave so differently?

To answer this question it might be useful to remember that the internal magnetic field is continuously being twisted: turbulence in the fluid flow inside the star causes twists the internal B field lines to continuously be created (Melatos & Peralta, 2007). The different radiative behaviour from AXP to AXP could be attributed to the different ways the internal twists of the magnetic field propagate outward into the magnetosphere. That the twists propagate outward in different manners could be due to the strength and the rigidity of the crust.

AXP 1E 2259+586 could have a very strong and rigid crust such that it takes a large accumulation of magnetic potential energy stored in the internal twists to be able to break it roughly once per decade and propagate outward. If the internal twists in the B field are confined inside, there are no new twists propagating into the magnetosphere. This conserves the geometry of the external field, which can explain the timing stability and the low timing noise of the source.

RXS J170849.0−400910 and 1E 1841−045 could have an even stronger crust but they could also be at the opposite extreme: have a very weak crust, either very plastic, so that it is continuously deformed, or brittle so that it is always broken. If the crust in these sources *is* extremely weak, the internal twists could be continuously propagating outward at the locations where they are generated, which would explain

the large timing noise of these two sources, the low-level scatter in the pulsed flux, *and* the unusually large luminosity. It is unclear whether the fact that these two sources are frequent glitchers is in support or in disagreement with the idea of a weak crust.

1E 1048.1−5937 could have a non-uniform crust: regions where the crust is weak and others were it is strong and rigid. In the regions where it is weak, the twists can be continuously propagating outward, leading to continuous changes in the outside torque. This, along with the asymmetry, would explain the large timing noise of the source, like in a balloon having several locations where the air is allowed to leak. The slow-rise flares could be a sign that the crust is plastic in some of the locations where it is weak enough to allow the internal twists to propagate out. It is unclear if this model for the crust can account for the large "oscillations" seen in the spin-down in 2003.

It is unclear what would make the crust sometimes weak and sometimes not. It is tempting to claim that the strength and rigidity of the crust is associated with the location of the source on the $P - \dot{P}$ diagram (Figure 1.2): RXS J170849.0−400910, 1E 1841−045, and 1E 1048.1−5937 are all clustered in a region away from 1E 2259+586. However, this claim does not hold because the SGRs, which are closer to 1E 1048.1−5937 on the diagram, have explosive outbursts that are similar to that of 1E 2259+586. Perhaps the location on the $P - \dot{P}$ diagram is telling us about the rate at which twists are being generated internally, which is a separate question from how easily they escape.

Assuming the hypothesis above about crustal strength and rigidity are correct, what are the implications of this for ordinary pulsars? In ordinary pulsars the flow of the internal fluid is also supposed to be turbulent, generating internal twists, but the field associated with these twists is weaker and likely causes less strain on the crust. The crust itself could either be *a.* strong and rigid, *b.* weak and plastic, or *c.* weak and brittle. If *a*, then we might expect to never see any radiative events from rotation-powered pulsars because of the low magnetic potential energy associated with the twists; already in the case of 1E 2259+586 we see a radiative event only once per decade. If *c*, then continuous monitoring of rotation-powered pulsars could reveal occasional radiative outbursts when the internal twists succeed in breaking the crust. Such an outburst has already been detected from the young rotation-powered pulsar in SNR Kes 75 (Gavriil et al., 2008).

Can the above hypothesis about crustal strength and rigidity be applied to SGRs? On average, the inferred external dipolar magnetic field is stronger for SGRs than for

AXPs[4]. In the past, three SGRs have exhibited giant flares (Mazets et al., 1979b; Borkowski et al., 2004; Hurley et al., 1999). SGRs also go through periods of activity where they exhibit "intermediate flares" always accompanied by forests of bursts (*e.g.* Israel et al. 2008b). Their outbursts are more energetic than those of AXPs. The total energy released in the outbursts can be attributed to how strong and how twisted the internal magnetic field is (the two are related). This would mean that the internal field of SGRs is stronger than that of AXPs, as is the case for the inferred external field. The observed bursts during the active phases of SGRs could be interpreted as the crust of SGRs being strong and rigid like that of 1E 2259+586. This makes the internal twists harder to escape, allowing for large episodes of variability once they do succeed in escaping. And perhaps once the crust is cracked at one location it weakens it globally and allows it to break elsewhere at several locations, which would explain why the pulsed fraction does not significantly increase in some SGR outbursts.

The above discussion demonstrates that it is difficult to relate something observable, like the presence or absence of radiative outbursts and the presence or absence of bursts, to something that we cannot directly measure, such as the strength and rigidity of the crust. Ideally we would be able to relate all observable properties (the external field inferred from P and $\dot{P}$, the temperature inferred from the spectrum, the glitch parameters inferred from phase-coherent timing, the shape of the pulse profile, the timing noise which is hard to quantify, etc), to things that we cannot directly observe and measure (the internal field, the internal temperature, the size of the reservoir of angular momentum, the geometry, etc.), putting all the clues together towards a comprehensive understanding of what magnetars are, how they form, and how they evolve. However, at the moment this is a tremendously difficult task, rendered even more complicated because of the large range of variability in the sources and by the lack of specific theories.

But the outlook is not all grim: even though we have not made great progress in understanding the internal parameters and the internal composition of AXPs, we have begun to see patterns: AXP glitches appear to be fractionally large. Their recoveries (whenever there are any) appear to be unusual in that $\dot{\nu}$ is very enhanced. Every radiative change is accompanied by a timing event, often a glitch, but the converse is not true.

Continued monitoring of the AXPs will probably increase the number of patterns that we can extract from the data by expanding the database observed of glitches and

[4]Data from the magnetar catalog.

radiative outbursts. The AXP monitoring program with *RXTE* has been ongoing for 12 years, impressive in human time but very small on astronomical time scales. Continued monitoring is especially important to catch the beginning of transient events, find out how fast the flux rises, and find out what happens first: the timing glitch or the rise in the flux. Improving the observing cadence will also help pinning the glitch parameters and increase the sensitivity to smaller glitches. Since instruments like those on board of *RXTE* cannot measure the total flux of the sources, accompanying monitoring observations by imaging instruments is important. Monitoring objects similar to AXPs, such as SGRs, is also important as monitoring high-magnetic-field rotation-powered pulsars to find out how often they exhibit magnetar-like events. Work on the theoretical front is also needed to be able to relate the observable quantities to the model parameters. For example, we attempted to quantify pulse profile changes several times throughout this thesis but we have been unable to extract any clear conclusion from this analysis because of the lack of specific pulse-profile related predictions of the theoretical model.

To sum up...

Anomalous X-ray Pulsars (AXPs) are unusual and active astronomical X-ray sources with extreme properties. Much theoretical and observational progress has been made since AXPs were recognized as a distinct class of sources. On the theoretical front, the magnetar model was put forth to attempt to explain both the properties of SGRs and those of AXPs, properties which have been and are still studied with a variety of instruments from the radio to the hard X-ray bands. The monitoring program of AXPs with *the Rossi X-ray Timing Explorer*, many of the findings of which are summarized in the Chapters of this thesis, has done its part by providing insight into the timing properties of these objects, and by showing the various kinds of radiative outbursts that these sources undergo. Indeed the monitoring observations, combined with observations by imaging instruments and observations outside the X-ray band, show that AXPs exhibit a tremendous range of variable behaviour, which poses a challenge for any model that attempts to explain them. Thus, even though they have been now studied for over a decade, there remains much to be discovered and much to be explained about these mysterious objects.

Appendices

Appendix A

Some Glitch Statistics

The rotational parameters for all 287 glitches detected between 1969 and 2006 are compiled in Table 1.2 of C. Peralta's PhD thesis (Peralta, 2006). below is a short discussion on glitch statistics extracted from this table.

A.1 Glitch Frequency

We can extract the following statistics from the Table in Peralta (2006): out of the 101 pulsars that have glitched, 66 of them glitched only once. Five are exceptionally active with more than 10 glitches: the Crab pulsar, the Vela pulsar, PSR J1341−6220, PSR J0537−6910, and PSR J1740−3015. All five are young (1.2×10^3 yr $\lesssim \tau_c \lesssim$ 2.1×10^4 yr), with consequently large magnitudes of spin-down rates (6.8×10^{-12} s^{-2} $\lesssim |\dot{\nu}| \lesssim$ 3.8×10^{-10} s^{-2}). The Crab pulsar ($P \sim 0.033$ s) and the Vela pulsar ($P \sim 0.091$ s) are two of the most closely monitored pulsars. Most glitches of the Crab pulsar have a fractional amplitude $\Delta\nu/\nu \sim (0.5-25)\times10^{-9}$, while those of the Vela pulsar have $\Delta\nu/\nu \sim (1000-4000)\times10^{-9}$. The Vela pulsar glitches at approximately regular intervals (every ~ 3 yr). The Crab pulsar glitches every 2−6 yr.

A.2 Glitch Sizes

Some pulsars experience a wide range of glitch amplitudes, whereas the range is narrow in other objects. The smallest glitch was observed in PSR J0358+5413, with $\Delta\nu/\nu \sim 3\times10^{-11}$ (Janssen & Stappers, 2006); however with glitches that small, it is difficult to distinguish between glitches and timing noise. Only 5 glitches were ever reported to have a *fractional* frequency jump $\Delta\nu/\nu > 1\times10^{-5}$ as of 2008 Decem-

ber. These are: *a)* an unpublished glitch in PSR J2337+6151 with $\Delta\nu/\nu \sim 2\times10^{-4}$ (Kramer & Lyne, personal communication with C. Peralta, Peralta 2006), *b)* a glitch in radio pulsar PSR J1806-2125 with $\Delta\nu/\nu \sim 1.6\times10^{-5}$ (Hobbs et al., 2002), *c)* a glitch during the 2006 outburst of Anomalous X-ray Pulsar CXOU J164710.2-455216 with $\Delta\nu/\nu \sim 6\times10^{-5}$ (Israel et al., 2007), although this claim has been disputed due to the pulse profile changes near the time of the glitch (Woods, 2006; Gavriil et al., 2006b), *d)* a glitch in Anomalous X-ray Pulsar 1E 1048.1−5937 with $\Delta\nu/\nu \sim 1.6\times10^{-5}$ (Chapter 5 of this thesis), *e)* an *anti*-glitch in Soft Gamma Repeater 1900+14 with $\Delta\nu/\nu \sim -2.1\times10^{-5}$ (Woods et al., 1999), although this event happened during a gap in the data making it impossible to know how abrupt the decrease in frequency was, and whether it was preceded by an increase in frequency which over-recovered as is seen in PSR J1846−0258 (Livingstone et al., 2009).

Appendix B

Soft Gamma Repeaters: Characteristics of Individual Sources

The list of the currently known Soft Gamma Repeaters (not including candidate extragalactic bursting SGRs) is the following:

1. **SGR 0526−66.** This source is located in the LMC and is the only SGR in the above list with a plausible association with a supernova remnant, although other associations have been suggested (see references in Hurley et al. 1999b). Note that even this association is not universally agreed upon (Gaensler, 2004). This SGR is described in detail in Table B.1.

2. **SGR 1627−41.** This SGR is described in detail in Table B.2.

3. **SGR 1806−20.** This SGR is described in detail in Table B.3.

4. **SGR 1900+14.** This SGR is described in detail in Table B.4.

5. **Recently discovered SGR 0501+4516.** This SGR was very recently discovered. The only reports about it as of 2008 December are in the form of GCN circulars and Astronomer's Telegrams (ATELs). The source was discovered to emit X-ray bursts in 2008 August (Holland et al., 2008; Barthelmy et al., 2008; Palmer & Barthelmy, 2008). The pulsation period ($P \sim 5.76$ s) and the period derivative ($\dot{P} \sim 1.5{\times}10^{-11}$) were measured with *RXTE* (Gogus et al., 2008a,b; Woods et al., 2008a,b). The spectrum was fit to a power-law + blackbody model (*e.g.* Rea et al. 2008).

6. **Candidate Soft Gamma Repeater SGR 1801−23.** In 1997 June, during a period in which SGR 1806−20 was undergoing a phase of intense activity, two series of bursts were observed with four spacecrafts from the location of SGR 1801−23. The spectra and the distributions of the bursts were consistent with those of SGRs (Cline et al., 2000). Since the source did not show any activity since then, and since a quiescent counterpart has not been detected, it is classified as a candidate SGR.

7. **Candidate Soft Gamma Repeater SWIFT J195509+261406.** This SGR was discovered as a gamma-ray burst on 2007 June 06 (Markwardt et al., 2007). Follow-up observations in the X-rays and in the optical bands showed a point source whose X-ray luminosity (when not bursting) was orders of magnitude smaller than those of the AXPs. The observations also showed multiple soft X-ray bursts and seconds-long optical flares (Stefanescu et al., 2008; Castro-Tirado et al., 2008). The X-ray observations do not overlap with the times of the optical flares, however, they both agree on when the peak of the flaring activity was. It is debated whether the source is an Low-Mass X-ray Binary or an isolated neutron star displaying a new manifestation of magnetar activity. The source ceased all bursting activity a few days after the initial gamma-ray burst.

Overview of SGR 0526−66	
Discovery	A giant flare and several bursts was detected from SGR 0526−66 in 1979 (Mazets et al., 1979b; Cline et al., 1980). The flare was followed by an afterglow emission with an apparent 8-s periodicity.
Active Periods	1979−1983
Distance and Associations	The source of the 1979 bursts was quickly localized to the supernova remnant N49 (also known as SNR 0525-66.1) in the Large Magellanic Cloud (Evans et al., 1980) at a distance of $\sim$ 50 kpc (Capaccioli et al., 1990). This is the only SGR with a solid SNR association.
Quiescent Counterpart	Rothschild et al. (1994) identified the quiescent counterpart of SNR 0525−66.1 to be RX J052600.3−660433, a bright X-ray source ($L_x \sim 1\times10^{36}$erg s^{-1}) in data from the *ROSAT* satellite from 1992, in 0.1−2.4 keV. The quiescent counterpart was also detected in data from the *Chandra X-ray Observatory* (*CXO*) from 2000 and 2001. The soft spectrum of the source was fit to a blackbody + power-law model. The power-law index (~ -3.14) is the largest of all SGRs making this the SGR with the softest spectrum in quiescence (Kulkarni et al., 2003).
Timing	The period ($P \sim 8.05$ s) and period derivative ($\dot{P} \sim 6.5\times10^{-11}$) were measured in *CXO* data from 2000 and 2001 (Kulkarni et al., 2003), yielding a spin-down luminosity of $\sim 5\times10^{33}$erg s^{-1}.

Table B.1 Overview of SGR 0526−66

Overview of SGR 1627−41	
Discovery	An intense burst was detected from SGR 1627−41 in 1998 by the *Compton Gamma Ray Observatory* (Kouveliotou et al., 1998). The source emitted over a hundred bursts in the following six weeks that were observed by several X-ray satellites (Feroci et al., 1998; Woods et al., 1999; Hurley et al., 1999a; Smith et al., 1999; Mazets et al., 1999a).
Active Periods	June−July 1998, the source reactivated in 2008 May with a "forest of bursts" (Palmer et al., 2008; Esposito et al., 2009).
Distance and Associations	The emission from SGR 1627−41 is heavily absorbed ($N_H \sim 9{\times}10^{22}$ cm^{-2}). The distance to the source is estimated to be ~ 11 kpc (Corbel et al., 1999). Esposito et al. (2008b) newly proposed an association with a faint supernova remnant.
Quiescent Counterpart	The X-ray counterpart was discovered one month after the 1998 outburst (Woods et al., 1999). Monitoring of the counterpart showed that its 2−10 keV luminosity decayed in the years following the 1998 activity and that this was accompanied by a spectral softening (Kouveliotou et al., 2003; Mereghetti et al., 2006). The most recent reported value for the luminosity is $\sim 10^{34}$ erg s^{-1} in 2−10 keV, and the most-recent spectral fits favor a blackbody + power-law spectral model (Esposito et al., 2008b)
Timing	Pulsations with a period of $P \sim 2.6$ s were detected from the quiescent counterpart of the source 4 months after the 2008 May outburst (Esposito et al., 2008b).

Table B.2 Overview of SGR 1627−41

Overview of SGR 1806−20	
Discovery	The first soft gamma-ray burst was detected from SGR 1806−20 in 1979 (Laros et al., 1986).
Active Periods	This is the most burst-prolific SGR and it showed several periods of activity since the time of its discovery, including a giant flare in 2004 December (Borkowski et al., 2004).
Distance and Associations	SGR 1806−20 is associated with a cluster of massive stars at an estimated distance of $\sim$ 15 kpc (Corbel & Eikenberry, 2004). The absorption towards the source is large ($N_H \sim 6.8\times10^{22}$ cm^{-2} (Mereghetti et al., 2005).
Quiescent Counterpart	The X-ray counterpart of SGR 1806−20 was discovered with the *ASCA* satellite (Murakami et al., 1994). Its flux is variable. For instance, it started to rise in 2003 along with the spectrum getting harder until the 2004 giant flare after which the flux started to decay (Woods et al., 2007). The luminosity of the counter part before 2003 was $\sim 5\times10^{35}$erg s^{-1} (Woods et al., 2007; Corbel & Eikenberry, 2004).
Timing	Periodicity (P ∼7.56) was found from observations near the 1996 November active period. The spin-down was found by comparing the period found in this observation to the period subsequently found in data from 1993. (Kouveliotou et al., 1998). Woods et al. (2007) presented a long-term study of the timing of SGR 1806−20 where they showed that the frequency derivative changed from $\sim -1.5\times10^{-12}$ s^{-2} to $\sim -8.7\times10^{-12}$ s^{-2} in 2000, and that during the months leading up to the giant flare there were some possible short-lived deviations from steady spin-down. One month before the flare, all observations were suspended due to Sun-angle constraints. Extrapolating the last pre-flare and first post-flare ephemerides to the time of the flare, they find an insignificant difference between the two predicted frequencies. The spin-down luminosity of the source is $\sim 5\times10^{34}$erg s^{-1}.

Table B.3 Overview of SGR 1806−20

Overview of SGR 1900+14	
Discovery	The first three soft gamma-ray bursts were detected from SGR 1900+14 in 1979 by the *Venera 11* and the *Venera 12* space probes (Mazets et al., 1979a).
Active Periods	SGR 1900+14 had several periods of activity since 1979 including a giant flare in 1998 August (Hurley et al., 1998; Hurley et al., 1999)
Distance and Associations	SGR 1900+14 is likely associated with a cluster of massive stars at an estimated distance of 12−15 kpc (Vrba et al., 2000).
Quiescent Counterpart	Outside of the active periods the luminosity of the source is $(1.8-2.8)\times10^{35}$erg s^{-1} in the 2−10 keV band (Woods et al., 2001).
Timing	In 1998 April, between two periods of activity of SGR 1900+14, Hurley et al. (1999b) pointed the *ASCA* telescope at the location of the point source associated with the SGR (known from *ROSAT* data. They discovered pulsations with $P \sim 5.2$ s. Woods et al. (1999) discussed the history of the timing behaviour of this source and showed that a large anti-glitch appeared to have occurred in a three-months gap with no observations near the time of the giant flare, although the possibilities of a glitch which over-recovered or of a fast but not instantaneous change in the period cannot be ruled out. The period derivative varies between $5-12\times10^{-11}$ (see Woods et al. 1999 and references therein). The spin-down luminosity is $\sim2\times10^{34}$ erg s^{-1}.

Table B.4 Overview of SGR 1900+14

Appendix C

Anomalous X-ray Pulsars: Characteristics of Individual Sources

A literature review of the observational properties of the 10 sources listed in Table 1.1 and reported as of 2008 December is presented below. The AXPs monitored with *RXTE* are discussed in greater detail.

1E 2259+586

Discovery: 1E 2259+586 was first detected with the *Einstein X-ray Observatory* in 1979 as a strong compact soft X-ray source at the center of supernova remnant G109.1-1.0 (Gregory & Fahlman, 1980). Soon afterwards it was found to be an X-ray pulsar (Fahlman & Gregory, 1981). The surrounding supernova was subsequently mapped at several wavelengths. After the discovery, and for many years, 1E 2259+586 was classified as a binary system (*e.g.* Ritter 1984; Lipunov & Postnov 1985; Stella et al. 1996). Although some thought that it was a rapidly rotating white dwarf (Pandey, 1996).

1978−1984: The pulse period and X-ray spectrum of 1E 2259+586 were observed with the *Tenma* satellite in 1983, with *EXOSAT* in 1984, and with the *Ginga* satellite in 1987 (Koyama et al., 1987; Hanson et al., 1988; Morini et al., 1988; Koyama et al., 1989). The pulse period was determined to be 6.978675 ± 0.000010 s in the earlier observation, and an average spin-*down* rate ($\dot{P} \sim 5{\times}10^{-13}$) was measured, leading to an inferred dipole surface magnetic field of $0.6{\times}10^{14}$ G. The X-ray spectrum was found to be much softer than usual binary X-ray pulsars, but different from that of known isolated X-ray pulsars such as the crab. The average intensity of the source appeared not to vary significantly. The double-peaked pulse profile was found to be partially energy dependent. The observed luminosity was found to be higher than the spin-down luminosity. Observations taken in 1978 with the High Energy Astronomy Observatories *HEAO-I* were analysed and it was found that the spin-down trend extends to earlier times (Davies et al., 1990).

1978−1996: Baykal & Swank (1996) summarized the flux and pulse frequency evolution of 1E 2259+586 as measured with *Tenma*, *EXOSAT*, and *Ginga* above, with *Ginga*, *BBXRT*, and *ASCA* in Iwasawa et al. 1992 and Corbet et al. 1995, and with *ROSAT* observations from 1993. They showed that 1E 2259+586 undergoes periods of spin-up

that are consistent with accretion torques, and that the flux of the source occasionally fluctuates by a factor <10. Corbet et al. (1995) also found the spectrum to be well-fit by a combination of a power-law and a blackbody with temperature ~ 0.5 keV; this was later confirmed by Parmar et al. (1998). Mereghetti et al. (1998), reported on the first *RXTE* observations of the source in 1996, confirmed the steady spin-down, and derived stringent limits on possible binary parameters.

1997−2002: Kaspi et al. (1999) reported on 2.6 years of *RXTE* monitoring of 1E 2259+586, starting in 1997. They showed that for this time span, the pulsar spin-down rate was extremely stable, but that $\dot{\nu}$ was smaller by $\sim 10\%$ than the average spin-down inferred from incoherent frequency observations made over the last 20 yr. Then, in 2001, Gavriil & Kaspi (2002) reported on the continued timing stability of 1E 2259.1+586, for which phase coherence has been maintained over 4.5 years. They specified that the double-peaked pulse profile is not evolving with time but has some energy dependence. Because of the large field of view of *RXTE*, Kaspi et al. (1999) and Gavriil & Kaspi (2002) could not track the evolution in the luminosity of 1E 2259+586. To do this, imaging observations were needed. Between 1998 and 2002 there was a single imaging observation of the source done on 2000 January 11 with *Chandra* where they refines the position, the spectral parameters, and did phase-resolved spectroscopy. They reported a value for the flux which was consistent with the lower archival values summarized in Baykal & Swank (1996).

Outburst in 2002 June: On 2002 June 18, Kaspi et al. (2002) reported several X-ray bursts in a routine *RXTE* observation of 1E 2259+586. Follow-up analysis of *RXTE* observations of the source done by Kaspi et al. (2003) and Woods et al. (2004) showed that the source suffered a major outburst, in which over 80 X-ray bursts were detected in 4 hr. The bursts ranged in duration from 2 ms to 3 s. They simultaneously observed increases of the pulsed and persistent X-ray emission by over an order of magnitude relative to quiescent levels. Both decayed significantly during the course of the observation, and continued to decay afterwards. Correlated spectral hardening was also observed, with the spectrum subsequently softening. They also observed a pulse profile change, in which the amplitudes of the two peaks in the pulse profile were swapped. The profile relaxed back to its pre-outburst morphology after 6 days. The pulsar also underwent a sudden spin-up ($\Delta\nu/\nu \sim 4\times10^{-6}$) followed by a large (factor of ~ 2) increase in spin-down rate that persisted for more than 18 days. They also observed an infrared enhancement. Kaspi et al. (2003) specified that compared to the other AXPs monitored with *RXTE*, this had been the AXP with the most stable behaviour. They discussed how several aspects of this outbursts, especially the forest of bursts, are reminiscent of SGR flares. The bursts were further studied in Gavriil et al. (2004).

2003−2008: Zhu et al. (2008) presented an analysis of five XMM-Newton observations of the anomalous X-ray pulsar (AXP) 1E 2259+586 taken in 2004 and 2005 during its relaxation following its 2002 outburst, and showed that the decay of the total flux is well-modeled by a power law. An analysis of *RXTE* monitoring observations shows that the enhancement in the spin-down following the outburst completely ended by the end of 2002 and that the pulsed flux reached a value consistent with the pre-outburst at the end of 2005 (Chapter 6). From 2003 until the end of 2008 the spin-down was very stable and was consistent with the pre-outburst value. The source had a small glitch in 2007 March, but the spin-down and the luminosity were not affected (Dib et al. 2008b,

Chapter 6). Of the five AXPs monitored with *RXTE*, 1E 2259+586, which is the AXP with the smallest inferred magnetic field and the smallest $\dot{\nu}$, had the smallest deviations from a linear spin-down (smallest RMS timing residuals) outside of the 2002 outburst.

4U 0142+61

Discovery: Because the X-ray spectrum of 4U 0142+61 is soft, it was originally believed to be an accreting black hole. However, Israel et al. (1994) discovered X-ray pulsations in an *EXOSAT* observation from 1994. They argued that it is likely to be a Low-Mass X-ray Binary with a light companion.

1994−1999: White et al. (1996) studied the soft X-ray spectrum of the source in *ASCA* data and showed that it well fit by a combination of a blackbody + power law. They also studied archival *Einstein* and *ROSAT* data and showed that the pulsations were present there too. From the study of the spectrum, they suggested that 4U 0142+61 is probably an isolated pulsar, possibly undergoing spherical or disk accretion. The observed properties seemed consistent with the suggestion by van Paradijs et al. (1995) that this pulsar is powered by accretion from the remnant of a Thorne-Zytkow object (neutron star inside the envelope of a giant star, usually the former companion). Wilson et al. (1999) compiled a list of the measured frequencies from all archival data of 4U 0142+61 as well as from *RXTE* data from 1996 and estimated the long-term linear frequency derivative. Israel et al. (1999b) added to the above list of observations *BeppoSax* data from 1997 and 1998. Paul et al. (2000) analysed *ASCA* data of this source and showed that the spectrum was consistent with that from 1994 and remarkably stable. Similarly, Gavriil & Kaspi (2002) reported that the source was stable enough for phase-coherent timing.

2000−2006 February: Gavriil & Kaspi (2002) monitored 4U 0142+61 with *RXTE* in 1997 and in 2000 and reported on its high spin-down stability during each of the two years. Morii et al. (2005) reported on a possible glitch having occurred in 1999 after comparing the frequency obtained from an *ASCA* observation with those predicted by the 1997 and 2000 *RXTE* ephemerides. Dib et al. (2007a) (Chapter 2) showed that the glitch is possible but not necessarily required by the data. Dib et al. (2007a) also studied the timing, the pulsed flux, and the pulse profile of the source from 2000 and 2006 (see Chapter 2) and showed that the pulse profile is slowly evolving and that the 2−10 keV pulsed flux was slowly rising. The increase in the pulsed flux was determined to be 29±8% after converting the pulsed flux from counts/sec/PCU to erg/s/cm^2. There were hints that the rise in the pulsed flux was in the soft band which was consistent with the hints of spectral softening reported by Gonzalez et al. (2007) from the analysis of archival *XMM* data. Juett et al. (2002) and Patel et al. (2003) also studied the spectrum obtained from 2 *Chandra* observations in details. They confirmed the previously reported spectral parameters and found no features in the spectrum. Juett et al. (2002) discussed the implications of this for the AXP atmosphere models and for the magnetic field. It is interesting to note that this AXP was the first magnetar from which optical pulsations were detected (Kern & Martin, 2002), and remains one of only two, along with AXP 1E 1048.1−5937 (see Section 1.2.5).

2006 March−2008: 4U 0142+61 entered an active phase in 2006 March. It exhibited 6 X-ray bursts, the last was on February 2007, the pulse morphology changed and slowly recovered, and the frequency behaved as though it was recovering from a glitch, although the glitch parameters were difficult to determine because of the pulse profile changes (see Chapter 3). The pulsed flux underwent changed as well, but only for the duration

of the observations containing the bursts. *XMM* observations near the burst epochs a $\sim$ 10% increase (Gonzalez et al., 2007). The pulse profile slowly returned to the long-term average in the months following the bursts.

Note that this is the AXP with the lowest pulse fraction ($\sim$ 5%, Woods & Thompson 2006).

1RXS J170849.0−400910

Discovery: 1RXS J170849.0−400910 was discovered with *ASCA* in 1996 during a Galactic plane survey (Sugizaki et al., 1997). The observed energy spectrum in the 0.8−10 keV range was soft and was well-fitted by a power-law. The pulse period ($\sim$ 10.99 s) and the flux were not observed to vary during the 14-hr observation. An analysis of two *ROSAT* observations taken in 1994 and in 1997 showed that the source's X-ray flux was constant, allowed the measurement of a frequency derivative, and proved the absence of a massive companion. A soft blackbody component was found to improve the spectral fits, and the luminosity was estimated to be near 10^{36} erg s^{-1} (Israel et al., 1999a).

1998−2008: *RXTE* monitoring of this source started in 1998 and proved that the spin-down of 1RXS J170849.0−400910 was sufficiently stable to allow phase-coherent timing (Kaspi et al., 1999). In this period of time, 3 definite glitches and 3 candidate glitches were observed (Kaspi et al. 2000; Kaspi & Gavriil 2003; Dall'Osso et al. 2003,Chapter 5), the first of these was the first glitch detected from an AXP (Kaspi et al., 2000). Only one of these glitches was followed by a recovery (Chapter 5). From 1998 to 2008 there were no large changes in the pulsed flux. Also during this period, the source was observed very sparsely with different X-ray imaging satellites such as *Chandra* and *XMM*. Rea et al. (2005) and Campana et al. (2007) analysed the imaging observations and showed the source's phase-average flux to be variable. They also claimed a correlation between the flux variations and the glitches. This correlation is disputed however because of the chance of cross-calibration systematic errors between the different imaging instruments, because the authors allowed the neutral Hydrogen column density (N_H) to vary from observation to observation, and because they held kT fixed (Gavriil et al., 2009a).

1E 1841−045

Discovery: Originally an unresolved *Einstein* point-source near the geometrical center of supernova remnant Kes73, with a refined position from *ROSAT*, 1E 1841−045 was observed with the *ASCA* Observatory on 1993, October 11-12, as a Performance and Verification target (Vasisht & Gotthelf, 1997). The spectrum of the source was well-fitted with a soft power-law, and a periodicity search found pulsations at $\sim$ 11.78 s. The luminosity was determined to be on the order of 10^{35} erg s^{-1}.

1999−2001: Gotthelf et al. (2002) monitored 1E 1841−045 between 1999 and 2001 using *RXTE*. They found that the source was rotating with sufficient stability to derive a phase-connected timing solution. A linear ephemeris spanning these two years was found to be consistent with measurements of the pulse period in archival observations made over the previous 15 years with the *Ginga*, *ASCA*, *RXTE*, and *BeppoSAX* observatories, even though the phase residuals suggested the presence of large "timing noise". The pulsed flux during these two years was constant.

1999−2008: *RXTE* continued to monitor 1E 1841−045. Dib et al. (2008a) (Chapter 4) reported that the source exhibited three large glitches Dib et al. (2008b) reported that

the source exhibited an additional large glitch (see Chapter 3). None of the reported glitches had an exponential recovery. During the years when the source was monitored with *RXTE*, the 2−10 keV pulsed flux, defined to be the pulsed fraction multiplied by the total flux, was measured and it was very stable (Chapter 3). The question arose of whether the total flux of the source was also stable or whether any variations in the total flux were accompanied by a change in the pulsed fraction that lead to the pulsed flux staying constant. To answer this question, Zhu et al. (2009) extracted total flux measurements from the handful of archival observations of the source done with imaging telescopes. Their results showed that the total phase-averaged flux was also constant, however the results are preliminary and contamination of the data from the nearby supernova cannot be ruled out.

1E 1048.1−5937

Discovery: 1E 1048.1-5937 was discovered on 1979 July 13 during *Einstein* imaging observations of the Carina nebula. The signal was 65% pulsed in the 0.2−4 keV band, with a period of $\sim$ 6.44 s. An earlier observation failed to detect any source with strength greater than 1/10 the above signal and the source was thus thought to be variable. The X-ray spectrum was fit to a power-law, and the source was thought to be a binary (Seward et al., 1986).

1980-2001: Mereghetti (1995) showed that the spin-down derived from the *Einstein*, *Exosat*, and *Ginga* data from before 1990 is incompatible with that measured from *ROSAT* data in 1992 and 1993. The $\dot{\nu}$ derived from *ROSAT* data was $\sim -7.0\times10^{-13}$ s^{-2}, significantly more negative than that measured before 1990. This enhanced spin-down trend continued in 1995 and 1996 (Mereghetti et al., 1998). Oosterbroek et al. (1998) analysed the spectrum obtained from 1997 *BeppoSax* data and found that it is well-fit by an absorbed power-law and blackbody model. They found the spin-down to be less enhanced. Paul et al. (2000) studied *ASCA* data from 1998. They showed that the intensity of the source was similar to previous *ASCA* data but that the spin-down was remarkably unstable from observation to observation. They noted that the spin-down rate and its variations in this source are much larger than can normally be produced by an accretion disk with a very low mass accretion rate corresponding to its low X-ray luminosity. Kaspi et al. (2001) reported on $\sim$ 4 yr of *RXTE* monitoring of 1E 1048.1-5937. They showed that timing behaviour of this pulsar is different from that of the other AXPs being monitored with RXTE. They reported that the pulsar showed significant deviations from simple spin-down such that phase-coherent timing is very difficult over time spans longer than a few months. They found that the deviations from simple spin-down were not consistent with single "glitch" type events, nor were they consistent with radiative precession. They also showed that in spite of the rotational irregularities, the pulsar exhibits neither pulse profile changes nor large pulsed flux variations. Tiengo et al. (2002) analysed *XMM* data from 2000, and showed that the spectral parameters did not vary significantly from 1996 to 2000. All the data were consistent with a luminosity near 5×10^{33} erg s^{-1}.

2002-2004: Israel et al. (2002) reported variability in the IR counterpart of 1E 1048.1−5937, originally discovered by Wang & Chakrabarty (2002). Then, Mereghetti et al. (2004) reported on 2 new imaging X-ray observations: a *Chandra* observation in 2002 August and an *XMM* observation 2003 June. The pulsed fraction measured in the *XMM* observation was significantly lower than that measured in

2000, and the luminosity measured in both observations were significantly larger than that measured in 2000. In the mean time, Gavriil & Kaspi (2004) were monitoring the source with *RXTE*, and they observed 2 slow-rising pulsed flux flares. The first one peaked at the end of 2001 and the second one peaked mid-2002. Both flares lasted several months and had well-resolved few-week-long rises. A few months after the start of the decay of the second flare, the pulsar went through large (factor > 12) changes in $\ddot{\nu}$ on time scales of weeks to months, something never seen in an AXP before. It is unclear whether this timing-related episode and the preceding radiative flare are related (see Chapter 5). Gavriil et al. (2002) also reported two bursts from the direction of this source, which happened near the peak of the first pulsed flux flare. One of the two bursts was accompanied by short-term pulsed flux enhancement. Two other bursts were detected from this source at later dates. Tiengo et al. (2005) reported on an additional *XMM* observation of 1E 1048.1−5937 in 2004, where the flux was lower than in 2003 but still not back to its 2000 value, and where the pulsed fraction was higher than in 2003 but still not back to its 2000 values. They reported an anti-correlation between the total flux and the pulsed fraction.

2004-2007 March: After the above events, and from mid-2004 to 2007 March, 1E 1048.1−5937 went through a quiet phase. There was little variation in the spin-down, in the pulsed flux measured by *RXTE*, and in the total flux measured in a handful of X-ray imaging observations (Tam et al. 2008a, Dib et al. 2009b, Chapter 5). Gaensler et al. (2005) studied the region surrounding 1E 1048.1−5937 in the 21 cm wavelength (21 cm radiation is emitted by neutral hydrogen), and found that the data was consistent with an expanding hydrogen shell. They interpreted this as a wind bubble blown by a star 30−40 $M_{\odot}$ in mass, but no such star was readily identified. They suggested the wind bubble was blown by the massive progenitor of 1E 1048.1−5937 and consequently proposed that magnetars originate from more massive progenitors than do radio pulsars. This, they argues, may be evidence that the initial spin period of a neutron star is correlated with the mass of its progenitor and implies that the magnetar birthrate is only a small fraction of that for radio pulsars.

2007 march-2008: In 2007 March, the source reactivated again (Tam et al. 2008a, Dib et al. 2009b, Chapter 5). The pulsed flux rose by a factor ~ 3, and the total flux rose by a factor of ~ 7. This was simultaneous with the largest AXP glitch observed by *RXTE* (Section 1.1.14). A re-analysis of the *RXTE* data performed in Dib et al. (2009b) (Chapter 5) showed that the previous two flares observed from the source were also accompanied by timing events. Tam et al. (2008a) analysed imaging observations from before and after the glitch and also derived an anti-correlation between the pulsed fraction and the total flux. After the initial onset of the outburst, the timing and radiative parameters slowly recovered. A few months later, the source started experiencing large and rapid changes in $\ddot{\nu}$ for the second time (Chapter 6). Once again it is unclear whether these changes in the timing are related to the preceding radiative change which occurred almost a year beforehand.

Note that on average, this is the AXP with the highest pulses fraction in the 2−10 keV band ($> 50\%$, Woods & Thompson 2006).

CXOU J010043.1−721134

Discovery: The X-ray source CXOU 010043.1−721134 in the Small Magellanic Cloud (SMC) was first detected with the *Einstein* satellite in 1979, and later with *ROSAT*

and *ASCA*. Its periodicity ($P \sim 8.0$ s) was first noticed in an archival search for X-ray pulsations carried out on a 2001 *Chandra* observation of a nearby field (Lamb et al., 2002). Its X-ray luminosity was measured to be on the order of 10^{35} erg s^{-1}, assuming a distance to the SMC of 60 kpc (Lamb et al., 2002, 2003; Majid et al., 2004). A luminosity of this order of magnitude and a long spin period suggested that this object may be an Anomalous X-ray Pulsar. It is the source with the lowest interstellar absorption of all AXPs and SGRs.

2001−2005: McGarry et al. (2005) analysed *Chandra* observations of this source from 2004, and estimated the period derivative to be $\dot{P} \sim 1.88\times10^{-11}$ leading to an inferred dipole surface magnetic field of 3.9×10^{14} G. They found that the source has an X-ray luminosity of $\sim 2\times10^{35}$ erg s^{-1} (0.5−10 keV), orders of magnitude larger than the spin-down luminosity. McGarry et al. (2005) showed that the source was successfully fit to a blackbody plus a power law tail. However, Tiengo et al. (2008) performed a deep *XMM* of the source and showed that a combination of two blackbodies fit the spectrum better.

CXO J164710.2−455216

Discovery: In 2005, Muno et al. (2006b) discovered CXO J164710.2−455216 as an X-ray pulsar with a period of $\sim$ 10 s in the young Galactic cluster of massive stars Westerlund 1 during two *Chandra* observations. They placed an upper limit on the period derivative which implied that the spin-down luminosity was larger than the X-ray luminosity. Several spectral models fit the data equally well. They argued that the progenitor of this pulsar had an initial mass $>$40 M$_\odot$. The source was observed again with *XMM* on 2006 September 16, at a lower flux level (Muno et al., 2006a). The inferred long-term spin-down rate ($\dot{P} \sim 9\times10^{-12}$) implied a magnetic field of $\sim3\times10^{14}$ G. The pulse profile was single peaked (Muno et al., 2006a; Gavriil et al., 2006b).

Outburst in 2006 September: 4.3 days later, on September 21, *SWIFT* detected a 20−ms long hard X-ray burst from the source (Krimm et al., 2006a,b). The total energy contained in the burst was $\sim 10^{37}$ erg (Israel et al., 2007). Following the burst, target of opportunity observations with *Chandra*, *XMM*, and *SWIFT* took place (Gavriil et al., 2006b; Woods et al., 2006; Campana & Israel, 2006; Israel & Campana, 2006; Israel et al., 2006). All observations confirmed a flux enhancement followed by a rapid decay, changes in the spectrum, and changes in the pulse profile such that the profile became multi-peaked. Israel et al. (2007) also claimed that glitch of size $\Delta\nu/\nu \sim6\times10^{-5}$ occurred at the beginning of this outburst although the glitch size has been disputed (Woods & Kaspi 2009, Woods 2006).

XTE J1810−197

Discovery: Following the report of renewed burst activity from SGR 1806-20 on 2003 July 14 (Hurley et al., 2003), Ibrahim et al. (2003a) observed the field of view of SGR 1806−20 with *RXTE* on July 15 and reported pulsations with a period of $\sim$ 5.54 s, inconsistent with the known period of SGR 1806−20. Markwardt et al. (2003) specified that this source has been in the field of view in several *RXTE* observations since 2002, but that it only started to be detectable in 2003 January. In the two months preceding the detection, the field of view was not observed due to sun-angle constraints.

2003 (flux and timing): Ibrahim et al. (2004) analysed the *RXTE* observations of J1810−197 between 2003 January and 2003 December including a variety of observa-

tions dedicated to several of the sources that are in the very crowded field of view. They showed that the pulsar is spinning down with a $\dot{P} \sim 10^{-11}$ showing significant timing noise, implying a dipolar magnetic field of $\sim 3{\times}10^{14}$ G and an X-ray luminosity that is 2 orders of magnitude larger than the spin-down luminosity. Ibrahim et al. (2004) also showed that the source was present as an unmodulated signal in archival *ASCA* and *ROSAT* data at a level 100 times fainter than in 2003. This source is classified as a "transient" AXP because of the order-of-magnitude changes in its X-ray flux.

2003 (spectra): Gotthelf et al. (2004); Halpern & Gotthelf (2005); Gotthelf & Halpern (2005) studied the spectra of XTE J1810−197 with *Chandra* and *XMM* and archival *ROSAT* observations and showed that prior to the outburst, the spectrum could be described by a soft blackbody, and that after the outburst the spectrum could be described by either a blackbody + power law model or by a combination of two blackbodies. They showed for the first two years after the outburst, that the flux was decaying exponentially and that the spectrum was evolving.

2003 (bursts): Woods et al. (2005) studied 4 X-ray bursts detected with *RXTE* from J1810−197 that occurred between 2003 September and 2004 April. All 4 bursts occurred near pulse maximum and had a prolonged tail. The pulsar showed an enhancement in the pulsed flux in the burst tails. Woods et al. (2005) argued that the bursts detected from these three objects are sufficiently similar to one another, yet significantly different from those seen from soft gamma repeaters, that they likely represent a new class of bursts from magnetar candidates exclusive to the anomalous X-ray pulsar-like sources.

2004−2006 (Radio Data): Halpern et al. (2005) reported the detection of a radio point source at the location of J1810−197 in 2004. This was the first detection of a magnetar in the radio band. Camilo et al. (2006) observed the source in 2006 with several radio instruments and found that it was several times brighter than in 2004. They also detected pulsations at the pulsar period and showed that the radio brightness had large fluctuations. Camilo et al. (2007c) showed that the radio emission was highly polarized and that the radio spectrum was flat. Camilo et al. (2007a) studied the evolution of the pulse profile and of the timing properties of the source using several radio instruments from 2006 May to 2006 December, where they show that the source is fading and large fluctuations in the pulse shape. They also show that the source continues to spin-down but is noisy and overall, $\dot{\nu}$ was becoming significantly *less* negative.

1E 1547.0−5408

Discovery: The X-ray source 1E 1547.0−5408 was discovered in 1980 by *Einstein* during a search for X-ray counterparts of unidentified X-ray sources (Lamb & Markert, 1981). A comparison of the X-ray flux of 1E 1547.0−5408 between 1980 and 2006 observed by *Einstein*, *ASCA*, *XMM*, and *Chandra* done by Gelfand & Gaensler (2007) reveals that its absorbed 0.5−10 keV X-ray flux decreased during this period by a factor of ~ 7. Gelfand & Gaensler (2007) also showed that the spectrum was well modeled by a blackbody + power law model and that the source is located at the center of a radio shell which is possibly a previously unidentified supernova remnant. This prompted them to suggest that the source is a neutron star, and possibly a magnetar. They did not detect any X-ray pulsations from the source.

2007 June: Camilo et al. (2007b) observed 1E 1547.0−5408 with the *Parkes* radio telescope in Australia in 2007 June and detected pulsations from it at a period of ~ 2.069 s,

the smallest period seen in a magnetar. The detected pulse profile was much wider than most ordinary (rotation-powered) long period pulsars, and it fluctuated. They also estimated the $\dot{P}$ to be $2\times10-11$, which, together with the value of P, imply that this is the magnetar with the largest $|\dot{\nu}|$ and the largest spin-down luminosity (using equation1.2). This luminosity ($\sim 10^{35}$ erg s^{-1}) only slightly exceeds its X-ray luminosity derived from a contemporaneous *Swift* observations which shows that the source's s X-ray flux was $\sim$ 3 times higher than the highest historic level and $\sim$ 16 times higher than the lowest level.

2007 June−2007 October: Following the discovery of radio pulsations, Halpern et al. (2008) studied the X-ray emission of 1E 1547.0−5408 from 2007 June to 2007 October with *Swift* and *XMM*. They showed that the X-ray flux slowly faded by about $\sim$ 50% from June to August, then it stabilized. They also detected faint X-ray pulsations with *XMM*. During this period of time, $\dot{\nu}$ systematically decreased by 25% (Camilo et al., 2008).

Outburst in 2008 October: As of the end of 2008, there were no reports on the source's activity from 2008 January to 2008 October. On 2008 October 03, *SWIFT* ($<$ 1 s) soft ($<$ 100 keV) bursts in under 2 hours from the location of 1E 1547.0−5408 (Krimm et al., 2008a,b). An analysis of the *SWIFT* data following the burst showed that the source was $>$50 times brighter than the lowest reported level and that the spectrum was significantly harder (Page et al., 2008; Esposito et al., 2008a). Both *SWIFT* and *RXTE* reported X-ray pulsations and a frequency derivative more negative than the one reported in the radio data in 2007 (Esposito et al., 2008a; Dib et al., 2008c; Israel et al., 2008a). Dib et al. (2008c) also reported several bursts in the follow-up *RXTE* data. As of 2008 December, continued monitoring shows that $\dot{\nu}$ continued to become more negative in the two months following the bursts (unpublished work by this group) at a rate faster than the one reported in 2007.

This source is referred to as a "transient" magnetar because of the order of magnitude variations in its X-ray luminosity on a time scale of years, and because its quiescent flux is much fainter than that of the non transient AXPs.

J1845−0258

Discovery: Torii et al. (1998) and Gotthelf & Vasisht (1998) discovered a previously unknown X-ray source in a 1993 *ASCA* observation of the field of view of the supernova remnant Kes75. An FFT showed that this source pulsates at $P \sim 6.97$ s. The source had a low luminosity and was heavily absorbed. Gaensler et al. (1999) proposed that this source is associated with supernova remnant G29.6+0.1.

1997−2003: The field of view was observed again in 1997, 1999, 2001, and 2003 with several satellites including *Chandra* (see references in Tam et al. (2006)). In these observations, a source with a lower luminosity was discovered (AX J184453-025640). But it is unclear whether this source is the unpulsed counterpart of J1845−0258. If it is not, the upper limits set on the flux of J1845−0258 would indicate that the source was $\sim$ 350 times fainter in 2003 than it was in 1993.

Appendix D

Magnetar Neighbours (on the $P-\dot{P}$ Diagram)

Magnetars are isolated neutron stars. Observations over the whole range of the electromagnetic spectrum allowed the discovery of many classes of isolated pulsars. It is possible that the existence of all these classes reflects a large variety in the birth properties of neutron stars, but it is also possible that some of these classes are linked by evolutionary paths. The different classes are compared below, and possible evolutionary links are discussed.

At the high magnetic end, there are first **SGRs** (5 confirmed), believed to be magnetars. From Section 1.2.2 and Appendix B, we know their inferred magnetic fields ($1.5-21 \times 10^{14}$ G), their anomalously high luminosities ($\sim 10^{33-35}$ erg s^{-1}), and their quiescent soft X-ray spectra (traditionally fit to a blackbody, (kT$\sim$ 0.5 keV) + power law ($\Gamma \sim 1-3$)). During their periods of activity, SGRs exhibit hundreds of bursts and sometimes giant flares.

Also at the high magnetic end there are the **AXPs** (9 confirmed), believed to be magnetars. Three AXPs are associated with supernova remnants. From Section 1.2.3 and Appendix C, we know the inferred magnetic fields of AXPs ($0.6-7 \times 10^{14}$ G), their anomalously high luminosities ($\sim 10^{33-35}$ erg s^{-1}), and their soft X-ray spectra (traditionally fit to a blackbody, (kT$\sim$ 0.5 keV) + power law ($\Gamma \sim 2-4$)). During their periods of activity, AXPs occasionally exhibit bursts, flux variations, and variation in the timing parameters on many different time scales. Their outbursts are less energetic, and on average less frequent than those of SGRs. The 2 AXPs with the widest range of variability (both transients) have shown radio pulsations. The monitored AXPs exhibit various degrees of timing noise with 1E 2259+586, the AXP with the lowest inferred magnetic field, being the most stable (see Chapter 6).

Isolated neutron stars also include the **XDINs** (introduced in Section 1.1.5). They are a small group of seven radio-quiet, close-by X-ray pulsars, characterized by purely thermal spectra with typical temperatures $kT \lesssim 0.1$ keV and periods P in the range 3−11 s (*e.g.* Haberl 2007). Their luminosities are on the order of 10^{30-31} erg s^{-1} (Haberl, 2004); and at least in one case (source RX J0720.4−3125) this luminosity is larger than the spin-down luminosity (Haberl, 2004). The recently measured spin period derivative in two sources gives magnetic fields of $2-3 \times 10^{13}$ G (Kaplan & van Kerkwijk, 2005a,b). Studies have also revealed several absorption lines in the X-ray spectra which are interpreted as cyclotron resonance absorption lines by protons or heavy ions and/or atomic transitions shifted to X-ray energies by strong magnetic fields of the order of 10^{13} G. None of the XDINs are associated with supernova remnants.

Arguably the least-understood isolated neutron stars are those dubbed "Central Compact Objects" (**CCOs**). They are seven (as of 2007 December) radio-quiet soft X-ray sources located close to the centers of supernova remnants. They have a steady flux, but unlike young rotation-powered pulsars, they lack a discernible pulsar wind nebula (see Pavlov et al. 2004 and de Luca 2008 for reviews). The luminosity of CCOs is on the order of 10^{33-34} erg s^{-1} (10^{32} in two cases). Their spectra are best characterized as hot blackbody emission of $kT_{BB} \sim 0.4$ keV, rather than by power-law models. This is significantly hotter than radio pulsars or other radio-quiet neutron stars, and similar to the temperature of the AXPs. In two of the sources (1E 1207.4−5209 in G296.5+10.0 and and CXOU J185238.6+004020 in Kes 79), a period of a few hundreds of milliseconds has been measured, and a very small upper limit on the period derivative was found, indicating that these two sources are weakly magnetized neutron stars born spinning near the currently observed period. In one other source (CXOU J232327.9+584843 in CasA), fast-moving IR features were interpreted as interstellar dust, heated by an energetic travelling pulse, which suggested that instead of being weekly magnetized, the source could be a quiescent magnetar. The most peculiar object of this class is the compact object in RCW103, which contrary to the other members of the class, exhibits X-ray flux variations on time scales of years, and sinusoidal modulations every ~ 6.7 hours. The power source and the magnetic field of these objects (but especially the latter source) are subject of debate.

Finally, the most common type of isolated neutron stars are ordinary **rotation-powered pulsars**. Among these pulsars, there are some with a very high magnetic field. As of 2008 December, there are 53 objects with an inferred dipolar magnetic

field of B $>1\times10^{13}$ G, 8 objects with $>4\times10^{13}$ G[1], and two with B greater than that of 1E 2259+586, the AXP with the smallest inferred magnetic field. Among the 53 objects, 2 are radio-quiet, several are detected in both the radio band and the X-ray band (with the X-ray emission being fainter than that of the AXPs, and either pulsed or unpulsed), and many are X-ray quiet. The X-ray spectra are not consistent from source to source. Sometimes the emission is purely thermal (like in the case of J1718−3718, the rotation-powered pulsar with the second-highest inferred magnetic field), sometimes it is non thermal, and sometimes it is a mix (*e.g.* Pivovaroff 2000; Kaspi & McLaughlin 2005; Kaspi et al. 2004).

One interesting high-B rotation-powered pulsar is the 326−ms pulsar **J1846−0258** (the rotation-powered pulsar with the sixth-highest inferred magnetic field, B=4.9×10^{13} G), located in supernova remnant Kes75. In 2006, it exhibited magnetar-like X-ray bursts and an associated magnetar-like increase in the pulsed flux (Gavriil et al., 2008). This was accompanied by a large glitch which over-recovered (Livingstone et al., 2009). Note that unlike some magnetar glitches, rotation-powered pulsar glitches are usually not accompanied by radiative changes. In addition, the pulsar suffered a significant increase in timing noise, unprecedented for a rotation-powered pulsar. The spectrum of J1846−0258, usually fit to a power-law of index ~ -1.2 became softer (new power-law index ~ -1.9). While the spectral index became more magnetar-like, it is usually the case that the spectra of magnetars becomes harder, not softer during outburst. The reason of the softening here could be that the pulsar developed an additional thermal component. Unfortunately this is difficult to verify because of the large absorption.

The above events occured in what seems to be a transition object between rotation-powered pulsars and magnetars: The SGRs, having the highest inferred B, exhibit giant flares and are prolific bursters. The AXPs show sporadic bursts and more modest and less frequent outbursts. The pulsar in Kes 75, a rotation-powered pulsar monitored for years with *RXTE*, exhibited in 2006, for the first time, magnetar-like behaviour. This is a significant discovery because it suggests that there might be a continuum of magnetar-like activity throughout all neutron stars, which depends on spin-inferred magnetic-field strength (Gavriil et al., 2008).

A continuum of magnetar-like behaviour could be due to an evolutionary path between rotation-powered pulsars and AXPs (Lyne, 2004; Heyl & Hernquist, 2005), or to a difference between the birth properties of these two classes of objects. In

[1]Data from the ATNF pulsar catalog.

either case, the magnetic field cannot be the only parameter determining how often the magnetar-like behaviour would happen, or how strongly it will manifest, because there is an overlap between the inferred B of rotation-powered pulsars and that of the AXPs. There is also an overlap between the B of AXPs and that of SGRs. There must therefore be additional parameters causing the different behaviours of the rotation-powered pulsars and AXPs, such as their geometry or orientation (*e.g.*, Zhang & Harding 2000; Kulkarni et al. 2003). Another possibility is that magnetars originate from more massive progenitors than do radio pulsars (*e.g.* Eikenberry et al. 2004, see Section 1.2.7).

One can ask the same question about AXPs and SGRs: what explains the difference in their behaviour? One plausible notion is that AXPs and SGRs are linked temporally. Specifically, three out of the six AXPs are associated with supernova remnants, whereas only SGR 0526−66 has a plausible SNR association (Gaensler et al., 2001). If this is because the SNRs associated with SGRs have faded or been left, then this suggests that SGRs may be an older population, possibly a later stage in the evolution of AXPs. However, this hypothesis has two problems. First, the rotational periods of SGRs are similar to those of AXPs, about 10 s. Second, inferred magnetic field strengths of SGRs are similar to (and perhaps even larger than) those of AXPs (Hurley, 2000; Mereghetti, 2008). Thus, there is no strong period or B-field evolution between the two groups. Another possibility is that the difference between AXPs and SGRs is due to the configuration of the magnetic field. This configuration can be time-dependent (Kulkarni et al., 2003).

In any case, at this point, a coherent picture about the links between the different classes of isolated neutron stars has yet to emerge.

Appendix E

Notes for Table 6.1

- a. MJD range used for fitting the glitch.
- b. Total frequency jump at the glitch epoch.
- c. Total fractional frequency jump at the glitch epoch.
- d. For the glitches where no recovery was observed immediately after the glitch, this parameter represents the total jump in the frequency derivative at the glitch epoch. For the glitches with an exponential recovery, this represents the long-term increase in the frequency derivative. This parameter is extremely sensitive to the amount of data included when doing the glitch fit; Especially for noisy sources.
- e. Timescale of the exponential recovery, if any.
- f. Known radiative events associated with the glitch and observed with *RXTE*.
- g. Magnetic fields here are calculated via $B \equiv 3.2 \times 10^{19}\sqrt{P\dot{P}}$ G, where P is the spin period in seconds and $\dot{P}$ is the period derivative (see Section 1.1.6).
- h. The model used to fit this glitch consists of a combination of rising and falling exponentials, see Woods et al. (2004) for details. The $\Delta\nu$ reported here is the maximum $\Delta\nu$ observed when comparing the pre-glitch and post-glitch frequencies.
- i. Entries with the value "0" are consistent with being zero.
- j. Panels 1 and 3 of Figure 6.1 show that a glitch might have occurred in the observing gap. The ranges of $\Delta\nu$ and of $\Delta\dot{\nu}$ reported here were obtained by extending the pre-gap ephemeris (consisting of a frequency and a frequency derivative) forward, and the best-fit ephemeris of the two years after the gap (consisting of a frequency and a frequency derivative) backward to the gap boundaries.

- k. This is classified as a candidate glitch because the claim of a large sudden frequency jumps is based on a single observation, the first of an active phase which the source entered in 2007. The TOA for that observation might be affected by pulse profile changes (Chapter 3). If this TOA is omitted, the initial sudden spin-up is less significant, although it is clear that a change in $\dot{\nu}$ occured. Also, even if this TOA is omitted, extending the post-recovery ephemeris backward in time makes it look as though an anti-glitch occurred (see Figure 3.9).

- l. The glitch marked the onset of an active phase in which there was a short-term pulsed flux increase associated with the bursts (Chapter 3). There also was a subtle $29\pm8\%$ increase in the pulsed flux in the years preceding the active phase which might have been associated with the glitch (Chapter 2).

- m. These candidate glitches occurred in an observing gap. The frequency after the gap was higher than expected given the pre-gap ephemeris. Because the pre-gap and post-gap TOAs can easily be fit with a polynomial of degree 4, (Chapter 4) classified this event as a candidate glitch.

- n. Israel et al. (2007) classified this event as a glitch.

- o. The difference between the value reported in Israel et al. (2007) and that reported in Chapter 4 can be attributed to the number of TOAs used when fitting for the glitch parameters.

- p. The difference between the sign of the value reported in Israel et al. (2007) and that reported in Chapter 4 can be attributed to the number of TOAs used when fitting for the glitch parameters.

- q. In Chapter 4, we reported on three candidate glitches from RXS J170849.0−400910. Only two appear in this table because the last of the candidates happened shortly after Glitch 3, and was very close to the end of the data set available at the time, making the glitch parameters uncertain. Moreover, *several* similar events occurred in the subsequent months suggesting that candidate glitch 3 was an episode of large timing noise rather than a glitch. Also, it can easily be fit with a polynomial of degree 4.

- r. In Chapter 4, we reported two possible sets of parameters for the first glitch from 1E 1841−045. After the publication, and with the help of additional TOAs extracted from *XMM* data, we were able to constrain the fit parameters and to show that the timing solution that we reported as least likely for that glitch (the one with the smaller frequency jump) was the correct one.

- s. Starting in 2002 November, and for the next 450 days, AXP 1E 1048.1−5937 exhibited extreme $\dot{\nu}$ noise (Chapter 5). Several glitches might have occurred during this time period. The glitches that we are reporting here are from outside this period. There also has been unusual noise and a timing anomaly near the

onset of the first pulsed flux flare where a glitch might have occurred. In the table, we are reporting on the glitches that accompanied the second and the third pulsed flux flares from this source.

- t. The parameters of this glitch are not very well constrained because of unusually large pulse profile changes at the onset of the flare that is associated with the glitch (Chapter 5). This glitch is classified as a candidate glitch because the source was so noisy near this epoch, it is hard to distinguish rapid noise from sudden jumps in the frequency and frequency derivative.

Bibliography

Alpar, M. A. 2001, ApJ, 554, 1245

Alpar, M. A., Anderson, P. W., Pines, D., & Shaham, J. 1981, ApJ, 249, L29

—. 1984a, ApJ, 276, 325

—. 1984b, ApJ, 278, 791

Alpar, M. A., Chau, H. F., Cheng, K. S., & Pines, D. 1993, ApJ, 409, 345

Alpar, M. A., Cheng, K. S., & Pines, D. 1989, ApJ, 346, 823

Alpar, M. A., Langer, S. A., & Sauls, J. A. 1984c, ApJ, 282, 533

Alpar, M. A. & Pines, D. 1993, in Isolated Pulsars, ed. R. E. K. A. van Riper & C. Ho (Cambridge University Press), 17–27

Alpar, M. A., Pines, D., & Cheng, K. S. 2000, Nature, 348, 707

Anderson, P. W., Alpar, M. A., Pines, D., & Shaham, J. 1982, Phil Mag A, 45, 227

Anderson, P. W. & Itoh, N. 1975, Nature, 256, 25

Archibald, A. M., Dib, R., & Kaspi, V. M. 2009, ApJ, in preparation

Archibald, A. M., Dib, R., Livingstone, M. A., & Kaspi, V. M. 2008, in American Institute of Physics Conference Series, Vol. 983, 40 Years of Pulsars: Millisecond Pulsars, Magnetars and More, 265–267

Arzoumanian, Z., Nice, D. J., Taylor, J. H., & Thorsett, S. E. 1994, ApJ, 422, 671

Baade, W. & Zwicky, F. 1934, Proceedings of the National Academy of Science, 20, 254

Bak, P., Tang, C., & Wiesenfeld, K. 1987, Physical Review Letters, 59, 381

Barthelmy, S. D., Beardmore, A. P., Burrows, D. N., Cummings, J. R., Gehrels, N., Guidorzi, C., Holland, S. T., Kennea, J. A., Mao, J., Marshall, F. E., Pagani, C., Palmer, D. M., Perri, M., Sakamoto, T., Ukwatta, T. N., & Vetere, L. 2008, GRB Coordinates Network, 8113, 1

Baykal, A. & Swank, J. 1996, ApJ, 460, 470

Baykal, A., Swank, J. H., Strohmayer, T., & Stark, M. J. 1998, A&A, 336, 173

Beloborodov, A. M. 2008, ArXiv e-prints/0812.4873

Beloborodov, A. M. & Thompson, C. 2007, ApJ, 657, 967

Bhattacharya, D. & Soni, V. 2007, ArXiv e-prints/0705.0592

Bignami, G. F., Caraveo, P. A., Luca, A. D., & Mereghetti, S. 2003, Nature, 423, 725

Borkowski, J., Gotz, D., Mereghetti, S., Mowlavi, N., Shaw, S., & Turler, M. 2004, GRB Coordinates Network, 2920, 1

Bradt, H. V., Rothschild, R. E., & Swank, J. H. 1993, A&AS, 97, 355

Brown, E. F. & Cumming, A. 2009, ApJ, 698, 1020

Camilo, F., Cognard, I., Ransom, S. M., Halpern, J. P., Reynolds, J., Zimmerman, N., Gotthelf, E. V., Helfand, D. J., Demorest, P., Theureau, G., & Backer, D. C. 2007a, ApJ, 663, 497

Camilo, F., Kaspi, V. M., Lyne, A. G., Manchester, R. N., Bell, J. F., D'Amico, N., McKay, N. P. F., & Crawford, F. 2000, ApJ, 541, 367

Camilo, F., Ransom, S., Halpern, J., Reynolds, J., Helfand, D., Zimmerman, N., & Sarkissian, J. 2006, Nature, 442, 892

Camilo, F., Ransom, S. M., Halpern, J. P., & Reynolds, J. 2007b, ApJ, 666, L93

Camilo, F., Reynolds, J., Johnston, S., Halpern, J. P., & Ransom, S. M. 2008, ApJ, 679, 681

Camilo, F., Reynolds, J., Johnston, S., Halpern, J. P., Ransom, S. M., & van Straten, W. 2007c, ApJ, 659, L37

Campana, S. & Israel, G. L. 2006, The Astronomer's Telegram, 893, 1

Campana, S., Rea, N., Israel, G. L., Turolla, R., & Zane, S. 2007, A&A, 463, 1047

Canal, R. & Gutiérrez, J. 1997, in Astrophysics and Space Science Library, Vol. 214, White dwarfs, ed. J. Isern, M. Hernanz, & E. Garcia-Berro, 49–+

Capaccioli, M., della Valle, M., D'Onofrio, M., & Rosino, L. 1990, ApJ, 360, 63

Carroll, B. W. & Ostlie, D. A. 2006, An introduction to modern astrophysics (Benjamin Cummings; 2 edition)

Castro-Tirado, A. J., de Ugarte Postigo, A., Gorosabel, J., Jelínek, M., Fatkhullin, T. A., Sokolov, V. V., Ferrero, P., Kann, D. A., Klose, S., Sluse, D., Bremer, M., Winters, J. M., Nuernberger, D., Pérez-Ramírez, D., Guerrero, M. A., French, J., Melady, G., Hanlon, L., McBreen, B., Leventis, K., Markoff, S. B., Leon, S., Kraus, A., Aceituno, F. J., Cunniffe, R., Kubánek, P., Vítek, S., Schulze, S., Wilson, A. C., Hudec, R., Durant, M., González-Pérez, J. M., Shahbaz, T., Guziy, S., Pandey, S. B., Pavlenko, L., Sonbas, E., Trushkin, S. A., Bursov, N. N., Nizhelskij, N. A., Sánchez-Fernández, C., & Sabau-Graziati, L. 2008, Nature, 455, 506

Chatterjee, P. & Hernquist, L. 2000, ApJ, 543, 368

Chatterjee, P., Hernquist, L., & Narayan, R. 2000, ApJ, 534, 373

Cheng, K. S., Ho, C., & Ruderman, M. 1986, ApJ, 300, 500

Cline, T., Frederiks, D. D., Golenetskii, S., Hurley, K., Kouveliotou, C., Mazets, E., & van Paradijs, J. 2000, ApJ, 531, 407

Cline, T. L., Desai, U. D., Pizzichini, G., Teegarden, B. J., Evans, W. D., Klebesadel, R. W., Laros, J. G., Hurley, K., Niel, M., Vedrenne, G., Estoolin, I. V., Kouznetsov, A. V. an Zenchenko, V. M., Hovestadt, D., & Gloeckler, G. 1980, ApJ, 237, L1

Corbel, S., Chapuis, S., Dame, T. M., & Durouchoux, P. 1999, ApJ, 526, L29

Corbel, S. & Eikenberry, S. S. 2004, A&A, 419, 191

Corbet, R. H. D., Smale, A. P., Ozaki, M., Koyama, K., & Iwasawa, K. 1995, ApJ, 443, 786

Cordes, J. M. & Lazio, T. J. W. 2002, astro-ph/0207156

Cumming, A. & Macbeth, J. 2004, ApJ, 603, L37

Dall'Osso, S., Israel, G. L., Stella, L., Possenti, A., & Perozzi, E. 2003, ApJ, 599, 485

Davies, S. R., Coe, M. J., & Wood, K. S. 1990, MNRAS, 245, 268

de Luca, A. 2008, in American Institute of Physics Conference Series, Vol. 983, 40 Years of Pulsars: Millisecond Pulsars, Magnetars and More, ed. C. Bassa, Z. Wang, A. Cumming, & V. M. Kaspi, 311–319

Dedeo, S., Psaltis, D., & Narayan, R. 2001, ApJ, 559, 346

den Hartog, P. R., Hermsen, W., Kuiper, L., Vink, J., in't Zand, J. J. M., & Collmar, W. 2006, A&A, 451, 587

Dessart, L., Burrows, A., Ott, C., & Livne, E. 2007, in American Institute of Physics Conference Series, Vol. 924, The Multicolored Landscape of Compact Objects and Their Explosive Origins, ed. T. di Salvo, G. L. Israel, L. Piersant, L. Burderi, G. Matt, A. Tornambe, & M. T. Menna, 457–459

Dhillon, V. S., Marsh, T. R., Hulleman, F., van Kerkwijk, M. H., Shearer, A., Littlefair, S. P., Gavriil, F. P., & Kaspi, V. M. 2005, MNRAS, 363, 609

Dhillon, V. S., Marsh, T. R., Littlefair, S. P., Copperwheat, C. M., Kerry, P., Dib, R., Durant, M., Kaspi, V. M., Mignani, R. P., & Shearer, A. 2009, MNRAS, 394, L112

Dib, R., Gavriil, F. P., & Kaspi, V. M. 2009a, ApJ, in preparation

Dib, R., Kaspi, V., Gavriil, F., & Woods, P. 2006, The Astronomer's Telegram, 845, 1

Dib, R., Kaspi, V. M., & Gavriil, F. P. 2007a, ApJ, 666, 1152

—. 2008a, ApJ, 673, 1044

Dib, R., Kaspi, V. M., & Gavriil, F. P. 2008b, in American Institute of Physics Conference Series, Vol. 983, 40 Years of Pulsars: Millisecond Pulsars, Magnetars and More, 239–243

—. 2009b, ApJ, 702, 614

Dib, R., Kaspi, V. M., Gavriil, F. P., & Woods, P. M. 2007b, The Astronomer's Telegram, 1041, 1

—. 2008c, The Astronomer's Telegram, 1769, 1

Dierckx, F. 1975, J. Comput. Appl. Math., 1, 165

Dodson, R. G., McCulloch, P. M., & Lewis, D. R. 2002, ApJ, 564, L85

Donati, P. & Pizzochero, P. M. 2003, Phys. Rev. Lett., 90, 211101+

Duncan, R. C. & Thompson, C. 1992, ApJ, 392, L9

Durant, M. & van Kerkwijk, M. H. 2005, ApJ, 627, 376

—. 2006a, ApJ, 650, 1070

—. 2006b, ApJ, 650, 1082

Durant, M., van Kerkwijk, M. H., & Hulleman, F. 2004, in IAU Symposium, 251–+

Eichler, D. & Cheng, A. F. 1989, ApJ, 336, 360

Eichler, D., Gedalin, M., & Lyubarsky, Y. 2002, ApJ, 578, L121

Eikenberry, S. S., Matthews, K., LaVine, J. L., Garske, M. A., Hu, D., Jackson, M. A., Patel, S. G., Barry, D. J., Colonno, M. R., Houck, J. R., Wilson, J. C., Corbel, S., & Smith, J. D. 2004, ApJ, 616, 506

Ekşı, K. Y. & Alpar, M. A. 2003, ApJ, 599, 450

Ertan, Ü. & Alpar, M. A. 2003, ApJ, 593, L93

Ertan, Ü., Erkut, M. H., Eksi, K. Y., & Alpar, M. A. 2007, ApJ, 657, 441

Ertan, Ü., Göğüş, E., & Alpar, M. A. 2006, ApJ, 640, 435

Esposito, P., Israel, G. L., Rea, N., Krimm, H. A., Palmer, D. M., Gehrels, N., Helmy, S. D. B., Mereghetti, S., Tiengo, A., & Gotz, D. 2008a, The Astronomer's Telegram, 1763, 1

Esposito, P., Tiengo, A., Mereghetti, S., Israel, G. L., De Luca, A., Götz, D., Rea, N., Turolla, R., & Zane, S. 2008b, ArXiv e-prints/0812.0014

Esposito, P., Tiengo, A., Mereghetti, S., Israel, G. L., DeLuca, A., Götz, D., Rea, N., Turolla, R., & Zane, S. 2009, ApJ, 690, L105

Evans, W. D., Klebesadel, R. W., Laros, J. G., Cline, T. L., Desai, U. D., Pizzichini, G., Teegarden, B. J., Hurley, K. ands Niel, M., Vedrenne, G., Estoolin, I. V., Kouznetsov, A. V., Zenchenko, V. M., & Kurt, V. G. 1980, ApJ, 237, L7

Fahlman, G. G. & Gregory, P. C. 1981, Nature, 293, 202

Fernández, R. & Thompson, C. 2007, ApJ, 660, 615

Feroci, M., Costa, E., Amati, L., Piro, L., Martino, B., di Ciolo, L., Coletta, A., & Frontera, F. 1998, IAU Circ., 6945, 3

Flanagan, C. S. 1990, Nature, 345, 416

Flanagan, C. S. 1996, in Astronomical Society of the Pacific Conference Series, Vol. 105, IAU Colloq. 160: Pulsars: Problems and Progress, ed. S. Johnston, M. A. Walker, & M. Bailes, 103–+

Frail, D. A. & Weisberg, J. M. 1990, AJ, 100, 743

Göhler, E., Wilms, J., & Staubert, R. 2005, A&A, 433, 1079

Gaensler, B. M. 2004, Advances in Space Research, 33, 645

Gaensler, B. M., Gotthelf, E. V., & Vasisht, G. 1999, ApJ, 526, L37

Gaensler, B. M., McClure-Griffiths, N. M., Oey, M. S., Haverkorn, M., Dickey, J. M., & Green, A. J. 2005, ApJ, 620, L95

Gaensler, B. M., Slane, P. O., Gotthelf, E. V., & Vasisht, G. 2001, ApJ, 559, 963

Gavriil, F. P. 2001, Master's thesis, McGill University

Gavriil, F. P., Dib, R., & Kaspi, V. M. 2009a, ApJ, in preparation

—. 2009b, ArXiv e-prints/0905.1256, submitted to ApJ

Gavriil, F. P., Dib, R., kaspi, V. M., & Woods, P. M. 2007a, The Astronomer's Telegram, 998, 1

Gavriil, F. P., Gonzalez, M. E., Gotthelf, E. V., Kaspi, V. M., Livingstone, M. A., & Woods, P. M. 2008, Science, 319, 1802

Gavriil, F. P. & Kaspi, V. M. 2002, ApJ, 567, 1067

—. 2004, ApJ, 609, L67

Gavriil, F. P., Kaspi, V. M., & Woods, P. M. 2002, Nature, 419, 142

—. 2004, ApJ, 607, 959

Gavriil, F. P., Kaspi, V. M., & Woods, P. M. 2006a, ApJ, 641, 418

Gavriil, F. P., Kaspi, V. M., Woods, P. M., & Dib, R. 2007b, The Astronomer's Telegram, 1076, 1

Gavriil, F. P., Woods, P. M., & Kaspi, V. M. 2006b, The Astronomer's Telegram, 901, 1

Gelfand, J. D. & Gaensler, B. M. 2007, ApJ, 667, 1111

Ghosh, P., Angelini, L., & White, N. E. 1997, ApJ, 478, 713

Gogus, E., Woods, P., & Kouveliotou, C. 2008a, GRB Coordinates Network, 8118, 1

—. 2008b, The Astronomer's Telegram, 1677, 1

Gold, T. 1968, Nature, 218, 731

Goldreich, P. & Julian, W. H. 1969, ApJ, 157, 869

Gonzalez, M. E., Dib, R., Kaspi, V. M., Woods, P. M., Tam, C. R., & Gavriil, F. P. 2007, ArXiv e-prints/0708.2756, submitted to ApJ

Goossens, M. 2003, An Introduction to Plasma Astrophysics and Magnetohydrodynamics (Kindle Edition) (Springer)

Gotthelf, E. V., Gavriil, F. P., Kaspi, V. M., Vasisht, G., & Chakrabarty, D. 2002, ApJ, 564, L31

Gotthelf, E. V. & Halpern, J. P. 2005, ApJ, 632, 1075

Gotthelf, E. V., Halpern, J. P., Buxton, M., & Bailyn, C. 2004, ApJ, 605, 368

Gotthelf, E. V. & Vasisht, G. 1998, New Astronomy, 3, 293

Gotthelf, E. V., Vasisht, G., & Dotani, T. 1999, ApJ, 522, L49

Gregory, P. C. & Fahlman, G. G. 1980, Nature, 287, 805

Gunn, J. E. & Ostriker, J. P. 1970, ApJ, 160, 979

Haberl, F. 2004, Advances in Space Research, 33, 638

—. 2007, Ap&SS, 308, 181

Halpern, J. P. & Gotthelf, E. V. 2005, ApJ, 618, 874

Halpern, J. P., Gotthelf, E. V., Becker, R. H., Helfand, D. J., & White, R. L. 2005, ApJ, 632, L29

Halpern, J. P., Gotthelf, E. V., Reynolds, J., Ransom, S. M., & Camilo, F. 2008, ApJ, 676, 1178

Hanson, C. G., Dennerl, K., Coe, M. J., & Davis, S. R. 1988, A&A, 195, 114

Heger, A., Woosley, S. E., & Spruit, H. C. 2005, ApJ, 626, 350

Hessels, J. W. T., Ransom, S. M., Stairs, I. H., Freire, P. C. C., Kaspi, V. M., & Camilo, F. 2006, Science, 311, 1901

Hewish, A., Bell, S. J., Pilkington, J. D., Scott, P. F., & Collins, R. A. 1968, Nature, 217, 709

Heyl, J. S. & Hernquist, L. 1997a, ApJ, 489, L67

—. 1997b, ApJ, 491, L95

Heyl, J. S. & Hernquist, L. 1999, MNRAS, 304, L37

Heyl, J. S. & Hernquist, L. 2005, ApJ, 618, 463

Hirano, S., Shibazaki, N., Umeda, H., & Nomoto, K. 1997, ApJ, 491, 286

Hobbs, G., Lyne, A., & Kramer, M. 2006, Chinese Journal of Astronomy and Astrophysics Supplement, 6, 020000

Hobbs, G., Lyne, A. G., Joshi, B. C., Kramer, M., Stairs, I. H., Camilo, F., Manchester, R. N., D'Amico, N., Possenti, A., & Kaspi, V. M. 2002, MNRAS, 333, L7

Hobbs, G., Lyne, A. G., Kramer, M., Martin, C. E., & Jordan, C. 2004, MNRAS, 353, 1311

Holland, S. T., Barthelmy, S. D., Baumgartner, W. H., Beardmore, A. P., Burrows, D. N., Cummings, J. R., Evans, P. A., Gehrels, N., Godet, O., Guidorzi, C., Kennea, J. A., Mangano, V., Mao, J., Marshall, F. E., O'Brien, P. T., Osborne, J. P., Pagani, C., Page, K. L., Palmer, D. M., Perri, M., Sakamoto, T., Sbarufatti, B., Starling, R. L. C., Stratta, G., & Ukwatta, T. N. 2008, GRB Coordinates Network, 8112, 1

Hulleman, F., van Kerkwijk, M. H., & Kulkarni, S. R. 2004, A&A, 416, 1037

Hurley, K. 2000, in The Fifth Compton Symposium; AIP Conference Proceedings No. 510, ed. M. L. McConnell & J. M. Ryan (New York: AIP Press), 515

Hurley, K., Boggs, S. E., Smith, D. M., Duncan, R. C., Lin, R., Zoglauer, A., Krucker, S., Hurford, G., Hudson, H., Wigger, C., Hajdas, W., Thompson, C., Mitrofanov, I., Sanin, A., Boynton, W., Fellows, C., von Kienlin, A., Lichti, G., Rau, A., & Cline, T. 2005, Nature, 434, 1098

Hurley, K., Cline, T., Mazets, E., Barthelmy, S., Butterworth, P., Marshall, F., Palmer, D., Aptekar, R., Golenetskii, S., Ill'Inskii, V., Frederiks, D., McTiernan, J., Gold, R., & Trombka, T. 1999, Nature, 397, 41

Hurley, K., Cline, T., Smith, D. M., Lin, R. P., McTiernan, J., Schwartz, R., Wigger, C., Hajdas, W., Zehnder, A., von Kienlin, A., Lichti, G., Rau, A., Ricker, G., Atteia, J.-L., Kawai, N., Lamb, D., Woosley, S., Doty, J., Vanderspek, R., Villasenor, J., Crew, G., Monnelly, G., Butler, N., Jernigan, J. G., Levine, A., Martel, F., Morgan, E., Prigozhin, G., Braga, J., Manchanda, R., Pizzichini, G., Shirasaki, Y., Graziani, C., Matsuoka, M., Tamagawa, T., Torii, K., Sakamoto, T., Yoshida, A., Fenimore, E., Galassi, M., Tavenner, T., Donaghy, T., Boer, M., Olive, J.-F., & Dezalay, J.-P. 2003, GRB Coordinates Network, 2297, 1

Hurley, K., Kouveliotou, C., Mazets, E., & Cline, T. 1998, The Astronomer's Telegram, 23, 1

Hurley, K., Kouveliotou, C., Woods, P., Mazets, E., Golenetskii, S., Frederiks, D. D., Cline, T., & van Paradijs, J. 1999a, ApJ, 519, L143

Hurley, K., Li, P., Kouveliotou, C., Murakami, T., Ando, M., Strohmayer, T., van Paradijs, J., Vrba, F., Luginbuhl, C., Yoshida, A., & Smith, I. 1999b, ApJ, 510, L111

Ibrahim, A., Markwardt, C., Swank, J., Hurley, K., Cline, T., & Parke, W. 2003a, GRB Coordinates Network, 2306, 1

Ibrahim, A. I., Markwardt, C. B., Swank, J. H., Ransom, S., Roberts, M., Kaspi, V., Woods, P. M., Safi-Harb, S., Balman, S., Parke, W. C., Kouveliotou, C., Hurley, K., & Cline, T. 2004, ApJ, 609, L21

Ibrahim, A. I., Swank, J. H., & Parke, W. 2003b, ApJ, 584, L17

Israel, G. L. & Campana, S. 2006, The Astronomer's Telegram, 896, 1

Israel, G. L., Campana, S., Dall'Osso, S., Muno, M. P., Cummings, J., Perna, R., & Stella, L. 2007, ApJ, 664, 448

Israel, G. L., Covino, S., Stella, L., Campana, S., Haberl, F., & Mereghetti, S. 1999a, ApJ, 518, L107

Israel, G. L., Covino, S., Stella, L., Campana, S., Marconi, G., Mereghetti, S., Mignani, R., Negueruela, I., Oosterbroek, T., Parmar, A. N., Burderi, L., & Angelini, L. 2002, ApJ, 580, L143

Israel, G. L., Dall'Osso, S., Campana, S., Muno, M., & Stella, L. 2006, The Astronomer's Telegram, 932, 1

Israel, G. L., Esposito, P., Rea, N., Krimm, H. A., Palmer, D. M., Gehrels, N., Mereghetti, S., Tiengo, A., Senziani, F., Gotz, D., & Zane, S. 2008a, The Astronomer's Telegram, 1770, 1

Israel, G. L., Götz, D., Zane, S., Dall'Osso, S., Rea, N., & Stella, L. 2007, A&A, 476, L9

Israel, G. L., Mereghetti, S., & Stella, L. 1994, ApJ, 433, L25

Israel, G. L., Oosterbroek, T., Angelini, L., Campana, S., Mereghetti, S., Parmar, A. N., Segreto, A., Stella, L., Van Paradijs, J., & White, N. E. 1999b, A&A, 346, 929

Israel, G. L., Romano, P., Mangano, V., Dall'Osso, S., Chincarini, G., Stella, L., Campana, S., Belloni, T., Tagliaferri, G., Blustin, A. J., Sakamoto, T., Hurley, K., Zane, S., Moretti, A., Palmer, D., Guidorzi, C., Burrows, D. N., Gehrels, N., & Krimm, H. A. 2008b, ApJ, 685, 1114

Iwasawa, K., Koyama, K., & Halpern, J. P. 1992, PASJ, 44, 9

Jahan-Miri, M. 2005, New Astronomy, 11, 157

Jahoda, K., Markwardt, C. B., Radeva, Y., Rots, A. H., Stark, M. J., Swank, J. H., Strohmayer, T. E., & Zhang, W. 2006, ApJS, 163, 401

Jahoda, K., Swank, J. H., Giles, A. B., Stark, M. J., Strohmayer, T., Zhang, W., & Morgan, E. H. 1996, Proc. SPIE, 2808, 59

Jahoda, K., Swank, J. H., Giles, A. B., Stark, M. J., Strohmayer, T., Zhang, W., & Morgan, E. H. 1996, in Proc. SPIE Vol. 2808, p. 59-70, EUV, X-Ray, and Gamma-Ray Instrumentation for Astronomy VII, Oswald H. Siegmund; Mark A. Gummin; Eds., 59–70

Janssen, G. H. & Stappers, B. W. 2006, A&A, 457, 611

Jones, P. B. 1998, MNRAS, 296, 217

—. 2002, MNRAS, 335, 733

Juett, A. M., Marshall, H. L., Chakrabarty, D., & Schulz, N. S. 2002, ApJ, 568, L31

Kaplan, D. L. & van Kerkwijk, M. H. 2005a, ApJ, 628, L45

—. 2005b, ApJ, 635, L65

Kaspi, V., Dib, R., & Gavriil, F. 2006, The Astronomer's Telegram, 794, 1

Kaspi, V. M. 2007, Ap&SS, 308, 1

Kaspi, V. M., Chakrabarty, D., & Steinberger, J. 1999, ApJ, 525, L33

Kaspi, V. M. & Gavriil, F. P. 2003, ApJ, 596, L71

Kaspi, V. M., Gavriil, F. P., Chakrabarty, D., Lackey, J. R., & Muno, M. P. 2001, ApJ, 558, 253

Kaspi, V. M., Gavriil, F. P., & Woods, P. M. 2002, GRB Coordinates Network, 1432, 1

Kaspi, V. M., Gavriil, F. P., Woods, P. M., Jensen, J. B., Roberts, M. S. E., & Chakrabarty, D. 2003, ApJ, 588, L93

Kaspi, V. M. & Helfand, D. J. 2002, in Astronomical Society of the Pacific Conference Series, Vol. 271, Neutron Stars in Supernova Remnants, ed. P. O. Slane & B. M. Gaensler, 3–+

Kaspi, V. M., Lackey, J. R., & Chakrabarty, D. 2000, ApJ, 537, L31

Kaspi, V. M. & McLaughlin, M. A. 2005, ApJ, 618

Kaspi, V. M., Roberts, M. S. E., & Harding, A. K. 2004, in Compact Stellar X-ray Sources, ed. W. H. G. Lewin & M. van der Klis (UK: Cambridge University Press), in press (astro-ph/0402136)

Kern, B. & Martin, C. 2002, Nature, 415, 527

Kouveliotou, C. 2004, in CfA Colloquium Lecture Series Talk

Kouveliotou, C., Dieters, S., Strohmayer, T., van Paradijs, J., Fishman, G. J., Meegan, C. A., Hurley, K., Kommers, J., Smith, I., Frail, D., & Murakami, T. 1998, Nature, 393, 235

Kouveliotou, C., Eichler, D., Woods, P. M., Lyubarsky, Y., Patel, S. K., Göğüş, E., van der Klis, M., Tennant, A., Wachter, S., & Hurley, K. 2003, ApJ, 596, L79

Kouveliotou, C., Kippen, M., Woods, P., Richardson, G., Connaughton, V., & McCollough, M. 1998, IAU Circ., 6944, 2

Koyama, K., Hoshi, R., & Nagase, F. 1987, PASJ, 39, 801

Koyama, K., Nagase, F., Ogawara, Y., Shinoda, K., Kawai, N., Jones, M. H., Williams, O. R., Watson, M. G., Makishima, K., & Ohashi, T. 1989, PASJ, 41, 461

Krawczyk, A., Lyne, A. G., Gil, J. A., & Joshi, B. C. 2003, MNRAS, 340, 1087

Krimm, H., Barthelmy, S., Campana, S., Cummings, J., Israel, G., Palmer, D., & Parsons, A. 2006a, GRB Coordinates Network, 5581, 1

—. 2006b, The Astronomer's Telegram, 894, 1

Krimm, H. A., Beardmore, A. P., Burrows, D. N., Capalbi, M., Evans, P. A., Gehrels, N., Godet, O., Guidorzi, C., Holland, S. T., Hunsberger, S. D., Kennea, J. A., Mao, J., Markwardt, C. B., O'Brien, P. T., Oates, S. R., Page, K. L., Palmer, D. M., Romano, P., Sbarufatti, B., Starling, R. L. C., Tagliaferri, G., & Troja, E. 2008a, GRB Coordinates Network, 8311, 1

Krimm, H. A., Beardmore, A. P., Gehrels, N., Page, K. L., Palmer, D. M., Starling, R. L. C., & Ukwatta, T. N. 2008b, GRB Coordinates Network, 8312, 1

Kuiper, L., Hermsen, W., den Hartog, P., & Collmar, W. 2006, ApJ, 645, 556

Kuiper, L., Hermsen, W., & Mendez, M. 2004, ApJ, 613, 1173

Kulkarni, S. R., Kaplan, D. L., Marshall, H. L., Frail, D. A., Murakami, T., & Yonetoku, D. 2003, ApJ, 585, 948

Lamb, R. C., Fox, D. W., Macomb, D. J., & Prince, T. A. 2002, ApJ, 574, L29

—. 2003, ApJ, 599, L115

Lamb, R. C. & Markert, T. H. 1981, ApJ, 244, 94

Laros, J. G., Fenimore, E. E., Fikani, M. M., Klebesadel, R. W., & Barat, C. 1986, Nature, 322, 152

Larson, M. B. & Link, B. 2002, MNRAS, 333, 613

Lattimer, J. M. & Prakash, M. 2001, ApJ, 550, 426

Link, B. & Epstein, R. I. 1996, ApJ, 457, 844

Link, B., Epstein, R. I., & Lattimer, J. M. 1999, Phys. Rev. Lett., 83, 3362

Lipunov, V. M. & Postnov, K. A. 1985, A&A, 144, L13+

Livingstone, M. A., Kaspi, V. M., Gavriil, F. P., & Gotthelf, E. V. 2009, ApJ, in preparation

Livingstone, M. A., Kaspi, V. M., Gavriil, F. P., & Manchester, R. N. 2005, ApJ, 619, 1046

Lorimer, D. R. & Kramer, M. 2004, Handbook of Pulsar Astronomy (Handbook of pulsar astronomy, by D.R. Lorimer and M. Kramer. Cambridge observing handbooks for research astronomers, Vol. 4. Cambr idge, UK: Cambridge University Press, 2004)

Lyne, A. G. 2004, in IAU Symposium, Vol. 218, Young Neutron Stars and Their Environments, ed. F. Camilo & B. M. Gaensler, 257–+

Lyne, A. G. & Graham-Smith, F. 2005, Pulsar Astronomy (Pulsar Astronomy, by Andrew G. Lyne and Francis Graham-Smith, pp. . ISBN 0521839548. Cambridge, UK: Cambridge University Press, 2 005.)

Lyne, A. G. & Lorimer, D. R. 1994, Nature, 369, 127

Lyne, A. G., Manchester, R. N., Lorimer, D. R., Bailes, M., D'Amico, N., Tauris, T. M., Johnston, S., Bell, J. F., & Nicastro, L. 1998, MNRAS, 295, 743

Lyne, A. G., Pritchard, R. S., & Shemar, S. L. 1995, Journal of Astrophysics and Astronomy, 16, 179

Lyne, A. G., Shemar, S. L., & Graham-Smith, F. 2000, MNRAS, 315, 534

Lyne, A. G., Smith, F. G., & Pritchard, R. S. 1992, Nature, 359, 706

Lyubarsky, Y., Eichler, D., & Thompson, C. 2002, ApJ, 580, L69

Lyutikov, M. 2002, ApJ, 580, L65

—. 2003, MNRAS, 339, 623

Majid, W. A., Lamb, R. C., & Macomb, D. J. 2004, ApJ, 609, 133

Manchester, R. N., Hobbs, G. B., Teoh, A., & Hobbs, M. 2005, AJ, 129, 1993

Markwardt, C. B., Ibrahim, A. I., & Swank, J. H. 2003, The Astronomer's Telegram, 167, 1

Markwardt, C. B., Pagani, C., Evans, P., Gavriil, F. P., Kennea, J. A., Krimm, H. A., Landsman, W., & Marshall, F. E. 2007, The Astronomer's Telegram, 1102, 1

Marsden, D. & White, N. E. 2001, ApJ, 551, L155

Marsden, R., Lingenfelter, R. E., Rothschild, R. E., & Higdon, J. C. 2001, ApJ, 550, 397

Mazets, E. P., Aptekar, R. L., Butterworth, P. S., Cline, T. L., Frederiks, D. D., Golenetskii, S. V., Hurley, K., & Il'Inskii, V. N. 1999a, ApJ, 519, L151

Mazets, E. P., Cline, T. L., Aptekar', R. L., Butterworth, P. S., Frederiks, D. D., Golenetskii, S. V., Il'Inskii, V. N., & Pal'Shin, V. D. 1999b, Astronomy Letters, 25, 635

Mazets, E. P., Golenetskii, S. V., & Gur'yan, Y. A. 1979a, Sov. Astron. Lett., 5, 343

Mazets, E. P., Golenetskii, S. V., Ilinskii, V. N., Apetkar, R. L., & Guryan, Y. A. 1979b, Nature, 282, 587

McCulloch, P. M., Hamilton, P. A., McConnell, D., & King, E. A. 1990, Nature, 346, 822

McGarry, M. B., Gaensler, B. M., Ransom, S. M., Kaspi, V. M., & Veljkovik, S. 2005, ApJ, 627, L137

McKenna, J. & Lyne, A. G. 1990, Nature, 343, 349

McLaughlin, M. A., Lyne, A. G., Lorimer, D. R., Possenti, A., Manchester, R. N., Camilo, F., Stairs, I. H., Kramer, M., Burgay, M., D'Amico, N., Freire, P. C. C., Joshi, B. C., & Bhat, N. D. R. 2004, ApJ, 616, L131

Melatos, A. & Peralta, C. 2007, ApJ, 662, L99

Melatos, A., Peralta, C., & Wyithe, J. S. B. 2008, ApJ, 672, 1103

Melrose, D. 2004, in IAU Symposium, Vol. 218, Young Neutron Stars and Their Environments, ed. F. Camilo & B. M. Gaensler, 349–+

Mereghetti, S. 1995, ApJ, 455, 598

Mereghetti, S. 2008, A&A Rev., 15, 225

Mereghetti, S., Esposito, P., Tiengo, A., Turolla, R., Zane, S., Stella, L., Israel, G. L., Feroci, M., & Treves, A. 2006, A&A, 450, 759

Mereghetti, S., Israel, G. L., & Stella, L. 1998, MNRAS, 296, 689

Mereghetti, S. & Stella, L. 1995, ApJ, 442, L17

Mereghetti, S., Tiengo, A., Esposito, P., Götz, D., Stella, L., Israel, G. L., Rea, N., Feroci, M., Turolla, R., & Zane, S. 2005, ApJ, 628, 938

Mereghetti, S., Tiengo, A., Stella, L., Israel, G. L., Rea, N., Zane, S., & Oosterbroek, T. 2004, ApJ, 608, 427

Miller, M. C. 1992, MNRAS, 255, 129

Molkov, S. V., Cherepashchuk, A. M., Lutovinov, A. A., Revnivtsev, M. G., Postnov, K. A., & Sunyaev, R. A. 2004, Astronomy Letters, 30, 534

Morii, M., Kawai, N., & Shibazaki, N. 2005, ApJ, 622, 544

Morii, M., Sato, R., Kataoka, J., & Kawai, N. 2003, PASJ, 55, L45

Morini, M., Robba, N. R., Smith, A., & van der Klis, M. 1988, ApJ, 333, 777

Muno, M., Gaensler, B., Clark, J. S., Portegies Zwart, S., Pooley, D., de Grijs, R., Stevens, I., & Negueruela, I. 2006a, The Astronomer's Telegram, 902, 1

Muno, M. P. 2007, in American Institute of Physics Conference Series, Vol. 924, The Multicolored Landscape of Compact Objects and Their Explosive Origins, ed. T. di Salvo, G. L. Israel, L. Piersant, L. Burderi, G. Matt, A. Tornambe, & M. T. Menna, 166–173

Muno, M. P., Clark, J. S., Crowther, P. A., Dougherty, S. M., de Grijs, R., Law, C., McMillan, S. L. W., Morris, M. R.and Negueruela, I., Pooley, D., Portegies Zwart, S., & Yusef-Zadeh, F. 2006b, ApJ, 636, L41

Muno, M. P., Gaensler, B. M., Clark, J. S., de Grijs, R., Pooley, D., Stevens, I. R., & Portegies Zwart, S. F. 2007, MNRAS, 378, L44

Murakami, T., Tanaka, Y., Kulkarni, S. R., Ogasaka, Y., Sonobe, T., Ogawara, Y., Aoki, T., & Yoshida, T. 1994, Nature, 368, 127

Oosterbroek, T., Parmar, A. N., Mereghetti, S., & Israel, G. L. 1998, A&A, 334, 925

Özel, F. & Guver, T. 2007, ApJ, 659, L141

Pacini, F. 1967, Nature, 216, 567

Page, D., Lattimer, J. M., Prakash, M., & Steiner, A. W. 2004, ApJS, 155, 623

Page, K. L., Beardmore, A. P., & Krimm, H. A. 2008, The Astronomer's Telegram, 1761, 1

Palmer, D., Esposito, P., Barthelmy, S., Cummings, J. R., Gehrels, N., Israel, G. L., Krimm, H., Sakamoto, T., & Starling, R. 2008, GRB Coordinates Network, 7777, 1

Palmer, D. M. & Barthelmy, S. D. 2008, GRB Coordinates Network, 8115, 1

Pandey, U. S. 1996, A&A, 316, 111

Parmar, A. N., Oosterbroek, T., Favata, F., Pightling, S., Coe, M. J., Mereghetti, S., & Israel, G. L. 1998, A&A, 330, 175

Patel, S. K., Kouveliotou, C., Woods, P. M., Tennant, A. F., Weisskopf, M. C., Finger, M. H., Wilson, C. A., Göğüş, E., van der Klis, M., & Belloni, T. 2003, ApJ, 587, 367

Paul, B., Kawasaki, M., Dotani, T., & Nagase, F. 2000, ApJ, 537, 319

Pavlov, G. G., Sanwal, D., & Teter, M. A. 2004, in IAU Symposium, Vol. 218, Young Neutron Stars and Their Environments, ed. F. Camilo & B. M. Gaensler, 239–+

Peralta, C. A. 2006, PhD thesis, University of Melbourne

Pethick, C. J. & Ravenhall, D. G. 1999, in Pulsar Timing, General Relativity and the Internal Structure of Neutron Stars, ed. Z. Arzoumanian, F. Van der Hooft, & E. P. J. van den Heuvel, 177–+

Pines, D. & Alpar, M. A. 1985, Nature, 316, 27

Pivovaroff, M. J. 2000, PhD thesis, Massachusetts Institute of Technology

Radhakrishnan, V. & Manchester, R. N. 1969, Nature, 222, 228

Rea, N., Israel, G. L., Stella, L., Oosterbroek, T., Mereghetti, S., Angelini, L., Campana, S., & Covino, S. 2003, ApJ, 586, L65

Rea, N., Israel, G. L., Testa, V., Stella, L., Mereghetti, S., Tiengo, A., Oosterbroek, T., Mangano, V., Campana, S., Covino, S., Curto, G. L., & Perna, R. 2004a, The Astronomer's Telegram, 284

Rea, N., Mereghetti, S., Israel, G. L., Esposito, P., Tiengo, A., & Zane, S. 2008, The Astronomer's Telegram, 1688, 1

Rea, N., Oosterbroek, T., Zane, S., Turolla, R., Méndez, M., Israel, G. L., Stella, L., & Haberl, F. 2005, MNRAS, 361, 710

Rea, N., Testa, V., Israel, G. L., Mereghetti, S., Perna, R., Stella, L., Tiengo, A., Mangano, V., Oosterbroek, T., Mignani, R., Curto, G. L., Campana, S., & Covino, S. 2004b, A&A, 425, L5

Richards, D. W. & Comella, J. M. 1969, Nature, 222, 551

Ritter, H. 1984, A&AS, 57, 385

Rosswog, S. & Bruggen, M. 2003, Introduction to High-Energy Astrophysics (Introduction to High-Energy Astrophysics, by Stephan Rosswog and Marcus Bruggen, pp. 376. Cambridge University Press, 2003)

Rothschild, R. E., Kulkarni, S. R., & Lingenfelter, R. E. 1994, Nature, 368, 432

Ruderman, M., Zhu, T., & Chen, K. 1998, ApJ, 492, 267

Seward, F. D., Charles, P. A., & Smale, A. P. 1986, ApJ, 305, 814

Shabanova, T. V. 1998, A&A, 337, 723

—. 2005, MNRAS, 356, 1435

—. 2007, Ap&SS, 308, 591

Shapiro, S. L. & Teukolsky, S. A. 1983, Black Holes, White Dwarfs and Neutron Stars. The Physics of Compact Objects (New York: Wiley–Interscience)

Shemar, S. L. & Lyne, A. G. 1996, MNRAS, 282, 677

Smith, D. A., Bradt, H. V., & Levine, A. M. 1999, ApJ, 519, L147

Staelin, D. H. & Reifenstein, E. C. 1968, Science, 162, 1481

Stairs, I. H. 2004, Science, 304, 547

Stefanescu, A., Kanbach, G., Słowikowska, A., Greiner, J., McBreen, S., & Sala, G. 2008, Nature, 455, 503

Stella, L., Mereghetti, S., & Israel, G. L. 1996, Memorie della Societa Astronomica Italiana, 67, 1053

Strohmayer, T. E. & Ibrahim, A. I. 2000, apjl, 537, L111

Sugizaki, M., Nagase, F., Torii, K. I., Kinugasa, K., Asanuma, T., Matsuzaki, K., Koyama, K., & Yamauchi, S. 1997, PASJ, 49, L25

Swank, J. H., Jahoda, K., Zhang, W., Giles, A. B., Marshall, F. M., Bradt, H. V., Levine, A. M., Morgan, E. H., Remillard, R. A., Rothschild, R. E., Gruber, D. E., Hink, P. L., & Pelling, M. R. 1995, in The Lives of the Neutron Stars, ed. M. A. Alpar, U. Kiziloglu, & J. van Paradijs, 525–+

Tam, C. R., Gavriil, F. P., Dib, R., Kaspi, V. M., Woods, P. M., & Bassa, C. 2008a, ApJ, 677, 503

—. 2008b, ApJ, 677, 503

Tam, C. R., Kaspi, V. M., Gaensler, B. M., & Gotthelf, E. V. 2006, ApJ, 652, 548

Tam, C. R., Kaspi, V. M., van Kerkwijk, M. H., & Durant, M. 2004, ApJ, 617, L53

Thompson, C. & Beloborodov, A. M. 2005, ApJ, 634, 565

Thompson, C. & Duncan, R. C. 1993, ApJ, 408, 194

Thompson, C. & Duncan, R. C. 1993, in American Institute of Physics Conference Series, Vol. 280, American Institute of Physics Conference Series, ed. M. Friedlander, N. Gehrels, & D. J. Macomb, 1085–1089

Thompson, C. & Duncan, R. C. 1995a, in Astronomical Society of the Pacific Conference Series, Vol. 72, Millisecond Pulsars. A Decade of Surprise, ed. A. S. Fruchter, M. Tavani, & D. C. Backer, 301–+

Thompson, C. & Duncan, R. C. 1995b, MNRAS, 275, 255

Thompson, C. & Duncan, R. C. 1996, ApJ, 473, 322

—. 2001, ApJ, 561, 980

Thompson, C., Duncan, R. C., Woods, P. M., Kouveliotou, C., Finger, M. H., & van Paradijs, J. 2000, ApJ, 543, 340

Thompson, C., Lyutikov, M., & Kulkarni, S. R. 2002, ApJ, 574, 332

Tiengo, A., Esposito, P., & Mereghetti, S. 2008, ApJ, 680, L133

Tiengo, A., Göhler, E., Staubert, R., & Mereghetti, S. 2002, A&A, 383, 182

Tiengo, A., Mereghetti, S., Turolla, R., Zane, S., Rea, N., Stella, L., & Israel, G. L. 2005, A&A, 437, 997

Torii, K., Kinugasa, K., Katayama, K., Tsunemi, H., & Yamauchi, S. 1998, ApJ, 503, 843

van Paradijs, J., Taam, R. E., & van den Heuvel, E. P. J. 1995, A&A, 299, L41

Vasisht, G. & Gotthelf, E. V. 1997, ApJ, 486, L129

Vasisht, G., Gotthelf, E. V., Torii, K., & Gaensler, B. M. 2000, ApJ, 542, L49

Vrba, F. J., Henden, A. A., Luginbuhl, C. B., Guetter, H. H., Hartmann, D. H., & Klose, S. 2000, ApJ, 533, L17

Wang, N., Manchester, R. N., Pace, R., Bailes, M., Kaspi, V. M., Stappers, B. W., & Lyne, A. G. 2000, MNRAS, 317, 843

Wang, Z., Bassa, C., Kaspi, V. M., Bryant, J. J., & Morrell, N. 2008, ApJ, 679, 1443

Wang, Z. & Chakrabarty, D. 2002, ApJ, 579, L33

Wang, Z., Chakrabarty, D., & Kaplan, D. L. 2006, Nature, 440, 772

White, N. E., Angelini, L., Ebisawa, K., Tanaka, Y., & Ghosh, P. 1996, ApJ, 463, L83

Wilson, C. A., Dieters, S., Finger, M. H., Scott, D. M., & van Paradijs, J. 1999, ApJ, 513, 464

Wong, T., Backer, D. C., & Lyne, A. 2001, ApJ, 548, 447

Woods, P. 2006, in Chandra Proposal, 2296–+

Woods, P. M., Gogus, E., & Kouveliotou, C. 2008a, GRB Coordinates Network, 8166, 1

—. 2008b, The Astronomer's Telegram, 1691, 1

Woods, P. M. & Kaspi, V. M. 2009, ApJ, in preparation

Woods, P. M., Kaspi, V. M., & Gavriil, F. P. 2006, The Astronomer's Telegram, 929, 1

Woods, P. M., Kaspi, V. M., Thompson, C., Gavriil, F. P., Marshall, H. L., Chakrabarty, D., Flanagan, K., Heyl, J., & Hernquist, L. 2004, ApJ, 605, 378

Woods, P. M., Kouveliotou, C., Finger, M. H., Göğüş, E., Wilson, C. A., Patel, S. K., Hurley, K., & Swank, J. H. 2007, ApJ, 654, 470

Woods, P. M., Kouveliotou, C., Göğüş, E., Finger, M. H., Swank, J., Smith, D. A., Hurley, K., & Thompson, C. 2001, ApJ, 552, 748

Woods, P. M., Kouveliotou, C., Gavriil, F. P., Kaspi, M., V., Roberts, M. S. E., Ibrahim, A., Markwardt, C. B., Swank, J. H., & Finger, M. H. 2005, ApJ, 629, 985

Woods, P. M., Kouveliotou, C., van Paradijs, J., Finger, M. H., & Thompson, C. 1999, ApJ, 518, L103

Woods, P. M., Kouveliotou, C., van Paradijs, J., Finger, M. H., Thompson, C., Duncan, R. C., Hurley, K., Strohmayer, T., Swank, J., & Murakami, T. 1999, ApJ, 524, L55

Woods, P. M., Kouveliotou, C., van Paradijs, J., Hurley, K., Kippen, R. M., Finger, M. H., Briggs, M. S., Dieters, S., & Fishman, G. J. 1999, ApJ, 519, L139

Woods, P. M. & Thompson, C. 2006, in Compact Stellar X-ray Sources, ed. W. H. G. Lewin & M. van der Klis (UK: Cambridge University Press)

Woods, P. M. & Thompson, C. 2006, in Compact stellar X-ray sources. eds. W. H. G. Lewin and M. van der Klis

Yakovlev, D. G., Levenfish, K. P., & Shibanov, Y. A. 1999, Phys.-Uspekhi, 42, 737, astro-ph/9906456

Yakovlev, D. G. & Pethick, C. J. 2004, ARAA, 42, 169

Zavlin, V. E. & Pavlov, G. G. 2004, Memorie della Societa Astronomica Italiana, 75, 458

Zhang, B. & Harding, A. K. 2000, ApJ, 535, L51

Zhu, W., Kaspi, V. M., & Dib, R. 2009, ApJ, in preparation

Zhu, W., Kaspi, V. M., Dib, R., Woods, P. M., Gavriil, F. P., & Archibald, A. M. 2008, ApJ, 686, 520

– THE END –